Inaugural dissertation

for

obtaining the doctoral degree

of the

Combined Faculty of Mathematics, Engineering and Natural Sciences

of the

Ruprecht - Karls - University

Heidelberg

Presented by

M. Sc. Caroline Simon

born in Haan, Germany

Oral examination: 16.05.2022

Organization of microtubules and the atypical centrosome of *Plasmodium falciparum* during blood-stage schizogony

Referees: Prof. Dr. Michael Lanzer

Dr. Sergio Acebrón

Summary

Proliferation of the malaria-causing parasite *Plasmodium falciparum* in human erythrocytes is associated with all clinical symptoms of the disease. However, organization and dynamics of critical cell division structures are poorly studied. The parasite divides by an atypical division mode, called schizogony. It is characterized by several rounds of asynchronous nuclear divisions, which lead to formation of a multinucleated parasite stage before cytokinesis. Centriolar plaques, the centrosomes of *Plasmodium*, are key regulators of schizogony as they organize spindle microtubules. The detailed organization of centriolar plaques and microtubules, however, remains elusive and their dynamics have not yet been analyzed during schizogony.

Detailed visualization of microtubules and centriolar plaques has been limited by the small size of the parasite and slow adaptation of advanced microscopy techniques. In my PhD project, I established RescueSTED nanoscopy as well as correlative light and electron microscopy for *Plasmodium* blood-stages. Combining these technologies with ultrastructure expansion microscopy, I revealed the bipartite organization of the centriolar plaque consisting of an amorphous extranuclear and a DNA-free intranuclear compartment. The compartments are connected through a neck-like structure within the nuclear membrane. My data demonstrates that hemispindle microtubules are nucleated from the intranuclear region, before the centriolar plaque is further assembled as indicated by centrin accumulation at the extranuclear compartment. Using co-immunoprecipitations, I identified a novel centrin-interacting protein essential for parasite growth. The highly dynamic hemispindles are rearranged into a short mitotic spindle, organized by two duplicated centriolar plaques prior to spindle extension. Segregated nuclei then undergo consecutive rounds of asynchronous nuclear divisions at an increased pace.

By integrating state-of-the-art microscopy techniques, I provide a refined model of nuclear division and centriolar plaque organization during the highly divergent division of *P. falciparum*. Both the technological and biological progress made in this PhD project will bring forward the cell biological understanding of malaria parasite proliferation.

Zusammenfassung

Die Vermehrung des Malaria-verursachenden Parasiten *Plasmodium falciparum* in menschlichen Erythrozyten geht einher mit allen klinischen Symptomen der Erkrankung. Organisation und Dynamiken der kritischen Zellteilungsstrukturen sind jedoch nur unzureichend untersucht. Der Parasit teilt sich mit Hilfe einer untypischen Teilungsform, die Schizogonie genannt wird. Diese ist geprägt von mehreren Runden asynchroner Kernteilungen, die zur Ausbildung eines vielkernigen Parasitenstadiums führen, bevor die Zytokinese stattfindet. Zentrioläre Plaques, die Zentrosomen von *Plasmodium*, sind Hauptregulatoren der Schizogonie, da sie die Spindelmikrotubuli organisieren. Die detaillierte Organisation der zentriolären Plaques und der Mikrotubuli bleibt jedoch unklar, und ihre Dynamiken während der Schizogonie wurden bisher nicht analysiert.

Die detaillierte Visualisierung der Mikrotubuli und der zentriolären Plaques wurde bisher durch die kleine Größe des Parasiten sowie die langsame Anpassung von fortschrittlichen Mikroskopietechniken eingeschränkt. In meiner Doktorarbeit habe ich RescueSTED-Nanoskopie sowie korrelative Licht- und Elektronenmikroskopie für die Blutstadien von *Plasmodium* etabliert. Durch die Kombination dieser Techniken mit Ultrastruktur-Expansionsmikroskopie konnte ich die zweiteilige Organisation der zentriolären Plaque aufzeigen, die aus einem amorphen extranukleären und einem DNS-freien intranukleären Kompartiment zusammengesetzt ist. Die Kompartimente sind miteinander durch eine Hals-ähnliche Struktur in der Kernmembran verbunden. Meine Daten zeigen, dass Hemispindel-Mikrotubuli von der intranukleären Region aus gebildet werden, bevor die zentrioläre Plaque weiter zusammengesetzt wird, wie die Akkumulation von Centrin im extranukleären Kompartiment nahelegt. Mithilfe von Ko-Immunpräzipitationen habe ich ein neues Protein identifiziert, das mit Centrin interagiert und unentbehrlich ist für das Parasitenwachstum. Die hochdynamischen Hemispindeln werden in eine kurze mitotische Spindel umgestaltet, die von zwei duplizierten zentriolären Plaques organisiert wird, bevor sich die Spindel verlängert. Daraufhin unterlaufen die getrennten Kerne mit erhöhter Geschwindigkeit aufeinander folgende Runden asynchroner Kernteilungen.

Durch Einbeziehung von hochmodernen Mikroskopietechniken stelle ich ein verbessertes Modell der Kernteilung und der Organisation der zentriolären Plaque während der ungewöhnlichen Teilung von *P. falciparum* auf. Sowohl die technologischen als auch die biologischen Fortschritte dieser Doktorarbeit werden das zellbiologische Verständnis der Vermehrung des Malariaparasiten voranbringen.

Contents

List of Abbreviations

3D	three-dimensional
AA	Acrylamide
AB	Ammonium bicarbonate
AFC	Adaptive focus control
AFS	Automated freeze Substitution
APC	Anaphase promoting complex
APS	Ammonium persulfate
Ark	Aurora-related kinase
BB	Basal body
BF	Brightfield
BIS	N,N′-methylenbisacrylamide
BSD	Blasticidin
Cdc31	Cell division control protein 31
CDK	Cyclin-dependent kinase
cDNA	complementary DNA
CenH3	Centromere-specific histone H3
CEP	Centrosomal protein
CLEM	Correlative light and electron microscopy
CP	Centriolar plaque
CRK4	Cdc2-related protein kinase 4
cRPMI	complete RPMI
CRT	Chloroquine resistance transporter
DFMO	DL-α-difluoromethylornithine
DHFR	Dihydrofolate reductase
DIC	Differential interference contrast
DNA	Deoxyribonucleic acid
DTE	Dithioerythritol
DTT	Dithiothreitol
EB1	End binding 1
Ex-M	Expansion microscopy
Exp1	Exported protein 1
FA	Formaldehyde
F-actin	Filamentous actin
FIB-SEM	Focused ion beam scanning electron microscopy
f-MAST	*P. falciparum* merozoite assemblage of subpellicular microtubules

FS	Freeze-substitution
FWHM	Full width at half maximum
GA	Glutaraldehyde
GCP	γ-Tubulin complex component
γTuRC	γ-Tubulin ring complex
gDNA	genomic Deoxyribonucleic acid
GFP	Green fluorescent protein
GlcN	Glucosamine
glmS	Glucosamine-6-phosphate activated ribozyme
GOI	Gene of interest
HA	Hemagglutinin
hDHFR	Human dihydrofolate reductase
HEPES	4-(2-hydroxyethyl)-1-piperazineethanesulfonic acid
HPF	High-pressure freezing
hpi	Hours post infection
HSP	Heat shock protein
HyD	Hybrid detectors
IFA	Immunofluorescence assay
IMC	Inner membrane complex
IP	Immunoprecipitation
iRBCs	Infected red blood cells
iRPMI	incomplete RPMI
kDa	Kilodaltons
LNG	Lightning
MACS	Magnetic-activated cell sorting
MORN1	Membrane occupation and recognition nexus 1
mRNA	Messenger RNA
MTOC	Microtubule-organizing center
MZT1	Mitotic-spindle organizing protein 1
NA	Numerical aperture
Nek	NIMA (never in mitosis a)-related kinase
NLS	Nuclear localization sequence
NPC	Nuclear pore complex
Nup	Nucleoporin
PALM	Photo-activated localization microscopy
PBS	Phosphate-buffered saline
PCM	Pericentriolar material
PCNA	Proliferating cell nuclear antigen
PCR	Polymerase chain reaction
Pf	Plasmodium falciparum
PFA	Paraformaldehyde
Plk	Polo-like kinase

PMT	Photomultiplier tube
POC	Proteome of the centriole
PPM	Parasite plasma membrane
PSF	Point spread function
PV	Parasitophorous vacuole
PVM	Parasitophorous vacuole membrane
RBC	Red blood cell
RescueSTED	Reduction of state transition cycles STED
REX2	Ring-exported protein 2
RIPA buffer	Radioimmunoprecipitation assay buffer
RNA	Ribonucleic acid
ROS	Reactive oxygen species
RPMI	Roswell Park Memorial Institute
RT	Room temperature
SA	Sodium acrylate
SAC	Spindle assembly checkpoint
SAS	Spindle assembly abnormal protein
SBP1	Skeleton-binding protein 1
SDS-PAGE	Sodium dodecyl sulphate–polyacrylamide gel electrophoresis
SIM	Structured illumination microscopy
SiR	Silicon rhodamine
SLI	Selection-linked integration
Slp	Sfi1-like protein
SMLM	Single-molecule localization microscopy
SPB	Spindle pole body
STED	Stimulated emission depletion
STORM	Stochastic optical reconstruction microscopy
TEM	Transmission electron microscopy
TEMED	Tetramethylethylendiamine
TGD	Targeted gene disruption
UA	Uranyl acetate
U-ExM	Ultrastructure expansion microscopy
UV	Ultraviolet
WHO	World Health Organization
wt	Wild type

Chapter 1

Introduction

1.1 Malaria

Malaria is caused by unicellular, eukaryotic parasites of the *Plasmodium* genus which are transmitted to humans by female *Anopheles* mosquitoes. Malaria is a life-threatening human infectious disease most severely affecting people in sub-Saharan Africa, causing symptoms such as high fever, chills, vomiting, tiredness and headaches. Severe cerebral malaria is caused by parasite sequestration in the brain vasculature and is associated with seizures, coma and death (Idro et al., 2010). Despite global efforts to decrease human malaria burden, the decline in deaths has halted and recently numbers even increased (World Health Organization, 2021). For 2020, the World Health Organization (WHO) estimates 241 million cases and 627 000 deaths, the latter mainly attributed to children under the age of five (World Health Organization, 2021).

The term malaria is derived from italian "mal aria" ("bad air") as it was assumed that the disease is caused by the air close to swamps before Alphonse Laveran discovered *Plasmodium* as causative agent in 1880 (Cox, 2010). The protozoan *Plasmodium* belongs to the phylum of apicomplexan parasites, including various other unicellular parasites such as *Toxoplasma gondii*. More than 200 *Plasmodium* species have been described to date, causing malaria in various mammals, birds and reptiles. Five *Plasmodium* species have been identified as causative agents for human malaria, including *P. falciparum*, *P. malariae*, *P. vivax*, *P. ovale* and *P. knowlesi* (Sato, 2021). The latter was well-known to cause malaria in macaques and was only recently described to infect humans (Singh et al., 2004; Singh and Daneshvar, 2013; Ahmed and Cox-Singh, 2015; Imwong et al., 2019). Among the five species, *P. falciparum* is the deadliest human pathogen, accounting for more than 90% of all malaria deaths world-wide (Snow, 2015).

Emerging resistances of the parasite against antimalarial drugs as well as insecticide-resistant mosquito populations hamper the combat against malaria. The only approved vaccine against *Plasmodium* is RTS,S. However, RTS,S shows only a modest efficacy of 36% in children and 26% in infants after three doses and a booster (Arora et al., 2021). As a basis for new antimalarial interventions and discovery of possible

vaccine targets, it is critical to study the unusual biology of *Plasmodium* throughout its complex life cycle.

1.2 The *Plasmodium* life cycle

In its life cycle, *Plasmodium* is alternating between the human host and female *Anopheles* spp. mosquitoes, the definitive hosts (Figure 1.1). The parasite needs to overcome several bottlenecks during its life cycle in which a small number of *Plasmodium* cells replicate massively to establish stable parasite populations in distinct tissues of the two hosts. These proliferation steps exhibit a striking plasticity in terms of produced numbers of progeny and the time needed for replication. An overview of the individual proliferation steps is depicted in Figure 1.2.

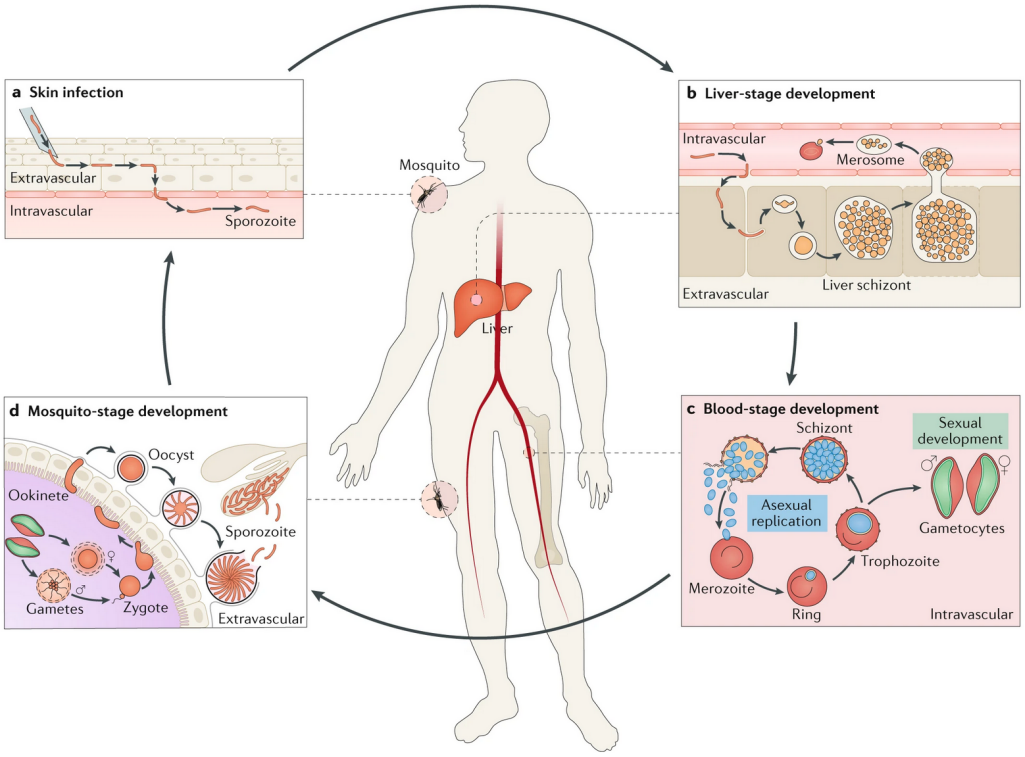

FIGURE 1.1: The *Plasmodium falciparum* life cycle. (a) After a female *Anopheles* mosquito injected sporozoites into the human skin during a blood meal, parasites are transported to the liver via the bloodstream. (b) In the liver, parasites invade hepatocytes, multiply, and merozoites are packed into merosomes. These rupture in the vasculature and release merozoites. (c) Merozoites infect red blood cells and develop from ring stages into trophozoites and asexually replicate in the schizont stage which releases around 20 merozoites into the bloodstream to infect new erythrocytes. Intraerythrocytic stages can also perform a switch and develop into gametocytes, the sexual stages of *Plasmodium*. (d) Once ingested by a mosquito during a blood meal, male and female gametocytes develop into gametes in the mosquito midgut, a process which includes rapid divisions in the males. After fertilization, the motile zygote (ookinete) develops into an oocyst which settles underneath the basal lamina of the midgut epithelium and produces several 1000 sporozoites. These are transported to the salivary glands to be transmitted to a human host during the next blood meal. For more details of the life cycle, see text. Figure from Venugopal et al. (2020).

One bottleneck is the transmission of the parasite to the mosquito. Small numbers of gametocytes, the sexual stages of *Plasmodium* developing in human erythrocytes, are

ingested by a female mosquito while taking a blood meal. In the mosquito midgut, the environmental conditions trigger male and female gametocytes to undergo gametogenesis (Sinden et al., 1996; Billker et al., 1997; Garcia et al., 1998). In this process, female macrogametocytes develop into macrogametes, while male microgametocytes complete three rounds of division in only 15 min, forming polyploid nuclei with eight genome copies (Sinden et al., 1978). Finally, eight haploid, motile microgametes are formed, which leave the erythrocyte in a process called exflagellation (Sinden et al., 2010). Male and female gametes fuse in the mosquito midgut, forming a diploid zygote. Motile zygotes, also called ookinetes, undergo meiosis, leave the midgut lumen by migration through the midgut epithelium, and finally settle between epithelium and basal lamina (Vlachou et al., 2006). Here, ookinetes develop into oocysts (Carter et al., 2007) and perform many divisions to form several thousand uninucleated sporozoites in a process called sporogony (Schrével et al., 1977; Sinden and Strong, 1978; Rosenberg and Rungsiwongse, 1991). Motile sporozoites are released from oocysts into the mosquito hemolymph by bursting or budding in vesicle-like structures (Klug and Frischknecht, 2017). Sporozoites are transported to, and invade salivary glands.

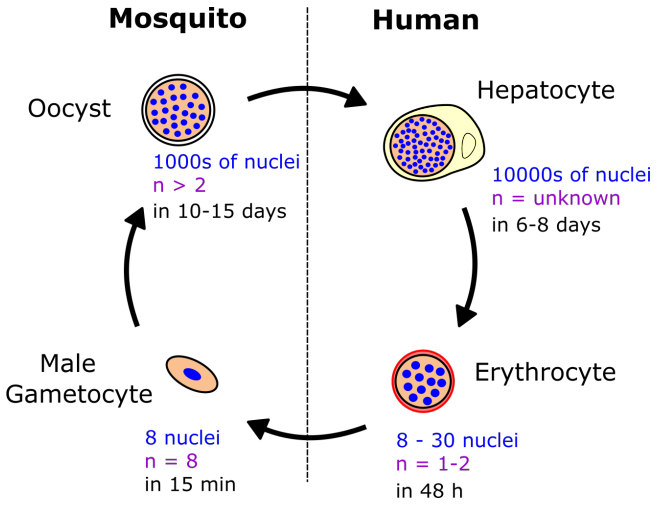

FIGURE 1.2: Schematic overview of *P. falciparum* proliferative stages across the entire life cycle. In the mosquito host, divisions take place in male gametocytes and in oocysts. After transmission to humans, parasites replicate in hepatocytes before repeated cycles of intraerythrocytic divisions lead to exponential growth of the parasite. For each stage, the number of nuclei and therefore the final number of produced progeny is depicted. "n" denotes the intermediate number of genome copies per nucleus (ploidy), before every new cell is provided with a single genome copy. Please note that proliferative stages show high plasticity in both the numbers of progeny produced and the time required for replication. Figure adapted from Simon et al. (2021b).

When the female mosquito takes another blood meal, sporozoites are deposited in the human skin along with mosquito saliva while the mosquito is probing for a blood vessel (Sidjanski and Vanderberg, 1997; Vanderberg and Frevert, 2004; Amino et al., 2006). This step represents another critical bottleneck in the parasite's life cycle as tiny numbers of sporozoites are transmitted, with reported numbers usually below 50 and only sometimes exceeding 100 or more (Beier, 1998; Frischknecht et al., 2004; Medica

and Sinnis, 2005). In addition, not all of the transmitted parasites will make it to the human liver, where the next proliferation step occurs. Instead, some stay in the skin or migrate to lymph nodes and will be eliminated (Amino et al., 2006). Only those sporozoites that find a blood vessel and enter the lumen are transported to the liver via the bloodstream (Frevert et al., 2005; Prudêncio et al., 2006). Sporozoites glide along liver sinusoids and reach hepatocytes by transmigration through a Kupffer or endothelial cell (Frevert et al., 2005; Tavares et al., 2013). Further, sporozoites transmigrate through several hepatocytes before developing in one hepatocyte inside a parasitophorous vacuole (Mota et al., 2001). Now, compensation for the low number of parasites transmitted to the human host occurs by massive proliferation. For *P. falciparum*, in 6-8 days tens of thousands of new parasites are produced in a single hepatocyte by asexual divisions, also known as liver-stage schizogony (Shortt et al., 1951; Vaughan and Kappe, 2017). Although parasites replicate massively, liver stages are not associated with any clinical symptoms of malaria. The new parasite stages, the merozoites, are packed into vesicles, so-called merosomes, and transported via the bloodstream into small lung capillaries (Sturm et al., 2006). Upon merosome burst, merozoites are released and actively invade human red blood cells. During invasion, a moving junction is formed giving rise to the parasitophorous vacuole, which is derived from the erythrocyte membrane and surrounds the parasite (Cowman et al., 2017; Geoghegan et al., 2021).

In the parasitophorous vacuole, parasites develop from mobile ring stages into stationary, fast-growing trophozoites, with both stages profoundly remodelling the host erythrocyte (Maier et al., 2009; Grüring et al., 2011). The parasite takes up hemoglobin from the host cell to attain amino acids by hemoglobin digestion (Pishchany and Skaar, 2012). However, toxic heme is a by-product of this reaction which is further detoxified by the parasite into the non-toxic biocrystal hemozoin (Coronado et al., 2014). Hemozoin is stored in the digestive vacuole of the parasite and starts accumulating in trophozoite stages. Trophozoites further develop into schizonts which undergo several rounds of asynchronous nuclear divisions without cytokinesis, leading to formation of multinucleated cells (Leete and Rubin, 1996). This division mode is known as blood-stage schizogony. In the course of schizogony, 8 to 30 merozoites are produced by a single *P. falciparum* parasite (Reilly et al., 2007; Dorin-Semblat et al., 2008; Stewart et al., 2020), with an average of 22 and 20 merozoites measured in two recent fluorescent microscopy-based studies (Garg et al., 2015; Simon et al., 2021b). Mononuclear merozoites are released into the bloodstream upon egress and can invade new red blood cells for further exponential growth. Blood-stage development and egress are synchronized in the human host, releasing new invasive merozoites after a fixed time, e.g. every 48 hours after infection with *P. falciparum*. The synchronous release of massively replicated parasites into the blood is associated with periodic fever in patients suffering from malaria (Hawking, 1970; Garcia et al., 2001). In addition to these symptoms directly associated with *Plasmodium* replication, intraerythroytic development is also involved in symptoms of severe malaria cases.

Mediated by *P. falciparum* erythrocyte membrane protein-1 (PfEMP1) presentation in membrane-protrusions, so-called knobs, late-stage infected erythrocytes can cytoadhere to endothelial cells in the brain vasculature, causing severe neurological complications (MacPherson et al., 1985).

In a small proportion of human red blood cells, parasites will not replicate, but will develop into sexual stages: male microgametocytes and female macrogametocytes via gametocytogenesis. Five distinct stages during gametocyte development have been characterized (Sinden and Smalley, 1979). While early development of gametocytes mainly takes place in the bone marrow (stage I-IV gametocytes), mature gametocytes of stage V can be found in the bloodstream (Joice et al., 2014; Aguilar et al., 2014). Here, male and female gametocytes can again be taken up by a female mosquito during a blood meal, closing the life cycle of *Plasmodium*.

1.3 Schizogony in *Plasmodium* blood-stages

P. falciparum blood-stage parasites divide by schizogony (Leete and Rubin, 1996) (Figure 1.3). Schizogony is characterized by multiple DNA replications and nuclear divisions, which are not directly followed by cytokinesis (Francia and Striepen, 2014). Thereby, parasites with multiple genome copies are formed before cytokinesis, assembly of daughter cells and egress.

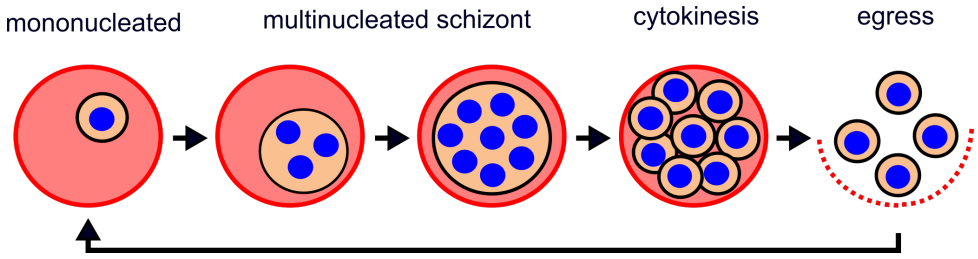

FIGURE 1.3: Schematic of *Plasmodium falciparum* blood-stage schizogony. Inside human erythrocytes, mononucleated parasites undergo several asynchronous rounds of nuclear divisions. Thereby, multinucleated schizonts are formed with uneven numbers of nuclei, which share a common cytoplasm. After a final synchronous division, cytokinesis occurs. Infectious daughter parasites are assembled and released into the bloodstream upon egress. Dark red, erythrocyte plasma membrane; red, erythrocyte cytoplasm; black, parasite plasma membrane; beige, *Plasmodium* cytoplasm; blue, nucleus. Figure from Simon et al. (2021a).

The first DNA replication during *P. falciparum* blood-stage schizogony starts around 24 to 32 hours post infection (hpi) of the erythrocyte (Inselburg and Banyal, 1984; Arnot et al., 2011; Ganter et al., 2017). Onset of DNA replication is regulated by the cdc2-related protein kinase 4 (CRK4), as CRK4-depleted parasites show inhibited DNA replication and a complete block in nuclear division (Ganter et al., 2017). In the course of schizogony, replication dynamics change from faster synthesis rates and replication origins that are widely spaced to slower synthesis rates and origins spaced more closely (Stanojcic et al., 2017).
Two models on the cell cycle in schizonts were described in the literature: One was

favoring nuclear division after each DNA replication (Leete and Rubin, 1996; Arnot et al., 2011), another one multiple rounds of DNA synthesis followed by multiple divisions (Arnot and Gull, 1998; Gupta et al., 2018). In a recent study, Klaus et al. (2021) disentangled these events and clearly demonstrated alternating rounds of DNA replication (S phase) and nuclear division (comparable to M phase). Therefore, multinucleated cells (coenocytes) are formed during schizogony with a maximum of two genome copies per nucleus (immediately before nuclear division) (Klaus et al., 2021). This is in contrast to divisions in mosquito stages, in which polyploid nuclei are produced in microgametocytes and oocysts (Figure 1.2).

Although schizont nuclei share a common cytoplasm, divisions are asynchronous. Evidence of asynchrony was provided by uneven numbers of nuclei (Vickerman and Cox, 1967; Read et al., 1993), indicating nuclei dividing at different times. In addition, different microtubule structures associated with schizogony were observed in individual nuclei of a single parasite, indicating nuclei being in different stages of division (Read et al., 1993; Arnot et al., 2011). Recently it was shown that DNA replication in separated nuclei also happens at different times, demonstrating nuclear autonomy (Klaus et al., 2021). After several asynchronous nuclear divisions, a last relatively synchronous division was assumed which coincides with daughter cell assembly (Francia and Striepen, 2014; Rudlaff et al., 2020).

In contrast to *Plasmodium* blood-stage schizogony, in classical mitosis separation of sister chromatids of the chromosomes into two new nuclei is typically followed by cytokinesis. Thereby, two separate daughter cells are generated (Figure 1.4). Apart from this, several other differences between classical mitosis and *P. falciparum* blood-stage schizogony have been observed which are compared in detail in Figure 1.4.
In contrast to vertebrate cells, *Plasmodium* divides while keeping the nuclear envelope intact, comparable to closed mitosis of budding and fission yeast (Boettcher and Barral, 2013). Although partial leakages of the nuclear envelope during schizogony cannot be excluded, transmission electron microscopy (TEM) studies show continuous nuclear membranes during divisions (Aikawa et al., 1967; Aikawa and Beaudoin, 1968; Ladda, 1969; Klaus et al., 2021). Connections between nucleoplasm and cytoplasm are mediated by nuclear pore complexes. These increase in number until late trophozoite stage (up to 60 pores per nucleus) and are redistributed to the nuclei during schizogony (Weiner et al., 2011). Throughout divisions, no clear condensation of chromatin to chromosomes has been observed, neither in transmission electron microscopy images (Canning and Sinden, 1973) nor in immunofluorescence stainings in which DNA signals appeared diffuse during schizogony (Read et al., 1993; Gerald et al., 2011). However, differences in electron-dense heterochromatin and less electron-dense euchromatin can be observed in TEM (Weiner et al., 2011). To efficiently separate replicated DNA, microtubules have to attach to kinetochores which are associated with centromeres of the chromosomes. *Plasmodium* centromeres, marked by the centromeric histone variant PfCENH3, are clustering at one position

at the nuclear periphery in late trophozoites and throughout schizogony (Hoeijmakers et al., 2012). In multinucleated parasites, one centromere spot is visible per nucleus (Hoeijmakers et al., 2012). Kinetochore localization was studied in *P. berghei* schizogony using the outer kinetochore marker NDC80 (Zeeshan et al., 2021a). Imaging revealed the recruitment of NDC80 to a single spot at the nuclear periphery in early trophozoites, consistent with centromere positioning. During schizogony, each nucleus was associated with one or two NDC80 signals (Zeeshan et al., 2021a).

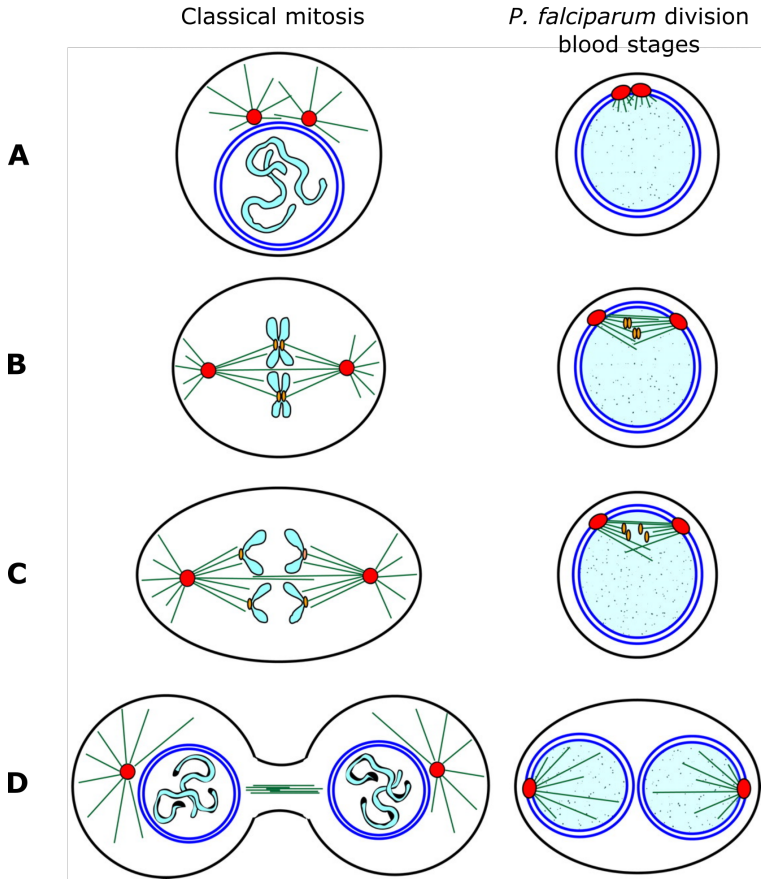

FIGURE 1.4: Comparison of classical open mitosis with a model of *P. falciparum* closed division in blood-stages. (A) In classical open mitosis as observed in mammalian cells, the centrosome (red) which organizes microtubules (green) in the cytoplasm is duplicated to prepare for division. Inside the nucleus (surrounded by the inner and outer nuclear membrane, dark blue), chromosomes (light blue) start to condense. In *P. falciparum*, the duplicated centrosome, also called centriolar plaque, is embedded into the nuclear membrane and organizes intranuclear microtubules. The DNA (light blue with dark spots) is not condensed. (B) Next in classical mitosis, the nuclear membrane is disassembled and centrosomes, positioned at opposite ends of the cell, organize a mitotic spindle with microtubules attaching to kinetochores (beige ovals) of the chromosomes. Chromosomes are aligned centrally at the metaphase plate. In *Plasmodium* division, intranuclear microtubules organized by the centriolar plaque connect to kinetochores while the DNA remains uncondensed. The *Plasmodium* nuclear envelope stays intact. (C) In mitosis, sister chromatids are separated to opposite poles of the cell. During divisions in schizogony, the replicated DNA also needs to be separated into two distinct nuclear bodies. How exactly this is performed is completely unknown. (D) Finally in classical mitosis, separated chromosomes start to decondense, nuclear membranes are assembled around the two genome copies and the mitotic spindle is disassembled. Typically, mitosis is directly followed by cytokinesis. In *Plasmodium* schizogony, separated genome copies are surrounded by discrete nuclear membranes. The mechanism of karyofission is not known. In the following, several rounds of DNA replication and nuclear division lead to formation of a multinucleated cell before cytokinesis occurs. Figure adapted from Gerald et al. (2011).

To regulate transition from nuclear divisions to cytokinesis, a counting mechanism has been suggested that stops divisions when a certain number of nuclei is reached (Klaus et al., 2021; Simon et al., 2021b). However, it is still under debate which factors "count" and influence the varying numbers of progeny produced (Simon et al., 2021b). After completion of nuclear divisions, segmentation occurs to demarcate new daughter parasites. Therefore, the parasite plasma membrane (PPM) and the inner membrane complex (IMC), a structure of flattened vesicles directly underlying the PPM, are encompassing the nascent daughter parasites (Harding and Meissner, 2014; Kono et al., 2016; Rudlaff et al., 2019). Finally, the parasitophorous vacuole ruptures, followed by rupture of the erythrocyte plasma membrane and release of new invasive merozoites into the bloodstream (Wickham et al., 2003).

To coordinate progression in the cell cycle, yeast as well as mammalian cells exhibit several checkpoints which halt progression through the cell cycle until certain criteria are met. For example, checkpoints controlling for cell growth in G1 and G2 phase have been described as well as a G2/M checkpoint, which checks for correct DNA synthesis before onset of mitosis (Barnum and O'Connell, 2014). In addition, the spindle assembly checkpoint (SAC) during mitosis controls for proper capturing of chromosomes by microtubules before transition to anaphase (Kops et al., 2020). In the *Plasmodium* cell cycle, canonical checkpoints are absent. For instance, a checkpoint comparable to SAC is probably missing as DNA replication and nuclear divisions can occur in presence of microtubule destabilizing agents (Fennell et al., 2006; Naughton and Bell, 2007). However, a recent study by Van Biljon et al. (2018) showed that DL-α-difluoromethylornithine (DFMO) can arrest *Plasmodium* cells in G1 phase indicating the potential existence of a G1/ S transition checkpoint. Many typical cell cycle regulators are absent in *Plasmodium*, however, cyclins, NIMA-related kinases (Nek1-4), Aurora-related kinases (Ark1-3) and calcium-dependent kinases (CDKs) have been described in the parasite (Doerig et al., 2002; Carvalho et al., 2013).
Regulation of *Plasmodium* DNA replication occurs on the level of individual nuclei, which show unequal distributions of episomally expressed proliferating cell nuclear antigen 1 (PCNA1) (Klaus et al., 2021). A likely regulatory hub for division of replicated DNA is the centrosome, also called the centriolar plaque (CP) in *Plasmodium*, as its duplication restricts the number of nuclear divisions (Fu et al., 2015).

1.4 The centriolar plaque

Centrosomes are microtubule-organizing centers (MTOC) that coordinate the formation of a mitotic spindle during division. In general, they are known as important regulators of the cell cycle as they duplicate once per cycle and initiate transition from G1 into S phase (Hinchcliffe et al., 2001). In *Plasmodium*, the centrosome is called the centriolar plaque (CP) (Aikawa et al., 1967).

1.4.1 Ultrastructural organization

The ultrastructural organization of distinct microtubule-organizing centers including vertebrate centrosomes and yeast spindle pole bodies (SPB) has been thoroughly described (Byers and Goetsch, 1975; De Harven, 1994; Ding et al., 1997). Exemplary transmission electron microscopy images are depicted in Figure 1.5. Centrosomes are characteristic cytoplasmic organelles with a pair of centrioles oriented at an angle of 90 degrees. Centrioles are cylinders composed of nine microtubule triplets arranged around a central cartwheel structure (Conduit et al., 2015). They are surrounded by a matrix of pericentriolar material (PCM) comprising several hundred different proteins. These include important factors for microtubule nucleation and anchoring such as γ-tubulin and pericentrin (Woodruff et al., 2014).
Saccharomyces cerevisiae spindle pole bodies do not contain centrioles. Instead, the SPB is composed of several plaque layers which are integrated into the nuclear envelope throughout closed mitosis (Figure 1.5). Six plaques have been identified, including an outer one in the cytoplasm, an inner one in the nucleoplasm, a central one, two intermediate layers and a layer including capped microtubules (Bullitt et al., 1997; O'Toole et al., 1999). While the outer and inner plaque are important for astral and intranuclear microtubule nucleation, respectively, the inner plaque mediates anchoring of the SPB in the nuclear membrane (Cavanaugh and Jaspersen, 2017).

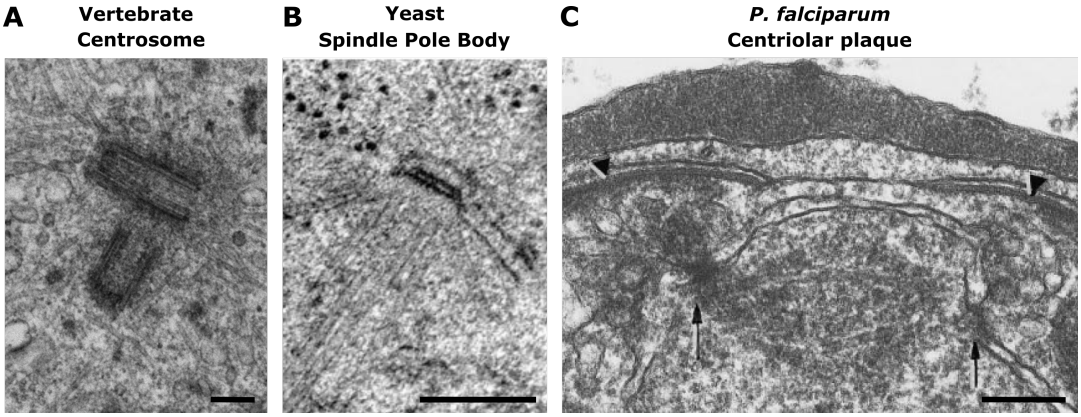

FIGURE 1.5: Ultrastructural comparison of microtubule-organizing centers (MTOCs) in different cell types. Transmission electron microscopy images are shown. (A) In vertebrate centrosomes, a central pair of centrioles, arranged at a right angle, is surrounded by pericentriolar material (PCM). Figure from Biomedical Electron Microscopy Unit, University of Liverpool. (B) The yeast spindle pole body (SPB) is embedded into the nuclear envelope throughout closed mitosis. Several characteristic plaque layers are associated with the nuclear membrane. Figure from Fisk et al. (2002). (C) Duplicated centriolar plaques (black arrows) of a *P. falciparum* parasite organizing a mitotic spindle during blood-stage schizogony. In contrast to yeast SPBs and vertebrate centrosomes, *Plasmodium* centriolar plaques show no clear structural features. They appear as electron-dense areas which are embedded into the nuclear envelope throughout closed divisions. Figure from Bannister et al. (2000b). All scale bars, 200 nm.

In contrast to vertebrate centrosomes and yeast spindle pole bodies, data about the ultrastructural organization of *Plasmodium* centriolar plaques is very limited. Our current understanding of centriolar plaque architecture is mainly based on transmission electron microscopy studies from the 1960s to 90s. In these studies, most of

them performed in oocysts of different *Plasmodium* species in the mosquito midgut (Terzakis et al., 1967; Garnham et al., 1969; Howells and Davies, 1971; Canning and Sinden, 1973; Schrével et al., 1977; Sinden and Strong, 1978), others in blood-stage schizonts (Aikawa et al., 1967; Aikawa and Beaudoin, 1968; Prensier and Slomianny, 1986; Sinou et al., 1998; Bannister et al., 2000b), the centriolar plaque appeared as an amorphous, electron-dense area at the nuclear envelope (Figure 1.5). Any clear structural features are absent from centriolar plaques in blood-stages and neither plaque layers nor centrioles have been observed. However, during male gametogenesis, centrioles, also known as basal bodies, organize axonemal microtubules (Garnham et al., 1967; Sinden et al., 1976; Zeeshan et al., 2019a). Basal bodies are probably formed *de novo* in male gametocytes but their localization is directed by the pre-existing centriolar plaque (Francia et al., 2015; Sinden et al., 2010; Rashpa and Brochet, 2022).

Centriolar plaques seem (at least partially) embedded into the nuclear envelope. Electron-dense areas on both sides of the nuclear membrane as well as in the nuclear envelope itself have been associated with the centriolar plaque (Figure 1.5). Early oocyst studies describe the connection of a cytoplasmic and a nucleoplasmic site of the centriolar plaque via a nuclear pore (Canning and Sinden, 1973; Schrével et al., 1977; Sinden and Strong, 1978). Interestingly, during sporogony in oocyst stages, cup-shaped invaginations of the nuclear membrane have been observed at the sites of centriolar plaques which are enriched with nuclear pores (Canning and Sinden, 1973; Schrével et al., 1977). However, a detailed view on centriolar plaque morphology and its association with the nuclear membrane and nuclear pore complexes is missing to date. Furthermore, it remains elusive whether the electron-dense regions observed are reminiscent of the pericentriolar material observed around centrioles in vertebrate centrosomes.

In another apicomplexan parasite, *Toxoplasma gondii*, the centrosome shows a bipartite organization into an inner and outer core (Suvorova et al., 2015). The two cores exhibit a distinct protein composition and centrosome duplication is performed sequentially starting with the outer core (Suvorova et al., 2015). Although similarities of *T. gondii* and *P. falciparum* centrosomes might be observed, transmission electron microscopy images show clear differences. For example, *T. gondii* centrosomes show a pair of parallel centriole-like structures associated with a characteristic centrocone structure (Francia and Striepen, 2014) not present in *Plasmodium*.

1.4.2 Composition

The composition of centriolar plaques is almost completely unknown. Only very few of the several hundred proteins of vertebrate centrosomes are conserved in *Plasmodium* (Suvorova et al., 2015; Tomasina et al., 2021). An overview of conserved centrosomal proteins and the limited information about these in *Plasmodium* centriolar plaques are summarized in Table 1.1.

TABLE 1.1: Centrosomal proteins conserved in *P. falciparum*. Ark-1, Aurora-related kinase-1; APC3, Anaphase promoting complex 3; BB, Basal body; CP, Centriolar plaque; GCP, γ-Tubulin complex component; IP, Immunoprecipitation; MZT1, Mitotic-spindle organizing protein 1; POC1, Proteome of the centriole 1; SAS, Spindle assembly abnormal protein, SPB, Spindle pole body. Based on the table published by Suvorova et al. (2015).

Protein	*P. falciparum* ID PF3D7_	Localization / Further Information	Source
Centriole proteins			
Centrin1	0107000	in co-IP with *P. berghei* Centrin4-GFP	Roques et al. (2019)
Centrin2*	1446600	in co-IP with *P. berghei* Centrin4-GFP	Roques et al. (2019)
Centrin3	1027700	at CP	Mahajan et al. (2008)
Centrin4*	1105500	at CP in *P. berghei* gametogenesis	Roques et al. (2019)
unknown protein**	0710000	centrin-binding motifs as in Sfi1	Suvorova et al. (2015)
SAS4	1458500	at BB in *P. berghei* microgametogenesis	Rashpa and Brochet (2022)
SAS6	0607600	at BB in *P. berghei* microgametogenesis	Marques et al. (2015), Rashpa and Brochet (2022)
SAS6-like	1316400	at apical complex in *P. berghei* ookinetes and sporozoites	Wall et al. (2016)
POC1	0826700	unknown localization	Tomasina et al. (2021)
Microtubule nucleation			
γ-tubulin	0803700	at CP in *P. berghei* microgametogenesis	Rashpa and Brochet (2022)
putative GCP	0933500	unknown localization	
putative GCP	1443600	unknown localization	
putative GCP	1453400	unknown localization	
MZT1	1339800	at CP in *P. knowlesi*	unpublished data, Ann-Kathrin Mehnert
Mitotic regulation			
Ark-1	0605300	transiently at duplicated CPs	Reininger et al. (2011)
APC3***	0501700	at CP in *P. berghei* schizonts	Wall et al. (2018)
Yeast SPB			
SPB protein****	0303500	at CP	unpublished data, Marta Machado

* no sequence conservation, but alveolate-specific centrins

** no sequence conservation, but conserved centrin-binding motifs that are observed in Sfi1 proteins

*** low sequence similarity with human APC proteins; human APC/C not at centrosome

**** no sequence similarity with any *S. cerevisiae* or *S. pombe* protein

Centrins and Sfi1

Centrins are small, highly-conserved, canonical centrosome proteins with four EF-hand domains for calcium-binding (Dantas et al., 2012). While Cdc31, the centrin-homologue in yeast, was clearly shown to be important for spindle pole body duplication (Paoletti et al., 2003), the role of centrins in human centrosomes is not conclusive. Mammals express four different centrins. Expression of Centrin1 and Centrin4 has been linked to retina/testis and to ciliated cells, respectively (Wolfrum and Salisbury,

1998; Hart et al., 1999; Gavet et al., 2003). However, Centrin2 and -3 are present in human centrosomes. Whether these centrins are involved in centrosome duplication is still under debate. While Salisbury et al. (2002) and Yang et al. (2010) concluded that Centrin2 plays an important role for duplication, another study described vertebrate centrosome duplication even in absence of three centrins (Dantas et al., 2011). Instead, centrins were shown to be involved in nucleotide excision repair, correct centriolar architecture and ciliogenesis (Dantas et al., 2011; Prosser and Morrison, 2015; Bouhlel et al., 2021).

In *P. falciparum*, four different centrins are expressed (Mahajan et al., 2008). Two of these, PfCentrin1 and PfCentrin3 correspond to mammalian Centrin1/2/4 and Centrin3, respectively. However, PfCentrin2 and -4 are specific for the alveolate phylum *Plasmodium* belongs to (Mahajan et al., 2008). Centrin1-3 are likely essential for *Plasmodium* as disruption and endogenous tagging were not successful in *P. berghei* (Roques et al., 2019). Using immunofluorescence stainings, PfCentrin3 was shown to localize to centriolar plaques during *P. falciaprum* blood-stage schizogony (Mahajan et al., 2008). Additionally, *P. berghei* Centrin4 is present at centriolar plaques during schizogony (Roques et al., 2019). Interestingly, Roques et al. (2019) identified all four *P. berghei* centrins in mass spectrometry analysis when co-immunoprecipitations were performed using Centrin4-GFP-expressing schizonts. This data indicates localization of all four centrins to the centriolar plaque and a possible interaction of those (Roques et al., 2019). However, the function of centrins in *Plasmodium* remains elusive.

An important interaction partner of centrins in yeast and mammalian cells is Sfi1. Sfi1 is a long, filamentous protein containing several centrin-binding repeats (Li et al., 2006). In *S. cerevisiae*, Sfi1 and Cdc31 are part of the half-bridge of the SPB and involved in SPB duplication (Baum et al., 1986; Spang et al., 1993; Kilmartin, 2003; Rüthnick et al., 2021). Duplication is initiated by oligomerization of Sfi1 proteins at their C-termini and assembly of a daughter SPB at the free, distal N-termini (Burns et al., 2015; Cavanaugh and Jaspersen, 2017). Human Sfi1, which also contains centrin-binding repeat motifs, localizes to centrosomes (Kilmartin, 2003; Kodani et al., 2019). A recent study by Bouhlel et al. (2021) revealed that Sfi1 is important for recruitment of Centrin2/3 to the distal tip of the centriole as well as for ciliogenesis and correct centriole architecture. In *Plasmodium*, the Sfi1 protein is not conserved. However, a large protein with conserved centrin-binding repeat sequences has been identified (Suvorova et al., 2015), which might resemble the centrin-interaction partner Sfi1.

Various centriolar plaque proteins

Various kinases regulate distinct steps of mitosis in animal cells including centrosome duplication, separation and maturation. These include polo-like kinases (Plks), aurora kinases, cyclin-dependent kinases (CRK) and NIMA (never in mitosis gene a)-related kinases (Neks) (Wang et al., 2014). While polo-like kinases are not conserved in *Plasmodium*, three aurora-related kinases (Ark1-3) have been identified (Reininger et al., 2011). Aurora kinases are highly conserved serine/threonine kinases, regulating several important steps during mitosis in mammalian cells such as centrosome

maturation, chromosome alignment and separation (Goldenson and Crispino, 2015). *P. falciparum* Ark-1 transiently localizes to duplicated centriolar plaques with one focus each at the two microtubule organizing centers (Reininger et al., 2011). Ark-1 is not present simultaneously in all nuclei of a multinucleated parasite, consistent with asynchrony of nuclear divisions (Read et al., 1993; Reininger et al., 2011). In *P. falciparum*, four NIMA-related kinases (Nek1-4) are present. Albeit low expression in intraerythrocytic stages (Otto et al., 2010), a recent study suggested epistatic interactions of Nek-1 with Ark-1 in blood-stages mediating resistance to the human Aurora kinase inhibitor Hesparadin (Morahan et al., 2020).

Human spindle assembly abnormal protein (SAS) 6 is a core component of the centriole cartwheel (Marteil et al., 2017) and SAS4/CPAP is involved in several processes including centriole duplication/elongation and PCM recruitment (Varadarajan and Rusan, 2018). SAS4 and -6 are conserved in *Plasmodium*, however, their expression is mainly restricted to male gametocytes, while expression in blood-stages is low (Otto et al., 2010; Lasonder et al., 2016). Both proteins have been shown to localize to basal bodies during *P. berghei* male gametogenesis and it has been suggested that they are present at the centriolar plaque before basal body formation (Marques et al., 2015; Rashpa and Brochet, 2022). Depletion of SAS6 during male gametogenesis leads to diminished numbers of basal bodies and defects in axonemal microtubule formation as well as malformed microgametes lacking a nucleus (Marques et al., 2015).
Data on conservation of various centrosomal proteins (CEPs) is controversial. While Suvorova et al. (2015) included CEP 76, 97, 120 and 250 in a table of centrosomal proteins conserved in *Plasmodium*, in a recent review by Tomasina et al. (2021) no homologs were allocated to the four CEPs. Instead, homologs of CEP 72, 110, 135 and 170 were reported (Tomasina et al., 2021). Due to these inconsistencies, CEPs are not included in Table 1.1 listing centrosomal proteins conserved in *Plasmodium*. In the related apicomplexan parasite *T. gondii*, CEP250 localized to the outer and inner core of the centrosome (Suvorova et al., 2015). However, whether CEP250 or other CEPs are associated with *Plasmodium* centriolar plaques remains to be investigated.

γ-Tubulin
Growth of microtubules from the centrosome needs to by tightly controlled in both space and time to coordinate the elaborate division process. Nucleation of microtubules at centrosomes is mediated by complexes formed around γ-tubulin, namely the γ-tubulin small complex (γTuSC) and γ-tubulin ring complex (γTuRC) (Kollman et al., 2011). γ-Tubulin is conserved in the *Plasmodium* genome (Maessen et al., 1993) and is mainly expressed at schizogony onset in blood-stages, 32 hpi (Otto et al., 2010). In immunofluorescence stainings, Fowler et al. (2001) localized punctate γ-tubulin signals to the apical ends of subpellicular microtubules in emerging and free merozoites of *P. falciparum*. A recent study further shows association of γ-tubulin with the centriolar plaque during microgametogenesis in *P. berghei* (Rashpa and Brochet, 2022). These studies indicate a conserved localization and function of γ-tubulin at microtubule-organizing centers of *Plasmodium*.

Recently a study by Wall et al. (2018) showed localization of the anaphase promoting complex protein APC3 of *P. berghei* in punctate structures to the centrosome, partially colocalizing with centrin and γ-tubulin. In another interesting study, co-immunoprecipitations of *P. falciparum* γ-tubulin in blood-stages identified PfSec13 (Dahan-Pasternak et al., 2013), a protein previously identified as part of the nuclear pore complex (Kehrer et al., 2018). The study by Dahan-Pasternak et al. (2013) indicates association of PfSec13 with centriolar plaques.

1.5 Microtubule organization during schizogony

Microtubule composition and characteristics

Centriolar plaques serve as microtubule-organizing centers coordinating mitotic spindle microtubules during schizogony. Microtubules are part of the cytoskeleton in eukaryotic cells including *Plasmodium* parasites. They are hollow cylinders with an outer diameter of about 25 nm which are typically composed of 13 protofilaments (Janke and Magiera, 2020). Each protofilament contains stacked heterodimers of α- and β-tubulin (Janke and Magiera, 2020). Various isotypes of these highly conserved globular molecules are present among different species. In *Plasmodium*, two α-tubulin isotypes (Holloway et al., 1989, 1990) and one β-tubulin (Delves et al., 1989) were characterized. While α-tubulin II shows high expression in microgametocytes, α-tubulin I is the prevalent isotype in intraerythrocytic stages (Delves et al., 1990; Kooij et al., 2005; Fennell et al., 2008; Otto et al., 2010; Lasonder et al., 2016). Production of tubulin in blood-stages is stage-dependent, with highest amounts present during schizogony and segmentation (Sinou et al., 1998; Fennell et al., 2008) indicating an increased requirement during divisions. In addition to tubulin isotypes, microtubule diversity and regulation is mediated by post-translational modifications of tubulins. While a number of modifications such as phosphorylation, acetylation, methylation or ubiquitylation have been reported in other species (Janke and Magiera, 2020), to date polyglutamylation is the only modification identified for *Plasmodium* tubulins (Fennell et al., 2008; Bertiaux et al., 2021). Polyglutamylation is seen in microtubules associated with the inner membrane complex, however, data on tubulin in mitotic microtubules is not conclusive (Fennell et al., 2008; Bertiaux et al., 2021).

Microtubules are polar, with a minus-end decorated with α-tubulin, and β-tubulin exposed at the plus-end (Desai and Mitchison, 1997). Microtubules are no static cytoskeletal elements. Instead, they switch rapidly between polymerization and depolymerization, a process known as dynamic instability (Mitchison and Kirschner, 1984; Brouhard, 2015). Changes from growth to shrinkage (catastrophe) and shrinkage to growth (rescue) mainly happen at the fast-growing, highly dynamic microtubule plus-ends, while the minus-ends are more stable (Desai and Mitchison, 1997). Minus-ends are typically anchored at microtubule-organizing centers (Akhmanova and Steinmetz, 2019), where nucleation of microtubules from a template, the γTuSC or γTuRC, takes place (Roostalu and Surrey, 2017). Alternatively, *in vitro*, nucleation

of microtubules can also happen spontaneously when a certain amount of tubulin molecules is reached. Recently, for the first time, Hirst et al. (2022) purified *P. falciparum* blood-stage tubulin and determined *Plasmodium* microtubule dynamics *in vitro*. While microtubule polymerization velocity was comparable to bovine microtubules, depolymerization velocity was significantly faster in *Plasmodium* microtubules (Hirst et al., 2022). In contrast to bovine microtubules, frequencies of microtubule catastrophe and rescue were both significantly lower in *P. falciparum* (Hirst et al., 2022).

Microtubules during schizogony

Using microtubule stabilizing agents such as taxol and taxol derivatives, several studies revealed an important role of microtubules for proper blood-stage development (Pouvelle et al., 1994; Schrével et al., 1994; Sinou et al., 1998; Naughton and Bell, 2007). Moreover, microtubule destabilizers such as the herbicide oryzalin lead to abnormal microtubule structures during schizogony and inhibit progression in intraerythrocytic development (Fennell et al., 2006). Various microtubule structures have been described during schizogony. These include so-called hemispindles, mitotic spindles and tubulin-rich plaques. All of these microtubule arrangements are exclusively observed inside of nuclei as revealed by transmission electron microscopy (TEM) and immunofluorescence assays (IFA) (Aikawa et al., 1967; Aikawa and Beaudoin, 1968; Bannister et al., 2000b; Mahajan et al., 2008). Although one study described cytoplasmic microtubules in *P. falciparum* oocysts (Sinden and Strong, 1978), commonly no astral microtubules comparable to those in yeast or vertebrates were detected during divisions (Canning and Sinden, 1973).

Hemispindles are composed of microtubules radially extending from the site of a single centriolar plaque into the nucleoplasm. They have been described in oocyst division as well as during schizogony using TEM (Terzakis et al., 1967; Aikawa and Beaudoin, 1968; Aikawa et al., 1967; Schrével et al., 1977; Sinou et al., 1998) and immunofluorescence stainings (Sinou et al., 1998; Read et al., 1993; Fennell et al., 2006; Gerald et al., 2011; Bertiaux et al., 2021).

Plasmodium mitotic spindles are bipolar with microtubules organized by two centriolar plaques. Measuring only 0.5-1 µm in length (Prensier and Slomianny, 1986; Bannister et al., 2000b; Gerald et al., 2011), mitotic spindles are exceptionally small when compared to microtubule-organizing centers in other organisms. Three different types of microtubules are present in oocyst mitotic spindles. These include microtubules extending from a centriolar plaque, which are not connected to another centriolar plaque (radiating microtubules); microtubules connecting two centriolar plaques (continuous microtubules); and those that are connected to kinetochores, contacting the chromosomes (kinetochore microtubules) (Canning and Sinden, 1973; Schrével et al., 1977). However, analysis of distinct types of microtubules in mitotic spindles of *P. falciparum* blood-stages is sparse.

Tubulin-rich plaques were exclusively observed in immunofluorescence stainings and were often equated with the centriolar plaque (Read et al., 1993; Arnot et al., 2011). However, centriolar plaques measured in TEM are much smaller (200-300 nm)

than the tubulin-rich plaques observed in IFAs, which rather correspond to the size of mitotic spindles (0.5-1 µm) (Gerald et al., 2011). To date, it remains unclear how tubulin/microtubules are arranged in tubulin-rich plaques.

In pre-mitotic intraerythrocytic stages, diffuse tubulin signals were observed in IFAs indicating unassociated tubulin molecules (Read et al., 1993; Sinou et al., 1998; Arnot et al., 2011). One model of *Plasmodium* division describes the initial formation of hemispindle microtubules (Schrével et al., 1977). It suggests that after hemispindle duplication, they move to opposite sites in the nucleus and merge to form a mitotic spindle (Schrével et al., 1977). Although this model was based on studies of division in oocyst stages, it was also considered for blood-stage schizogony (Read et al., 1993). Hemispindle lengths of 0.5-0.7 µm measured in TEM studies are consistent with the small size of the full mitotic spindle (up to 1 µm) after potential hemispindle fusion (Gerald et al., 2011). However, hemispindles measured in immunofluorescence stainings are extensive structures of 2-4 µm, bringing fusion of hemispindles into question (Gerald et al., 2011). Whether microtubule length and number play an important role for the function of hemispindles and mitotic spindles as recently described for sporozoites (Spreng et al., 2019) remains elusive. Another study of division in oocyst stages suggests that hemispindle microtubules are present during late anaphase (Canning and Sinden, 1973), indicating a role in late division. Recent live-cell imaging of microtubule-associated kinesin-5 in *P. berghei* gave first insights into microtubule dynamics during schizogony including mitotic spindle elongation (Zeeshan et al., 2020). However, hemispindles were not detected. Direct visualization of microtubule dynamics using time-lapse microscopy will be needed to clarify function and order of appearance of various microtubule structures.

After finishing nuclear divisions, cytoplasmic microtubules have been observed during segmentation (Read et al., 1993; Sinou et al., 1998; Gerald et al., 2011), which are associated with the inner membrane complex (Harding and Meissner, 2014). Arranged in a radial way, these microtubules, also referred to as *P. falciparum* merozoite assemblage of subpellicular microtubules (f-MAST), are reminiscent of spokes in a cartwheel, and associated with the nuclei of nascent daughter parasites (Read et al., 1993; Fowler et al., 1998, 2001; Gerald et al., 2011).

1.6 Advanced microscopy techniques to study *Plasmodium* asexual blood-stage division

Studying *Plasmodium* blood-stage divisions has been hindered by the small size of the parasite and by the slow adaptation of advanced imaging techniques. Cutting-edge super-resolution and correlative microscopy will be required to understand the detailed organization of division structures of this small parasite. Further, establishment of long-term time-lapse microscopy will enable investigation of microtubule and centriolar plaque dynamics during schizogony.

Live-cell imaging

Imaging of living cells using time-lapse microscopy represents a powerful tool to study dynamic biological processes on the level of individual cells. Cell divisions include duplication of the centrosome and substantial rearrangements of chromosomes, microtubules, kinetochores, several organelles and (nuclear) membranes (Carlton et al., 2020). These dynamics can by captured and studied using live-cell imaging. To investigate divisions of *P. falciparum* parasites in intraerythrocytic stages, individual cells need to be imaged over a period of more than ten hours of schizogony. Importantly, *Plasmodium* divisions in blood-stages cannot be synchronized as it is commonly done in other species (Campbell, 1957; Davis et al., 2001). In addition, nuclear divisions during schizogony are asynchronous (Vickerman and Cox, 1967; Read et al., 1993; Arnot and Gull, 1998). Due to nuclear autonomy, it will be key to study dynamics of individual nuclei of a single parasite to gain insight into regulation of schizogony (Klaus et al., 2021). However, time-lapse microscopy of *Plasmodium* displays several challenges. *Plasmodium* parasites are highly sensitive to light and even low light intensities lead to an acidification of the cytosol due to a selective disruption of the acidic digestive vacuole (Wissing et al., 2002). Only recently, live-cell imaging was used to unravel kinesin-5 dynamics during *P. berghei* schizogony and microgametogenesis (Zeeshan et al., 2020). In combination with immunofluorescence stainings, kinesin-5 association with microtubules including the dynamic mitotic spindle was shown (Zeeshan et al., 2020). Although this study displayed the possibility of live-cell imaging of *Plasmodium* parasites during schizogony, no individual parasites were followed over time, but different exemplary cells shown for distinct time points or stages. However, in another study, Grüring et al. (2011) performed real time-lapse microscopy of individual *P. falciparum* parasites throughout intraerythrocytic development in four dimensions, mainly using differential interference contrast (DIC) at 30-60 min time intervals. However, time-lapse microscopy of *Plasmodium* blood-stages with two or even three fluorogenic probes remains sparse (Klaus et al., 2021).

In *Plasmodium*, genetic modifications and therefore tagging of proteins with fluorescent proteins is a time-consuming step. Hence, fluorogenic dyes such as the membrane marker BODIPY have been used for *Plasmodium* live-cell imaging (Elmendorf and Haldar, 1994; Hanssen et al., 2008; Grüring et al., 2011) and display an important tool for microscopy studies (Grüring and Spielmann, 2012; Broichhagen and Kilian, 2021). Recent development of sophisticated fluorogenic dyes such as silicon rhodamine (SiR)-tubulin (Lukinavičius et al., 2014), SiR-Hoechst (Lukinavičius et al., 2015) or MaP555-actin (Wang et al., 2020) will open new possibilities for *Plasmodium* blood-stage time-lapse microscopy. These dyes exhibit outstanding signal-to-noise ratios which allow reduction of excitation light intensity. Furthermore, silicon rhodamine dyes are excited with far-red light of low intensity (Lukinavičius et al., 2013). Therefore, phototoxicity can be reduced which will be essential to increase viability of *Plasmodium* blood-stages for time-lapse microscopy of divisions

using several fluorogenic probes.

Imaging of living *Plasmodium* cells might be revolutionized by lattice light-sheet microscopy (De Niz et al., 2017), which was recently adapted for time-lapse microscopy of blood-stage parasites (Geoghegan et al., 2021). Lattice light-sheet microscopy is characterized by excitation with a structured, ultrathin light sheet used to successively excite fluorophores and acquire images of the sample in 3D. Thereby, high spatiotemporal resolution with low photobleaching and phototoxicity is achieved (Chen et al., 2014). In the study by Geoghegan et al. (2021), they used 4D lattice light-sheet microscopy to unravel that the *Plasmodium* parasitophorous vacuole membrane (PVM) is formed mainly from the erythrocytic plasma membrane.

Super-resolution imaging

Another challenge for microscopy of both living and fixed *Plasmodium* cells is the small size of the parasite during intraerythrocytic development. Parasite growth is restricted to the size of human erythrocytes. While the late-stage parasite occupies the entire erythrocyte, merozoites as well as early ring stages measure around 1-2 µm (Bannister et al., 2000a), which is comparable to the size of a *Plasmodium* nucleus. As a consequence, intranuclear structures such as microtubules are restricted to approximately 2 µm in length, which is significantly shorter than mitotic spindle microtubules in other species (Goshima and Scholey, 2010). Thus, classical widefield and confocal microscopy, in which resolution is restricted to the diffraction limit of light, are unable to resolve details of these structures. Super-resolution microscopy techniques can overcome this limitation and enable a lateral resolution of less than 200 nm (Sahl et al., 2017).

Several diffraction-limited techniques are used to increase resolution. These include deconvolution, Airyscan microscopy and 3D structured illumination microscopy (SIM) (Sahl et al., 2017). During image acquisition, each optical system adds optical blur to the signals, an effect known as convolution. (Adaptive) deconvolution uses an algorithm to reverse convolution and to reassign the signals to their origins based on the point spread function (PSF) (Sahl et al., 2017). Therefore, acquired signals appear sharper and better resolved. Deconvolution can be applied to both time-resolved images of living parasites and fixed cells.

Airyscan microscopy and 3D SIM improve lateral resolution around 1.6- and 2-fold, respectively, and reach an axial resolution of around 250 nm (3D SIM) and 350 nm (Airyscan) (Sahl et al., 2017; Huff et al., 2017). Airyscan microscopy is based on a confocal system using an airyscan detector with 32 detection elements, each associated with a pinhole (Huff, 2015). For instance, Airyscan microscopy has been used to investigate daughter cell segmentation in blood stages (Rudlaff et al., 2019) or interaction of mitochondria and nuclei of parasites persisting treatment with the antimalarial artemisinin (Connelly et al., 2021). In contrast to Airyscan microscopy, 3D SIM uses a widefield system in which many images are acquired using shifted, structured illumination patterns (Heintzmann and Huser, 2017). To analyse images, they need to be reconstructed by computation. Applications for SIM in *Plasmodium*

research include studies on erythrocyte invasion by merozoites (Riglar et al., 2011), IMC reorganization during asexual development and merozoite formation (Yeoman et al., 2011) as well as investigations of cytokinesis (Absalon et al., 2016). Although both Airyscan and 3D SIM are compatible with live-cell imaging, to my knowledge they have never been used for time-lapse microscopy of blood-stage *Plasmodium* parasites.

In contrast to diffraction-limited microscopy techniques, the resolution limit is completely broken in diffraction unlimited concepts (Sahl et al., 2017). These include stimulated emission depletion (STED) and single-molecule localization microscopy (SMLM) techniques such as stochastic optical reconstruction microscopy (STORM) and photo-activated localization microscopy (PALM) (Lelek et al., 2021). In *Plasmodium*, single-molecule localization microscopy was used to study knob architecture in blood-stages (Looker et al., 2019; Sanchez et al., 2019). However, due to the required extensive image processing, SMLM approaches are far from regular usage in *Plasmodium* research .
In STED super-resolution microscopy, excited fluorophores are hit by photons of the depletion (STED) laser arranged in a donut-shape fashion. These fluorophores are transferred to their ground states emitting light shifted to the far-red end of the spectrum which is not detected. Thus, classical emission of fluorescence is restricted to a diffraction-unlimited spot in the center of the donut (Klar et al., 2000; Hell, 2003). In contrast to SMLM, STED super-resolution microscopy was applied in several *Plasmodium* studies on liver stages (Prado et al., 2015; Burda et al., 2017) and on blood-stages investigating invasion of human erythrocytes by merozoites (Volz et al., 2016). However, in late trophozoites and in schizonts, hemozoin crystals in the digestive vacuole prevent regular STED microscopy: When hemozoin crystals are hit by the high-intensity STED laser, they absorb the energy and heat up leading to an immediate destruction of the entire infected red blood cell (Schloetel et al., 2019). At the onset of this study, it was impossible to image an entire z-plane of a hemozoin-containing blood-stage parasite, limiting STED nanoscopy to small, selected regions with some distance to hemozoin crystals.

In an innovative super-resolution development known as expansion microscopy (Ex-M), cells are immunostained and embedded into a hydrogel in which they are physically expanded in an isotropic way (Chen et al., 2015). With an expansion factor of 4.5-fold, 3D super-resolution images with multiple colors can be taken on a conventional confocal microscope with a resolution comparable to STED. In a recent publication by Gambarotto et al. (2019), the concept of ultrastructure expansion microscopy (U-ExM) was introduced, in which antibody-labeling is performed after a first expansion step. Therefore, the relative distance of the fluorophore to the epitope is shorter, leading to a more precise signal (Gambarotto et al., 2019). Over the course of this PhD thesis, Bertiaux et al. (2021) readily applied U-ExM to *Plasmodium* parasites, visualizing microtubule structures in gametocytes and schizont stages.

Electron microscopy

Although recent progress in super-resolution microscopy has been made and some techniques are already adapted for *Plasmodium* (De Niz et al., 2017), highest resolution is still reached using electron microscopy (EM) techniques. Most structural data on blood-stage schizogony is based on classical transmission electron microscopy (Aikawa et al., 1967; Aikawa and Beaudoin, 1968; Prensier and Slomianny, 1986; Sinou et al., 1998; Bannister et al., 2000b). For three-dimensional ultrastructural analysis of *Plasmodium* parasites, focused ion beam scanning electron microscope (FIB-SEM) and electron tomography are powerful tools (Eshar et al., 2011). Resolution is lower in FIB-SEM than in electron tomography, however, reconstruction of entire erythrocytes is possible. FIB-SEM has been used to analyze the 3D architecture of *P. falciparum* chromatin and nuclear pore distribution during intraerythrocytic development (Weiner et al., 2011) as well as cytokinesis events in 3D (Rudlaff et al., 2020). Further, cryo-electron tomography of *Plasmodium* blood-stages revealed a connection of Maurer's clefts, which are membranous structures found in *Plasmodium*-infected erythrocytes, with the erythrocyte membrane via actin (Cyrklaff et al., 2011) or stalk-like tethers (Hanssen et al., 2008).

Sophisticated correlative light and electron microscopy (CLEM) combines the strengths of fluorescence and transmission electron microscopy to correlate fluorescent signals to the ultrastructural context of the cell (De Boer et al., 2015). CLEM approaches can be divided into 1.) protocols in which fluorescent imaging (e.g. time-lapse microscopy) precedes sample fixation, preparation and TEM imaging and 2.) on-section CLEM, in which sample preparation for electron microscopy is followed by fluorescence and TEM microscopy, both performed on sections (Kukulski et al., 2011, 2012; De Boer et al., 2015). However, as both approaches are challenging and time-intensive, they are still in the initial phase of adaptation for *Plasmodium* research (Matz et al., 2015; Birnbaum et al., 2020; Klaus et al., 2021).

1.7 Thesis objectives

To understand the unconventional division of the malaria-causing parasite *Plasmodium falciparum* in human red blood cells, investigation of critical division structures is required. In my PhD project I aimed to elucidate centriolar plaque and microtubule organization using advanced microscopy techniques.

In detail, the aims of my work included:

1) Establishment of STED super-resolution microscopy for *Plasmodium* parasites undergoing schizogony to present a detailed visualization of *P. falciparum* division structures.

2) Characterization of microtubule reorganization during blood-stage schizogony and elucidation of their dynamics. Thereby, I intended to clarify controversial data about various microtubule arrangements described in early electron and fluorescence microscopy studies. Integrating centriolar plaque dynamics, I aimed to provide a model of the different steps of nuclear division during schizogony.

3) Shed light on the detailed organization of centriolar plaques during schizogony. Using advanced microscopy techniques, I aimed to increase our current understanding of this critical organelle beyond the present view as an unstructured electron-dense region associated with the nuclear membrane. In particular, I wanted to clarify the exact position of the centriolar plaque in respect to the nuclear envelope during the closed divisions of the parasite.

4) Identification and validation of novel centriolar plaque proteins. Very few centrosomal proteins are conserved in *Plasmodium* centriolar plaques and to date mainly centrins have been used as markers. Identification of new centriolar plaque proteins will lay a foundation for functional analyses and will provide a first step towards understanding the role of the centriolar plaque in coordinating schizogony.

Chapter 2

Results

2.1 Dynamics of centriolar plaques and microtubules during schizogony

Dynamics of microtubules and the duplicaton of microtubule organizing centers have been extensively studied in vertebrate cells and model organisms such as *S. cerevisiae*. However, dynamics of these fundamental structures during blood-stage schizogony of *Plasmodium* parasites have to date never been visualized at the single-cell level over time. To elucidate how *Plasmodium* organizes its chromosome segregation machinery and clarify inconsistencies in the literature on function and appearance of different microtubule structures, I analyzed dynamics of centriolar plaques and microtubules during schizogony.

2.1.1 Dynamic reorganization of microtubules during schizogony

To elucidate centriolar plaque and microtubule dynamics, I established confocal time-lapse microscopy of *P. falciparum* blood-stage parasites. To visualize centriolar plaques, we aimed to tag PfCentrin1 with GFP. As endogenous tagging of Centrins1-3 in *P. berghei* has recently been unsuccessful (Roques et al., 2019), Nicolas Lichti C-terminally tagged PfCentrin1 with GFP expressed from an episomal construct (subsection 4.1.6, subsection 4.2.3) in addition to endogenous Centrin1. To visualize microtubules and nuclei, I labeled PfCentrin1-GFP expressing parasites with the live-cell microtubule dye SPY555-Tubulin (published as Map555-Tubulin, Wang et al. (2020)) and the infrared live DNA dye 5-SiR-Hoechst (Bucevičius et al., 2019) before time-lapse microscopy (Figure 2.1).
First microtubule signals could be detected in late mononucleated parasites. From that time point onward, each nucleus was consistently associated with a single microtubule structure (Figure 2.1). Microtubule structures of multinucleated parasites always showed one or two PfCentrin1-GFP signals attached (Figure 2.1). Unfortunately, parasites labeled even with minor amounts of 5-SiR-Hoechst (22 nM) were usually not able to complete a single nuclear division. Instead, nuclei were stuck in the mitotic spindle stage, which I identified by one bright microtubule signal

accompanied with duplicated PfCentrin1-GFP signals. Any other live DNA dye I tested also showed defects in mitotic progression.

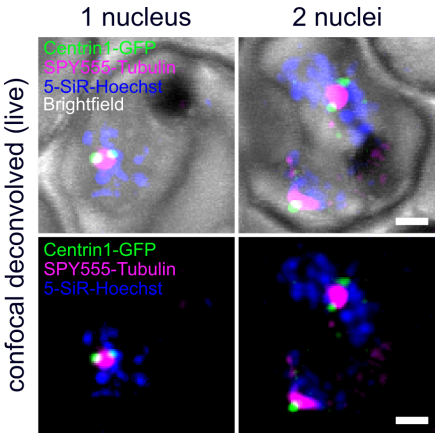

FIGURE 2.1: During blood-stage schizogony each nucleus of *Plasmodium falciparum* is associated with a single microtubule structure. Confocal deconvolved live-cell still images of two individual human red blood cells infected with NF54 *P. falciparum* parasites with one and two nuclei expressing PfCentrin1-GFP (green) from an episomal vector. Cells were labeled with SPY555-Tubulin (magenta) and 5-SiR-Hoechst (blue). Images show maximum intensity projections of the fluorescent signals. Time points are normalized to hemispindle collapse (start of mitotic spindle formation). Scale bars indicate 1 µm.

To enable unperturbed completion of nuclear divisions, I omitted labeling of the cells with 5-SiR-Hoechst and applied gentle imaging conditions to reduce phototoxicity. To enhance the contrast of the very weak signals, the Lightning module for adaptive deconvolution was used (subsection 4.2.9). Combined, this allowed detection of microtubule and centriolar plaque dynamics of individual parasites over the course of schizogony with a time resolution of 5 min on a confocal microscope. Time-lapse microscopy was either started before any microtubule or PfCentrin1-GFP signal was detected or in cells with a single microtubule arrangement indicating a mononucleated cell. Figure 2.2 shows an example of the first nuclear division during schizogony in a PfCentrin1-GFP expressing parasite labeled with SPY555-Tubulin.
First microtubule signals were detected in late trophozoite stages (mononucleated, with hemozoin). These long, radial microtubules were dynamically polymerizing and depolymerizing and have previously been described as hemispindle microtubules (Schrével et al., 1977; Sinou et al., 1998; Read et al., 1993). Next, a PfCentrin1-GFP signal was detected at the pole where hemispindle microtubules originated (Figure 2.2). The phase of dynamic hemispindle microtubules was followed by collapse of the hemispindle and an increase of SPY555-Tubulin signal close to the PfCentrin1-GFP signal. Next, a second Centrin1-GFP signal could be detected, indicating centriolar plaque duplication (Figure 2.2, time point = 0) and formation of a mitotic spindle. Mitotic spindle microtubules elongated and formed an extended spindle, separating the two PfCentrin1-GFP signals (Figure 2.2). Next, the extended spindle ruptured and left two hemispindle structures which collapsed again to prepare for mitotic spindle formation and consecutive rounds of nuclear division (Figure 2.2). Already from

the second and third nuclear division onward, microtubule signals and therefore divisions were asynchronous. Frequently in live-cell imaging, the first PfCentrin1-GFP signal was not detected before accumulation of the microtubule signal, which is associated with mitotic spindle formation.

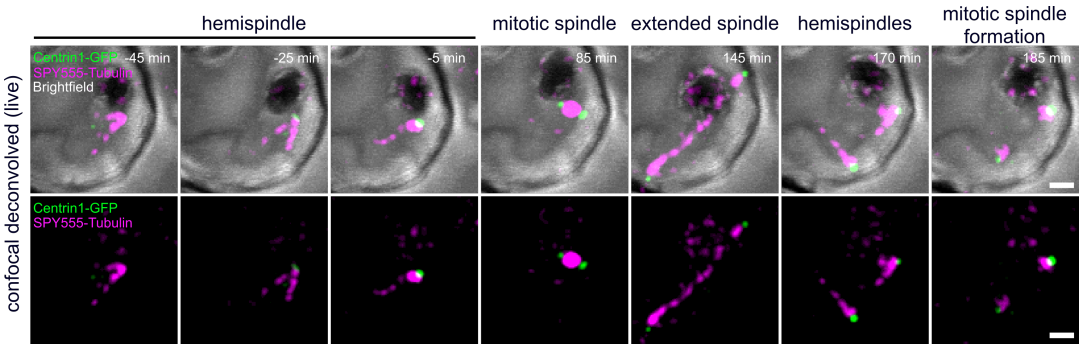

FIGURE 2.2: Microtubules are rearranged from dynamic hemispindles into mitotic spindles and extended spindles during schizogony. Deconvolved confocal still images of a human erythrocyte infected with a PfCentrin1-GFP (green) expressing NF54 parasite imaged by time-lapse microscopy show the first division during schizogony. Cells are labeled with SPY555-Tubulin (magenta) to visualize microtubule dynamics. Images are maximum intensity projections. Scale bars are 1 µm.

2.1.2 Durations of microtubule stages in the first division are significantly longer than in subsequent divisions

To compare the timespan of different microtubule stages, I manually determined durations of hemispindle, mitotic spindle and extended spindle stages for the first three nuclear divisions of *P. falciparum* blood-stage schizogony (Figure 2.3). Average durations were determined and normalized to the start of mitotic spindle formation (Figure 2.3A). Note that for the hemispindle microtubule stage of the first division a minimum average duration is depicted as most of the analyzed cells (n = 32/36) already showed a hemispindle when time-lapse microscopy was started. In the second and third nuclear division, average durations of mitotic spindle stages outreached hemispindle and extended spindle phases (Figure 2.3A). In comparison, in the first division parasites stayed much longer in hemispindle stage before a mitotic spindle was formed (Figure 2.3). This is consistent with my observation that all three microtubule stages of the first nuclear division last significantly longer than in the second and third division (Figure 2.3B).

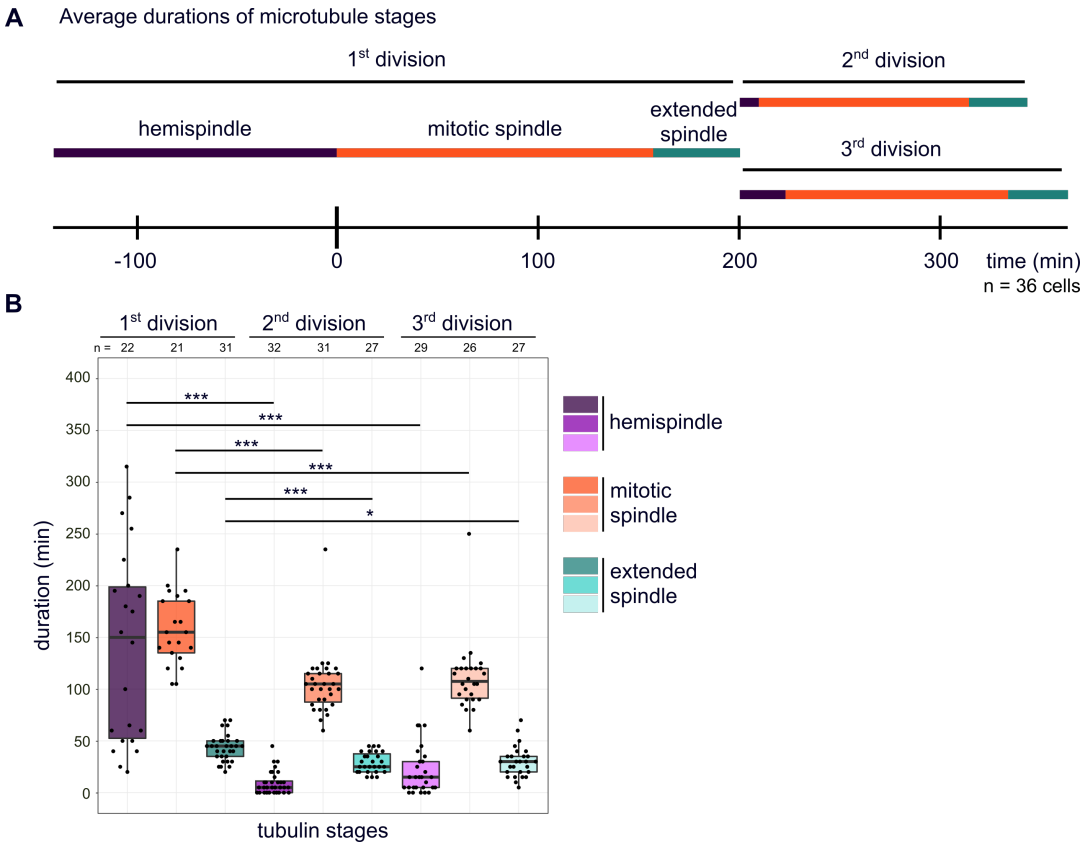

FIGURE 2.3: Microtubule stages of the first division last significantly longer than in the second and third division of schizogony. Quantification of hemispindle, mitotic spindle and extended spindle microtubule stages during the first three divisions of schizogony in *P. falciparum* NF54 blood stages expressing PfCentrin1-GFP imaged by time-lapse microscopy (Figure 2.2). In total, 36 cells were analyzed in three experiments. Note that for the hemispindle stage in the first division a minimum duration was quantified as most of the analyzed cells (n= 32/36) already showed a hemispindle when time-lapse microscopy was started. (A) Average durations of microtubule stages normalized to the start of first mitotic spindle formation. Duration of the hemispindle in the first division is the minimal average duration. (B) Quantification of individual microtubule stage durations. To test for significant differences, a Welch One-Way ANOVA test was performed followed by pairwise comparisons using Games-Howell test.

2.1.3 Centrin signal appearance and duplication during schizogony

I manually determined stable appearance of a first and a second (duplicated) PfCentrin1-GFP signal (Figure 2.4) from time-lapse microscopy data (Figure 2.2). Fluorescence intensities of PfCentrin1-GFP signals varied between cells due to different expression levels (likely different numbers of episomal constructs). Therefore, it was sometimes difficult to precisely determine the initial appearance of PfCentrin1-GFP signals in parasites with a low signal compared to background. Often, the first clear centrin focus appeared at the transition from hemispindle into mitotic spindle stage (Figure 2.4A). Rarely, the first PfCentrin1-GFP fluorescent signal of a cell was already observed in hemispindle stage, often it appeared later in mitotic spindle stage (Figure 2.4A). Very rarely, a parasite was not expressing PfCentrin1-GFP or in such low amounts that I could not detect any clear centrin foci with my imaging settings. I

observed the second Centrin1-GFP signal (duplicated centrin) during mitotic spindle microtubule stage, on average 65 min after the first centrin focus (Figure 2.4B).

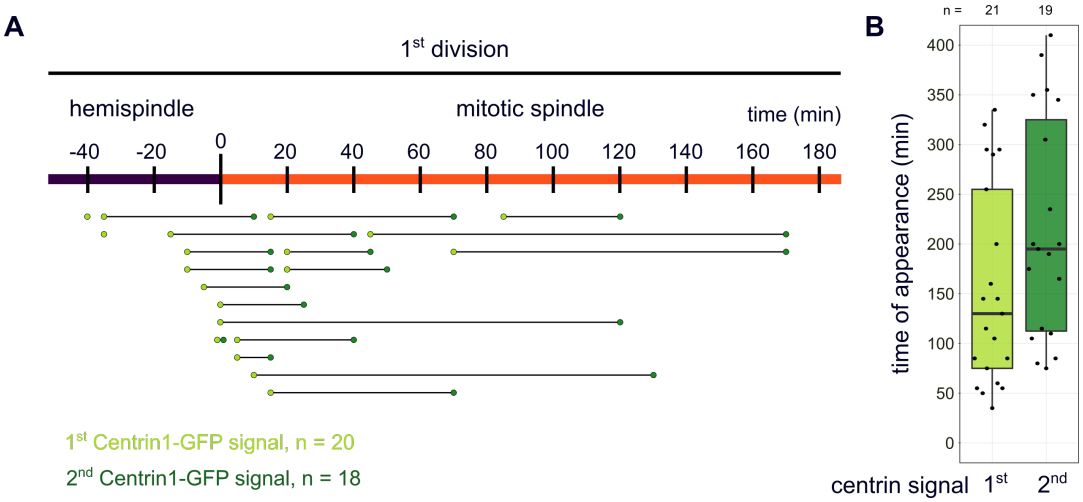

FIGURE 2.4: Variations in detection of initial and duplicated centrin signals during the first division of schizogony. (A) Quantification of time points of the first (n = 20, three replicates) and second (n = 18, three replicates) clearly detectable PfCentrin1-GFP signals in blood-stages of NF54 *P. falciparum* parasites imaged by time-lapse microscopy (Figure 2.2). Times were normalized to start of mitotic spindle formation (accumulated tubulin signal). (B) As in (A), but times of PfCentrin1-GFP signal appearance were normalized to start of the respective time-lapse microscopy movie. First PfCentrin1-GFP signal, n = 21; second PfCentrin1-GFP signal, n = 19; three replicates each.

2.2 Establishing an immunofluorescence staining protocol for RescueSTED nanoscopy of *Plasmodium* schizonts

Confocal time-lapse microscopy revealed separate microtubule stages and their order of appearance during blood-stage schizogony of *P. falciparum*. However, I could neither resolve individual microtubules e.g. of hemispindles nor analyze the exact localization of centriolar plaques in relation to microtubules and microtubule nucleation sites. To overcome the diffraction limit of light and visualize these structures with higher resolution, I established stimulated emission depletion (STED) super-resolution microscopy for fixed *P. falciparum* blood-stages during schizogony. In the following, I will describe the establishment of the protocol in detail before focusing on the insights gained by the technique in terms of centriolar plaque and microtubule organization.

2.2.1 Fixation of infected red blood cells solely with paraformaldehyde (PFA) results in altered erythrocyte morphology

Reliable immunolabeling is crucial to perform STED nanoscopy. Therefore, my colleague Ann-Kathrin Mehnert and I aimed to improve the widely-used immunofluorescence staining protocol by Tonkin et al. (2004) for STED microscopy of

infected red blood cells (iRBCs). Immunofluorescence labeling can either be performed in suspension or on a RBC monolayer seeded on a glass surface coated e.g. with Concanavalin-A as described by Grüring et al. (2011). The first step before immunofluorescence staining is fixation of cells. In general, cells can either be fixed by protein precipitation using organic solvents such as methanol or acetone or by protein crosslinking with PFA or glutaraldehyde (GA). To fix *Plasmodium* blood-stage parasites via crosslinking, cells are typically incubated with 4% PFA and 0.0075% GA. While fixation with higher GA concentrations hinders antibody binding, fixation solely with PFA induces RBC lysis (Tonkin et al., 2004). Tonkin et al. (2004) determined the minimally required amount of 0.0075% GA which provides a good compromise of RBC cellular fixation and antibody binding when staining is done in suspension. However, GA is well-known to have detrimental effects on immune epitopes, to increase background fluorescence and quench fluorescent proteins. Therefore, fixation of eukaryotic cells is commonly performed with PFA only. As we are not interested in structures of the RBC itself but in optimal visualization of parasitic proteins, lysis of the RBC by PFA fixation is not harmful per se. In solution, staining of lysed cells is not feasible as infected RBCs can no longer be pelleted by centrifugation, which is, however, necessary for each washing step in the protocol. Therefore, we focused on immunofluorescence staining of iRBCs seeded on Concanavalin-A coated glass surfaces. To improve the protocol, we started with a comparison of erythrocyte morphology and immunolabeling of parasites fixed with 0.0075% GA/4% PFA/PBS with cells fixed with 4% PFA/PBS for 20 min at 37 °C (Figure 2.5, subsection 2.2.2).

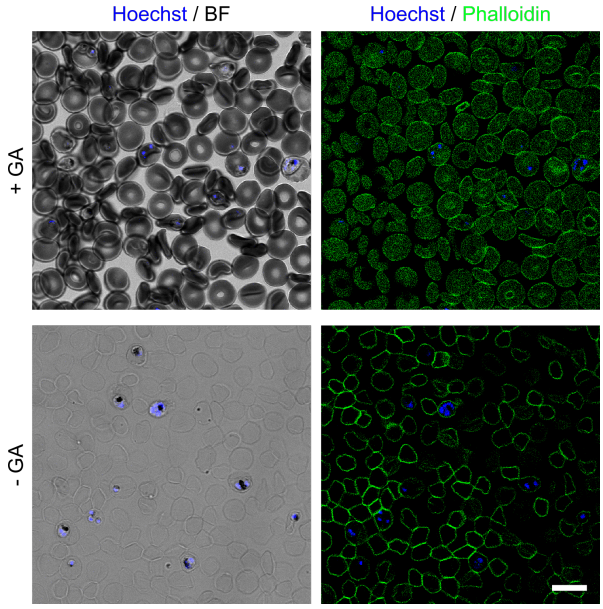

FIGURE 2.5: Human erythrocytes partly infected with *P. falciparum* appear more translucent and show improved Phalloidin staining intensity when fixed with PFA only. Confocal overview images of human erythrocytes, some infected with *P. falciparum* NF54 wt parasites. Cells were fixed with 4% PFA with or without addition of 0.0075% glutaraldehyde, immunolabeled with Phalloidin-Alexa Fluor 488 (green) to visualize erythrocytic F-actin and stained with Hoechst (blue) to label *Plasmodium* DNA. Identical acquisition and contrast settings were applied for both conditions, the images show maximum intensity projections. Scale bar is 10 µm.

After fixation of RBCs without GA, the erythrocyte monolayer lost its faint red-brown color and remained translucent, indicating hemoglobin-containing cytoplasm was (at least partially) washed out from RBCs. This loss of hemoglobin was observed in the washing steps after fixation, latest during permeabilization with Triton-X-100, indicating RBC lysis occurs only after completion of cellular fixation. Consistent with this observation, cells fixed in absence of GA appeared more translucent in brightfield (BF) images, facilitating identification of infected RBCs (Figure 2.5). Moreover, Ann-Kathrin Mehnert and I observed slight changes in erythrocyte shape and morphology when cells were fixed in absence of GA (Figure 2.5). Immunolabeling of red blood cell filamentous actin via Phalloidin-Alexa Fluor 488 appeared in the periphery as well as in the cytoplasm when cells were fixed with GA. In contrast, without GA, filamentous actin labeling was more concentrated at the periphery of the erythrocytes and showed a much higher signal intensity, while cytoplasmic actin signals were very weak or not detectable (Figure 2.5). From a practical perspective, in both conditions we reliably achieved continuous red blood cell monolayers without loss of parasites during fixation and high numbers of infected parasites.

2.2.2 Fixation of parasites with PFA increases immunofluorescence labeling density and signal intensity of parasitic structures

Next, we tested the effect of glutaraldehyde addition during iRBC fixation on immunofluorescence labeling of parasitic structures. Therefore, Ann-Kathrin and I immunolabeled different structures and compartments of the parasite after fixation in presence or absence of 0.0075% GA. We imaged parasites at similar stages using the same microscopy settings, and compared localization and intensities of the acquired signals at identical contrast settings (Figure 2.6). Our observations can be differentiated into three categories: antibodies that showed comparable signals with and without GA, antibodies that showed clearer signals or higher signal intensities in absence of GA, and finally antibodies that did not show specific signals with GA, but in the absence of GA (Figure 2.6).

Labeling of nuclear pores using antibodies directed against the nucleoporin 116 (anti-Nup116) (Guizetti et al., 2013) did not show obvious differences between fixation in the presence or absence of GA (Figure 2.6C). In both conditions, trophozoites showed irregular signals associated with the nucleus and signal intensities were comparable. Antibodies against skeleton-binding protein 1 (anti-SBP1, Figure 2.6D) which is present at Maurer's clefts (Blisnick et al., 2000) and against exported protein 1 (anti-Exp1, Figure 2.6A), a marker for the parasitophorous vacuole (PV) (Günther et al., 1991; Simmons et al., 1987), both fall in the category of antibodies with clearer/higher signals when cells were fixed without GA. In presence of GA, the PV was only incompletely labeled with anti-Exp1 antibodies. In contrast, without GA we observed a continuous labeling of the PV with higher signal intensities (Figure 2.6A). Using anti-SBP1 antibodies to visualize Maurer's clefts, we detected a comparable

labeling pattern in the host erythrocyte in presence and absence of GA during fixation of the parasites. However, signal intensities for most of the detected foci were greatly increased without GA (Figure 2.6D). Similar results were obtained with an anti-α-tubulin antibody (Figure 2.6B), which enabled detection of hemispindle and mitotic spindle microtubules in schizonts that were fixed in the presence of GA. However, signal intensities were greatly increased when GA was not added to the fixing solution. Similar results were obtained with an anti-α-tubulin antibody (Figure 2.6B), which enabled detection of bright hemispindle and mitotic spindle microtubules in schizonts fixed in absence of GA. When parasites were fixed in presence of 0.0075% GA, signal intensities were decreased and microtubules could only be detected after massive contrast adjustments, saturating the signal in parasites fixed without GA (Figure 2.6B).

Finally, two antibodies that we tested showed no detectable fluorescent signals when cells were fixed with addition of GA, but showed a specific staining in absence of GA. These antibodies included one directed against *P. berghei* heat shock protein 70 (anti-PbHSP70, Figure 2.6E) (Tsuji et al., 1994) located in the parasite cytoplasm, and an anti-centrin antibody (Figure 2.6F) as a marker for centriolar plaques (Mahajan et al., 2008; Roques et al., 2019). In absence of GA, HSP70 was almost evenly distributed in the cytoplasm, while for the anti-centrin antibody, one or two distinct centrin foci per nucleus were detected during schizogony.

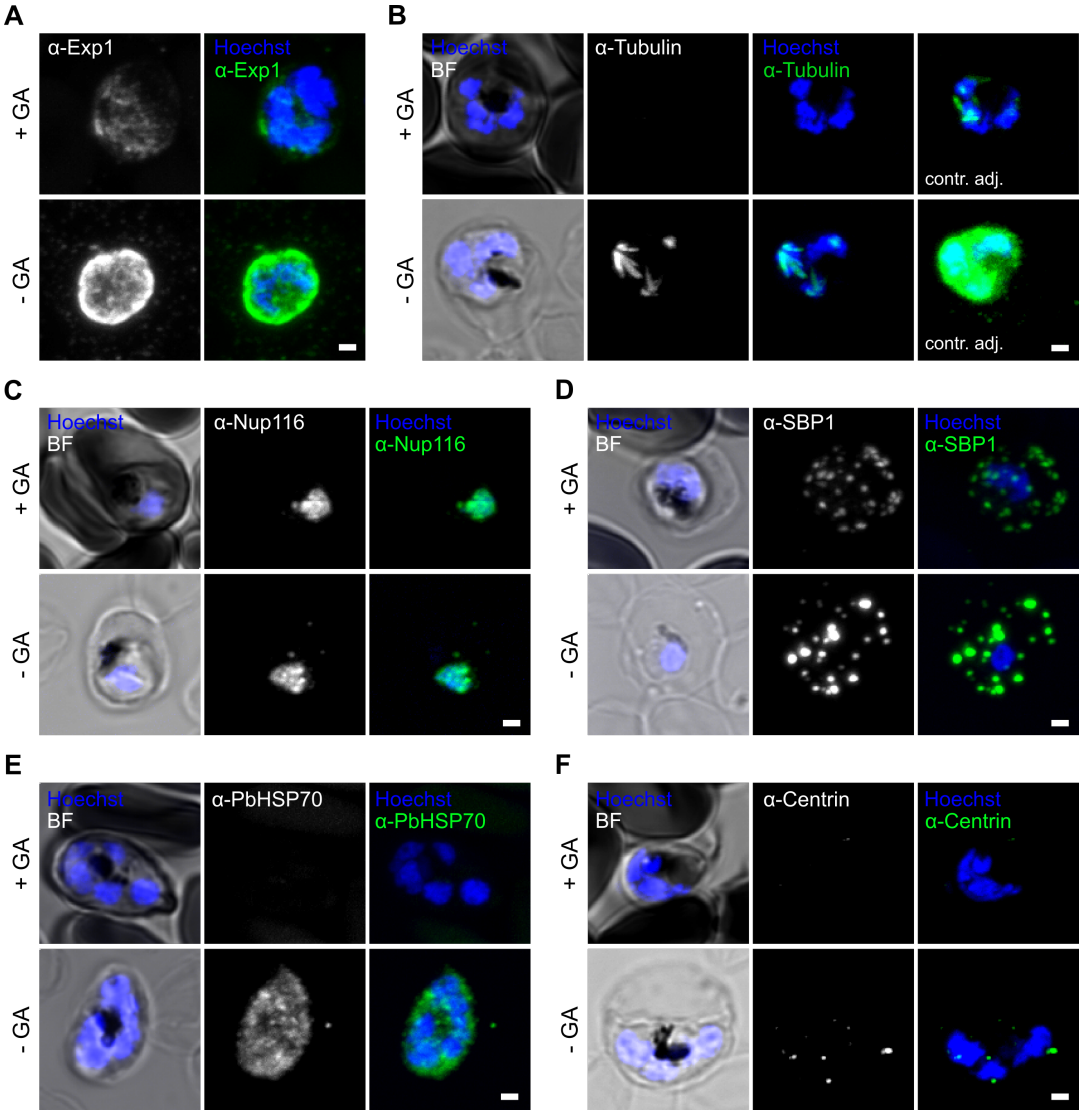

FIGURE 2.6: Increased immunofluorescence labeling signal intensity in *P. falciparum* blood stage parasites when fixed with PFA only. Confocal images of NF54 wt-infected human erythrocytes fixed with 4% PFA either with or without addition of 0.0075% glutaraldehyde (GA). Cells were stained with Hoechst (blue) and immunolabeled using antibodies against parasitic structures (green), including (A) the parasitophorous vacuole (anti-Exp1), (B) microtubules (anti-α-tubulin), (C) nuclear pores (anti-Nup116), (D) Maurer's clefts (anti-SBP1), (E) cytoplasm (anti-PbHSP70) and (F) centriolar plaques (anti-centrin). Image acquisition and contrast adjustments were identical for +/- GA conditions, except where indicated (contr. adj.). All images are maximum intensity projections, except brightfield. Scale bars are 1 µm.

Moreover, Ann-Kathrin compared the labeling density (percentage of parasites with a detectable fluorescent signal) of immunostained parasites fixed with PFA in presence or absence of GA. As this part of the protocol establishment was exclusively performed by Ann-Kathrin Mehnert (Mehnert et al., 2019), I will not show the figures in this work but briefly summarize her results as they are important for the following establishment of RescueSTED imaging. Using anti-Exp1, anti-PbHSP70 and anti-SPB1 antibodies, Ann-Kathrin observed a much higher labeling density for all of the stainings when parasites were fixed without GA in contrast to fixation with GA (Mehnert et al., 2019). However, Hoechst labeling density did not show any

differences between the two conditions (Mehnert et al., 2019).
In conclusion, fixation of seeded *P. falciparum*-infected RBCs with 4% PFA in absence of GA consistently improves immunolabeling efficiency and density and in addition increases signal intensities. Hence, our improved immunofluorescence staining protocol might be preferable for visualization of intraparasitic proteins and in particular for super-resolution microscopy techniques such as STED nanoscopy which require high signal-to-noise ratios and high, stable signal intensities.

2.2.3 Hemispindle microtubules are sensitive to PBS treatment

In immunofluorescence stainings using anti-α-tubulin antibodies, Ann-Kathrin was initially unable to visualize hemispindle microtubules when *P. falciparum*-infected erythrocytes were fixed immediately after seeding (Figure 2.7). However, when seeded parasites were allowed to recover for several hours to overnight in complete culture medium, hemispindle microtubules were consistently detected in parasites undergoing schizogony (Figure 2.7). To test whether incubation of blood-stage parasites in PBS during the seeding process destructs hemispindle microtubules, I washed and seeded parasites in incomplete culture medium (complete medium containing Albumax prevents binding of red blood cells to Concanavalin-A coated surfaces) and fixed them directly using 4% PFA in PBS. After immunolabeling, these parasites regularly showed hemispindle microtubules (data not shown). I concluded that hemispindle microtubules are sensitive to incubation of cells in PBS but can be restored in culture medium. For all following immunofluorescence stainings in this study, parasites were either seeded in PBS and allowed to recover in complete medium for at least several hours before fixation or seeded in incomplete medium with flexible time of fixation with 4% PFA (subsection 4.2.5).

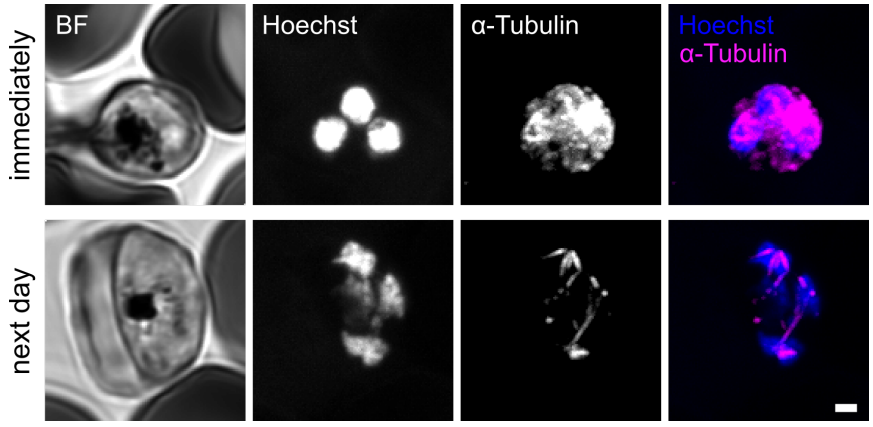

FIGURE 2.7: Overnight incubation of *P. falciparum* parasites after seeding in PBS enables hemispindle microtubule detection. Confocal images of NF54 wt-infected erythrocytes dissolved in PBS while seeding, fixed immediately or on the next day. Cells were immunolabeled with anti-α-tubulin antibody (magenta) and stained with Hoechst (blue). For acquisition, laser intensities were adjusted to enable detection of signals despite fixation with glutaraldehyde addition. Images show maximum intensity projections, except for brightfield. Scale bar is 1 µm.

2.2.4 RescueSTED enables super-resolution microscopy of parasites containing hemozoin

After having established a significantly improved immunofluorescence staining protocol for *P. falciparum*-infected red blood cells, I aimed to test whether the protocol is suitable for STED super-resolution microscopy of immunofluorescently labeled parasite structures. However, classical STED nanoscopy is not applicable for *Plasmodium* blood-stages containing hemozoin. When the STED depletion laser hits the highly absorbing hemozoin crystals (Cai et al., 2016) in the digestive vacuole, the parasite is disrupted immediately. Therefore, so far only small areas of *Plasmodium* schizonts in good distance to hemozoin could by imaged via STED microscopy without cell damage. To image entire schizonts and simultaneously avoid parasite destruction, I tested the Rescue (Reduction of State transition Cycles) adaptive illumination module from Abberior Instruments. Using RescueSTED, a confocal probing step is applied before the STED laser is used to acquire super-resolution images. Therefore, a signal threshold is defined which needs to be reached in the confocal image, before the STED depletion laser is automatically turned on. Thereby, areas with low fluorescent signals are not imaged in STED mode, massively reducing the light dose and therefore bleaching of the sample. The adaptive illumination is applied individually on the level of every single pixel of the image and allows acquisition of z-stacks as well as 3D STED imaging. As hemozoin crystals show very low fluorescent signals, the STED depletion laser is not turned on in these areas and parasite cells stay intact.

I applied our improved immunofluorescence staining protocol on seeded *P. falciparum* NF54 wt-infected red blood cells, which I stained with Hoechst and anti-α-tubulin antibodies (Figure 2.8). Hoechst signals were acquired in confocal mode, while α-tubulin signals were imaged using RescueSTED. Confocal signal thresholds often had to be adapted for each parasite imaged. Destruction of parasites still occurred in some cases, especially when high tubulin signals were in close proximity to hemozoin. I successfully imaged tubulin signals throughout intraerythrocytic development of entire z-planes of *P. falciparum* parasite cells using RescueSTED (Figure 2.8).
In ring stages I never detected any tubulin signals (Figure 2.8A). Also in most of the trophozoites (one nucleus, with hemozoin) no tubulin signal (72%, Figure 2.8A,C) was detected. Trophozoites with a signal either showed a single tubulin cluster or hemispindle microtubules (Figure 2.8A, C) in the nucleus. Clustered tubulin signals are likely mitotic spindle microtubules that were identified before using confocal time-lapse microscopy (Figure 2.2). In multinucleated parasites (early schizonts and late schizonts, Figure 2.8B), almost each nucleus was associated with an intranuclear microtubule structure, either with a clustered tubulin signal (60% of the nuclei) or with hemispindle microtubules (30% of the nuclei, Figure 2.8C). This is consistent with nuclei constantly dividing during schizogony and hemispindles and mitotic spindles being intermediate stages during these divisions (section 2.1). RescueSTED revealed individual nucleation sites of hemispindle microtubules, which could not be

distinguished before via confocal microscopy (Figure 2.8B).
After completion of schizogony in segmented parasites, microtubules are associated with the inner membrane complex of newly forming merozoites (Figure 2.8B). With RescueSTED I could resolve that two microtubules are usually aligned together. These two microtubules could not be distinguished in confocal images and hence appeared as a single microtubule structure (Figure 2.8B, zoom-in).

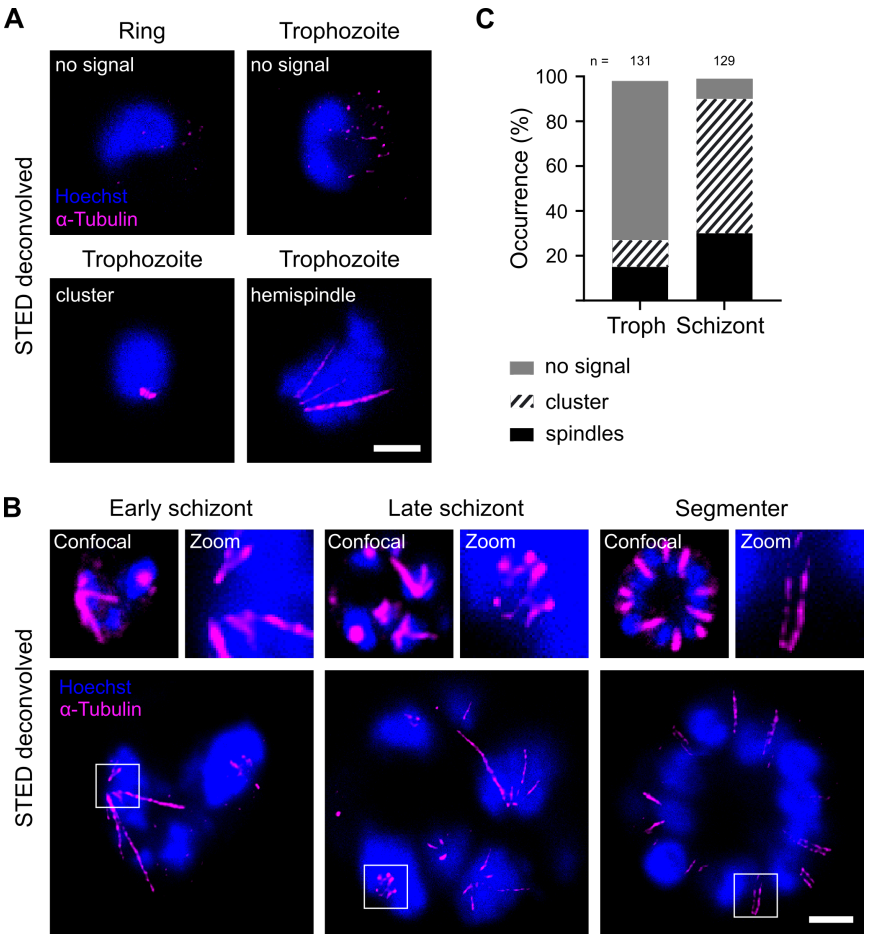

FIGURE 2.8: RescueSTED enables super-resolution microscopy of microtubule structures throughout intraerythrocytic development. (A) RescueSTED deconvolved images of fixed mononucleated NF54 wt parasites labeled with anti-α-tubulin antibody (magenta) and stained with Hoechst (blue). Tubulin signals were acquired using RescueSTED and overlayed with confocal Hoechst images. Single image slices are shown. (B) As in (A) for multinucleated parasite stages. Insets show the corresponding confocal images and zoom-ins. (C) Quantification of trophozoite and schizont nuclei with no tubulin signal, clustered tubulin signals and spindle structures, including hemispindles and extended spindles. Note that I never detected more than one microtubule structure per nucleus. In total, microtubule structures were analyzed in 131 trophozoites and 46 schizonts (129 nuclei) using confocal microscopy. All scale bars are 1 µm.

All in all our improved immunofluorescence staining protocol is well-suited for STED super-resolution microscopy of hemozoin-containing *Plasmodium* parasites undergoing schizogony and revealed details about microtubule organization in blood-stages.

2.3 Organization of centriolar plaques and microtubules during schizogony

Time-lapse microscopy revealed that mitotic microtubules are organized into hemispindles, mitotic spindles and extended spindles during blood-stage schizogony of *P. falciparum* (section 2.1). However, the precise localization of centriolar plaques in respect to microtubules could not be resolved via confocal microscopy as well as the exact appearance and duplication of the centrin signal. Therefore I aimed to overcome the resolution limit of classical confocal microscopy using our improved immunofluorescence staining protocol for RescueSTED as well as an adapted ultrastructure expansion microscopy (U-ExM) protocol to analyze centriolar plaque and mitotic microtubule organization with super-resolution.

2.3.1 Centriolar plaques organize hemispindles, mitotic spindles and extended spindles during schizogony

To first elucidate details of *Plasmodium* centriolar plaque and microtubule arrangements throughout intraerythrocytic development, I performed dual-color STED nanoscopy of anti-centrin and anti-α-tubulin antibody-labeled cells combined with confocal microscopy of Hoechst signals. Figure 2.9 shows distinct microtubule organization states during blood-stage development arranged in accordance with their order of appearance during live-cell imaging (section 2.1).

In early trophozoites (mononucleated, with hemozoin) neither a centrin nor a tubulin signal was detected (Figure 2.9). Later mononucleated stages showed intranuclear microtubules, arranged as hemispindle or mitotic spindle. Hemispindles either showed no specific centrin signal or were associated with a single centrin focus from which hemispindle microtubules of different length were branching out in various directions within the nucleus (Figure 2.9). The fact that only 46% of all hemispindle-stage mononucleated cells were associated with centrin is consistent with late appearance of the PfCentrin1-GFP signal during time-lapse microscopy (Figure 2.2, Figure 2.4). This indicates that hemispindle microtubules are nucleated before centrin is recruited to the centriolar plaque. In contrast to hemispindles in mononucleated cells, all hemispindles observed after the first nuclear division in multinucleated parasites were associated with a centrin signal.
After collapse of the hemispindle, trophozoites showed mitotic spindle microtubules (clustered tubulin) which always displayed two distinct centrin signals. In contrast, live-cell imaging data often showed clustered tubulin structures with a single centrin signal. This is most likely due to the limited sensitivity during confocal time-lapse microscopy. The two centrin signals of the mitotic spindle were arranged either next to each other, likely in an early state of mitotic spindle formation, or on opposite sites of the microtubules, corresponding to a late or mature mitotic spindle (Figure 2.9). Using RescueSTED, individual microtubules were still difficult to resolve. Therefore, a clear

transition state from hemispindle into mitotic spindle arrangement of microtubules alongside duplication of the centrin signal was never identified. However, sometimes all hemispindle branches were exceptionally short. This stage might be associated with the transitioning from hemispindle into a mitotic spindle. Interestingly, late mitotic spindles showed a central gap in the tubulin signal separating microtubules organized by the two centriolar plaques. Furthermore, the tubulin-free zone in the center of the mitotic spindle showed a Hoechst signal. Therefore, the central gap is likely indicating the site of kinetochore attachment for chromosome separation.

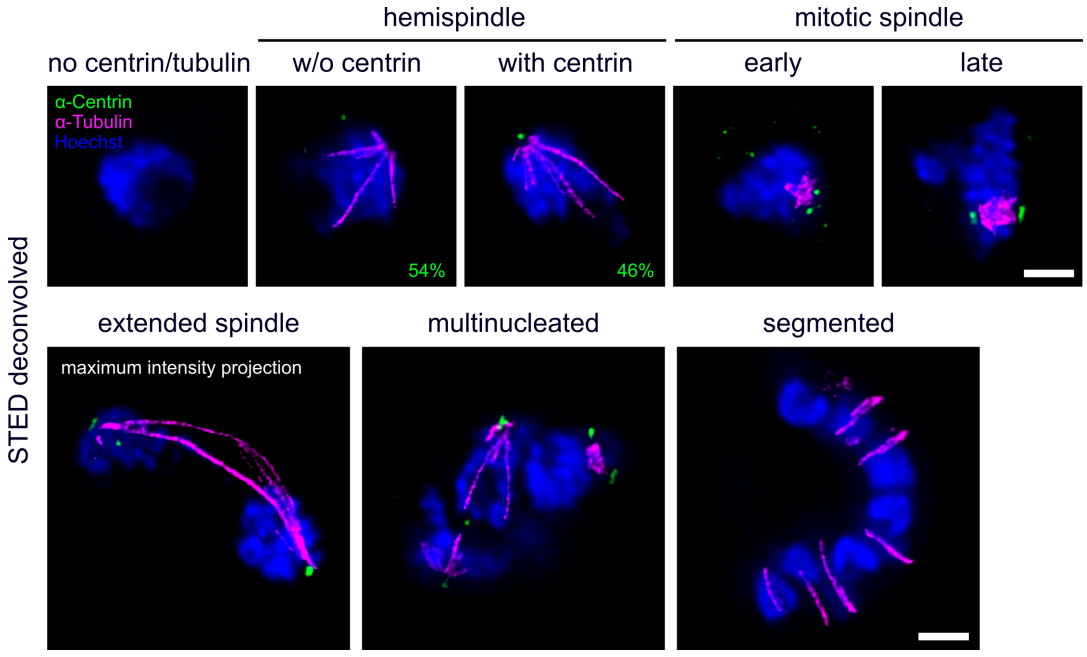

FIGURE 2.9: RescueSTED reveals structural details of hemispindles, mitotic spindles and extended spindles during schizogony. Deconvolved dual-color RescueSTED images of fixed mono- and multinucleated 3D7 *P. falciparum* parasite cells expressing tagged nuclear pore protein Nup313 via the integrated pSLI-Nup313-3xHA_glmS construct. Cells were labeled with anti-PfCentrin3 (green) and anti-α-tubulin (magenta) antibodies and stained with Hoechst (blue). While PfCentrin3 and tubulin signals were acquired with RescueSTED, Hoechst images were taken in confocal mode. All images are single slices, except for the extended spindle. Early trophozoite stages neither show a tubulin nor a centrin signal. Later mononucleated cells in the hemispindle microtubule stage either showed no centrin signal (54%) or were associated with a centrin signal (46%). Centrin signals were quantified in 3D7 wt cells using confocal microscopy (n = 52 cells, one immunofluorescence staining). Scale bars are 1 µm.

In parasites with two nuclei, I occasionally detected an extended spindle with microtubules reaching from the centriolar plaque of one nucleus to the centriolar plaque of the other nucleus (Figure 2.9). In addition to these long microtubules likely pushing apart the two nuclei, I sometimes observed additional, shorter intranuclear microtubules. In multinucleated parasites, each nucleus displays one of the three microtubule arrangements described and therefore showed one or two centrin signals (Figure 2.9). Regularly, individual nuclei of the same parasite were associated with different microtubule structures (in Figure 2.9: two with a hemispindle, one with a mitotic spindle) stressing the asynchrony of nuclear divisions. Throughout schizogony, I never detected any cytoplasmic or astral microtubules. Interestingly,

with RescueSTED I consistently detected a gap between the centrin signal and the start of microtubule signals in all three microtubule organizational states.
After finishing schizogony, in segmented parasites centrin signals could no longer be detected. Segmented parasites further lack intranuclear microtubules but instead display doublet microtubules in the cytosol, underlying the inner membrane complex of the parasite (Figure 2.8, Figure 2.9).

2.3.2 Mitotic spindle microtubules are much shorter and denser than hemispindle microtubules

RescueSTED nanoscopy revealed the detailed organization of microtubules and centriolar plaques during schizogony. However, triple-color STED microscopy is in general very challenging and on our system we are limited to two colors. Furthermore, imaging of several z-slices and therefore three-dimensional (3D) analyses are challenging due to bleaching and sometimes destruction of parasites in one of the z-slices even with RescueSTED.
Therefore, Johanna Bauer, under my supervision, adapted an ultrastructure expansion microscopy (U-ExM) protocol (Gambarotto et al., 2019) for detailed visualization of microtubules and centriolar plaques during *P. falciparum* blood-stage schizogony in 3D. For U-ExM, we seeded and PFA-fixed infected red blood cells and incorporated them into a hydrogel. This was followed by immunolabeling, physical expansion and imaging of entire cells in 3D on a confocal microscope. We typically achieved a 4.5-fold isotropic expansion of the cells resulting in the same increase in axial and lateral resolution. The resolution gained with U-ExM was comparable to RescueSTED or slightly higher with the advantage of reliable 3D imaging and the use of four colors.

Using U-ExM, we confirmed the detailed organization of centrin and microtubules in hemispindle and mitotic spindle stages (Figure 2.10) observed with RescueSTED. Hemispindles showed variable numbers of intranuclear microtubule branches, with a minimum of 2 and a maximum of 11 branches and an average of 5.7 branches per hemispindle (Figure 2.10C). Hemispindle microtubules were branching out in several different directions of the nucleus while microtubule length varied substantially from 120 nm to more than 3 µm (measured in 3D, Figure 2.10B), the latter clearly exceeding the nuclear diameter. In contrast, mitotic spindle microtubules were much more densely packed and significantly shorter than in hemispindle stage (Figure 2.10A, B). Mitotic spindle microtubules were on average 535 nm long and showed less variation in size than hemispindle microtubules (Figure 2.10B).

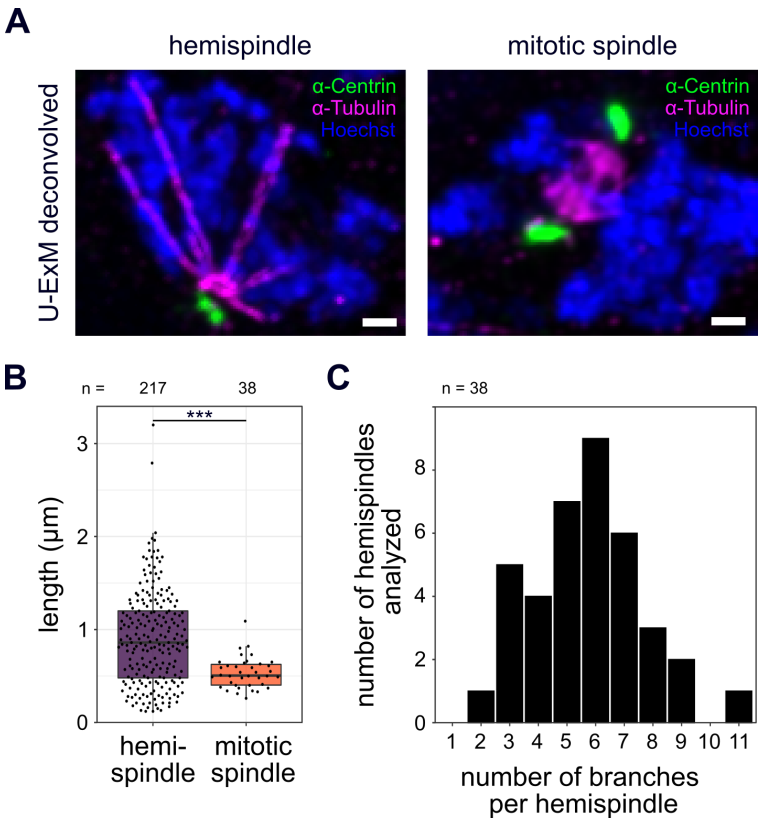

FIGURE 2.10: Ultrastructure expansion microscopy (U-ExM) facilitates super-resolution microscopy of hemispindles and mitotic spindles in 3D on a conventional confocal microscope. (A) Deconvolved confocal images of hemispindle and mitotic spindle microtubule structures in two 3D7 parasites expressing Nup313-3xHA_glmS physically expanded in a hydrogel using U-ExM. Tubulin (magenta) was visualized using two anti-α-tubulin and one anti-β-tubulin antibody. Cells were additionally labeled with anti-PfCentrin3 (green) antibody and stained with Hoechst (blue). Images are maximum intensity projections, scale bars are 1 µm (size after expansion). (B) Quantification of hemispindle branches length (n = 217, corrected by a measured expansion factor of 4.5) and mitotic spindle length (n = 38) in 3D based on tubulin signals in expanded 3D7 Nup313-3xHA_glmS cells (2 replicates). A significant difference in hemispindle and mitotic spindle length was determined using Welch's t-test. (C) Quantification of number of branches per hemispindle (n = 38 cells, 2 replicates) in 3D7 Nup313-3xHA_glmS cells.

2.4 The function of hemispindle microtubules remains elusive

In the literature different interpretations of hemispindle microtubules are discussed. One model, based on sporogony in *P. berghei*, hypothesizes duplication of the hemispindle before fusion of two hemispindles to form a mitotic spindle (Schrével et al., 1977; Gerald et al., 2011). In another interpretation, hemispindles were described as post-anaphase spindles (Canning and Sinden, 1973). However, as I never saw hemispindle fusion and hemispindles were also detected before the first division, both explanations are in contradiction to our time-lapse microscopy data. Therefore, I aimed to understand whether hemispindles fulfill a specific function and if so, which one.

2.4.1 Hemispindles sometimes extend the nuclear body

Towards understanding of hemispindle function during schizogony, I, interestingly, detected that individual hemispindle branches are sometimes extending the Hoechst-labeled nuclear body (Figure 2.11). These microtubules were either accompanied with a protrusion of Hoechst signal (Figure 2.11, lower panel) or no Hoechst signal was detectable at the tip of the microtubule branch (Figure 2.11, upper panel). Microtubules extending the nuclear body were detected in both multi- and mononucleated cells, indicating that they are not or not exclusively leftovers from extended spindle microtubules which just ruptured. In absence of a nuclear envelope marker for *Plasmodium*, I was unable to determine whether these microtubule tips are exceeding the nuclear membrane or are positioned within the nucleus.

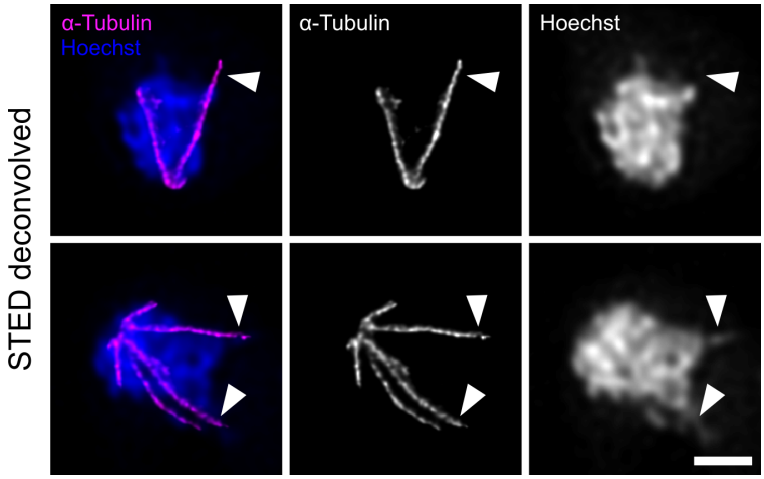

FIGURE 2.11: Hemispindle microtubules can extend the nuclear body, sometimes associated with a Hoechst signal. Deconvolved RescueSTED images of two mononucleated 3D7 Nup313-3xHA_glmS parasites with hemispindle microtubules extending the nuclear body. Cells were immunolabeled using anti-α-tubulin (magenta) antibody and stained with Hoechst (blue). Hoechst was taken in confocal mode, while tubulin signals were acquired with RescueSTED. Arrowheads indicate hemispindle branches extending the nuclear body, either without (upper panel) or with an accompanied Hoechst signal (lower panel). Images are single z-slices, scale bar is 1 µm.

2.4.2 Hemispindle microtubules are not directly interacting with centromeres

During vertebrate mitosis, microtubules undergo dynamic instability to "search" for a kinetochore. Once found, the kinetochore connects to the microtubule plus end and chromosomes are recruited to the metaphase plate of the bipolar spindle (Heald and Khodjakov, 2015). This mechanism, known as "search and capture" was first hypothesized by Kirschner and Mitchison (1986) and later experimentally demonstrated in living newt epithelial lung cells (Hayden et al., 1990; Rieder and Alexander, 1990). As hemispindle microtubules in *P. falciparum* blood-stages during schizogony repeatedly polymerize into various directions and depolymerize again, I speculated that hemispindles might play a role in searching for kinetochores and directing

them toward the centriolar plaque. In favor of this hypothesis, a recent publication showed that *Plasmodium* kinetochores are clustered at the nuclear periphery before and throughout schizogony (Hoeijmakers et al., 2012), suggesting controlled kinetochore localization.

To test whether hemispindles are involved in a "search and capture" mechanism, I analyzed the precise localization of centromeres in respect to hemispindle microtubules in *P. falciparum* schizont nuclei using RescueSTED. Therefore, I stained parasites with an anti-α-tubulin and an anti-CenH3 antibody (Figure 2.12). The latter is directed against the histone variant H3, which is specific for centromeres and shows their exact positioning (Hoeijmakers et al., 2012). Centromeric histone H3 signals were detected at the nuclear periphery close to the site where radial hemispindles originate. While former studies identified a single CenH3 signal per schizont nucleus (Hoeijmakers et al., 2012; Verma and Surolia, 2013), I observed several distinct signals which is most likely due to the increased resolution with RescueSTED. However, no co-localization of CenH3 and microtubules was observed, instead centromeres were usually located directly next to hemispindle microtubules (Figure 2.12). In addition, I never found centromeres at the tips or along hemispindle microtubules (Figure 2.12). In conclusion, hemispindle microtubules are not directly interacting with centromeres. Therefore, I could preclude the hypothesis of hemispindles being directly involved in searching for kinetochores and their clustering at the nuclear periphery.

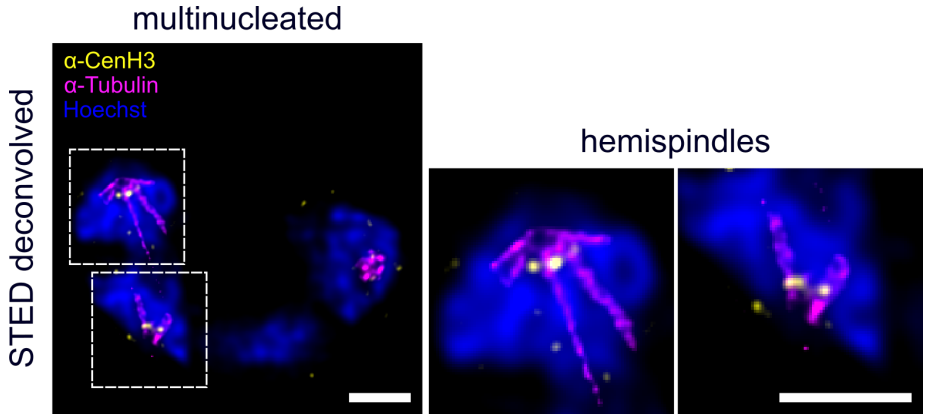

FIGURE 2.12: No direct interaction of hemispindle microtubule branches with centromeres. Deconvolved dual-color RescueSTED image of a 3D7 schizont expressing Nup313-3xHA_glmS. Cells were labeled with anti-CenH3 (yellow) antibody to visualize centromere localization, anti-α-tubulin (magenta) antibody and stained with Hoechst (blue). CenH3 and tubulin signals were acquired using RescueSTED, Hoechst signals in confocal mode. Zoom-ins show two individual nuclei in hemispindle stage, tubulin signals are not co-localizing with centromere signals. The images show a single z-slice of the cell. Scale bars, 1 µm.

2.4.3 Actively replicating nuclei are devoid of hemispindles

To figure out when hemispindle microtubules are present during the cell cycle and whether they are involved in DNA replication during S phase, Julien Guizetti stained microtubules in parasites episomally expressing proliferating cell nuclear antigen 1 tagged with GFP (PCNA1-GFP). The strain was kindly provided by the group of

Markus Ganter. PCNA forms a sliding clamp around the DNA at the replication fork, serves as a co-factor for DNA polymerases and recruits further proteins involved in DNA replication (Choe and Moldovan, 2017). Recently, Klaus et al. (2021) demonstrated that PCNA is transiently accumulating in changing subsets of nuclei during blood-stage schizogony of *P. falciparum* indicating only some nuclei are actively replicating their DNA at a given time.
Immunofluorescence stainings revealed that schizont nuclei without PCNA1-GFP signal were often associated with hemispindle microtubules (Figure 2.13A). In contrast, hemispindles were absent from PCNA1-positive, replicating nuclei of the same parasite cells. Instead, replicating nuclei were accompanied with clustered tubulin signals (mitotic spindles) (Figure 2.13A). Quantifications showed that 56% of all nuclei were PCNA1-positive and 97% of these showed mitotic spindle microtubules. PCNA1-negative nuclei were mostly associated with hemispindle microtubules (73%) (Figure 2.13B). This data indicates that hemispindle microtubules are not necessary for DNA replication, but, on the contrary, hemispindle microtubule polymerization might be actively prohibited during S phase.

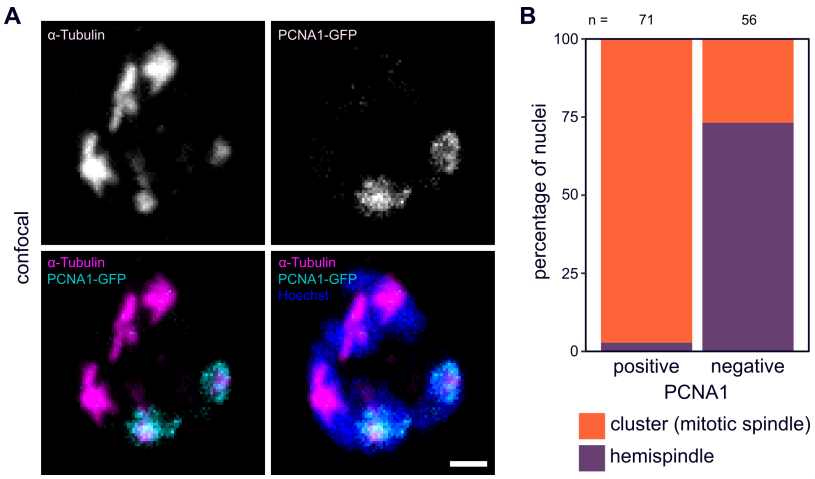

FIGURE 2.13: Actively replicating nuclei are devoid of hemispindles. (A) Confocal image of a 3D7 schizont expressing 3xNLS-mCherry and, to mark actively replicating cells, the proliferating cell nuclear antigen 1 tagged with GFP (PCNA1-GFP). The cell was labeled with anti-α-tubulin (magenta), anti-GFP (cyan) antibodies and stained with Hoechst (blue). The images show maximum intensity projections of the fluorescent signals. Scale bar, 1 µm. (B) Quantification of percentage of tubulin clusters and hemispindle microtubules in nuclei with and without PCNA1-GFP signal. For quantification, 71 PCNA1-GFP-positive nuclei (20 cells, one replicate) and 56 PCNA1-GFP-negative nuclei (18 cells, one replicate) were analyzed and the respective numbers normalized to 100%.

2.5 Bipartite organization of centriolar plaques

Next, I aimed to analyze the organization of *P. falciparum* centriolar plaques in more detail. In particular, I wanted to understand whether the centriolar plaque is inserted into the nuclear membrane as a study by Schrével et al. (1977) in *P. berghei* sporogony suggested.

2.5.1 Centriolar plaques are organized into an intra- and extranuclear compartment

Using U-ExM and RescueSTED super-resolution techniques, I consistently detected a substantial gap between the centrin signal and the origin of microtubule structures at the centriolar plaque (Figure 2.9, Figure 2.10) which had previously been described by Roques et al. (2019) and Bertiaux et al. (2021). I observed this gap in all three microtubule stages including hemispindles, mitotic and extended spindles (Figure 2.9, Figure 2.10). To analyze the detailed localization of centrin and microtubule start sites and test whether the centriolar plaque is embedded into the nuclear membrane, I needed a nuclear envelope marker. As such a marker does not exist for *Plasmodium* blood-stages, I used the nucleoporin Nup313, which was recently identified as a nuclear pore protein in *P. berghei* (Kehrer et al., 2018), to partially visualize the nuclear envelope. Marta Machado endogenously tagged Nup313 in *P. falciparum* with 3xHA as described in Simon et al. (2021a) and subsection 4.2.3.
RescueSTED microscopy of Nup313-3xHA expressing schizonts labeled with anti-HA, anti-centrin and anti-α-tubulin antibodies revealed that centrin signals consistently localize outside of the nucleus in hemispindles and mitotic spindle stages (Figure 2.14). While centrin is extranuclear, hemispindle and mitotic spindle microtubules were located on the intranuclear site of the nuclear pores throughout schizogony (Figure 2.14). My data indicates a bipartite organization of the centriolar plaque with the nuclear membrane separating an extranuclear, centrin-positive compartment from an intranuclear, microtubule-containing compartment.

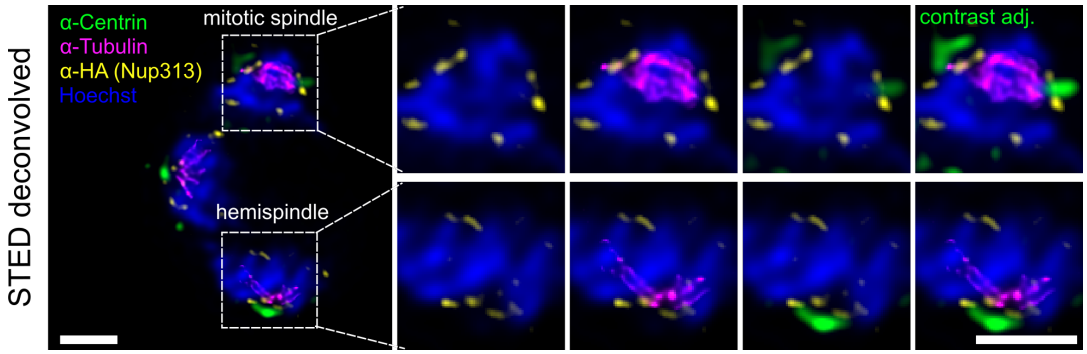

FIGURE 2.14: Bipartite organization of the centriolar plaque with extranuclear centrin and intranuclear microtubules. Deconvolved dual-color RescueSTED images of a 3D7 schizont expressing Nup313-3xHA_glmS. The cell was immunolabeled with anti-PfCentrin3 (green), anti-α-tubulin (magenta), anti-HA (yellow) antibodies and stained with Hoechst (blue). Tubulin and Nup313-signals were acquired using RescueSTED, PfCentrin3 and Hoechst signals using the confocal mode. Zoom-ins show nuclei with a mitotic spindle and a hemispindle, respectively. Images show a single z-slice, scale bars are 1 µm.

Interestingly, I always observed a region underlying the centrin and nuclear pore signals which was devoid of Hoechst signal and had not been described before.

2.5.2 The intranuclear compartment is free of DNA and RNA

The Hoechst-free region underlying centrin foci can not only be observed with super-resolution techniques, but was already clearly detectable using conventional confocal microscopy (Figure 2.15A).

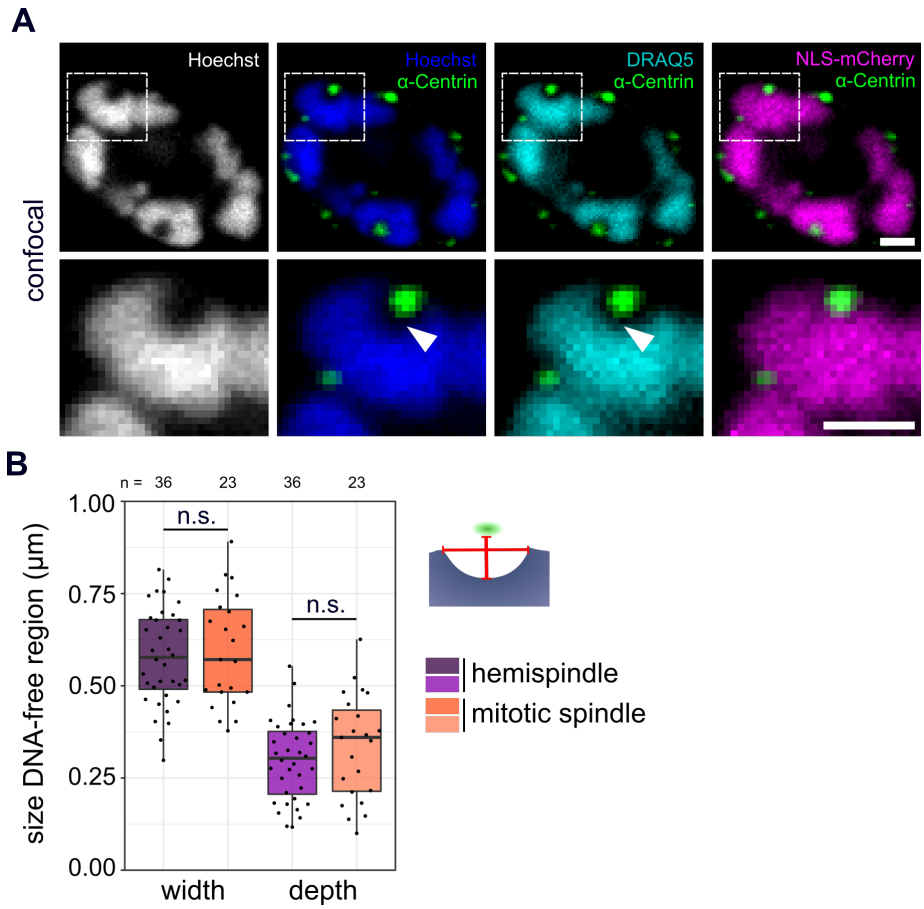

FIGURE 2.15: The intranuclear compartment of the centriolar plaque is free of DNA. (A) Confocal images of a 3D7 schizont episomally expressing 3xNLS-mCherry. mCherry signal was enhanced using RFP-Booster-Atto594 (magenta) and cells were labeled with anti-centrin (green) antibody. To stain DNA, the minor-groove intercalators Hoechst (blue) and DRAQ5 (cyan) were used. Lower panels show zoom-ins of an exemplary intranuclear DNA-free compartment (arrowheads) underlying the centrin signal. Images are single slices, scale bars are 1 µm. (B) Quantification of width and depth of DNA-free intranuclear centriolar plaque compartments in 3D7 wt hemispindle (n = 36, one replicate) and mitotic spindle (n = 23, one replicate) microtubule stages. Dimensions of the DNA-free region were determined in single z-slices as indicated in the schematic: Depth was measured from underneath the centrin signal to the deepest point of the DNA-free region, width at the widest diameter where the nuclear envelope is expected to be. To test for significant differences in width and depth of DNA-free regions between different tubulin stages, t-tests were performed.

To confirm that the region without Hoechst signal is indeed devoid of DNA and not resulting from inefficient labeling of chromatin with the minor-groove binder Hoechst, I co-stained parasites with DRAQ5, a DNA intercalator and minor-groove binder (Wang et al., 2017). DRAQ5 staining approved the DNA-free region associated with centrin signals (Figure 2.15A). Nuclear pore labeling already suggested that the DNA-free region underlying centrin foci is inside the nucleus (Figure 2.14). However, as nuclear pores are not continuously visualizing the outline of the nuclear envelope,

I additionally tested whether the DNA-free region is inside or outside the nucleus. Therefore, I used a cell line generated by Darius Klaschka and Marta Machado as described in Klaus et al. (2021), Simon et al. (2021a) and subsection 4.2.3, which episomally expresses mCherry tagged with three nuclear localization signals (NLS) to visualize the entire nucleoplasm (Figure 2.15A). In contrast to Hoechst and DRAQ5 labeling, no signal-free region beneath the centrin foci was detected (Figure 2.15A), supporting the notion that the DNA-free compartment associated with the centriolar plaque is indeed inside the nucleus. The size of the DNA-free intranuclear compartment was comparable between centriolar plaques organizing hemispindle or mitotic spindle microtubules (Figure 2.15B). The width of the DNA-free region was on average 580 nm in hemispindle stages (595 nm in mitotic spindles), the average depth, from underneath the centrin signal to the deepest point of the compartment, measured around 300 nm (335 nm in mitotic spindle stages, 300 nm in hemispindles, Figure 2.15B).

To further analyze whether RNA is present in the DNA-free compartment, I labeled schizonts with SytoRNASelect, which is selectively staining RNA over DNA. SytoRNASelect signals were excluded from a region right beneath the centrin foci, which was comparable to the DNA-free region. My data shows that the intranuclear compartment of the centriolar plaque is free of both DNA and RNA.

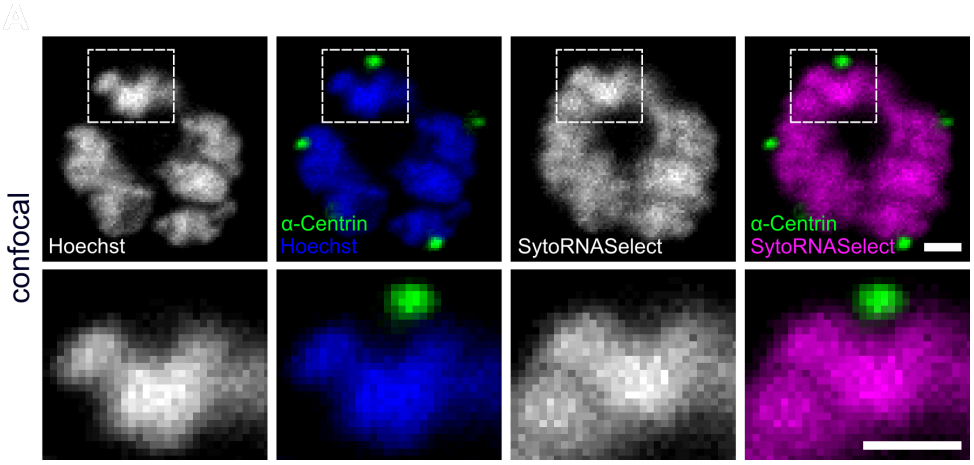

FIGURE 2.16: The DNA-free intranuclear compartment of the centriolar plaque is devoid of RNA. Confocal images of a 3D7 schizont episomally expressing Nup313-3xHA_glmS. Cells were immunolabeled with anti-PfCentrin3 (green) antibody and additionally stained with Hoechst (blue) and the RNA dye SYTO RNASelect (magenta). Bottom panels are zoom-ins of a single nucleus with a centriolar plaque. Images show a single z-slice of the cell, scale bars are 1 µm.

2.5.3 Intra- and extranuclear compartment are enriched with proteins

As the intranuclear compartment of the centriolar plaque in *P. falciparum* blood-stages is both free of DNA and RNA, Johanna Bauer, under my supervision, tested whether proteins are enriched in this area. To visualize regions with high protein density, we labeled cells with NHS esters coupled to Atto 594. NHS esters react with primary amines at the N-terminus of each polypeptide chain and with side-chains of lysine

residues, labeling proteins of any kind. While NHS ester labeling of non-expanded cells was not conclusive (data not shown), NHS ester staining of cells expanded via U-ExM was shown recently for *P. berghei* ookinetes (Bertiaux et al., 2021). Therefore, Johanna Bauer, under my supervision, performed U-ExM and stained *P. falciparum* schizonts with the NHS ester Atto 594 dye conjugate as well as Hoechst and co-labeled the cells either with anti-α-tubulin (Figure 2.17A) or anti-centrin antibodies (Figure 2.17B).

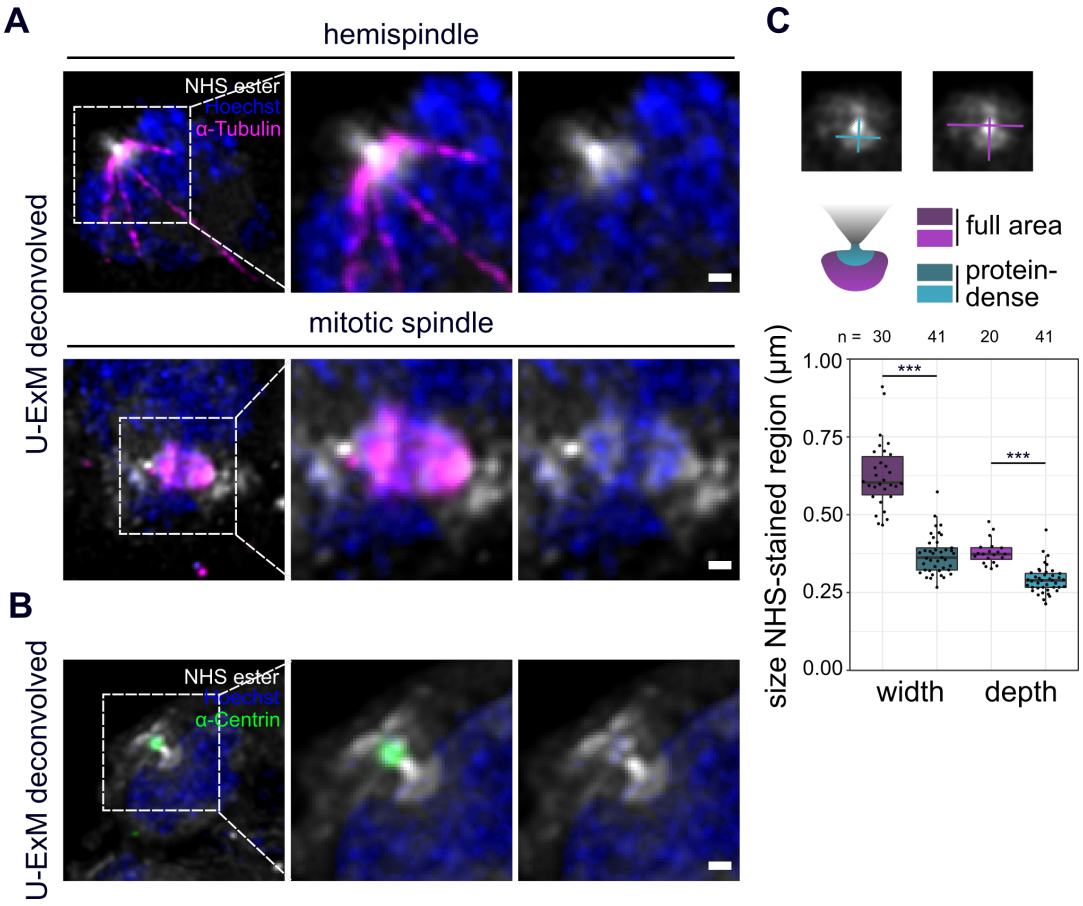

FIGURE 2.17: Centriolar plaque intra- and extranuclear compartments are protein-rich. (A) Deconvolved confocal U-ExM images of two individual 3D7 Nup313-3xHA_glmS schizont nuclei in hemispindle and mitotic spindle microtubule stage. Cells were labeled with anti-α-tubulin (magenta) antibody, stained with Hoechst (blue) and NHS ester Atto 594 dye conjugate (grey) to visualize proteins in bulk. Brighter staining indicates higher protein density. Scale bars, 1 µm (after expansion). (B) As in (A), but nuclei were labeled with anti-PfCentrin3 (green) instead of anti-α-tubulin antibody. (C) Quantification of width and depth of the complete NHS ester-stained intranuclear region of the centriolar plaque and the smaller highly protein-dense region within (see example images and schematic). Significant differences in width and depth of the two NHS-ester-stained regions were determined using Mann–Whitney U tests. For quantification, NHS-ester stained regions of 14 schizonts (one replicate) were analyzed.

NHS ester labeling indicated a high protein density in the intranuclear as well as in the extranuclear compartment of the centiolar plaque (Figure 2.17A,B). The two compartments were connected via a neck, which showed highest protein density and likely indicates where both regions are connected through the nuclear envelope. Often, the protein-dense area at the centriolar plaque reminded of an hourglass

shape. This data indicates that the protein-dense centriolar plaque region stretches from the cytosol to the nucleoplasm. While parts of the extranuclear protein-dense area were overlapping with centrin (Figure 2.17B), the intranuclear protein-enriched region partially co-localized with microtubule signals, especially with mitotic spindles (Figure 2.17A). Within the intranuclear compartment, we further identified two regions with graded protein-density: A smaller, very protein-dense, inner region and a wider region with slightly lower protein-density. While the smaller region on average measured 370 nm in width and 290 nm in depth, the wider region was significantly larger (width: 630 nm, depth: 380 nm, Figure 2.17C). The dimensions of the wider protein-dense region were comparable to the size of the DNA-free regions analyzed in Hoechst-labeled, non-expanded cells (Figure 2.15B).
In summary, the data indicates a bipartite organization of the centriolar plaque with an extranuclear centrin-containing compartment and a DNA- and RNA-free intranuclear compartment which are on both sides embedded into protein-dense material connecting the two compartments via a single, highly protein-enriched neck.

2.6 Ultrastructural organization of mitotic microtubules and the bipartite centriolar plaque

Although super-resolution microscopy techniques such as STED and U-ExM visualized centrin and microtubule signals at unprecedented resolution, we are still missing ultrastructural details in particular of structures that we are missing fluorescent markers for, such as the nuclear membrane. To analyze the in-depth organization of centriolar plaques and associated microtubules, I established different protocols for transmission electron microscopy (TEM) and correlative light and electron microscopy (CLEM) combined with tomography of high-pressure frozen *P. falciparum* cells during schizogony.

2.6.1 Electron microscopy confirms a continuous nuclear membrane at centriolar plaques

To visualize the nuclear membrane and analyze detailed features around the centriolar plaque, I imaged *P. falciparum* schizonts using TEM. Therefore, I performed high-pressure freezing of multinucleated parasites, followed by freeze-substitution in a mixture of osmium tetroxide and uranyl acetate and embedding of the sample pellet in Spurr's resin as described in subsection 4.2.12. After trimming and sectioning of the sample, I imaged 70 nm thin sections using TEM. Figure 2.18 shows a TEM image of a schizont nucleus, likely in hemispindle stage. The nuclear membrane at the likely position of the centriolar plaque was continuous: I observed no invagination of the nuclear membrane, which is consistent with my fluorescence microscopy data (Figure 2.14, Figure 2.15). Hemispindle microtubules were originating in the area underlying the nuclear membrane. This area was delineated by a non-membranous

boundary-like structure and might be associated with the intranuclear compartment of the centriolar plaque. However, the area was slightly smaller in width (circa 450 nm) and depth (circa 190 nm) than the average DNA-free region and full NHS ester-stained region (Figure 2.15, Figure 2.17). An electron-dense region at the nuclear membrane is probably associated with the centriolar plaque. However, due to the absence of any clear structural elements, identification of the centriolar plaque was challenging especially when microtubules were also difficult to detect (Figure 2.18).

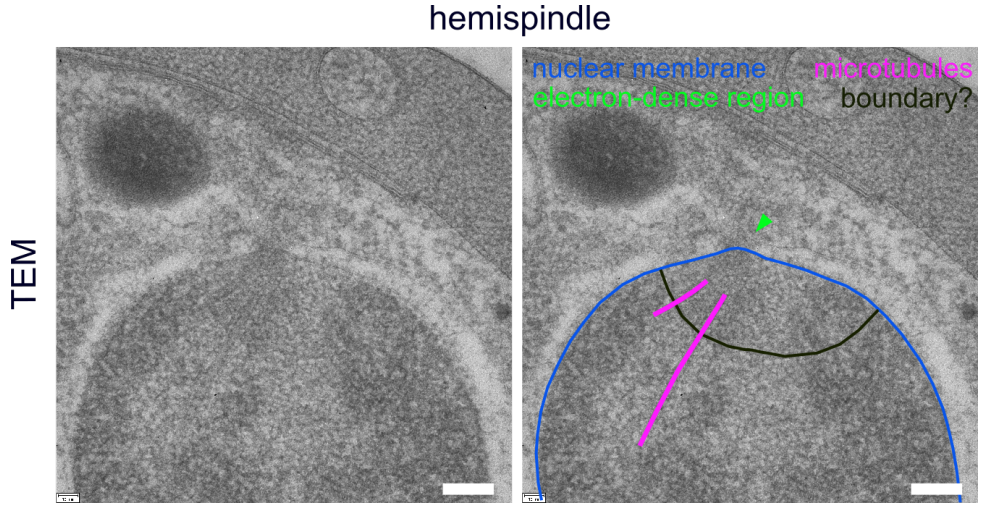

FIGURE 2.18: Transmission electron microscopy confirms that the nuclear membrane is not invaginated at the centriolar plaque. Transmission electron microscopy (TEM) image of a high-pressure frozen NF54 wt schizont nucleus with a centriolar plaque organizing hemispindle microtubules. The annotated copy on the right highlights the continuous nuclear membrane (blue), an electron-dense region likely associated with the centriolar plaque (green arrowhead) and a boundary-like structure possibly confining the intranuclear compartment of the centriolar plaque from which microtubules (magenta) are nucleated. Scale bars, 100 µm.

2.6.2 Establishing correlative light and electron microscopy (CLEM) for *Plasmodium* blood stages

To unambiguously identify centriolar plaque localization in transmission electron microscopy images, I established an on-section correlative light and electron microscopy (CLEM) protocol for *Plasmodium* schizonts expressing PfCentrin1-GFP based on the approach by Kukulski et al. (2011) and Kukulski et al. (2012). Protocols including treatment of high-pressure frozen *Plasmodium* schizonts with osmium tetroxide and embedding in Epon or Spurr's resin provide good contrast and ultrastructural preservation (Figure 2.18). However, these approaches are not suitable for CLEM as osmium and Epon/Spurr are well-known to eliminate fluorescence of conventional fluorescent proteins such as GFP.

To preserve PfCentrin1-GFP signals in high-pressure frozen schizont pellets, I performed the freeze-substitution in 0.3% uranyl acetate in absence of osmium tetroxide. Next, I embedded cells in the Lowicryl HM20, which is polymerized by UV light, before I performed on-section widefield fluorescence and transmission electron microscopy (subsection 4.2.14, Figure 2.19A). Using UV-polymerized HM20 samples,

only thin layers and regions of the sample pellet showed sufficient polymerization and therefore embedding of infected red blood cells. In regions with poor embedding, cells showed inadequate ultrastructural preservation, but bright fluorescence signals. However, these were mostly unspecific. In contrast, in iRBCs which showed good embedding and ultrastructural features I detected no or very low fluorescent signals (Figure 2.19A). In the rare cases in which a PfCentrin1-GFP signal was retained in well-embedded parasites, it was often unclear whether the fluorescence signal was specific and associated with a centriolar plaque (Figure 2.19A, zoom-ins). Anti-correlation of good embedding/ultrastructural preservation and fluorescent signals preserved in the samples made it virtually impossible to correlate specific PfCentrin1-GFP fluorescent signals with TEM images of sufficient quality.

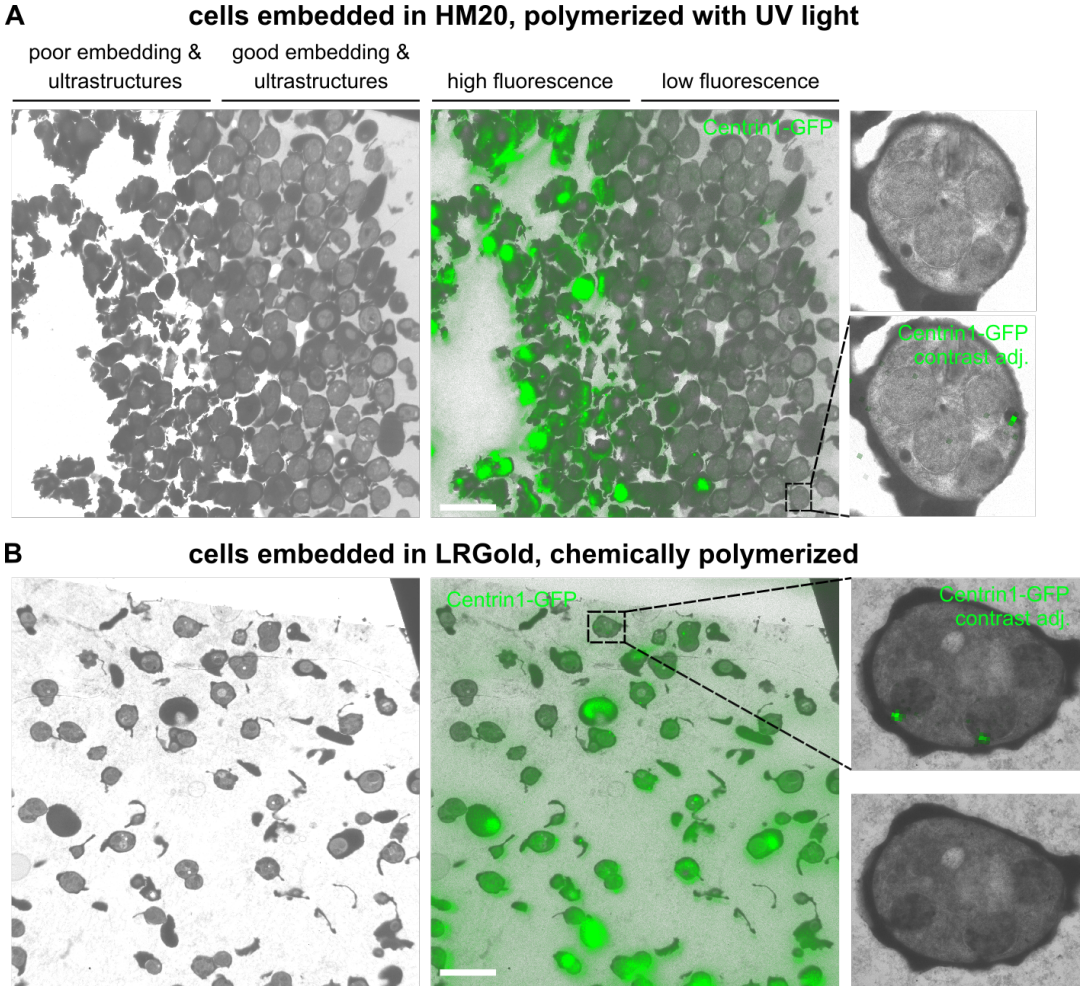

FIGURE 2.19: For CLEM, embedding of *P. falciparum*-infected erythrocytes in LRGold with chemical polymerization is superior to UV-polymerized HM20 Lowicryl embedding. (A) TEM image (left) and overlay with widefield fluorescence image (on-section CLEM, middle) of high-pressure frozen NF54 parasites episomally expressing PfCentrin1-GFP (green). Samples were embedded in the Lowicryl HM20, which was polymerized with UV light, trimmed and sectioned (250 nm). Zoom-ins show a well-preserved schizont which shows a dim, probably unspecific PfCentrin1-GFP signal. (B) As for (A), but cells were embedded in LRGold resin which was chemically polymerized by addition of benzoyl peroxide and sections were cut to 300 nm thickness. Zoom-ins show a schizont with sufficient ultrastructural preservation and two PfCentrin1-GFP signals associated with parasite nuclei. Scale bars, 10 µm.

A likely reason for inhomogeneous polymerization with UV light and embedding of *Plasmodium*-infected red blood cells is the parasite-specific hemozoin which highly absorbs light in the visible and UV range (Cai et al., 2016; Menyaev et al., 2016; Balasubramanian et al., 1984). Dense sample pellets of hemozoin-containing schizonts might therefore hinder penetration of UV light into the sample pellet leading to polymerization of only a thin sample layer at the surface.

As an alternative, I tested embedding of PfCentrin1-GFP expressing schizonts into LRGold resin, which can be polymerized at room temperature by addition of the chemical initiator benzoyl peroxide. In contrast to HM20-embedding, ultrastructural preservation and fluorescence signal conservation were not anti-correlated in LRGold-embedded samples: Schizonts with specific, nuclei-associated PfCentrin1-GFP foci showed a reasonably good preservation of ultrastructural features (Figure 2.19B) although TEM quality was slightly reduced in comparison to HM20 embedding. It should be noted that cell density during high-pressure freezing is difficult to control and highly varied between cell pellets used for HM20- and LRGold embedding (Figure 2.19). Therefore, the influence of cell density on fluorescent signal retention and ultrastructural preservation still needs to be investigated.

CLEM approaches are always a compromise between quality of fluorescent and transmission electron microscopy images. For PfCentrin1-GFP expressing *P. falciparum* schizonts, LRGold embedding with polymerization upon addition of a chemical initiator was clearly superior to HM20 embedding and I therefore used it in the following for CLEM combined with tomography.

2.6.3 CLEM allows unambiguous identification of centriolar plaque position and confirms its bipartite organization

To combine a correlative light and electron microscopy (CLEM) approach for identification of centriolar plaques with electron tomography, I used my established on-section CLEM protocol (subsection 2.6.2). I incubated *P. falciparum* schizonts episomally expressing PfCentrin1-GFP with the live-cell-compatible fluorescent DNA dye 5-SiR-Hoechst (Bucevičius et al., 2019) before high-pressure freezing. Briefly, frozen sample pellets were freeze-substituted in uranyl acetate, embedded in LRGold by chemical polymerization, trimmed, and 300 nm sections were collected on grids before widefield fluorescence microscopy and electron tomography of the same cell were performed (subsection 4.2.14). With the help of overview images and finder grids, I relocated individual fluorescent cells in TEM images. The fluorescent image was correlated with a single section of the reconstructed tomogram via alignment of characteristic cellular features detected in both, fluorescence microscopy and TEM (Figure 2.20). All steps were performed by myself, except for acquisition of tilted series and reconstruction of the tomogram, which were performed by Juyeop Kim and Marek Cyrklaff.

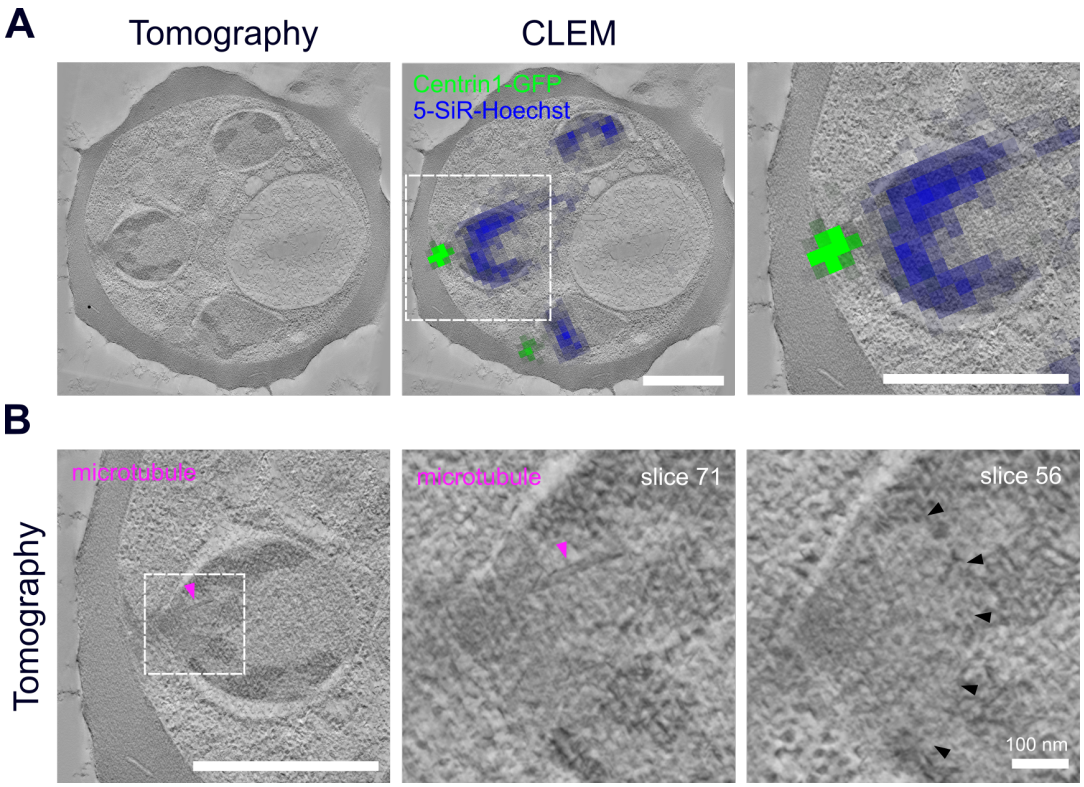

FIGURE 2.20: CLEM combined with tomography reveals unambiguous localization of centriolar plaques and confirms their bipartite organization. (A) Correlative light and electron microscopy (CLEM) combined with tomography of a NF54 schizont episomally expressing PfCentrin1-GFP (green). Cells were incubated with the live-cell DNA dye 5-SiR-Hoechst (blue), followed by high-pressure freezing of the cells, freeze-substitution, resin embedding, trimming and sectioning (300 nm) of the sample. After on-section widefield fluorescence microscopy, tilted TEM series were acquired, reconstructed, and the corresponding areas overlayed (CLEM). Zoom-in shows a single nucleus of the schizont with an extranuclear PfCentrin1-GFP signal clearly showing the position of the centriolar plaque. Scale bars, 1 µm. (B) Zoom-ins from the tomogram in (A). In slice 71 of the tomogram, a microtubule (magenta arrowhead) was detected emanating from the intranuclear compartment. In slice 56, black arrowheads indicate a boundary-like structure possibly indicating the edge of the intranuclear compartment. Scale bars are 1 µm, except where indicated.

PfCentrin1-GFP and 5-SiR-Hoechst fluorescent signals were both retained in the samples (Figure 2.20A) and centrin foci allowed the unambiguous localization of centriolar plaques in TEM images and reconstructed tomograms. PfCentrin1-GFP signals were detected in the cytoplasm closely associated with schizont nuclei (Figure 2.20A) which showed no invagination at the centriolar plaque. These observations are consistent with my immunofluorescence images displaying centrin localization in the extranuclear compartment of the centriolar plaque (Figure 2.14, Figure 2.15, Figure 2.17). 5-SiR-Hoechst fluorescent signals were usually absent in the region directly underlying the nuclear membrane at the centriolar plaque (Figure 2.20A), confirming a DNA-free intranuclear compartment of the centriolar plaque. However, 5-SiR-Hoechst signals were mainly associated with dense heterochromatin regions in the nuclei, which have a higher electron-density in TEM images than euchromatin (Figure 2.20). Restriction of the DNA signal to heterochromatin might be due to the limited material and binding of the DNA dye to a 300 nm thin section.

In one tomogram slice depicted in Figure 2.20B I could clearly identify a microtubule structure emanating from the intranuclear compartment. In another slice, a boundary-like structure can be surmised separating a region with a slightly different electron-density and the detected microtubule from the residual nucleus (Figure 2.20B, right image). This region measured circa 490 nm in width and 320 nm in depth and therefore corresponded well to the size of the DNA-free region and the full NHS ester-stained region measured in fluorescent images (Figure 2.15, Figure 2.17). This data indicates that the boundary might indeed delineate the intranuclear compartment of the centriolar plaque. To summarize, CLEM combined with tomography confirmed the organization of *P. falciparum* centriolar plaques into an extranuclear compartment with centrin and an intranuclear compartment associated with microtubules.

2.6.4 Individual microtubule minus-ends emanate from underneath the nuclear membrane

CLEM confirmed the bipartite centriolar plaque organization by correlating fluorescent images with reconstructed tomograms (subsection 2.6.3). However, microtubules were often difficult to identify in tomograms of cells embedded in LRGold which was polymerized chemically. In addition, quality of ultrastructural details was slightly lower than in samples embedded in the Lowicryl HM20, preventing identification of microtubule minus-ends. To resolve more microtubules and especially their minus-ends to analyze the exact position of microtubule nucleation complexes around γ-tubulin, Charlotta Funaya performed tomography of high-pressure frozen schizonts that I prepared and embedded in HM20 as described in subsection 2.6.2. In addition, Charlotta Funaya annotated the nuclear membrane, microtubules and microtubule minus-ends in reconstructed tomograms for 3D models (Figure 2.21).

Reconstructed tomograms of hemispindle stages revealed individual, long, intranuclear microtubules branching radially into the nucleoplasm (Figure 2.21A). Occasionally, microtubules were detected in protrusions of the nuclear membrane, an observation in line with immunofluorescence data showing hemispindle microtubules extending the nuclear body (subsection 2.4.1). This data indicates that hemispindle microtubules can deform the nuclear membrane, but do not penetrate it. Microtubule minus-ends were annotated by the ultrastructural appearance of microtubule tips. Previous studies have shown that microtubule minus-ends typically show a capped or closed structure while microtubule plus-ends are open (O'Toole et al., 2003; Höög et al., 2007). An example of microtubule minus-end annotation is depicted in Figure 2.22. Minus-ends of hemispindle microtubules were located at individual positions, closely underlying the nuclear membrane and a membrane-associated electron-dense area, likely accompanying the centriolar plaque (Figure 2.21A).

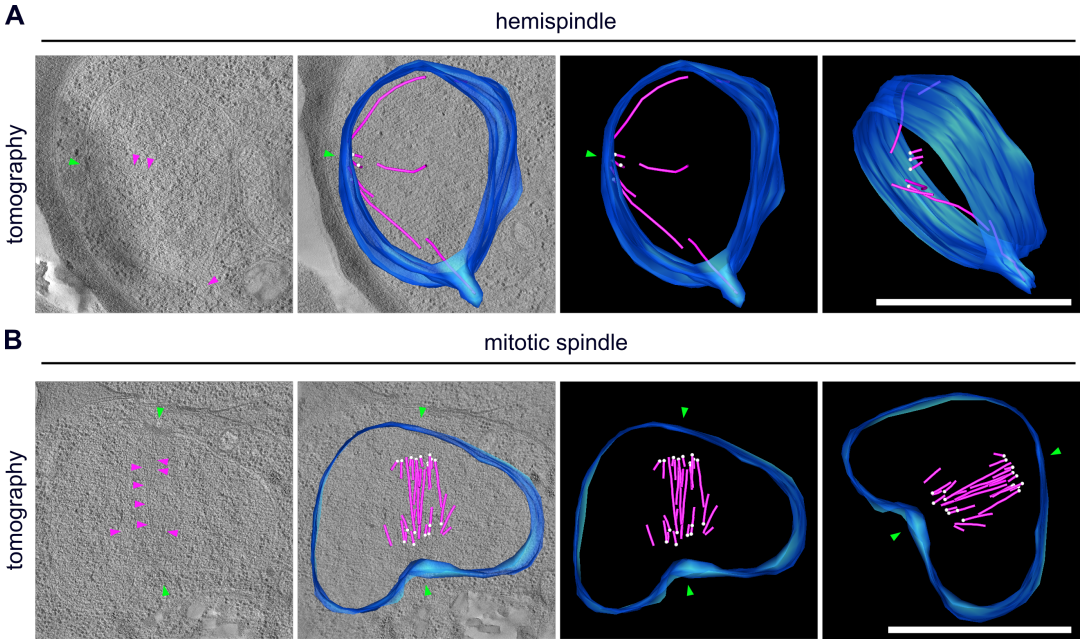

FIGURE 2.21: Distinct microtubule nucleation sites emanate from underneath the nuclear membrane in hemispindle and mitotic spindle microtubules. (A) Electron tomogram of a schizont nucleus 3D-reconstructed from tilted series of three 200 nm serial sections. For tomography, NF54 schizonts expressing PfCentrin1-GFP were high-pressure frozen, freeze-substituted, resin-embedded and the samples trimmed and sectioned before tilt-series were acquired. The left image shows a single slice of the tomogram with indicated microtubule structures (magenta arrowheads) and an electron-dense region in the nuclear envelope (green arrowhead) likely associated with the centriolar plaque. 3D models show annotations of the nuclear membrane (blue), microtubules (magenta) and microtubule minus-ends (white). (B) As in (A), but for a nucleus showing a mitotic spindle. For the reconstruction of the tomogram, tilted series of a single 200 nm section were used. Note that minus-ends of mitotic spindle microtubules localize at a significant distance to the nuclear membrane. Scale bars, 1 µm.

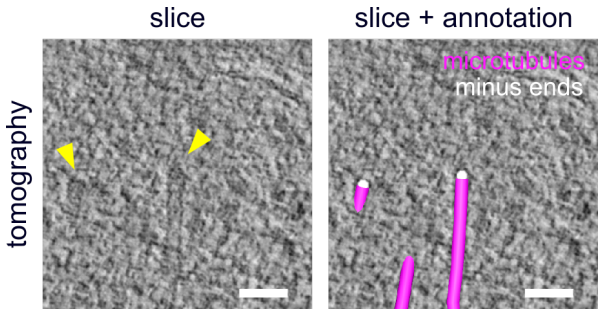

FIGURE 2.22: Identification of microtubule nucleating complexes in electron tomograms via capped microtubule minus-end structures. Zoom-in from one slice of the 3D-reconstructed electron tomogram of the mitotic spindle in Figure 2.21B. For electron tomography, NF54 schizonts expressing PfCentrin1-GFP were high-pressure frozen, freeze-substituted and resin-embedded. The sample was trimmed and 200 nm sections were cut. Yellow arrowheads indicate capped structures identifying microtubule minus-ends. The right image shows the same, annotated slice with tracking of microtubules (magenta) and microtubule minus-ends (white). Scale bars, 50 nm.

The reconstructed, annotated tomogram of a mitotic spindle stage (Figure 2.21B) shows two opposing electron-densities associated with the nuclear membrane, indicating centriolar plaque position. Although the mitotic spindle tomogram was reconstructed from a single 200 nm section while in the hemispindle tomogram

three consecutive sections were used, many more microtubules could be detected (Figure 2.21). These were in general shorter and denser than in hemispindles and positioned between the two potential centriolar plaques. While some microtubules were associated with a single centriolar plaque, others were spanning the complete region between the two microtubule-organizing centers (Figure 2.21B). In contrast to hemispindle stages, microtubule minus-ends of mitotic spindles were located at a substantial distance to the nuclear membrane (Figure 2.21, Figure 2.23). The shortest distance of minus ends to the nuclear envelope measured on average 58 nm for hemispindle microtubules, while the distance with an average of 148 nm was significantly larger for microtubule minus-ends of mitotic spindle stage (Figure 2.23).

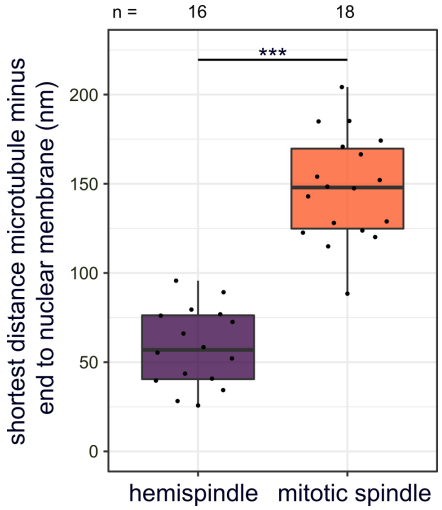

FIGURE 2.23: Microtubule minus-ends in mitotic spindles localize at a significantly greater distance to the nuclear membrane than in hemispindles. Quantification of the shortest distance from microtubule minus-ends to the nuclear membrane in mitotic spindle and hemispindle 3D-reconstructed electron tomograms of NF54 schizonts expressing PfCentrin1-GFP. In total, 18 minus-ends of mitotic spindle microtubules (one cell, Figure 2.21B) and 16 minus-ends of hemispindle microtubules (4 cells; Figure 2.21B, Figure 2.24) were analyzed. To test for significant differences, an unpaired t-test was performed.

A boundary-like non-membranous structure that was sometimes surmised in TEM (Figure 2.18) and CLEM images (Figure 2.20) likely delineating the intranuclear centriolar plaque compartment was not observed in the tomograms shown in Figure 2.21. Only occasionally, such a boundary was vaguely perceptible in some slices of reconstructed tomograms and might separate regions with slightly different electron density (Figure 2.24).

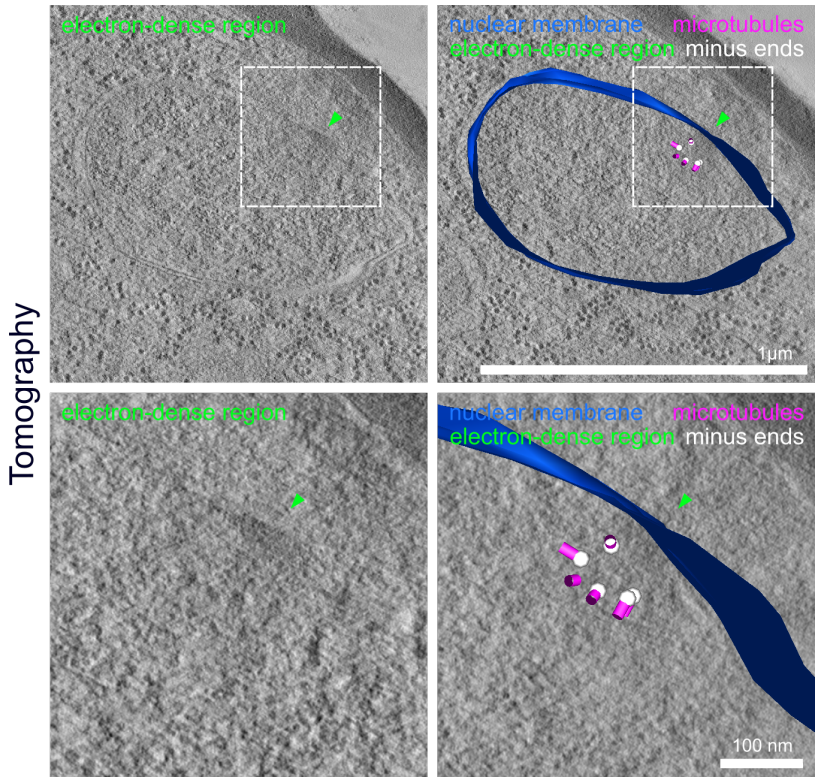

FIGURE 2.24: Intranuclear regions of centriolar plaques might be surmised in some sections of electron tomograms. Single slices and zoom-ins of a 3D-reconstructed electron tomogram of a high-pressure frozen NF54 schizont expressing PfCentrin1-GFP shows a single nucleus in hemispindle microtubule stage. The electron-dense region (green arrowhead) is likely associated with the centriolar plaque. On the right, annotated slices are shown: nuclear membrane (blue), microtubules (magenta) and microtubule minus-ends (white). Slight differences in electron density and boundary-like structures might indicate the intranuclear region of the centriolar plaque. Scale bars are as indicated.

All of the above results were published in peer-reviewed journals with me as first author. In the following I will proceed with outlining unpublished data of my PhD project.

2.7 Co-immunoprecipitations reveal a novel outer centriolar plaque protein

My study provides a novel view on the (ultra-)structural organization of the *Plasmodium* centriolar plaque during blood-stage schizogony. However, composition of the intra- and extranuclear compartment remains largely unknown. The only proteins shown to localize at centriolar plaques are Centrins1-4 (Mahajan et al. (2008); unpublished data, Yannik Voß) in the extranuclear compartment and Aurora-related kinase 1 (Ark1) (Reininger et al., 2011). To get a functional understanding of centriolar plaques, it is crucial to elucidate further components. Therefore, I aimed to identify novel centriolar plaque proteins, starting with the outer compartment represented by centrins.

2.7.1 Eleven centriolar plaque outer compartment candidates identified by co-immunoprecipitations

To identify novel outer centriolar plaque proteins, I used an *in vivo* proximity-labeling approach based on the engineered peroxidase APEX2 (Lam et al., 2015). Therefore, I treated living parasites episomally expressing PfCentrin3 tagged with APEX2 and 3xHA or Spot tag with biotin-phenol and hydrogen peroxide. APEX2 catalyzes the oxidation of biotin-phenol into a biotin-phenoxyl radical (Lam et al., 2015). This very short-lived radical reacts with proteins in close vicinity to the APEX2-tagged Centrin3 and covalently tags them with biotin. Biotinylated proteins can then be identified using streptavidin-based immunoprecipitations combined with mass spectrometry analysis (Lam et al., 2015).
IFAs using fluorophore-coupled streptavidin showed partial colocalization of biotinylated proteins with centrin foci (data not shown). In a western blot, I detected enrichment of biotinylated proteins in samples treated with biotin-phenol when compared to non-treated cells or to 3D7 wt parasites in absence/presence of biotin-phenol (data not shown). However, using mass spectrometry, I identified peptides of almost one third of all *P. falciparum* proteins (data not shown). Recently, co-immunoprecipitations of *P. berghei* Centrin4-GFP expressing parasites identified Centrins1-4 in mass spectrometry analysis, indicating their interaction (Roques et al., 2019). Although *P. falciparum* centrins are all localizing to the extranuclear compartment of the centriolar plaque (unpublished data, Yannik Voß), solely the bait, PfCentrin3 was identified in my APEX2-approach. Further, I detected only few of the centrosomal proteins conserved in *Plasmodium* (Suvorova et al., 2015), including putative centrosomal protein CEP76 (PF3D7_0603800) and spindle assembly abnormal protein 4 (Sas4, PF3D7_1458500). In summary, the identified peptides appeared rather unspecific.

As an alternative approach, I aimed to identify outer centriolar plaque proteins by co-immunoprecipitations using NF54 parasites episomally expressing PfCentrin1-,

2-, 3- or PfCentrin4-GFP. As western blotting suggested cleavage of the GFP-tag from PfCentrin4 proteins (data not shown), I, in collaboration with the lab of Mathieu Brochet in Geneva, performed co-immunoprecipitations of PfCentrin1-GFP (no cleavage), PfCentrin2-GFP (mild cleavage) and PfCentrin3-GFP (mild cleavage) expressing NF54 parasites. Exemplary western blots for co-immunoprecipitations of NF54 PfCentrin1- and 2-GFP after protein crosslinking are depicted in Figure 2.25. In total, I performed eight co-immunoprecipitations: 3x PfCentrin1-GFP (2x with, 1x without crosslinking), 3x PfCentrin2-GFP (2x with, 1x without crosslinking) and 2x PfCentrin3-GFP (1x with, 1x without crosslinking). However, as IPs of PfCentrin3-GFP mainly identified PfCentrin3 and PfCentrin1 by mass spectrometry, they were not included for analysis.

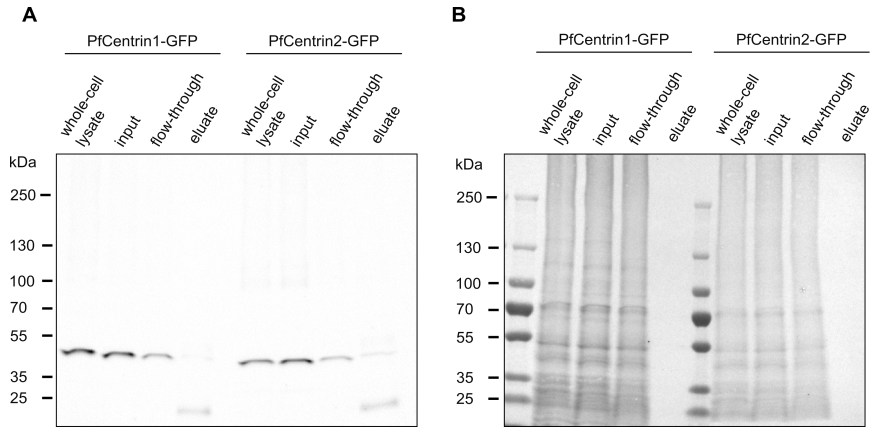

FIGURE 2.25: Co-immunoprecipitations of PfCentrin1- and PfCentrin2-GFP expressing NF54 cells show purification of GFP-tagged centrins. Large-scale co-immunoprecipitations were performed following crosslinking of saponin-lysed parasites with 1% formaldehyde. The "whole-cell lysate" corresponds to parasites additionally lysed via RIPA buffer. After sonication and centrifugation, the supernatant was taken as "input". Following incubation with anti-GFP antibody coupled magnetic dynabeads, the supernatant was taken as the "flow-through". After washing, the "eluate" sample with beads was collected, boiled in reducing SDS-PAGE sample buffer and beads removed before loading of the sample. 1×10^7 iRBCs were loaded per lane (cells counted before saponin-lysis). (A) Western blot, incubated with mouse anti-GFP antibody. The size of the band seen in all lanes fits to the molecular weight of circa 46 kDa expected for PfCentrin1 (19.6 kDa) or PfCentrin2 (19.3 kDa) added to the molecular weight of GFP (26.9 kDa). (B) Corresponding Ponceau-staining of the blot shown in (A).

Importantly, PfCentrin1-3 were detected in immunoprecipitations of both PfCentrin1- and PfCentrin2-GFP expressing cells. This is consistent with the study by Roques et al. (2019) indicating interaction of centrins in *P. berghei*. However, in contrast to Roques et al. (2019), I did not identify Centrin4 immunoprecipitated with the other centrins in *P. falciparum*. To narrow down the proteins identified by mass spectrometry, I first removed all obvious contaminants. To eliminate unspecific hits, I calculated peptide fold-changes using data from the previous PfCentrin3-APEX2 proximity labeling approach (3D7 wt +/- biotin-phenol; 3D7 PfCentrin3-APEX2-3xHA + biotin-phenol; 3D7 PfCentrin3-APEX2-Spot + biotin-phenol) as controls. All proteins with peptide counts enriched less than two-fold were discarded. After further removal of proteins with a clearly defined role in other cellular processes than division, I

compiled a list of eleven potential centriolar plaque outer compartment proteins for further analyses (Table 2.1). A number was assigned to each candidate/gene of interest (GOI) which is used in Table 2.1 and Table 2.2 as well as in subsection 4.1.5, subsection 4.1.6 and subsection 4.1.7. Please be aware that more replicates (minimum of three for crosslinked cells as well as for non-crosslinking) are needed to perform appropriate statistical analyses of the peptide hits. Additionally, controls such as a line expressing a centrosomal protein tagged with GFP are needed for proper analysis. These analyses might identify further centriolar plaque candidates that can easily be overlooked without statistical analysis.

TABLE 2.1: *P. falciparum* centriolar plaque candidates identified by co-immunoprecipitations and subsequent mass spectrometry analysis. The *piggyBac* mutagenesis index score predicts essentiality of genes for parasite growth - 1 means dispensible; the closer to 0, the more essential. hpi, hours post infection.

#	ID PF3D7_	Protein	*piggyBac* mutagenesis index score	transcription profile (hpi / percentile)
01	0308200	T-complex protein 1 subunit eta	0.134	24-32 hpi / 90%
02	0207100	conserved Plasmodium protein, unknown function	1	40-48; 0-8 hpi / 45-80%
03	1455200	methyltransferase, putative, unspecified product	0.763	peak 32 hpi / 80%
04	0203000	repetitive organellar protein, putative	1	32-48; 0 hpi / 25%
05	1135400	conserved Plasmodium protein, unknown function	0.456	40-48 hpi / 100%
06	1427900	leucine-rich repeat protein	0.132	peak 32 hpi / 90%
07	1312800	Uncharacterized protein	1	40-48; 0-8 hpi / 25-50%
08	0710000	conserved Plasmodium protein, unknown function	0.119	40-48 hpi / 40%
09	0619400	Cell division cycle protein 48 homologue, putative	0.425	40-48; 23-48 hpi / 90%
10	1419600	conserved Plasmodium protein, unknown function	0.149	peak 0 hpi / 70%
11	0406100	Vacuolar proton pump subunit B	0.350	16-32 hpi / 90%

The centriolar plaque candidate list includes six proteins with an assigned name and/or a potential function and five proteins of unknown function (Table 2.1). A recent *piggyBac* transposon mutagenesis screening predicts essentiality of *Plasmodium* genes for parasite growth (Zhang et al., 2018). Genes with a score of 1 are predicted to be dispensible, the closer the number gets to 0, the more likely these genes are essential. Table 2.1 shows that I identified proteins predicted to be essential as well as non-essential ones. Further, Table 2.1 gives an overview of the transcription profiles of the identified genes based on the study by Otto et al. (2010). Except for candidate PF3D7_1419600, all candidates showed a transcription peak in trophozoites and/or schizonts. This data indicates that the proteins might play a role during divisions, taking place from 32 to 48 hours post infection (hpi). The percentile gives the ranking of expression for the respective gene compared to all other transcripts, indicating

transcript abundance. A wide range of transcript abundancy was observed, from very low abundant ones (e.g. PF3D7_0203000) to very high abundant ones as for PF3D7_1135400 (Table 2.1). All in all, this data indicates that there is no obvious bias towards essential or non-essential genes as well as towards only high abundant transcripts.

2.7.2 Tagging and knockdown strategy to analyze centriolar plaque candidates

After identification of eleven centriolar plaque candidates (subsection 2.7.1), I aimed to verify and characterize the candidates. For endogenous GFP-tagging and conditional knockdown of the respective genes, I combined selection-linked integration (SLI) (Birnbaum et al., 2017) with the inducible glmS ribozyme system for conditional knockdown of gene transcripts (Prommana et al., 2013) (Figure 2.26A).

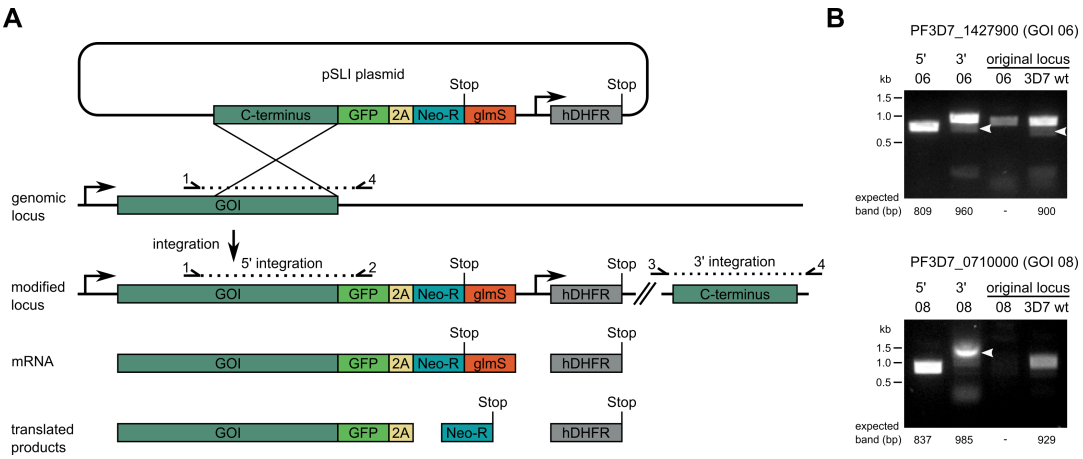

FIGURE 2.26: Endogenous GFP-tagging and conditional glmS-knockdown strategy of centriolar plaque candidates using selection-linked integration (SLI). (A) Schematic showing C-terminal endogenous tagging of centriolar plaque candidate genes (gene of interest, GOI) with GFP and, separated by a T2A skipping peptide, a neomycin-resistance cassette (Neo-R) coupled to the glmS ribozyme sequence using the SLI system. Plasmid-uptake by the parasites is selected via hDHFR expression, providing resistance to WR. After single-crossover integration into the target region, parasites start expressing the neomycin-resistance cassette, enabling selection for integration, in addition to the C-terminal, GFP-tagged gene of interest (GOI). Knockdown of the GOI can be induced by addition of glucosamine, which binds to the glmS transcript and induces self-cleavage on mRNA level. (B) Examplary PCRs for correct 5′ and 3′ integration of the pSLI plasmids for PF3D7_1427900 (GOI 06) and PF3D7_0710000 (GOI 08) into the respective genomic target regions. For 3D7 PF3D7_1427900, unmodified wt locus is still detectable. White arrowheads indicate additional bands which might be due to contaminations.

The SLI system is based on genomic integration of the complete pSLI plasmid via single-crossover which is controlled by a two-step selection process (Birnbaum et al., 2017). Transfected parasites containing pSLI will express human dihydrofolate reductase (hDHFR) mediating resistance to the drug WR99210. In addition, the pSLI plasmid contains a promoterless neomycin resistance cassette. Only upon single-crossover integration of the plasmid into the genomic target region, the neomycin resistance cassette will be expressed under control of the endogenous promoter

(Birnbaum et al., 2017). Neomycin is used to select for parasites with the integrated construct. The specific target sequence is separated from the neomycin resistance sequence by a picornavirus T2A peptide sequence which mediates ribosomal skipping during translation (Birnbaum et al., 2017; Szymczak et al., 2004). Therefore, the selectable marker is not attached to the target protein.
Conditional gene knockdown can be mediated by insertion of the glmS ribozyme sequence into the 3'-UTR of the target gene coding region (Prommana et al., 2013). Therefore, the glmS sequence will be present in the mRNA. Upon addition of glucosamine, which binds to the transcript of the glmS ribozyme, the ribozyme will induce self-cleavage. As a consequence, the mRNA will be degraded and a knockdown of the gene of interest is induced (Prommana et al., 2013).

In my approach, the target region of the pSLI plasmid contains the C-terminal sequence of the gene of interest (GOI) and a GFP sequence (Figure 2.26A). GOI and GFP are separated from the Neomycin resistance cassette and the glmS ribozyme sequence via a T2A skipping peptide (Figure 2.26A). In contrast to Birnbaum et al. (2017), I omitted the stop codon before the C-terminus of the GOI in the pSLI plasmid. Due to the lack of a promoter, the downstream C-terminus should not be expressed and even if, the short C-terminal part of the protein would be non-functional.
For all eleven centriolar plaque candidates, Tatiany Romão, under my supervision, performed cloning and transfection of the respective pSLI plasmids into 3D7 wt parasites. Correct 5' and 3' integration of the constructs were observed for six out of eleven candidates using PCRs (Figure 2.26B, Table 2.2). Example PCR results for the two centriolar plaque candidate genes PF3D7_1427900 (GOI 06) and PF3D7_0710000 (GOI 08) are shown in Figure 2.26B. In the 3D7 strain expressing PF3D7_1427900-GFP_glmS, unmodified wt locus was still detectable (Figure 2.26B). A limiting dilution cloning will be needed to eliminate residual 3D7 wt parasites. Additional bands detected in the PCRs might be due to a contamination (Figure 2.26B, white arrowheads). To unambiguously confirm correct integration, PCRs should be repeated and control PCRs on 3D7 wt genomic DNA with primers used to confirm 5' and 3' integration in the modified strains should be added. For five centriolar plaque candidates, PCRs were completely inconclusive and have to be repeated, too.

Preliminary localization data of GFP-tagged centriolar plaque candidates determined in fixed parasites with endogenous or enhanced GFP signal, is shown in Figure A.1 and summarized in Table 2.2. The cell division cycle protein 48 homologue PF3D7_0619400 is dispersed in the cytoplasm and in the nucleus, showing no association with the centriolar plaque (Figure A.1D). PF3D7_1455200-GFP signals were cytoplasmic, with foci sometimes localizing in close proximity to centrin (Figure A.1A). Interestingly, I detected that two candidates, PF3D7_1312800 and PF3D7_0203000, were associated with the parasite plasma membrane (PPM), sometimes with foci close to centrin (Figure A.1B,C), which might indicate a connection of the centriolar plaque to the plasma membrane. In the next two chapters, localization of the nuclear leucine-rich repeat protein PF3D7_1427900, and the uncharacterized *Plasmodium*

protein PF3D7_0710000 as well as their role for parasite growth in intraerythrocytic stages will be analyzed in more detail (subsection 2.7.3, subsection 2.7.4).

TABLE 2.2: Confirmation of endogenous tagging of centriolar plaque candidates via PCR and localization in *Plasmodium* blood stages determined in preliminary immunofluorescence stainings. +, 5′ and 3′ integration confirmed; -, PCRs not conclusive and integration not yet confirmed; PPM, Parasite plasma membrane.

#	ID PF3D7_	Protein	PCR	Localization (Preliminary data)
01	0308200	T-complex protein 1 subunit eta	-	?
02	0207100	conserved Plasmodium protein, unknown function	-	?
03	1455200	methyltransferase, putative, unspecified product	+	cytoplasm; close to centrin?
04	0203000	repetitive organellar protein, putative	+	PPM, some foci close to centrin
05	1135400	conserved Plasmodium protein, unknown function	-	?
06	1427900	leucine-rich repeat protein	+	nucleus
07	1312800	Uncharacterized protein	+	PPM, some foci close to centrin
08	0710000	conserved Plasmodium protein, unknown function	+	outer centriolar plaque
09	0619400	Cell division cycle protein 48 homologue, putative	+	nucleus and cytoplasm
10	1419600	conserved Plasmodium protein, unknown function	-	?
11	0406100	Vacuolar proton pump subunit B	-	?

2.7.3 The essential leucine-rich repeat protein PF3D7_1427900 is directed towards the centriolar plaque during schizogony

In co-immunoprecipitations of NF54 schizonts expressing PfCentrin1- and PfCentrin2-GFP followed by mass spectrometry analysis I identified the leucine-rich repeat protein PF3D7_1427900 as a novel centriolar plaque candidate (candidate 06) (subsection 2.7.1). During intraerythrocytic development, transcripts of PF3D7_1427900 are mainly present in trophozoites and schizonts with a peak 32 hours post infection (hpi) (Otto et al., 2010). Using 3D7 parasites expressing PF3D7_1427900-GFP_glmS, Tatiany Romão and I detected bright fluorescent signals in both living (data not shown) and fixed cells, the latter with GFP signals enhanced by GFP booster coupled to Atto 594 (Figure 2.27A). High fluorescent signals are in congruence with the overall high abundancy of PF3D7_1427900 transcripts during schizogony in comparison to other mRNA (Otto et al., 2010) hinting at high protein abundancy.
In early and mid-schizonts, PF3D7_1427900 was dispersed in nuclei, showing a distribution in patches (Figure 2.27A). Interestingly, the localization changed in the course of schizogony and PF3D7_1427900 was redirected towards centriolar plaques, being closest to centrin signals in segmented parasites, while still remaining intranuclear (Figure 2.27A). However, localization patterns varied between cells and performed IFAs.

To analyze the role of PF3D7_1427900 for intraerythrocytic parasite growth, Marta Machado and Tatiany Romão performed growth assays of 3D7 PF3D7_1427900-GFP_glmS parasites cultured in absence or presence of 3.5 mM glucosamine (GlcN) for inducible knockdown of PF3D7_1427900 mRNA (Figure 2.27B). Therefore, parasitemia was determined over three consecutive cycles (144 hours) in cells stained with SYBR Green I using flow cytometry (subsection 4.2.18). 3D7 PF3D7_1427900-GFP_glmS parasites cultured in absence of GlcN showed similar growth to 3D7 wt control cells (Figure 2.27B). In presence of 3.5 mM GlcN, 3D7 wt parasite growth was reduced, indicating negative side effects of GlcN. However, when 3D7 PF3D7_1427900-GFP_glmS parasites were incubated with 3.5 mM GlcN, all parasites were dead from the second cycle onwards (Figure 2.27B). This is consistent with a previous *piggyBac* transposon mutagenesis screening which predicted PF3D7_1427900 to be essential for parasite growth (mutagenesis index score: 0.132) (Zhang et al., 2018).

In summary, the essential leucine-rich repeat protein PF3D7_1427900 is an intranuclear protein which might be associated with centriolar plaques in late schizonts or segmenter stages during intraerythrocytic development.

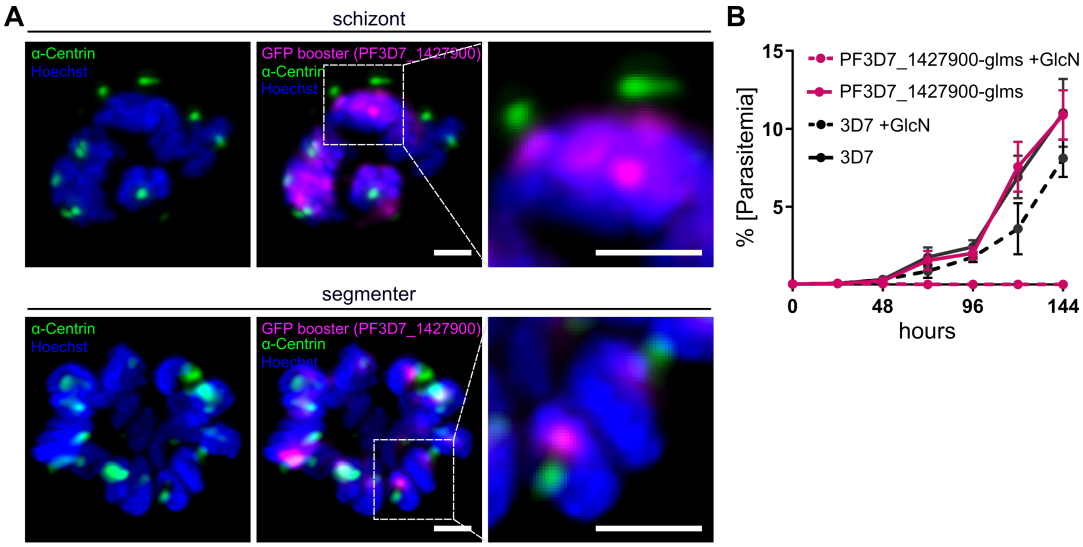

FIGURE 2.27: The leucine-rich repeat protein PF3D7_1427900 is essential for parasite growth and re-locates from dispersed nuclear localization towards centriolar plaques in segmenters. (A) Confocal images after automated adaptive deconvolution (LNG) of 3D7 multinucleated parasites endogenously expressing PF3D7_1427900-GFP_glmS. GFP signal was enhanced using GFP booster coupled to Atto 594 (magenta) and cells were labeled with anti-centrin (green) antibody and stained with Hoechst (blue). Right images show zoom-ins of representative localization of PF3D7_1427900 in nuclei of schizont and segmenter stages. Images are maximum intensity projections; scale bars, 1 µm. (B) Parasite growth assays of 3D7 PF3D7_1427900-GFP_glmS cells in absence or presence of 3.5 mM Glucosamine (GlcN) for inducible knockdown of PF3D7_1427900. 3D7 wt cells were used as controls. Parasitemia was determined over six days (3 cycles) via flow cytometry after SYBR Green I DNA-staining of infected red blood cells (n = 3 growth assays).

2.7.4 PF3D7_0710000 is an Sfi1-like protein in the extranuclear compartment of the centriolar plaque important for parasite growth

Another centriolar plaque candidate I identified in co-immunoprecipitations of NF54 PfCentrin1- and PfCentrin2-GFP parasites and subsequent mass spectrometry analysis is PF3D7_0710000 (candidate 08) (subsection 2.7.1), described on the PlasmoDB website as a conserved *Plasmodium* protein of unknown function. A well-known centrin-binding protein in diverse species such as *Saccharomyces cerevisiae*, *Homo sapiens* or *Toxoplasma gondii*, is Sfi1. In the context of Sfi1 conservation among different species, a recent study by Suvorova et al. (2015) described PF3D7_0710000 as a protein with no Sfi sequence similarity but presence of centrin-binding motifs. Comparing the centrin-binding motiv 6xxxxxxxx6xxx6xxWx (6 = hydrophobic amino acid; x = any amino acid) used by Suvorova et al. (2015) with PF3D7_0710000 protein sequence, I found 16 repeats of the motif (while in other proteins, a maximum of nine are present). In addition, I used the conserved Sfi1 repeat motif recently identified by comparison of *S. cerevisiae*, *S. pombe* and human Sfi1 (Kilmartin, 2003) to find centrin-binding sequences. As the complete motif AxxxxxxxLLxxxF/LxxWK/R is not present in any *P. falciparum* protein, I used only the more conserved end, F/LxxWK/R. This motif was present in 413 3D7 proteins, however, with seven in total, most repeats were found in PF3D7_0710000. Six of the seven motif repeats were present in the first half of the protein sequence. Due to presence of Sfi1 repeat domains but absence of general protein sequence conservation, I called PF3D7_0710000 Sfi1-like protein (Slp).

Another similarity between Sfi1 and Slp is their large size. Slp contains 3267 amino acids and has a molecular weight of 407 kDa. In the intraerythrocytic stages, Slp is mainly expressed between 40 and 48 hpi, but overall transcript abundancy is very low (Otto et al., 2010). In living 3D7 parasites endogenously expressing Slp-GFP_glmS, no GFP signal could be detected, which is reflecting low expression levels of the gene. Fixed 3D7 Slp-GFP_glmS parasites in which the GFP signal was enhanced using GFP booster-Atto 594, showed single foci closely associated with centrin signals throughout schizogony (Figure 2.28A). However, initially Tatiany Romão and I detected no colocalization of Slp and centrin. Slp, although clearly localizing to the extranuclear compartment of the centriolar plaque, was often directed closer towards the nucleus than centrin signals (Figure 2.28A, zoom-in).

To elucidate the role of Slp for parasite growth in blood-stages, Marta Machado and Tatiany Romão performed growth assays of 3D7 Slp-GFP_glmS cells cultivated in absence or in presence of 3.5 mM GlcN for conditional knockdown of Slp mRNA (Figure 2.28B). The growth assay for Slp was done analogous to the assay for PF3D7_1427900 (subsection 2.7.3): parasitemia was assessed by flow cytometry for three replicative cycles (144 h) using SYBR Green I-stained parasites (subsection 4.2.18). In comparison to 3D7 wt control cells, parasitemia was reduced to the same amount in Slp-GFP_glmS expressing cells (no GlcN) and 3D7 wt cells cultured

with GlcN (Figure 2.28B). The growth defect was even more pronounced in 3D7 Slp-GFP_glmS parasites treated with GlcN. However, although Slp is predicted to be essential for intraerythrocytic parasite growth based on a *piggyBac* transposon mutagenesis screening (Zhang et al., 2018), parasite growth was not completely prevented upon knockdown (Figure 2.28B).

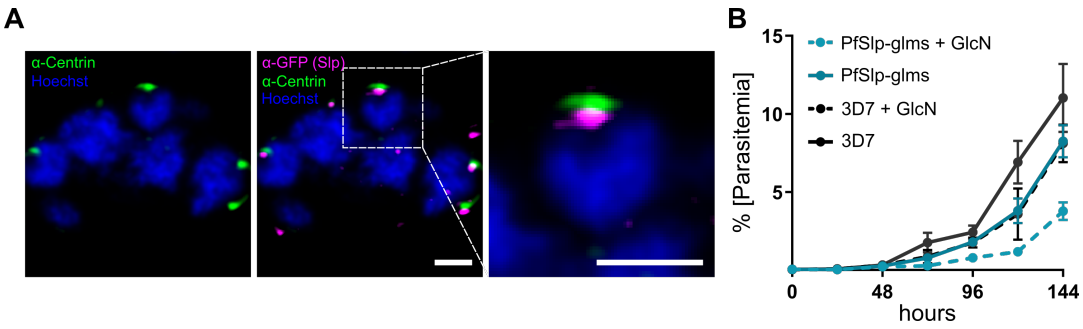

FIGURE 2.28: Sfi1-like protein (Slp) localizes to the outer compartment of the centriolar plaque and is important for parasite growth. (A) Confocal images after automated adaptive deconvolution (LNG) of a 3D7 schizont endogenously expressing Slp-GFP_glmS. GFP signal was enhanced using an anti-GFP antibody (magenta) and cells were additionally labeled with anti-centrin antibody (green) and stained with Hoechst (blue). Right image shows zoom-in of Slp signal closely associated with a centrin focus. Images are maximum intensity projections of some slices of the z-stack; scale bars, 1 µm. (B) Parasite growth assays of 3D7 Slp-GFP_glmS cells in absence or presence of 3.5 mM Glucosamine (GlcN) for inducible knockdown of Slp. 3D7 wt cells were used as controls. Parasitemia was determined over six days (3 cycles) via flow cytometry after SYBR Green I DNA-staining of infected red blood cells (n = 3 growth assays).

To sum up, PF3D7_0710000 is an Sfi1-like protein (Slp) closely associated with centrin in the extranuclear compartment of the centriolar plaque and is important for parasite growth during intraerythrocytic development. Future characterizations will shed light on the role of Slp during schizogony.

Chapter 3

Discussion

3.1 Establishment of advanced microscopy techniques for *Plasmodium* blood-stages

Microscopy is widely used to visualize organization and dynamics of mitotic structures in living and fixed cells. However, data about fundamental structures involved in *Plasmodium* cell divisions such as microtubules and centriolar plaques is mainly based on few, old transmission electron microscopy studies and detailed fluorescence microscopy analyses are rare. A prerequisite to study dynamic cell divisions during schizogony is the adaptation of advanced microscopy techniques for *P. falciparum* blood-stages. These adaptations are usually laborious and are complicated by specific challenges such as the small size of the parasite. In this study, I provide a novel immunofluorescence staining protocol which enables RescueSTED super-resolution microscopy of *Plasmodium* schizonts and I adapted an on-section CLEM approach (Kukulski et al., 2011, 2012) combined with tomography. In addition, I established recently developed imaging techniques such as U-ExM (Gambarotto et al., 2019) and time-lapse microscopy of blood-stage parasites (Grüring et al., 2011) in our lab and adapted them to investigate *Plasmodium* microtubules and centriolar plaques.

3.1.1 Time-lapse microscopy

Time-lapse microscopy of *Plasmodium* blood-stages over several hours was established by Grüring et al. (2011). They mainly focused on long-term imaging using DIC exclusively or together with the photoconvertible protein Dendra2 with a low temporal resolution of 20 min or 1 h. In contrast, other time-lapse microscopy studies on *Plasmodium* blood-stages applied short time intervals of 1-2 sec to investigate the fast process of red blood cell invasion by merozoites using DIC only (Gilson and Crabb, 2009; Yahata et al., 2021). An important achievement of this work and a simultaneous study by Klaus et al. (2021) is the combination of long-term fluorescent dual-color time-lapse microscopy of blood-stage development with high spatial and temporal resolution (z-stacks every 5 min). A *Plasmodium*-specific challenge for time-lapse microscopy is the dependency on host cell quality as blood from different donors is used for cultivating *Plasmodium* cells. Potential variations between host red blood

cells concerning age and overall quality/health add another layer of complexity and variation to sensitive experiments such as time-lapse microscopy. A major challenge for multi-color live-cell imaging is that the parasite is exceptionally light-sensitive. This might be due to the highly absorbing hemozoin crystals that induce acidification of the cytosol (Wissing et al., 2002). In addition, phototoxicity, mainly caused by generation of reactive oxygen species (ROS), is a general major issue during live-cell imaging (Icha et al., 2017). Although *Plasmodium* blood-stage parasites are cultivated/imaged at a low oxygen concentration of 5%, phototoxicity is still a problem. To further reduce phototoxicity, oxygen scavengers, also used for super-resolution microscopy, could be tested for *Plasmodium* imaging to reduce ROS generation from oxygen (Tosheva et al., 2020). However, it needs to be carefully assessed whether the reduction of oxygen has an impact on parasite viability. In addition, phototoxicity can be reduced by using far-red fluorogenic probes as longer wavelengths have less energy (Icha et al., 2017). Moreover, to minimize phototoxicity a compromise between light intensity and exposure time is required which still provides sufficient signal-to-noise ratios. To improve the ratio, image processing such as deconvolution used in this study will be helpful for interpretation of low signals detected.

Advanced microscopy techniques for time-lapse imaging

Time-lapse microscopy of *Plasmodium* might be revolutionized by lattice light sheet microscopy, which increases spatial and temporal resolution and, importantly, reduces phototoxicity (Chen et al., 2014). Lattice light-sheet microscopy was already used to study erythrocyte invasion by *Plasmodium* merozoites (Geoghegan et al., 2021; Ganter and Frischknecht, 2021), an extremely fast process of tens of seconds to minutes. The high temporal resolution of lattice light-sheet microscopy provides an auspicious opportunity to quantify dynamics of hemispindle microtubules and analyze their reorganization into a mitotic spindle during schizogony. In addition, reduced phototoxicity might allow live-cell imaging of more than two fluorescent probes at a time throughout schizogony.

Due to the small size of *Plasmodium* parasites, super-resolution microscopy techniques will be required to study dynamics of microtubules and centriolar plaques in more detail. Airyscan microscopy and 3D SIM, which can increase lateral and axial resolution around 1.6 and 2-fold, respectively (Sahl et al., 2017), have to date exclusively been used for fixed *Plasmodium* parasites (Riglar et al., 2011; Yeoman et al., 2011; Absalon et al., 2016; Rudlaff et al., 2019; Connelly et al., 2021). Adaptation of these super-resolution techniques for living *Plasmodium* parasites will provide new opportunities for studying dynamics during schizogony.

Fluorescent dyes for live-cell imaging

In this study, for the first time in *Plasmodium* research, I performed time-lapse microscopy of microtubules during schizogony (Figure 2.2). This was achieved using the cell-permeable fluorogenic dye SPY555-Tubulin (published as Map555-Tubulin, Wang et al. (2020)). SPY555-Tubulin belongs to an ever-growing family of dyes including e.g. SPY-DNA and SPY-actin which are constantly refined and enable bright

labeling of the respective structures with high specificity and low background signal (Wang et al., 2020). The dye SPY555-Tubulin is based on a fluorescent taxol derivative and was the only dye tested that labeled all microtubule stages observed also in fixed, immunostained parasites. In contrast, other taxol-derived tubulin dyes, such as SiR-tubulin were unable to stain hemispindle microtubules in living parasites (data not shown). The reason why microtubules in hemispindle stages were not labeled with other tubulin live dyes remains elusive and I cannot ensure that all hemispindle microtubule branches were visualized with SPY555-Tubulin. To stain chromatin, I tested the infrared Silicon rhodamine (SiR) dye 5-SiR-Hoechst (Bucevičius et al., 2019), which efficiently labeled parasite nuclei (Figure 2.1). However, divisions were not completed in presence of this dye even with minute concentrations of 22 nM. Instead, microtubules persisted in mitotic spindle stages and chromatin was not separated into distinct nuclei. This is consistent with recent observations that SiR-Hoechst induces cell cycle arrests in G2 in human cells (Sen et al., 2018) and Hoechst 33342 blocks transition of *P. falciparum* trophozoites into schizonts (Naughton and Bell, 2007). Therefore, extreme caution is required when using fluorescent Hoechst dyes for time-lapse microscopy of *Plasmodium* blood-stages. In general, fluorescent dyes should be tested for their influence on cell survival and changes in morphology of parasite blood-stages before application for time-lapse microscopy.

Protein labeling for live-cell imaging

To label the centriolar plaque in time-lapse microscopy, PfCentrin1 was episomally tagged with GFP (subsection 4.2.3). Although genetic tagging of genes remains time-intensive in *P. falciparum*, it is still the method of choice for proteins/cellular structures that cannot be labeled by fluorogenic dyes. However, fluorescent proteins show much lower brightness and photostability than organic dyes and are therefore not suitable for super-resolution live-cell imaging. Recently developed Halo-tag (Los et al., 2008) and SNAP-tag (Sun et al., 2011) are self-labeling protein tags which can irreversibly react with chloroalkanes and O6-benzylguanine derivatives, respectively (Xue et al., 2015), functionalized with an organic fluorophore for live-cell imaging (Urh and Rosenberg, 2012). Due to brightness and photostability, both Halo- and SNAP-tag can be applied to STED live-cell imaging (Erdmann et al., 2019). Tagging of *Plasmodium* centrins with Halo-tag already enabled STED live-cell imaging of the centriolar plaque for short periods of time (unpublished data, Yannik Voß). In the future, Halo- and SNAP-tag will provide new opportunities for long-term 3D SIM, Airyscan and lattice light-sheet microscopy of *Plasmodium* schizogony.

3.1.2 Super-resolution microscopy: RescueSTED and U-ExM

An immunofluorescence staining protocol for RescueSTED nanoscopy

As a requirement for STED nanoscopy of *Plasmodium* blood-stage parasites, I, together with Ann-Kathrin Mehnert, developed a reliable immunofluorescence staining protocol based on the widely-used protocol by Tonkin et al. (2004) and a cell seeding

protocol used e.g. by Spielmann et al. (2003). Major advancements of our protocol are the increased signal intensity and labeling density of parasite structures (Figure 2.6, Mehnert et al. (2019)). These are achieved by fixation exclusively with PFA, omitting even minor amounts of 0.0075% GA used by Tonkin et al. (2004). This enabled RescueSTED nanoscopy of blood-stage parasites (Figure 2.8). In addition, avoiding GA during fixation excludes well-known issues of GA such as deleterious effects on epitopes or high autofluorescence (Lee et al., 2013). This might be helpful as even fixation with low amounts of GA was for example not suitable to stain ring-exported protein 2 (REX2) (Spielmann et al., 2006).
In *Plasmodium* research, immunofluorescence stainings are frequently performed on air-dried blood smears after methanol fixation or after saponin-lysis of the RBCs. These methods, however, lead to poor preservation of parasitic structures. While our protocol induced slight changes in erythrocyte morphology, no alterations in parasite structures including their appearance in three dimensions could be observed (Mehnert et al., 2019). Therefore it is clearly superior to commonly applied protocols. In contrast to immunofluorescence stainings in suspension (Tonkin et al., 2004), antibody staining of seeded cells does not require centrifugation of cells which is not only convenient but also avoids loss of cells during washing steps. Furthermore, the seeding protocol enables generation of very consistent cell monolayers and is compatible with live-cell imaging (Grüring et al., 2011).
A limitation of this protocol is the red blood cell lysis induced by omitting GA during fixation (Tonkin et al., 2004), indicating that the cytosol is at least partially washed out. Therefore, our protocol might not be suitable to stain proteins located in the erythrocyte cytosol. Consistently, in a recent study by Diehl et al. (2021) using our staining protocol, phalloidin did not label cytosolic actin in the host red blood cell as it was previously detected in uninfected erythrocytes (Pan et al., 2018). However, the actin cytoskeleton underlying the host plasma membrane as well as the glycocalyx and KAHRP-proteins associated with knobs could be visualized (Diehl et al., 2021).
In summary, our user-friendly immunofluorescence staining protocol efficiently labels parasitic structures of seeded *Plasmodium* blood-stages with increased labeling densities and signal intensities. Thereby, it is not only superior for STED nanoscopy, but also for regular widefield/confocal microscopy techniques and will hopefully become a widely-used standard for immunofluorescence staining of *Plasmodium* structures in blood-stages.

STED nanoscopy

To enable STED microscopy of blood-stage parasites, I established RescueSTED (Staudt et al., 2011) for *Plasmodium* to overcome cell disruption by the high-intensity depletion laser. In this approach, the STED laser is only switched on when a signal threshold is reached in a confocal probing step. This enabled me to visualize microtubules during blood-stage development with unprecedented resolution (Figure 2.8). A major limitation of this technique is that confocal thresholds need to be adjusted carefully for every staining and sometimes for every imaged cell. Even if this is done

with care, destruction of cells can still occur, for example when a bright fluorescent signal is in close proximity to a hemozoin crystal.
In the future, another adaptive illumination development, called DyMIN STED, could be tested for *Plasmodium*. DyMIN adds another probing step by using minor STED laser powers which are successively increased when a signal is detected (Heine et al., 2017). Thereby, bleaching can be massively reduced which might be helpful for live-cell STED of *Plasmodium*. Simultaneously to my project, guided STED was developed to enable *Plasmodium* STED imaging on the basis of the DynMIN principle (Schloetel et al., 2019). In guided STED, the position of hemozoin crystals is determined and visualized by their high reflection of light. When the reflected light reaches a specific threshold, the adaptive illumination automatically deactivates the STED laser in this region of the cell to prevent destruction. While guided STED requires modification of commercial STED microscopes by addition of several filters (Schloetel et al., 2019), RescueSTED can be easily applied as the Rescue adaptive illumination is integrated into the STED microscope from Abberior instruments. This presents a major advantage of RescueSTED compared to guided STED. Another approach to enable STED imaging of *Plasmodium* blood-stages is the treatment of parasites with a hemozoin clearing agent which induces destruction of hemozoin crystals (personal communication, Jessica Kehrer). This is especially interesting when no STED microscope is available and for *Plasmodium* species with dispersed hemozoin crystals, which complicate guided and RescueSTED. However, concerns about interference with cellular structures and changes in morphology need to be addressed before the clearing agent can be applied regularily.

Ultrastructure expansion microscopy (U-ExM)
Ultrastructure expansion microscopy (U-ExM) is a technique to physically expand cells in a hydrogel to gain super-resolution images on a confocal microscope (Gambarotto et al., 2019). It was first adapted to various stages of the *Plasmodium* life cycle by Bertiaux et al. (2021), including *P. falciparum* schizonts, and, together with Johanna Bauer, I could easily establish the protocol in our lab (Figure 2.10, Figure 2.17). We discovered that quality and solubility of the purchased sodium acrylate, needed for gelation, is very critical for successful expansion and should be checked carefully in advance. In this study, we used PFA for fixation of parasites which was slightly superior to no fixation and methanol-fixation (data not shown). However, hemispindle microtubules sometimes showed "dotted" signals (Figure 2.17) especially when we tried to combine U-ExM with STED (data not shown), which might be due to epitope masking or partial disruption of microtubules. Recent experiments indicate that microtubule structures are better preserved by fixation with PFA in presence of GA (Laporte et al., 2022). Although GA was adverse for classical immunofluorescence stainings in *Plasmodium*, it might still be worth trying for U-ExM as cells are automatically permeabilized during the expansion process, facilitating antibody penetration. Further, cryo-fixation is a promising new development for U-ExM (Laporte et al., 2022), which shows even better preservation of microtubules

than after fixation with PFA and GA. Therefore, cryo-fixation U-ExM needs to be tested for *Plasmodium* blood-stages. Recently, pan-ExM was developed, which enables expansion of immunostained human cells up to 21-fold and allows immunolabeling (M'Saad and Bewersdorf, 2020). Although pan-ExM was successfully adapted to *Plasmodium* gametocytes, expansion was limited to 10-fold and antibody-labeling was not working (Rashpa and Brochet, 2022). However, NHS ester conjugate labeling revealed ultrastructural details almost comparable to TEM (Rashpa and Brochet, 2022). This makes it an attractive tool to further analyze the protein-dense region of the intra- and extranuclear compartment of the centriolar plaque detected in this project.

Comparison of RescueSTED and U-ExM for *Plasmodium* blood-stages

RescueSTED and U-ExM are two very distinct, attractive new techniques for super-resolution microscopy of *Plasmodium* blood-stages which are comparable concerning their lateral resolution. Sample preparation is very time-intense in U-ExM when compared to RescueSTED. For RescueSTED, a classical immunofluorescence staining, using STED-compatible secondary antibodies, is sufficient, while U-ExM requires an additional workday for gelation, denaturation and first expansion of the sample (subsection 4.2.8). In addition, antibody incubation times are much increased in U-ExM. Concerning the equipment U-ExM is clearly superior to STED as super-resolution images can be acquired on a conventional confocal microscope. This makes the technique available also for laboratories with no access to an expensive STED microscope. However, the stage of the microscope and the overall system should be very stable to avoid drift during imaging of expanded cells.

Importantly, isotropic U-ExM increases both lateral and axial resolution around 4.5-fold. In contrast, to increase axial resolution with STED, 3D STED imaging is required which inevitably comes at the expense of lateral resolution (Harke et al., 2008). Imaging several z-planes with RescueSTED is challenging in *Plasmodium*. Although z-stacks can in principle be acquired, with increased planes, the probability of cell destruction by the depletion laser rises, even with RescueSTED. In addition, with increased bleaching, fluorescent signals might be below the threshold for turning on the STED laser, which further complicates imaging of z-stacks with RescueSTED. At worst, important signals will not be detected, leading to misinterpretation of the data. Although imaging expanded cells in 3D takes a long time and requires a very stable sample, it is still easier than acquisition of 3D RescueSTED z-stacks.

With RescueSTED, super-resolution imaging is usually restricted to two to three colors, while the others are imaged in confocal mode. Although four-color STED was already demonstrated, it is extremely challenging and cannot be performed on every commercially available STED microscope (Ronnlund et al., 2014). Here, U-ExM is advantageous as all structures are expanded around 4.5-fold in every direction and therefore imaged with super-resolution.

In general, U-ExM casts several doubts, for example on whether all cellular structures indeed expanded isotropically and how the expansion factor can be tested and

controlled (Faulkner et al., 2020). This is especially important for measurements and quantifications done on expanded cells. Further, as proteins are denatured during U-ExM, a valid concern is the preservation of cellular structures. To sum up, when all doubts are kept in mind, I think U-ExM is superior for super-resolution microscopy of *Plasmodium* schizonts due to increased resolution in all dimensions and more convenient 3D, multi-color imaging on a conventional confocal microscope. To further increase the resolution, U-ExM can also be combined with STED microscopy (Gambarotto et al., 2019).

3.1.3 Correlative light and electron microscopy (CLEM) combined with tomography

In this study, I adapted an on-section CLEM approach (Kukulski et al., 2011, 2012) for *Plasmodium* schizont stages expressing PfCentrin1-GFP, labeled with the live dye 5-SiR-Hoechst and (subsection 2.6.2, Figure 2.20) and combined with tomography. To my knowledge, this is the first time, together with a study by Klaus et al. (2021), on-section CLEM was applied to *Plasmodium* blood-stages. In total, three different electron microscopy protocols were established, demonstrating the adaptations needed for specific applications. Best contrast was achieved with treatment of samples with osmium tetroxide and embedding in Spurr's resin (Figure 2.18). However, this protocol is not applicable to CLEM as osmium tetroxide and Epon/Spurr's resin eliminate fluorescence of conventional fluorescent proteins such as GFP. Only recently, Fu et al. (2020) developed a variant of the fluorescent protein mEos, called mEosEM, which can withstand osmium treatment as well as Epon embedding. To test this new tool for CLEM in *Plasmodium* research, Johanna Bauer tagged PfCentrin1 with mEosEM. In live-cell imaging, the signal showed fast bleaching. However, it remains to be tested whether the strain is suitable for CLEM after osmium treatment and embedding in Epon or Spurr's resin.
A serious technical challenge for TEM and CLEM of *Plasmodium*-infected RBCs is the poor embedding and therefore structural preservation of cells. This is due to poor polymerization of resins when UV light was used, while chemical polymerization lead to good embedding (Figure 2.19). I hypothesize that hemozoin crystals of the parasites, which highly absorb light in the visible and UV range (Cai et al., 2016; Menyaev et al., 2016; Balasubramanian et al., 1984), hinder penetration of UV light into dense sample pellets and thereby restrict polymerization to a thin sample layer at the surface. As it was virtually impossible to identify fluorescent cells with a good ultrastructural preservation in UV-polymerized samples, I made use of chemical polymerization. This allowed correlation of PfCentrin1-GFP signals with tomogram slices of reasonably good quality (Figure 2.20). However, to achieve optimal ultrastructures in tilted series for tomography, we used again UV-polymerized sample pellets (Figure 2.21). In general, sample embedding might be improved by mixing *Plasmodium*-infected RBCs with budding yeast before high-pressure freezing as done previously (Hale et al., 2017). Yeast is known to provide good sample pellets and

indeed improved iRBC sample embedding when I tested the protocol. However, as it is challenging to control the ratio of iRBCs to yeast, in the end only very few RBCs were present in the sample. Further tests are needed to see whether this technique is viable.
All in all, CLEM approaches always require compromises between the optimal conditions for fluorescence and for electron microscopy, especially when additionally combined with tomography.

3.2 Microtubule organization and dynamics during schizogony

In this study, I unraveled dynamics and ultrastructural organization of the distinct microtubule stages during *Plasmodium* schizogony. My current model of centrin and microtubule reorganization during the first division based on time-lapse and super-resolution microscopy is depicted in Figure 3.1 and discussed in the following section in more detail. Further, I will compare my observations with former models and discuss the detailed organization of the individual microtubule stages analyzed by super-resolution microscopy, CLEM, and tomography. Finally, I will discuss potential roles of hemispindle microtubules.

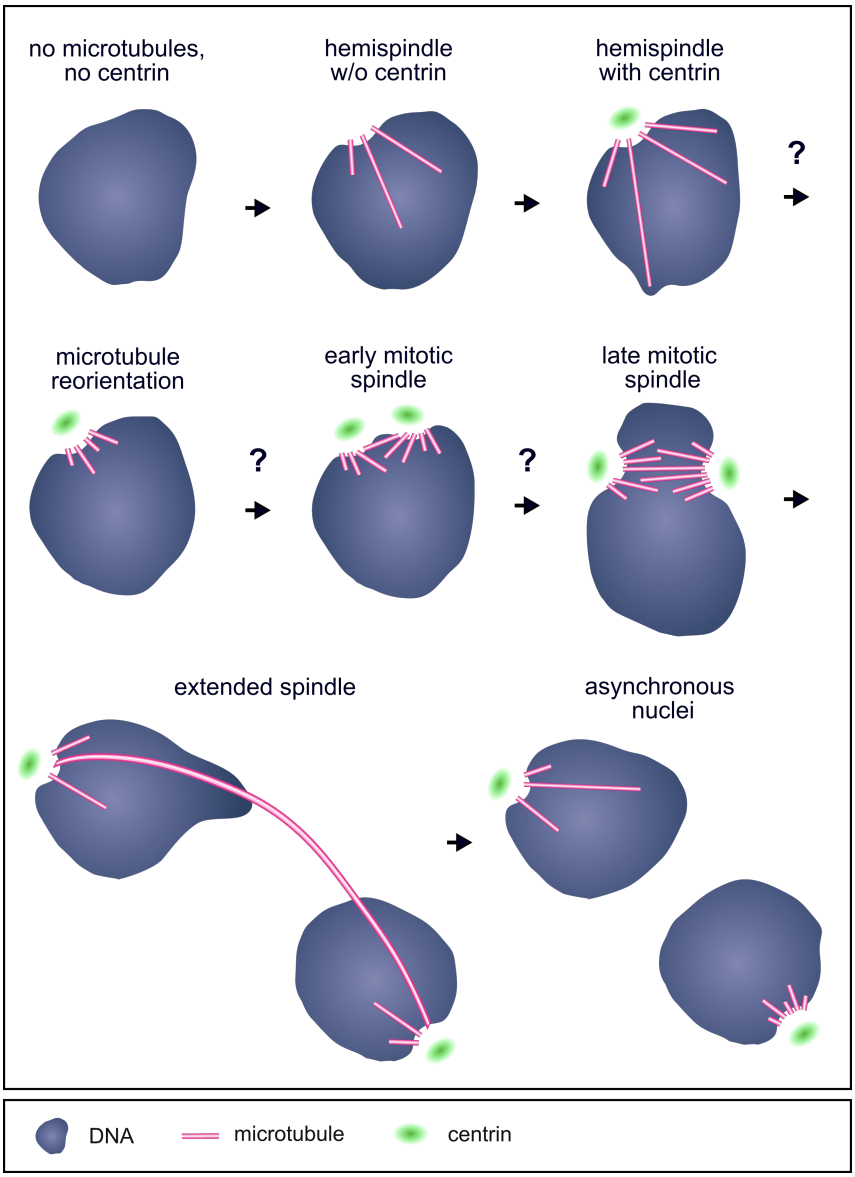

FIGURE 3.1: Working model of centrin and microtubule reorganization before and during the first nuclear division of *P. falciparum* blood-stage schizogony. It is unknown how hemispindle microtubules are rearranged into an early mitotic spindle and how microtubules are positioned in this early stage before the late (mature) mitotic spindle is established (indicated with question marks). Further, it remains to be tested whether in extended spindles microtubules connecting the two nuclei are indeed not accompanied by DNA as observed in RescueSTED microscopy.

3.2.1 Detailed explanation of microtubule organization and dynamics by taking the example of the first division

Before onset of schizogony in mononucleated *Plasmodium* blood-stages, no microtubule structures could be detected, neither in living cells (data not shown) nor fixed cells (Figure 2.8, Figure 2.9). This is consistent with previous studies, which reported only a diffuse cytosolic signal of anti-tubulin antibody-labeled parasites before start of schizogony (Read et al., 1993; Sinou et al., 1998) which might be due to soluble tubulin. Contrary to division in other species, at no point prior to segmentation I could detect cytoplasmic microtubules during *Plasmodium* blood-stage development.

Hemispindle microtubules

The first microtubule structures detected with time-lapse microscopy are radially extending hemispindle microtubules (Figure 2.2, Figure 2.9) which were already described previously (Terzakis et al., 1967; Aikawa et al., 1967; Aikawa and Beaudoin, 1968; Schrével et al., 1977; Read et al., 1993; Sinou et al., 1998; Fennell et al., 2006; Gerald et al., 2011). However, my study clarified that hemispindle microtubules are highly dynamic, which might facilitate later reorganization as discussed below. Hemispindle microtubules are present in mononucleated cells before the first division. Therefore, they are not exclusively present during late anaphase, as speculated previously (Canning and Sinden, 1973). All microtubule branches of the hemispindle are intranuclear, which is in line with previous observations (Aikawa et al., 1967; Aikawa and Beaudoin, 1968; Canning and Sinden, 1973; Bannister et al., 2000b; Mahajan et al., 2008), and originate from the site of a single centriolar plaque. However, microtubule minus-ends of hemispindles had individual nucleation sites at the centriolar plaque as observed by the capped-end structures in tomography (Figure 2.21) which were on average 58 nm distant to the nuclear membrane (Figure 2.23). This organization is reminiscent of budding yeast microtubules organized by the spindle pole body, which exhibit individual capped-ends in close proximity to the central plaque (Knop et al., 1999). Interestingly, in yeast these capped-ends are directly attached to the central plaque by electron-dense filaments, a structure not detected in *Plasmodium* hemispindles.

In this study, 5.7 microtubule branches were detected per hemispindle (Figure 2.10), while 4 were identified previously (Bertiaux et al., 2021). The observed difference might be explained by the use of 2D projections by Bertiaux et al. (2021), whereas in this study microtubules were counted in 3D. Hemispindle microtubule lengths were comparable to recent measurements (Bertiaux et al., 2021) and varied from 120 nm to 3 µm (Figure 2.10). To sum up, hemispindle microtubule number and length probably do not need to be tightly controlled to fulfill their specific function, in contrast to microtubules in sporozoite stages (Spreng et al., 2019). Interestingly, hemispindle microtubules are polymerized before centrin is present at the centriolar plaque (Figure 2.2, Figure 2.9). This might either be explained by spontaneous polymerization or by a later recruitment of centrin to the centriolar plaque while γ-tubulin might already be present as a template for microtubule nucleation. Unfortunately, attempts to tag *Plasmodium* γ-tubulin were unsuccessful and all tested antibodies were not giving a specific staining which might allow conclusions concerning the presence of γ-tubulin in early hemispindles. Later hemispindle microtubules showed a single centrin signal attached (Figure 2.2, Figure 2.9).

Time-lapse microscopy revealed highly dynamic growth and shrinkage of hemispindle microtubules (Figure 2.2). However, a recent study showed that polymerization velocity of *Plasmodium* microtubules *in vitro* is comparable to bovine microtubules and frequencies of microtubule catastrophe and rescue were even lower in *Plasmodium* than in bovine microtubules (Hirst et al., 2022). This data indicates that microtubule

polymerization in *Plasmodium* is not exceptionally fast. However, depolymerization velocity was significantly higher in *Plasmodium*, which might be important for transitioning from hemispindle microtubules to the on average much shorter mitotic spindle microtubules (Figure 2.10). Super-resolution time-lapse microscopy of microtubules with short time intervals of several seconds will be needed to quantify polymerization and depolymerization of hemispindle microtubules *in vivo*.

Reorganization of hemispindles into mitotic spindles

Next, hemispindle microtubules collapse and are reorganized into a mitotic spindle which is accompanied with the duplication of the centrin signal and therefore the centriolar plaque (Figure 2.2, Figure 2.9). I never detected a nucleus with more than one hemispindle. Based on this data, I can clearly discard the model of hemispindle duplication and fusion to form a mitotic spindle, which was proposed by Schrével et al. (1977) for oocyst division and also discussed for blood-stage schizogony (Read et al., 1993). Instead, I observed a fast transition from hemispindle to mitotic spindle organization which was difficult to define with the temporal resolution of 5 min and spatial resolution of the confocal microscope. To better resolve the reorganization of hemispindle microtubules into a mitotic spindle, images should be acquired every 30 s or faster using microscopy techniques with high resolution such as Airyscan or lattice light-sheet microscopy. Nevertheless it will be challenging to catch the microtubule reorganization which might take several minutes while the hemispindle is present for 140 min or longer (Figure 2.3) before the first mitotic spindle is formed. Hence, phototoxicity needs to be reduced as much as possible to increase parasite survival. Another limitation of this study is that the time of centrin (and centriolar plaque) duplication cannot be determined precisely, which complicates definition of rearrangement into the mitotic spindle. Dynamics and duplication of the centriolar plaque are discussed in more detail in subsection 3.3.4.

Mitotic spindle microtubules

Plasmodium mitotic spindle microtubules are detected as bright signal accumulations using confocal microscopy (Figure 2.2). Due to the small size of mitotic spindles and the compact arrangement of microtubules (Figure 2.21), no individual microtubules could be resolved, not even with super-resolution microscopy techniques (Figure 2.8, Figure 2.9, Figure 2.10, Figure 2.17). These accumulated signals have before been described as "tubulin-rich plaques" and were often equated with the centriolar plaque (Read et al., 1993; Arnot et al., 2011). However, using STED and U-ExM, I detected that accumulated fluorescent tubulin signals are always accompanied by two centrin signals, which are spatially separated from the microtubules (Figure 2.9, Figure 2.10). This data demonstrates that "tubulin-rich plaques" are not equal to centriolar plaques, but are bipolar mitotic spindle arrangements. Furthermore, the size of the "tubulin-rich plaques" or accumulations are in line with the average size of the *P. falciparum* mitotic spindle measured with U-ExM (Figure 2.10) and TEM (Prensier and Slomianny, 1986; Bannister et al., 2000b; Gerald et al., 2011). I detected late or mature mitotic spindles with opposing centrin signals as well as mitotic spindles with two centrin

signals in close proximity (Figure 2.9). The latter might be early mitotic spindles concluding the reorganization of the hemispindle into a mitotic spindle.

While tagging of *P. falciparum* γ-tubulin to identify microtubule orientation was in general not successful, tomography revealed microtubule minus-ends by their capped-end structure (Figure 2.22). To confirm microtubule orientation, the microtubule plus-end binding protein end binding 1 (EB1) (Morrison et al., 1998) could be tagged or labeled by immunofluorescence stainings. Tomography showed that minus-ends of mitotic spindle microtubules are positioned significantly further away from the nuclear membrane when compared to minus-ends of hemispindle microtubules (Figure 2.23). In contrast, in yeast mitotic spindles microtubule capped-ends are positioned in a specific layer of the spindle pole body and are directly tethered to the SPB inner plaque (Bullitt et al., 1997; O'Toole et al., 1999). Although most of the minus-ends of *Plasmodium* were aligned in a row (Figure 2.21), I could neither identify a structural connection to the intranuclear compartment of the centriolar plaque nor to the nuclear membrane. The increased distance of mitotic spindle microtubule minus-ends to the nuclear membrane compared to hemispindle microtubules might be due to forces generated during chromosome separation. In line with a possible loose connection of the microtubule minus-ends with the intranuclear compartment, the size of the intranuclear compartment is not altered in mitotic spindle stages (Figure 2.15, Figure 2.17). The nucleation of microtubules from an amorphous compartment in *Plasmodium* is reminiscent of the organization of meiotic microtubules in *Schizosaccharomyces pombe* (Funaya et al., 2012). Here, microtubules are nucleated with some distance to the nuclear membrane from an amorphous region which is associated with the cytoplasmic site of the SPB.

With an average length of 535 nm (Figure 2.10), *Plasmodium* mitotic spindles are exceptionally small when compared to mitotic spindles in other species (Goshima and Scholey, 2010). A conserved feature of mitotic spindle length is to scale with cell size (Krüger and Tran, 2020). Due to the small size of the parasite, which is restricted to the size of human erythrocytes (6-8 µm in length), an overall small size of the *Plasmodium* mitotic spindle is expected. In addition, the mitotic spindle size is limited to nuclear size during divisions. However, compared to similar-sized cells undergoing closed divisions such as budding and fission yeast, which establish 2 µm and 2.5 µm long metaphase spindles, respectively, (Goshima and Scholey, 2010) *Plasmodium* mitotic spindles are still particularly small. Interestingly, an upper limit of mitotic spindle length was observed in large cells (Wühr et al., 2008), raising the question whether there is also a minimal length and how this would be regulated. Many different studies have investigated the mechanisms behind mitotic spindle length scaling to cell size. For instance, several limiting components such as different kinesins, dynein or tubulin itself have been discussed (Goshima and Scholey, 2010; Krüger and Tran, 2020), but whether they might restrict *Plasmodium* mitotic spindle length remains to be investigated. In addition, it was shown that microtubule growth rates scale with cell size and therefore direct spindle length, meaning small cells have

slower polymerization rates (Lacroix et al., 2018). *In vitro*, polymerization speed of *Plasmodium* microtubules is comparable to bovine microtubules (Hirst et al., 2022). It will be interesting to compare *in vivo* microtubule growth rate and spindle length of *Plasmodium* with other cell types of comparable cell/nucleus size to investigate whether there might be a correlation.
Furthermore, it was proposed that spindle size of small cells not only depends on dynamics and length of the individual microtubules, but also on microtubule nucleation and therefore the number of microtubules in the mitotic spindle (Rieckhoff et al., 2020; Mitchison, 2020). Using tomography, we could visualize individual microtubules in *Plasmodium* mitotic spindles. As the tomogram was reconstructed from tilted series of a single 200 nm section which is not including the complete spindle, we could not determine the total amount of microtubules. To count microtubule numbers, tomograms of entire mitotic spindles have to be reconstructed. Although the exact number of microtubules per *Plasmodium* mitotic spindle remains unknown, numbers are likely more comparable to yeast mitotic spindles than to those of higher animals and plants which harbor maybe several thousands of microtubules (King and Hyams, 1982). Detailed analyses by Winey et al. (1995) showed that *S. cerevisiae* mitotic spindles are more minimalistic with around 32 microtubules connecting to the kinetochores of the 16 chromosomes and a few interpolar microtubules.

Early TEM studies on *Plasmodium* mitotic spindles suggested three different types of microtubules including kinetochore microtubules, continuous microtubules and radiating microtubules (Canning and Sinden, 1973; Schrével et al., 1977). Our tomogram of the mitotic spindle suggests the presence of continuous microtubules which are building a bridge between the two centriolar plaques (Figure 2.21). They might be involved in extension of the mitotic spindle, comparable to interpolar microtubules in other species (Gadde and Heald, 2004). However, interpolar microtubules are nucleated from the two different poles and overlap at the center of the spindle, while *Plasmodium* continuous microtubules seem to be polymerized from one pole. This would have consequences for the mechanism of spindle elongation and further studies will be needed to clearly confirm continuous microtubules in *Plasmodium* mitotic spindles before investigating their function. As I could not identify kinetochores with tomography (Figure 2.21), I could not distinguish between microtubules connected to kinetochores and radiating microtubules with free plus-ends. To visualize kinetochores, better contrast is needed which might be achieved in tomograms of osmium tetroxide-treated and Epon-embedded *Plasmodium* samples. In a highly sophisticated approach, kinetochores, e.g. marked by the kinetochore protein NDC80, and microtubules could be visualized using advanced super-resolution techniques such as the combination of U-ExM with STED, or Minflux, which increases resolution up to 1 nm in all dimensions (Sahl et al., 2017). These techniques will help to i) test whether radiating microtubules are present and if so to ii) count the number of radiating microtubules and kinetochore microtubules. In addition, mitotic spindles in eukaryotes typically contain astral microtubules (Gadde and Heald, 2004). However,

I could never detect astral microtubules in *Plasmodium* (neither in mitotic spindles nor in hemispindles), which is consistent with previous observations (Canning and Sinden, 1973).

Extended/anaphase spindle formation and rupture

The next step during *Plasmodium* divisions is the fast elongation of the mitotic spindle and formation of the extended spindle (Figure 2.2, Figure 2.9) which corresponds to the anaphase spindle in classical mitosis. At the maximum length of the extended spindle, I detected circa one to three microtubules or microtubule bundles connecting the two nuclei, which, based on Hoechst-staining, appear completely separated at this stage (Figure 2.9). These "connecting" microtubules might have emerged from the continuous microtubules detected in the mitotic spindle by elongation via a thus far unknown mechanism. *Plasmodium* spindle elongation might be mediated by kinesins, microtubule motor proteins that are well-known to transport large cargo to microtubule plus-ends, which in other species are also involved in several aspects of mitotic spindle function (Wordeman, 2010). Kinesin-5 has been shown to connect two adjacent microtubules of antiparallel orientation and mediate microtubule sliding, which elongates the mitotic spindle (Mann and Wadsworth, 2019). *Plasmodium* kinesin-5 localizes to the centriolar plaque, to mitotic spindles and partially to kinetochores during schizogony (Zeeshan et al., 2020). Further investigations of kinesin-5 localization in extended spindles might give a hint whether kinesin-5 is involved in *Plasmodium* spindle elongation. Another kinesin expressed in *Plasmodium* is kinesin-13, which has been shown to localize to kinetochores during schizogony. All other kinesins identified in *Plasmodium* were not present in blood-stages (Zeeshan et al., 2021b).

After having reached the maximum length, the extended spindle often lingers and length is slightly reduced without rupturing. This might be associated with relaxation after the maximum force for spindle elongation was reached. However, at which time the connecting microtubules of the extended spindle break and how this is mediated remains completely elusive. Interestingly, I observed several microtubules or microtubule bundles in extended spindles. Further studies will be needed to investigate whether nuclear fission occurs at a single position comparable to the thin internuclear bridge in fission yeast (Salas-Pino and Daga, 2019) or whether there is a wide bridge or even several fission sites, indicating an unusual way of nuclear fission. After rupture, extended spindle leftovers are detected which might also be interpreted as new hemispindle microtubules. Thus, hemispindle microtubules are present not only before formation of the first mitotic spindle, but also after extended spindle rupture before organization of new mitotic spindles.

Asynchrony of microtubule structures

Regularly, asynchrony of divisions can already be detected immediately after the first division is completed: While one nucleus is still associated with extended spindle remnants (hemispindle microtubules), a mitotic spindle is already present in the other one (Figure 2.1). This data is supported by a recent study, showing asynchronous DNA replication already from the two-nuclei stage onwards (Klaus et al., 2021). I detected that all microtubule stages were significantly longer in the first division than in the second and third (Figure 2.3). This is in line with markedly longer durations of the first DNA replication and the time between end of first S-phase to nuclear division (Klaus et al., 2021) in comparison to durations in the next divisions. This data indicates that the first nuclear division is an exception concerning duration. Interestingly, computer simulations suggest a gradual increase of nuclear cycle duration from the second division onwards which might be due to a limited resource required simultaneously by the individual nuclei during divisions (Klaus et al., 2021).

3.2.2 Function of the hemispindle

The function of hemispindle microtubules during schizogony remains elusive. Although co-stainings identified microtubules in close proximity to centromere-specific histone CenH3, no co-localization was detected (Figure 2.12). Therefore, I can exclude that hemispindles are directly involved in a mechanism in which microtubules "search" for chromosomes and are captured by kinetochores to direct chromosome orientation for segregation (Heald and Khodjakov, 2015). Instead, consistent with former studies on *Plasmodium* centromere and kinetochore localization (Hoeijmakers et al., 2012; Zeeshan et al., 2021a), centromeres clustered at the nuclear periphery and are likely positioned at the outer rim of the intranuclear compartment of the centriolar plaque (Figure 2.12). Thus, *Plasmodium* kinetochore clustering at the nuclear periphery is likely microtubule-independent as recently shown for budding yeast (Richmond et al., 2013).

Immunofluorescence stainings show that hemispindle microtubules are not present in PCNA1-positive (replicating) nuclei (Figure 2.13). This is in line with recent time-lapse microscopy experiments showing PCNA1-GFP accumulation and hemispindle collapse happen simultaneously in a nucleus (unpublished data, Marta Machado). This data indicates that upon S phase onset hemispindle microtubules immediately start to rearrange into a mitotic spindle.

A pure structural role of the hemispindle is unlikely as microtubule branches are very short-lived and usually branching into various different directions without a discernible order. However, they might still be involved in pulling or pushing cellular structures or organelles to organize the cell interior (Tolić-Nørrelykke, 2008) and prepare for divisons. Microtubule tips were sometimes causing nuclear membrane protrusions which were accompanied with or without Hoechst signals (Figure 2.11, Figure 2.21). As these protrusions were also present in mononucleated cells they

cannot solely be leftovers from ruptured extended spindles. Further, no other ultrastructural features were associated with these membrane protrusions and no specific order was observed, indicating that hemispindles might be randomly pushing the nuclear envelope.
I hypothesize that hemispindle microtubules might be akin to a "microtubule default stage" in *Plasmodium* which are polymerized spontaneously when a critical concentration of tubulin is reached in a nucleus (Walker et al., 1988). Similar to fission yeast that can undergo nuclear divisions without spindle microtubules (Castagnetti et al., 2010), hemispindles might not fulfill a critical function for *Plasmodium* divisions. However, they likely need to be depolymerized at onset of S phase for formation of mitotic spindles and controlled progression of schizogony.

3.3 The bipartite centriolar plaque

Centrosomes are highly diverse organelles playing a critical role in orchestrating eukaryotic cell divisions. Since early transmission electron microscopy studies, the *Plasmodium* centrosome, called centriolar plaque, is understood as an amorphous, electron-dense area embedded into the nuclear envelope. In this PhD study, I provide an entirely new view on the organization of the centriolar plaque and how it is associated with the nuclear membrane. In the following I will summarize my findings in a new working model of the centriolar plaque, compare its organization with centrosomes of other species and the yeast spindles pole body and discuss formation of the second centriolar plaque during division.

3.3.1 The centriolar plaque is organized into an extranuclear and an intranuclear compartment

In this study, I revealed a bipartite organization of the *Plasmodium* centriolar plaque into a protein-dense intra- and extranuclear compartment connected via a highly protein-dense neck likely spanning the nuclear envelope. I could never detect nuclear envelope invaginations associated with the centriolar plaque as previously observed in oocyst divisions (Canning and Sinden, 1973; Schrével et al., 1977). However, comparable to oocyst stages, the centriolar plaque is accompanied by nuclear pores (Figure 2.14). In contrast to the previous suggestion that centrin is located in the nuclear membrane (Mahajan et al., 2008), I consistently detected centrin outside of the nucleus (Figure 2.14, Figure 2.20). Underlying the centrin signal, an intranuclear extended compartment is associated with the centriolar plaque, which is free of DNA and RNA and functions as the site of microtubule nucleation (Figure 2.18, Figure 2.20, Figure 2.21). Based on these observations, I propose a novel working model of the centriolar plaque during blood-stage schizogony (Figure 3.2).

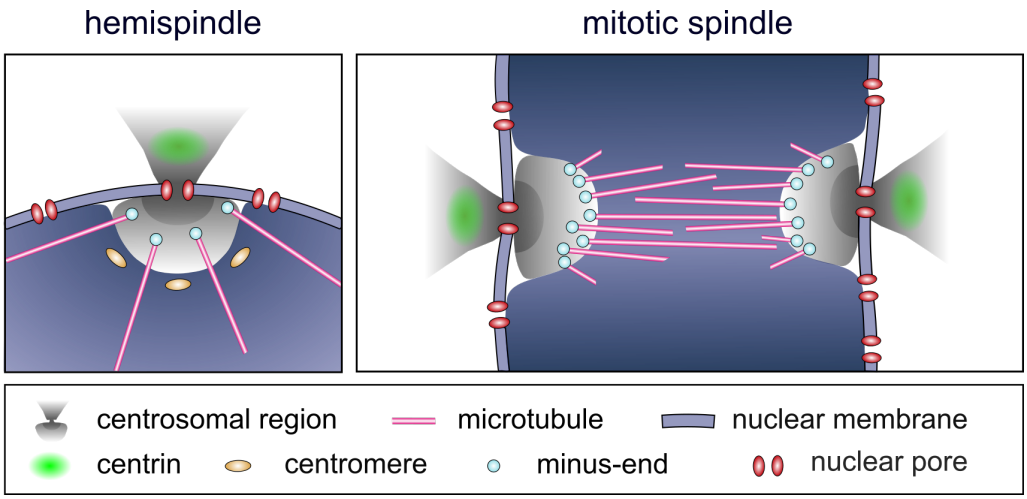

FIGURE 3.2: Working model of the *P. falciparum* centriolar plaque during blood-stage schizogony. Schematic of the centriolar plaque organization in hemispindle (left) and in mitotic spindle stage (right). The centriolar plaque has a bipartite organization with a cytosolic part and an extended intranuclear compartment. The mature mitotic spindle is organized by two opposing centriolar plaques. Whether the intra- and extranuclear compartment of the centriolar plaque are connected by a classical nuclear pore still needs to be investigated.

The bipartite organization of the *P. falciparum* centriolar plaque was recently confirmed by Liffner and Absalon (2021) via U-ExM of centrin, microtubules, NHS ester staining and BODIPY TRc to visualize membranes. Furthermore, a similar bipartite organization of the centriolar plaque was observed during *Plasmodium* male gametogenesis (Rashpa and Brochet, 2022). Comparable to blood-stages, microgametocyte centriolar plaques span the nuclear membrane and are composed of an extended intranuclear and an extranuclear compartment containing centrin. However, in activated male gametocytes the extranuclear compartment is associated with basal bodies which organize axonemal microtubules. While centrin is always present in the cytosol, γ-tubulin is mostly relocated from the cytosol into the intranuclear compartment upon gametocyte activation (Rashpa and Brochet, 2022) to nucleate intranuclear spindle microtubules. Unfortunately, several attempts during this PhD study to clearly visualize the position of γ-tubulin in *P. falciparum* blood-stages were unsuccessful. However, as nucleation of microtubules during schizogony is restricted to inside the nuclei, it is unlikely that a similiar relocation of γ-tubulin takes place at schizogony onset. Only after completion of schizogony, γ-tubulin is required in the cytosol for nucleation of subpellicular microtubules (Fowler et al., 2001). It will be interesting to investigate whether γ-tubulin relocation between cytosol and nucleus is mediated via the connection of the intra- and extranuclear compartment of the centriolar plaque.

The physical connection of the intranuclear compartment organizing mitotic spindles with the extranuclear basal bodies nucleating axonemal microtubules in microgametocytes indicates a timely and functional coordination of both processes (Rashpa and Brochet, 2022). In compliance with this model, the two compartments of blood-stage centriolar plaques might provide two regulatory hubs to coordinate chromosome

segregation of the respective nucleus with the mitotic state of other nuclei which all share one cytoplasm during asynchronous divisions. Akin to *Plasmodium* centriolar plaques, the *Toxoplasma* centrosome shows a bipartite organization with an inner and an outer core (Suvorova et al., 2015) which I will discuss in more detail in the next subsection. While the inner core of the *Toxoplasma* centrosome was suggested to regulate nuclear events, the outer core was proposed to regulate daughter cell formation (Suvorova et al., 2015; Tomasina et al., 2022). Likewise, the *Plasmodium* centriolar plaque outer compartment might play a role in switching from continuous rounds of nuclear divisions during schizogony to initiation of merozoite budding. The extranuclear compartment could also play an important structural role as it might tether the centriolar plaque to the plasma membrane or, in late stages, to rhoptries. This hypothesis is supported by several observations. First, in multinucleated parasites, centriolar plaques of the individual nuclei were typically directed towards the plasma membrane and only rarely oriented towards the center of the parasite (Figure 2.15, Figure 2.16). Second, I detected an extended funnel-like shape of the NHS ester-labeled extranuclear compartment directed away from the nucleus towards the plasma membrane (Figure 2.17). Third, co-IPs of PfCentrin-GFP in blood-stages identified several proteins that localize to the parasite plasma membrane (Figure A.1). Lastly, centriolar plaques might be connected to rhoptry development as electron tomography showed electron-dense, round structures in close proximity to centriolar plaques (personal communication, Juyeop Kim), which might be early rhoptries. This hypothesis is in line with a recent study showing close association of rhoptries with nuclei (Rudlaff et al., 2020). To investigate whether the extranuclear compartment develops over time, it will be interesting to quantify its shape and dimensions in different microtubule stages and throughout schizogony. The results can then be compared to the intranuclear compartment, which showed no difference in size between hemispindle and mitotic spindle stages (Figure 2.15, Figure 2.17).

3.3.2 Comparison of centriolar plaque architecture to centrosomes and the spindle pole body

Comparison to the *Toxoplasma gondii* centrosome

In contrast to *Plasmodium* centriolar plaques in blood-stages, the *Toxoplasma* centrosome contains centrioles (Francia and Striepen, 2014). Beyond that obvious difference, several similarities can be observed between the two MTOCs of these apicomplexan parasites during divisions. Both MTOCs are bipartite with two distinct compartments/cores. While the two compartments of the *P. falciparum* centriolar plaque are separated by the nuclear membrane, both cores of the *T. gondii* centrosome are presumably outside of the nucleus (Suvorova et al., 2015). However, since CLEM has never been applied to analyze the *Toxoplasma* centrosome, the position of the nuclear envelope in relation to the described cores and their components is not finally clarified. In the *Toxoplasma* centrosome, a distinct composition has been observed with Centrin1, Sfi1, SAS-6, CEP250 and γ-tubulin in the outer, and CEP250 and CEP250L

in the inner core (Suvorova et al., 2015). In both species, centrin is a marker for the outer compartment, however, as it co-localizes with the cartwheel-protein SAS6 in *T. gondii*, it is likely part of centrioles. Apart from centrins, the localization of the other centrosomal proteins studied in *Toxoplasma* have not yet been analyzed in *Plasmodium* blood-stages. The *Toxoplasma* inner core protein CEP250L might reside within the centrocone (Tomasina et al., 2022), a sub-compartment of the nucleus defined by the surrounding nuclear membrane, not present in *Plasmodium* (Striepen et al., 2007). In the centrocone, which likely also contains γ-tubulin in metaphase (Tomasina et al., 2022), microtubules are polymerized. These need to traverse the nuclear membrane to connect to the chromosomes (Striepen et al., 2007). As the site of microtubule nucleation, the centrocone resembles the inner compartment of the *Plasmodium* centriolar plaque, even though *Plasmodium* microtubules do not need to cross the nuclear membrane. A common marker for the centrocone is MORN1 (membrane occupation and recognition nexus 1) (Gubbels et al., 2006). To date, MORN1 localization in *Plasmodium* blood-stages has solely been investigated during segmentation and in merozoites (Ferguson et al., 2008; Rudlaff et al., 2019) and it will be worthwhile to test whether MORN1 localizes to the inner centriolar plaque compartment. To compare the two cores of *T. gondii* and *P. falciparum* MTOCs in detail, more centriolar plaque proteins need to be detected and their dynamics analyzed.

Comparison to yeast spindle pole bodies (SPBs)

Plasmodium and budding yeast undergo closed divisions without breakdown of the nuclear envelope. Yeast and *Plasmodium* evolved a microtubule-organizing structure that is associated with the nuclear membrane to coordinate intranuclear microtubules. In addition, budding yeast SPBs nucleate astral microtubules (Cavanaugh and Jaspersen, 2017), while I never detected any cytoplasmic microtubules in *Plasmodium* schizogony. The main parts of the *Plasmodium* centriolar plaque are positioned in extended compartments inside and outside of the nucleus and the "neck" region in the nuclear membrane is currently mainly understood as a connection. In contrast, the budding yeast SPB occupies the space directly in and around the nuclear envelope (Cavanaugh and Jaspersen, 2017). Consistently, microtubule nucleation sites are closely associated with the well-defined inner and outer plaque structures of the SPB (Bullitt et al., 1997; O'Toole et al., 1999), while a significant gap between nucleation sites and the nuclear membrane is observed especially in *Plasmodium* mitotic spindle stages (Figure 2.21, Figure 2.23). The amorphous microtubule-nucleating inner compartment is reminiscent of the extended, amorphous MTOC during meiosis of fission yeast (Funaya et al., 2012). In comparison to *Plasmodium*, this amorphous MTOC is positioned in the cytoplasm.

Comparison to vertebrate centrosomes

In comparison to *Plasmodium*, vertebrate cells undergo open mitosis and their centrosomes typically contain a central pair of centrioles (Conduit et al., 2015). The pericentriolar material/matrix (PCM) is the site of microtubule nucleation which is structured around the centrioles in clearly defined concentric toroids (Lawo et al.,

2012; Mennella et al., 2012). In *Plasmodium*, microtubule nucleation takes place in the intranuclear compartment of centriolar plaques which, similar to the PCM in early TEM studies (Woodruff et al., 2014), appears as an electron-dense, amorphous mass. However, it remains unclear whether the intranuclear compartment is reminiscent of the vertebrate PCM. Apart from γ-tubulin, no classical PCM proteins such as pericentrin, CEP192, or NEDD1 (Woodruff et al., 2014) are conserved in *Plasmodium*. Furthermore, no proteins have been identified in the *Plasmodium* intranuclear centriolar plaque which might provide a matrix-like, structural function.
Interestingly, mammalian centrins do not only localize to centrioles, but also to centriolar satellites that surround mammalian centrioles (Quarantotti et al., 2019). In the future, it will be interesting to see whether these extra-centriolar satellites might be similar to the pool of centrin detected in *Plasmodium*.

Comparison to the *Dictyostelium* centrosome

While budding and fission yeast as well as vertebrates belong to the eukaryotic supergroup of the opisthokonts, *Plasmodium* is not part of it. Therefore, it is of interest to compare the organization of centriolar plaques to the acentriolar centrosome of the amoeba *Dictyostelium*, which also does not belong to the opisthokonts. The *Dictyostelium* centrosome consists of a box-like core with three concentrical layers, surrounded by a corona with nodules, the sites of microtubule nucleation (Gräf et al., 2021). While the centrosome is present in the cytosol during interphase, it is inserted into an opening, also called fenestra, of the nuclear envelope at onset of mitosis before semi-conservative duplication (Ueda et al., 1999; Gräf et al., 2021). Whether the part of the *Plasmodium* centriolar plaque that spans the nuclear membrane is inserted into a comparable "fenestra"-like opening of the envelope or into a classical nuclear pore remains unclear and is discussed in further detail in the next subsection. Interestingly, *Dictyostelium* undergoes so-called semi-closed or semi-open mitosis in which there is no breakdown of the nuclear envelope, but it becomes leaky and allows transport of tubulin dimers and spindle assembly factors (Gräf et al., 2021). A breakdown of the *Plasmodium* nuclear envelope during schizogony has never been observed (Prensier and Slomianny, 1986; Sinou et al., 1998; Bannister et al., 2000b). However, it will be interesting to see whether schizogony is semi-closed, for instance to mediate transfer of γ-tubulin into the nuclei for intranuclear microtubule nucleation and back into the cytosol for nucleating subpellicular microtubules. To test the permeability of the nuclear membrane, erythrocytes could be pre-loaded with fluorophore-conjugated dextran, infected with *P. falciparum*, and nuclear versus cytosolic dextran signals compared between pre-division stages and dividing schizonts.

In summary, the *Plasmodium* centriolar plaque exhibits a unique organization as it is neither exclusively associated with the cytoplasm as observed in vertebrate centrosomes, nor mainly occupying the space in the nuclear membrane as e.g. the yeast SPB. Instead, extended compartments on the cytoplasmic (centrin-containing) and nuclear (microtubule nucleating) site are established in the centriolar plaque which build a continuum across the nuclear membrane.

3.3.3 Connection of the intra- and extranuclear compartment

In this study, I found a highly protein-dense connection, linking the intra- and extranuclear compartment of the centriolar plaque, observed via NHS ester labeling of expanded cells (Figure 2.17). This observation was recently confirmed both for *Plasmodium* blood-stages (Liffner and Absalon, 2021) and for male gametocytes (Rashpa and Brochet, 2022). It is plausible that the connection at the nuclear envelope might be mediated by a nuclear pore. This is supported by the presence of the nuclear pore protein Nup313 at the centriolar plaque (Figure 2.14) as well as by early electron microscopy studies in oocysts suggesting the integration of the centriolar plaque into a nuclear pore (Canning and Sinden, 1973; Schrével et al., 1977; Sinden and Strong, 1978). Transmission electron microscopy and tomography in this study further support the presence of nuclear pores at the centriolar plaque (Figure 2.18, Figure 2.20, Figure 2.21). However, immunostainings of Nup313 combined with NHS ester labeling will be required to confirm the presence of a nuclear pore at the protein-dense neck region. In addition, it is not entirely clear how many nuclear pores are directly associated with each centriolar plaque. Using NHS ester staining, I detected exclusively one protein-dense neck region per centriolar plaque, which is in line with the observations by Rashpa and Brochet (2022) in microgametocytes and suggests a single nuclear pore at the centriolar plaque. To make a final conclusion, the number of nuclear pores at the centriolar plaque needs to be counted, which can be done by electron tomography. It remains completely elusive whether the opening at the centriolar plaque is a "classical" nuclear pore or if it resembles the fenestra in the nuclear membrane in which the *Dictyostelium* centrosome or the yeast SPB are inserted. To test whether nuclear pores are remodeled into fenestra, the size of the nuclear envelope opening at the centriolar plaque needs to be quantified. It will be interesting to see whether the size extends the diameter of dilated and contracted nuclear pores (Zimmerli et al., 2021). Furthermore, analysis of the localization of additional nuclear pore proteins identified in *Plasmodium* (Kehrer et al., 2018) will provide an indication whether the composition of nuclear envelope openings is analogous to nuclear pore complexes.

3.3.4 Centriolar plaque dynamics and duplication

In this study, PfCentrin1 served as a marker for the extranuclear compartment to investigate dynamics and duplication of the centriolar plaque via time-lapse microscopy (section 2.1). A first centrin signal was observed when hemispindle microtubules were already nucleated (Figure 2.2, Figure 2.4). After the first nuclear division, each nucleus showed one or two centrin foci during schizogony, before centrin was no longer detectable in segmented cells (Figure 2.9). The appearance of hemispindle microtubules before the first centrin signal is detected points towards a gradual assembly of the centriolar plaque. The intranuclear compartment containing γ-tubulin for microtubule nucleation might be established before the extranuclear compartment.

More markers for the intra- and extranuclear compartment of the centriolar plaque will be needed to test whether intranuclear proteins are recruited first.
A second centrin signal was detected in mitotic spindles when bright accumulated microtubule signals were detected in time-lapse microscopy (Figure 2.2, Figure 2.4) followed by separation of the centriolar plaques during expanded spindle formation. However, due to imaging at the sensitivity limit it was challenging to define the exact time point of second centrin signal appearance and therefore duplication of the centriolar plaque. Using super-resolution microscopy, I occasionally detected hemispindles with two centrin signals indicating that centriolar plaque duplication might already occur in hemispindle stage. However, it remains elusive whether a second centrin signal was solely detected due to the increased resolution or because of an early stage of centriolar plaque duplication.
In light of the current model of an amorphous centriolar plaque, an important open question is how the centriolar plaque is duplicated to form a bipolar mitotic spindle. Various different strategies of MTOC duplication have evolved in different species. For example, in animal centrosomes the mother and daughter centriole establish procentrioles before they are separated (Nigg and Holland, 2018), while formation of a second yeast SPB is initiated by assembly of a satellite structure connected to the SPB via an elongated half-bridge. The satellite develops into a new SPB that will be integrated into the nuclear envelope (Fu et al., 2015). In *Plasmodium* it remains unknown whether centriolar plaque duplication is more comparable to animal centrosome separation or *de novo* formation as in yeast SPBs. The bipartite *T. gondii* centrosome duplicates stepwise from the outside to the inside. First, the centrin-containing outer core is duplicated, followed by the inner core and the centrocone (Suvorova et al., 2015). It will be interesting to see whether duplication of the *Plasmodium* centriolar plaque shows a similar stepwise duplication starting with the extranuclear compartment. However, in contrast to *T. gondii*, the two compartments of the *Plasmodium* centriolar plaque are connected via a neck in the nuclear envelope, which would complicate coordination of a stepwise extra- and intranuclear compartment duplication. Furthermore, the connecting part in the nuclear membrane also needs to be duplicated. For this, a second fenestra or nuclear pore has to be recruited to the centriolar plaque. Novel formation of a nuclear pore during each duplication is unlikely as it was shown recently that the maximum number of pores is reached in trophozoites, indicating that they are solely redistributed during schizogony (Weiner et al., 2011).
To gain insight into both assembly and duplication of the *Plasmodium* centriolar plaque it will be critical to identify novel components of the intra- and extranuclear compartment.

3.4 Identification of novel centriolar plaque proteins

The *S. cerevisiae* spindle pole body consists of 18 proteins (Cavanaugh and Jaspersen, 2017) and in human cells, more than 500 centrosomal proteins have been identified (Andersen et al., 2003) providing a complex picture of these microtubule-organizing centers. However, research on the *Plasmodium* centriolar plaque is currently limited to very few markers including centrins, Ark1 and γ-tubulin. To analyze organization and function of the centriolar plaque, more components of the intra- and extranuclear compartment need to be elucidated and characterized. In this study, I identified eleven novel centriolar plaque candidate proteins using co-immunoprecipitations. Two of those candidates, PF3D7_1427900 and PF3D7_0710000, were analyzed in more detail.

The leucine-rich repeat protein PF3D7_1427900 is essential for blood-stage growth of the parasite (Figure 2.27B). Despite the cytoplasmic localization of centrins used for IPs, PF3D7_1427900 was detected inside the nucleus, possibly associated with the intranuclear compartment at the end of schizogony (Figure 2.27A). The nuclear localization might be explained by the fact that peptides of the protein were exclusively found in a crosslinked sample, indicating that the extranuclear part of the centriolar plaque might form a complex with the intranuclear compartment. However, association of PF3D7_1427900 with the intranuclear compartment at the end of schizogony still needs to be confirmed e.g. via co-labeling with NHS ester using U-ExM. If PF3D7_1427900 is not directly associated with the intranuclear compartment, it might still be tethered to the intranuclear compartment of the centriolar plaque towards the end of schizogony.

Sfi1-like protein (Slp) is a novel extranuclear centriolar plaque component
PF3D7_0710000 is a novel protein of the centriolar plaque, which closely associates with centrin (Figure 2.28A). Despite lacking sequence conservation of Sfi1, the identified protein contains repeats of centrin-binding domains, which are characteristic for Sfi1 (Suvorova et al., 2015) (Figure A.2). Therefore, it was called Sfi1-like protein (Slp). In budding yeast, Sfi1 is a well-known interaction partner of Cdc31, the homolog of mammalian centrin. Recently, an interaction of Sfi1 with centrins was also suggested for human cells as they localize to a common distal pool of the centriole and depletion of Sfi1 prevented recruitment of centrin (Bouhlel et al., 2021). In *Plasmodium*, I detected Slp in close proximity to centrin, but no co-localization was observed (Figure 2.28A). However, preliminary RescueSTED images suggest a co-localization of centrin with Slp (personal communication, Christoph Wenz). In co-immunoprecipitations, Slp peptides were identified both in samples with and without crosslinking of PfCentrin1-GFP expressing cells, indicating that Slp might be a direct interaction partner of *Plasmodium* Centrin1. This data is in favor of a co-localization of *Plasmodium* Slp with centrins. However, more immunofluorescence images need to be analyzed to definitely determine Slp localization with respect to centrin.

For interpretation of immunofluorescence images using the 3D7 Slp-GFP_glmS strain, it needs to be taken into account that only the C-terminus of the protein is visualized with the GFP-tag while the N-terminus might localize at a slightly different position. This is important to consider as Slp is a large protein of more than 3200 amino acids and as it might have a long, filamentous structure similar to yeast Sfi1 (Li et al., 2006). In yeast, centrin-binding motifs were found central in the amino acid sequence of Sfi1 (Kilmartin, 2003; Li et al., 2006). In contrast, six out of seven centrin-binding motifs (F/LxxWK/R) in *Plasmodium* Slp are positioned in the first (N-terminal) half of the protein (Figure A.2), indicating that *Plasmodium* centrins might be preferably associated with the N-terminus. For yeast SPB duplication, Sfi1 proteins oligomerize at their C-termini with the N-termini connected to the SPB and the newly forming satellite, respectively (Li et al., 2006; Rüthnick et al., 2021). Therefore, in C-terminally GFP-tagged yeast Sfi1 one fluorescent signal was detected at the SPB, while two signals were observed with N-terminal tagging (Burns et al., 2015). It will be interesting to test whether *Plasmodium* Slp is also able to oligomerize in an antiparallel fashion. Therefore, generation of an additional cell line expressing N-terminally tagged Slp will be useful. Thereby, the number of signals and the localization with respect to centrins can be compared between N- and C-terminally tagged Slp and potential similarities to the yeast Cdc31/Sfi1 pair can be identified.

Knockdown of Slp massively reduced parasite growth in blood-stages (Figure 2.28B). Preliminary immunofluorescence stainings on schizonts with induced Slp knockdown did neither reveal an obvious knockdown phenotype concerning the microtubule structures during schizogony, the number of centrin signals per nucleus nor in the numbers of progeny produced per parasite when Slp was knocked down for two intraerythrocytic cycles (personal communication, Christoph Wenz). However, after one cycle of Slp knockdown merozoite numbers per segmented parasite were significantly reduced. In addition, a delay in parasite development was observed upon Slp knockdown (personal communication, Christoph Wenz). More analyses and quantifications will be needed to characterize the observed differences in detail. To confirm an efficient knockdown of Slp mRNA upon glucosamine addition, qPCRs will be needed. Verification of Slp knockdown on the protein level via western blotting will likely be impossible due to the large size of the protein (407 kDa).

3.5 Conclusion and outlook

In this study, I established U-ExM and RescueSTED super-resolution microscopy techniques as well as CLEM to study schizogony of *P. falciparum* during blood-stage development. In the future, these advanced imaging techniques will reveal structural details of the parasite at unprecedented resolution and facilitate investigation of *Plasmodium's* unusual biology.
This study unraveled centrin and microtubule dynamics during schizogony and I clarified the chronology of different microtubule structures and their detailed organization. A key open question arising from this project is how hemispindle microtubules are reorganized into a mitotic spindle and how this is regulated. Time-lapse microscopy at higher temporal and spatial resolution will be required to answer this question. In addition, it remains unclear how exactly chromosomes are separated during schizogony, which is critical as they remain uncondensed throughout divisions (Canning and Sinden, 1973; Read et al., 1993; Gerald et al., 2011). Super-resolution and time-lapse microscopy of fluorescently labeled kinetochores/centromeres in combination with microtubule labeling will provide first insights into chromosome separation. Another open question is whether the parasite divides by closed mitosis or by semi-closed divisions with partial openings or leakages of the nuclear envelope, potentially including local breakdowns of the nuclear envelope as observed in fission yeast (Dey et al., 2020). In addition, the mechanism of karyofission during schizogony is entirely elusive. To answer these questions, it is critical to discover/develop a reliable nuclear envelope marker for *Plasmodium* blood-stages.

This study provides an entirely new perspective on the organization of the *Plasmodium* centriolar plaque during blood-stage schizogony into an extranuclear compartment containing centrin, and an intranuclear, DNA- and RNA-free compartment involved in microtubule nucleation. These two compartments are protein-rich and connected via a thin neck-region in the nuclear envelope. The function and composition of the intra- and extranuclear compartment remain largely unknown. I identified a novel extranuclear component of the centriolar plaque, an Sfi-like protein (Slp), which might be an interaction partner of *Plasmodium* centrins. Co-immunoprecipitations of Slp will indicate whether the protein is directly interacting with centrins and will identify further candidates of the extranuclear compartment. In addition, Ann-Kathrin Mehnert identified mitotic-spindle organizing protein 1 (MZT1) as a novel intranuclear component of the centriolar plaque in *P. knowlesi* (unpublished data). Tagging of *P. falciparum* MZT1 will reveal whether it likewise localizes to the intranuclear centriolar plaque. If it does, it will be a good candidate to identify novel proteins of the intranuclear compartment via co-IPs as I was unsuccessful with tagging intranuclear *Plasmodium* γ-tubulin. These new markers will be helpful to answer another key question arising from my PhD project which is the assembly and duplication of the amorphous *Plasmodium* centriolar plaque. In addition, it will be interesting to investigate how centriolar plaques are involved in regulating the varying numbers

of progeny produced per parasite during schizogony. Analysis of mutant parasite lines with reduced or increased merozoite numbers per parasite (Dorin-Semblat et al., 2008; Mancio-Silva et al., 2013) will be helpful to pursue this question.

While I focused on blood-stage divisions in this study, it will be intriguing to investigate centriolar plaque and microtubule dynamics as well as organization in other replicative life cycle stages of *Plasmodium* in future projects. Initial studies on male gametogenesis visualized microtubule structures (Zeeshan et al., 2019b, 2020) and very recently a bipartite organization of the centriolar plaque similar to blood-stage schizonts (Rashpa and Brochet, 2022). However, a detailed investigation of oocyst centriolar plaques beyond early transmission electron studies are missing and liver-stage centriolar plaques have, to my knowledge, never been investigated. From an evolutionary perspective, this study broadens the current understanding of MTOC organization during divisions. In contrast to most eukaryotes, *Plasmodium* is not part of the ophistokonts, but belongs to the apicomplexan phylum which is located in substantial distance to all classical biological model organisms in the eukaryotic tree of life. This makes it an interesting candidate to explore and highlight MTOC diversity among eukaryotes.

To discover novel antimalarial agents, it is important to get a deeper understanding of the biology of *Plasmodium* to identify targets specific for the parasite. Therefore, the unusual division of the parasite which leads to massive proliferation and is associated with all clinical symptoms of malaria provides a promising starting point. *Plasmodium*-specific microtubule inhibitors have been identified in previous studies (Sinou et al., 1998; Fennell et al., 2006; Kappes and Rohrbach, 2007; Naughton and Bell, 2007) and it will be interesting to further investigate their exact mode of action and their potential as antimalarial drugs. The unusual organization and composition of *Plasmodium* centriolar plaques might also provide novel targets for malaria treatment which are required considering the fast emergence of resistances against currently used antimalarial agents.

Chapter 4

Materials and Methods

4.1 Materials

4.1.1 Key devices and instruments

Device/Instrument	Supplier
Leica TCS SP8 scanning confocal microscope	Leica Microsystems
STED/RESOLFT super resolution microscope	Abberior Instruments
Zeiss Axio Observer.Z1	Zeiss
Leica EM ICE	Leica Microsystems
Leica EM AFS2	Leica Microsystems
Leica EM UC7 ultramicrotome	Leica Microsystems
Attofluor™ Cell Chamber	Invitrogen
Jeol JEM-1400 80 kV	Jeol
Tecnai F20 TEM	FEI
Tecnai F30 TEM	FEI
QuadroMACS™ Separator with LS columns	Miltenyi Biotec
VarioMACS™ Separator with CS column	Miltenyi Biotec
Gene Pulser II with cuvettes	BioRad
BD FACSCelesta™ Cell Analyzer	BD Biosciences
Bioruptor®Pico sonication system, B01060003	Diagenode
Mini Trans-Blot®Cell, 1703930	Bio-Rad
ChemiDoc XRS+ Gel Imaging System	Bio-Rad
Lab-Tek II Chambered Coverglass	Thermo Fisher Scientific
µ-Dish 35 mm, high Glass Bottom	ibidi
µ-slide 8 Well Glass Bottom	ibidi
slot grids / mesh grids / finder grids	Plano
high-tilt holder, Model 2040	Fischione Instruments

4.1.2 Key chemicals and reagents

Chemicals/Reagents	Supplier	Usage
RPMI 1640 GlutaMAX, phenol-red (61870010)	gibco - Thermo Fisher Scientific	cell culture
Albumax II (11021045)	gibco - Thermo Fisher Scientific	cell culture
Hypoxanthine (Z-41-M)	c.c.pro GmbH	cell culture
Gentamycin sulphate solution (HN09.1)	Carl Roth GmbH	cell culture
HEPES (H4034)	Sigma-Aldrich	cell culture
Geneticin G-418 Sulphate (11811-031)	Thermo Fisher Scientific	cell culture
RPMI 1640, stable Glutamine, w/o phenol-red, 2 g/l $NaHCO_3$ (P04-16520)	PAN Biotech	cell culture
WR99210	Jacobus Pharmaceuticals	cell culture
Blasticidin, solution (ant-bl-1)	InVivoGen	cell culture
Geneticin™ Selective Antibiotic (G418 Sulfate)	Thermo Fisher Scientific	cell culture
Hemacolor® Rapid staining of blood smear Solution 2 (1.11956.2500)	VWR	cell culture
Hemacolor® Rapid staining of blood smear Solution 3 (1.11957.2500)	VWR	cell culture
D-Sorbitol (S1876-500G)	Sigma-Aldrich	cell culture
Concentrated erythrocytes (O+)	Blutbank Mannheim	cell culture
D-(+)-Glucosamine hydrochloride (GlcN)	Sigma-Aldrich	cell culture
Sodium acetate	Merck	DNA precipitation
EDTA	Sigma-Aldrich	DNA precipitation
Tris	Roth	various
Tris-HCl	AppliChem GmbH	various
Concanavalin A C2010	Sigma-Aldrich	cell seeding
Paraformaldehyde (PFA) EM-grade	Electron Microscopy Sciences	cell fixation
Phosphate-buffered saline (PBS)	gibco	various
Sodium borohydrate ($NaBH_4$)	Sigma-Aldrich	IFA
Glutaraldehyde solution, grade I, 25% in H_2O	Sigma-Aldrich	IFA
Triton-X-100	Sigma-Aldrich	IFA
Albumin (BSA)	Roth	IFA
Tween-20	Roth	IFA

Nuclease-free water (AM9937)	Ambion - Thermo Fisher Scientific	U-ExM
PolyDLysine (A3890401)	gibco	U-ExM
Ammonium persulfate (APS, 17874)	Thermo Fisher Scientific	U-ExM
Tetramethylethylendiamine (TEMED, 17919)	Thermo Fisher Scientific	U-ExM
Formaldehyde (FA, 36.5-38%, F8775)	SIGMA	U-ExM
Acrylamide (AA, 40%, A4058)	SIGMA	U-ExM
N,N'-methylenbisacrylamide (BIS, 2%, M1533)	SIGMA	U-ExM
Sodium Acrylate (SA, 7446-81-3)	SantaCruz Biotechnology	U-ExM
SDS	OLS OMNI Life Science	various
NaCl	Sigma-Aldrich	various
Saponin	Sigma-Aldrich	Cell lysis
Halt™Protease Inhibitor Cocktail, 78430	Thermo Fisher Scientific	RIPA buffer
4-12% Tris-glycine Gel (Novex™WedgeWell™, XP04122BOX)	Thermo Fisher Scientific	SDS-PAGE
Ponceau S solution, P7170	Sigma-Aldrich	WB
Dynabeads™ Protein G, magnetic, 10003D	Invitrogen	IP
PageRuler™ Plus Prestained Protein Ladder, 10 to 250 kDa, 26619	Thermo Fisher Scientific	SDS-PAGE
Amersham Protran Premium 0.45 NC nitrocellulose Western blotting membranes, 1060000	Cytiva	Wet transfer
CL Prime Western Blotting Detection Reagent, RPN2232	Amersham	WB
Pierce™16% Formaldehyde (w/v), Methanol-free, 28906	Thermo Fisher Scientific	Crosslinking
NuPAGE™LDS Sample Buffer	Invitrogen	WB
Spurr's resin	Serva	TEM
Formvar	Science Services	TEM
Lowicryl HM20	Polysciences	Tomography and CLEM
tri-Sodium citrate dihydrate	Sigma	Tomography and CLEM
Lead(II) nitrate	Merck	Tomography and CLEM

LRGold	London Resin Company	CLEM
benzoyl peroxide	Polysciences	CLEM

4.1.3 Buffers, media and solutions

Buffers/Media/ Solutions	Composition	Usage
Complete Cell Culture Medium (cRPMI)	RPMI 1640, phenol-red (500 ml bottle) 25 mM HEPES 12.5 µg/ml Gentamycin sulphate solution 0.2 mM Hypoxanthine 0.5% Albumax	cell culture
Incomplete Cell Culture Medium (iRPMI)	RPMI 1640, phenol-red (500 ml bottle) 25 mM HEPES 12.5 µg/ml Gentamycin sulphate solution	cell culture
Imaging medium	RPMI 1640, w/o phenol-red (500 ml bottle) 25 mM HEPES 12.5 µg/ml Gentamycin sulphate solution 0.2 mM Hypoxanthine 0.5% Albumax	cell culture
Freezing solution	28% glycerol 3% sorbitol 0.65% NaCl	cell culture
TE buffer, pH 7.5	10 mM Tris-HCl, pH 7.5 1 mM EDTA	transfection
Cytomix, pH 7.6	120 mM KCl 0.15 mM $CaCl_2$ 2 mM EGTA 5 mM $MgCl_2$ 10 mM K_2HPO_4/KH_2PO_4 25 mM HEPES	transfection
Monomer solution	19% w/v Sodium acrylate (SA) 10% w/v Acrylamide (AA) 0.1% w/v N,N'-methylenbisacrylamide 1x PBS (from 10x stock) 0.5% w/v APS* 0.5% w/v TEMED*	U-ExM
Denaturation buffer, pH 9.0	200 mM SDS 200 mM NaCl 50 mM Tris in ddH_20, pH 9.0	U-ExM

Formaldehyde/ Acrylamide mix	1.4% formaldehyde 2% acrylamide	U-ExM
Sodium acrylate solution	38% w/v SA in Milli-Q water	U-ExM
TEMED solution	10% v/v TEMED in nuclease-free water	U-ExM
APS solution	10% w/v APS in nuclease-free water	U-ExM
RIPA buffer	50 mM Tris-HCl, pH 8.0 150 mM NaCl 1% NP-40 0.5% sodium deoxycholate 0.1% SDS 1x protease inhibitor cocktail if necessary: 1 mM DTT	cell lysis
Laemmli buffer	0.1 M Tris-HCl, pH 7.2 4% SDS 20% glycerol 0.8 M β-mercaptoethanol a pipette tip of bromophenol blue	SDS gel
Tris-glycine running buffer	25 mM Tris 250 mM glycine 0.1% SDS	SDS gel
Tris-glycine transfer buffer	25 mM Tris 192 mM glycine 0.02% SDS 0-25% Methanol	WB
Blocking solution	5% milk powder 0.05% Tween-20 in PBS	WB
Wash solution	0.05% Tween-20 in PBS	WB
Quenching solution	0.125 M glycine in 10 ml PBS	Quenching
Freeze-substitution solution (TEM)	0.2% Osmium tetroxide (in H_2O) 0.1% uranyl acetate (UA) 5% H_2O in dry acetone	TEM
Freeze-substitution solution (CLEM and Tomography)	0.3% uranyl acetate (UA) in dry acetone	CLEM and Tomography

* added immediately before usage

4.1.4 Software and databases

Software/ Database	Supplier	Usage
3DMOD	University of Colorado	tomographic reconstruction/visualization
EM-Menu	TVIPS GmbH	TEM image acquisition
eTomo	University of Colorado	tomographic reconstruction/visualization
Fiji	Schindelin et al. (2012)	Image analysis
FlowJo	Tree Star	flow cytometry data analysis
GIMP	The GIMP Development Team	CLEM - Image overlay
GraphPad	Prism	Data analysis and visualization
Huygens professional	Scientific Volume Imaging	Deconvolution
Image Lab 4.1	Bio-Rad	WB image acquisition
Imaris	Oxford Instruments	3D data analysis
IMOD	Kremer et al. (1996)	tomographic reconstruction/visualization
Imspector	Abberior Instruments	STED image acquisition
Inkscape	Inkscape Project	Figure design
Overleaf	Overleaf	Write thesis
PlasmoDB	amo	Informatics resource
R	R Core Team (2021)	Data analysis and visualization
SerialEM	Mastronarde (2005)	Tilt series acquisition for tomography

4.1.5 Primers

For Plasmid	Name	Orientation	Sequence
pArl-PfCentrin1-GFP	-	forward	CGACCCGGGATGGTACCATGAGCAGAAAAAATCAAACTATG
pArl-PfCentrin1-GFP	-	reverse	TTCTTCTCCTTTACTCCTAGGAAATAAGTTGGTCTTTTTCATAATTC
pArl-PfCentrin2-GFP	-	forward	CGACCCGGGATGGTACCATGACCGATAACACAGCTG
pArl-PfCentrin2-GFP	-	reverse	TTCTTCTCCTTTACTCCTAGGTAAGAAGCTTTTTTTGGTCATTATTG
pArl-PfCentrin4-GFP	-	forward	CGACCCGGGATGGTACCATGAACACAATGTTAATTAAGG

pArl-PfCentrin4-GFP	-	reverse	TTCTTCTCCTTTACTCCTAGGTGAATCTGAATCAACATCAC
pSLI-Nup313-3xHA_glmS	0079	forward	CGCAGCGCATCGCCTTCTATCGCCTTCTTGACGAGTTCTTCTAACTCGAGTAATTATAGCGCCCGAACTAAGCG
pSLI-Nup313-3xHA_glmS	0080	reverse	GGTATAAATATATAAATAAGAAAAACGAACATTAAGCTGCCATATCCC
pSLI-Nup313-3xHA_glmS	0126	forward	CCTTAGCTCATTCAGGTTTTTGTTTCGAAAAAATTATTACACCTGTGACGCGTTATCCATACGATGTTCCTGATTATGC
pSLI-Nup313-3xHA_glmS	0127	reverse	GGATTTTCTTCTACATCTCCACATGTTAATAAACTTCCTCTTCCTTCTCCGTCGACAGCGTAATCAGGTACATCGTATGGATAAGAACC
pSLI-Nup313-3xHA_glmS	0163for	forward	ATAAGAATGCGGCCGCTAATGGATGTAATAAAAGTGATGATAGC
pSLI-Nup313-3xHA_glmS	0164rev	reverse	CGACGCGTATTTATCATATTTTGATTCATAAATTTATGCC
pSLI-Nup313-3xHA_glmS	P22	reverse	CGCTTCAGTGACAACGTCGAGCACAGC
pSLI-Nup313-3xHA_glmS	P91	forward	CACACAGGAAACAGCTATGACC
pSLI-Nup313-3xHA_glmS	P248	forward	AGATCTGATTCCATTTCTGG
pSLI-Nup313-3xHA_glmS	P249	reverse	GAGATAAGTAAGGATATACTTTTGC
pSLI-GOI-01-3xHA_glmS	-	forward	TGACACTATAGAATACTCGCGGCCGCGCTGGGAGAGTTGAAGATGCC
pSLI-GOI-01-3xHA_glmS	-	reverse	CAGCAGCAGCACCTCTAGCACGCGTTGAGTAAGGACTTCTCTGTGTTCC
pSLI-GOI-02-3xHA_glmS	-	forward	TGACACTATAGAATACTCGCGGCCGCCAAATTTGTTCATGTCCTGG
pSLI-GOI-02-3xHA_glmS	-	reverse	CAGCAGCAGCACCTCTAGCACGCGTTAAATCAACATTGCTCATTTTG
pSLI-GOI-03-3xHA_glmS	-	forward	TGACACTATAGAATACTCGCGGCCGCGTTGAAGAAATGTTATCAGAAGTG
pSLI-GOI-03-3xHA_glmS	-	reverse	CAGCAGCAGCACCTCTAGCACGCGTTTTGCTTGTATGTTTCTTTTTAC
pSLI-GOI-04-3xHA_glmS	-	forward	TGACACTATAGAATACTCGCGGCCGCTCGAGTGATGTAAGAAAAGAGATG

pSLI-GOI-04-3xHA_glmS	-	reverse	CAGCAGCAGCACCTCTAGCACGCGTAAAAAATACACTTTTATGAACAAACG
pSLI-GOI-05-3xHA_glmS	-	forward	TGACACTATAGAATACTCGCGGCCGCGATTGATTTAGATGATAAAAGG
pSLI-GOI-05-3xHA_glmS	-	reverse	CAGCAGCAGCACCTCTAGCACGCGTGCAAAATAAATTAATTAACTCTTT
pSLI-GOI-06-GFP_glmS	-	forward	TGACACTATAGAATACTCGCGGCCGCAATATCCCATCAATTGCTACC
pSLI-GOI-06-GFP_glmS	-	reverse	CAGCAGCAGCACCTCTAGCACGCGTTTCAAGTTTGGTTTTTTTTAGGTC
pSLI-GOI-07-3xHA_glmS	-	forward	TGACACTATAGAATACTCGCGGCCGCCCAGAAGCTCATCAAATTCATC
pSLI-GOI-07-3xHA_glmS	-	reverse	CAGCAGCAGCACCTCTAGCACGCGTTGTTTTCTCGTCTTCCTTTATGC
pSLI-GOI-08-GFP_glmS	-	forward	TGACACTATAGAATACTCGCGGCCGCAGTGAAAAGACTGATGAAGG
pSLI-GOI-08-GFP_glmS	-	reverse	CAGCAGCAGCACCTCTAGCACGCGTTTTTATCATGATAAGATTGTTAAGG
pSLI-GOI-09-3xHA_glmS	-	forward	TGACACTATAGAATACTCGCGGCCGCGCAGGAGATCGTGTTATGAATC
pSLI-GOI-09-3xHA_glmS	-	reverse	CAGCAGCAGCACCTCTAGCACGCGTTGAATACAAATCTTCATCTACAAC
pSLI-GOI-10-3xHA_glmS	-	forward	TGACACTATAGAATACTCGCGGCCGCAATGAAGAATTGTCTAAGCAG
pSLI-GOI-10-3xHA_glmS	-	reverse	CAGCAGCAGCACCTCTAGCACGCGTAGCCTTGTTTTGTACATTG
pSLI-GOI-11-3xHA_glmS	-	forward	TGACACTATAGAATACTCGCGGCCGCGCAAGAGAAGAAGTACCAGGT
pSLI-GOI-11-3xHA_glmS	-	reverse	CAGCAGCAGCACCTCTAGCACGCGTGTTGGCATGGTGACGTGG

4.1.6 Plasmids

Plasmid	Source
pArl-PfCentrin1-GFP	Simon et al. (2021a)
pArl-PfCentrin2-GFP	Nicolas Lichti, Yannik Voß
pArl-PfCentrin3-GFP	Tim Gilberger
pArl-PfCentrin4-GFP	Nicolas Lichti, Yannik Voß
p3-NLS-L3-mCherry	Simon et al. (2021a)
pSLI-Nup313-3xHA_glmS	Simon et al. (2021a)
pSLI-GOI-01-GFP_glmS	Tatiany Romão

pSLI-GOI-02-GFP_glmS	Tatiany Romão
pSLI-GOI-03-GFP_glmS	Tatiany Romão
pSLI-GOI-04-GFP_glmS	Tatiany Romão
pSLI-GOI-05-GFP_glmS	Tatiany Romão
pSLI-GOI-06-GFP_glmS	Tatiany Romão
pSLI-GOI-07-GFP_glmS	Tatiany Romão
pSLI-GOI-08-GFP_glmS	Tatiany Romão
pSLI-GOI-09-GFP_glmS	Tatiany Romão
pSLI-GOI-10-GFP_glmS	Tatiany Romão
pSLI-GOI-11-GFP_glmS	Tatiany Romão

4.1.7 Parasite cell lines

Strain	Parasite cell line	Source	Usage
NF54	wild type	Ponnudurai et al. (1981)	IFAs, TEM
NF54	PfCentrin1-GFP	Simon et al. (2021a)	Time-lapse microscopy
NF54	PfCentrin2-GFP	Nicolas Lichti, Yannik Voß	IPs
NF54	PfCentrin3-GFP	this study	IPs
NF54	PfCentrin4-GFP	Nicolas Lichti, Yannik Voß	IPs
3D7	wild type	Walliker et al. (1987)	IFAs, Quantifications
3D7	Nup313-3xHA_glmS	Simon et al. (2021a)	Mark nuclear membrane
3D7	3xNLS-mCherry	Simon et al. (2021a)	Identify nucleoplasm
3D7	PCNA1-GFP, 3xNLS-mCherry	Klaus et al. (2021)	Identify replicating cells
3D7	GOI-01-GFP_glmS	Tatiany Romão	CP candidate
3D7	GOI-02-GFP_glmS	Tatiany Romão	CP candidate
3D7	GOI-03-GFP_glmS	Tatiany Romão	CP candidate
3D7	GOI-04-GFP_glmS	Tatiany Romão	CP candidate
3D7	GOI-05-GFP_glmS	Tatiany Romão	CP candidate
3D7	GOI-06-GFP_glmS	Tatiany Romão	CP candidate
3D7	GOI-07-GFP_glmS	Tatiany Romão	CP candidate
3D7	GOI-08-GFP_glmS	Tatiany Romão	CP candidate
3D7	GOI-09-GFP_glmS	Tatiany Romão	CP candidate
3D7	GOI-10-GFP_glmS	Tatiany Romão	CP candidate
3D7	GOI-11-GFP_glmS	Tatiany Romão	CP candidate

4.1.8 Antibodies

Antibody	Species	Dilution*/ Conc.	Source
anti-α-tubulin B-5-1-2 T5168, monoclonal	mouse	1:500	Sigma-Aldrich
anti-α-tubulin TAT-1, monoclonal (00020911)**	mouse	1:250	Sigma
anti-β-tubulin KMX-1, monoclonal (MAB3408)**	mouse	1:250	Sigma
anti-TgCentrin1, polyclonal	rabbit	1:2000	Marc-Jan Gubbels
anti-PfCentrin3, polyclonal	rabbit	1:500	Yannik Voß, (Simon et al., 2021a)
anti-Centrin, clone 20H5	mouse	1:500-1000	Merck
anti-HA 3F10, monoclonal	rat	1:500	Sigma
anti-CenH3, polyclonal	rabbit	1:200	Alan Cowman, (Volz et al., 2010)
anti-GFP, monoclonal	rabbit	1:50	Thermo Fisher Scientific
anti-GFP, monoclonal, 1181446000	mouse	7 µg/100 µl beads; 1:2000 (WB)	Roche
anti-Exp1	rabbit	1:500	Jude Przyborski
anti-PfNup116	rabbit	1:50	Julien Guizetti
anti-SBP1	rabbit	1:500	Jude Przyborski
anti-PbHSP70	mouse	1:100	Ann-Kristin Mueller
anti-mouse-STAR580	goat	1:200	Abberior
anti-rabbit-Atto647	goat	1:200	Sigma
anti-rabbit-Atto594	goat	1:200	Sigma
anti-mouse-Atto647	goat	1:200	Sigma
anti-mouse-Atto594	goat	1:200	Sigma
anti-mouse IgG-HRP	goat	1:3000 (WB)	Sigma-Aldrich
anti-rat-Atto594	goat	1:200	Biomol
anti-rat-Alexa488**	goat	1:500	Thermo Fisher Scientific
anti-rabbit Alexa Fluor Plus 488	goat	1:1000	Thermo Fisher Scientific
anti-rabbit Alexa Fluor Plus 555	goat	1:1000	Thermo Fisher Scientific
anti-rabbit Alexa488	goat	1:1000	Thermo Fisher Scientific
RFP booster_Atto 594	-	1:200	ChromoTek
GFP booster_Atto 594	-	1:200	ChromoTek

* dilutions for regular IFAs; for U-ExM, antibodies were usually used two times more concentrated, see also subsection 4.2.8
** exclusively used for U-ExM; respective dilution of the antibody corresponds to dilution for U-ExM

4.1.9 Fluorescent dyes

Dye	Dilution*/ Concentration	Source
NHS ester-Atto 594 (AD 594-31)**	10 µg/ml	ATTO-TEC
SPY555-Tubulin (SC203)	1:2000	Spirochrome
SYTO RNASelect	500 nM	Thermo Fisher Scientific
DRAQ5	1:1000	Biostatus
5-SiR-Hoechst	1 µM for CLEM, 22 nM for live-cell	Jonas Bucevičius, (Bucevičius et al., 2019)
Hoechst33342	1:1000	Thermo Fisher Scientific
SYBR™ Green I Nucleic Acid Gel Stain	1:2000	Invitrogen

* dilutions for regular IFAs; for U-ExM, dyes were usually used two times more concentrated, see also subsection 4.2.8
** exclusively used for U-ExM; respective concentration of the dye corresponds to usage for U-ExM

4.2 Methods

4.2.1 Parasite culture

Plasmodium cell lines were cultured in human 0^+ erythrocytes in RPMI 1640 medium supplemented with 0.2 mM hypoxanthine, 25 mM HEPES at pH 7.3, 0.5% Albumax and 12.5 µg/ml gentamicin. The hematocrit was kept at 2.5% for routine culturing, and was increased up to 5% following transfections. Cells were grown in an incubator at 37°C, 5% O_2, 3% CO_2 and 90% humidity. Percentage of infected red blood cells (parasitemia) was monitored by thin blood smears after methanol-fixation and Hemacolor rapid staining of blood smears (Merck). Cultures were maintained at a parasitemia of about 1-5%. Synchronization of parasite cultures was performed by lysis of late-stage parasites via 5% sorbitol treatment for 10 min at 37 °C, followed by a washing step with incomplete culture medium (iRPMI), supplemented only with 25 mM HEPES and 12.5 µg/ml gentamicin (lacking hypoxanthine and Albumax).

4.2.2 Magnetic enrichment of late-stage parasites

Red blood cells infected with late-stage parasites were purified from ring stages and uninfected cells using magnetic-activated cell sorting (MACS). The enrichment is based on the paramagnetic properties of hemozoin present in late-stage parasites. For U-ExM (subsection 4.2.8), a QuadroMACS™ Separator (Miltenyi Biotec) with LS Columns (Miltenyi Biotec) was used to purify schizonts before seeding of cells (several columns were used in parallel). For higher yields and bigger cultures (up to 120 ml) often needed for transmission electron microscopy approaches, parasites were enriched with a VarioMACS™ Separator (Miltenyi Biotec), using a CS column (Miltenyi Biotec). The protocol for both separator systems is the same, volumes were adjusted to the size of the respective columns. A needle (G20, 0.9 mm diameter for VarioMACS™ Separator; or G23, 0.6 mm diameter for QuadroMACS™ Separator) was added to the column to reduce flow rate. Briefly, columns were inserted into the magnetic field and equilibrated with prewarmed complete (cRPMI) or incomplete (iRPMI) culture medium. Parasite culture with a parasitemia of 3-6% was centrifuged (2 min, 800 g), the pellet resuspended in a minimum of 8 ml of prewarmed cRPMI or iRPMI and loaded onto the column(s). After several washing steps with prewarmed iRPMI (3 times or until the flow-through was clear), columns were taken out of the magnetic field and late-stage parasites were eluted using prewarmed cRPMI.

4.2.3 Cloning strategies

As all plasmids used in this study were generated not by myself but various other people in the lab, I will not list in detail the slightly different protocols (with volumes) for enzymatic digestions, PCRs, gel electrophoreses, etc., but, instead, solely explain the cloning strategies used to generate the respective plasmids.

pArl-PfCentrin1-4-GFP plasmids

The plasmids pArl-PfCentrin1-4-GFP were generated for episomal over-expression of PfCentrins under the constitutive chloroquine resistance transporter (CRT) promoter in the NF54 background. The pArl-PfCentrin3-GFP plasmid was a kind gift from Tim Gilberger. Cloning of pArl-PfCentrin1-GFP, pArl-PfCentrin2-GFP and pArl-PfCentrin4-GFP was performed by Nicolas Lichti with the help of Yannik Voß (Simon et al., 2021a). The pArl-PfCentrin3-GFP plasmid, which contains a DHFR resistance cassette, was digested with the enzymes KpnI-HF and AvRII to cut out PfCentrin3. PfCentrin sequences were amplified from *P. falciparum* cDNA via PCR using respective forward and reverse primers (subsection 4.1.5). The pArl-backbone and the respective PfCentrin insert were ligated using Gibson assembly (Gibson et al., 2009). Correct assembly of the constructs was confirmed using Sanger sequencing.

p3-NLS-L3-mCherry plasmid

The plasmid p3×NLS-mCherry was generated for expression of mCherry under the constitutive hsp86 promoter in the nucleoplasm, which was mediated by coupling three nuclear localization sequences (NLS) to mCherry (Klaus et al., 2021; Simon et al., 2021a). Briefly, the p3xNLS-FRB-mCherry plasmid kindly provided by Tobias Spielmann (Birnbaum et al., 2017) was digested with the enzymes NheI and KpnI to cut out the FKBP-rapamycin binding domain (FRB) sequence. The backbone was ligated and the resulting construct, p3×NLS-mCherry, containing a blasticidin (BSD) resistance cassette, was checked for correct assembly via Sanger sequencing. Cloning of p3×NLS-mCherry was performed by Darius Klaschka; Marta Machado generated transgenic 3D7 parasites expressing the construct.

pSLI-Nup313-3xHA_glmS plasmid

To at least partially visualize the nuclear membrane of *P. falciparum* during schizogony, the nucleoporin Nup313 identified in *P. berghei* by Kehrer et al. (2018) was tagged with a hemagglutinin (HA) tag using selection-linked integration (SLI) (Birnbaum et al., 2017) as described in Simon et al. (2021a). Further, the construct contains a glmS ribozyme sequence for knockdown of Nup313 mRNA upon glucosamine (GlcN) addition (Prommana et al., 2013), which was, however, not induced in this study. Cloning of the construct pSLI-Nup313-3xHA_glmS and generation of transgenic 3D7 parasites was performed by Marta Machado; limiting dilution to obtain a clonal parasite line was done by Alexander Penning (subsection 4.2.4). To generate the construct, the glmS ribozyme sequence was amplified from the pArl_glmS plasmid (a kind gift from Jude Przyborski) via PCR using the primers 0079 and 0080 listed in subsection 4.1.5. The amplified glmS sequence was ligated into the GFP-containing plasmid pSLI-TGD (downstream of the NeoR/KanR resistance cassette) which was kindly provided by Tobias Spielmann (Birnbaum et al., 2017) using Gibson assembly (Gibson et al., 2009). This resulted in the plasmid pSLI-TGD_glmS. Next, the 3xHA sequence was amplified from the plasmid pDC2-cam-coCas9-U6.2-hDHFR, gifted from Marcus Lee (Lim et al., 2016), by PCR using the primers 0126 and 0127 (subsection 4.1.5). The amplified 3xHA sequence was ligated into pSLI-TGD_glmS digested with the

enzymes MluI and SalI (thereby excluding the GFP sequence from the plasmid). The sequence for targeted gene disruption (TGD) was removed via restriction digest with NotI and MluI and exchanged for the genomic sequence of Nup313 (without stop codon) amplified via PCR using primers 0163for and 0164rev (subsection 4.1.5). The plasmid sequence was verified by Sanger sequencing before transfection.

pSLI-GOI-GFP_glmS plasmids

To examine the localization of eleven outer centrosomal candidate proteins identified in this study via co-immunoprecipitations (subsection 4.2.16) followed by mass spectrometry analysis (subsection 4.2.17), each candidate gene of interest (GOI) was endogenously tagged with GFP using the selection-linked integration (SLI) system (Birnbaum et al., 2017). In addition, a glmS ribozyme sequence was coupled to the construct for inducible knockdown of candidate mRNA (Prommana et al., 2013) upon addition of glucosamine (GlcN). Constructs were generated by Tatiany Romão with the help of Yannik Voß. Generation of transgenic 3D7 parasites expressing the respective constructs was performed by Tatiany Romão under my supervision. To generate pSLI-GOI-GFP_glmS constructs, the pSLI-CRK4-GFP_glmS plasmid kindly provided by Marta Machado was digested with the enzymes NotI-HF and MluI-HF to cut out the CRK4 sequence. Genomic sequences of all eleven candidate genes were amplified by PCR from *P. falciparum* NF54 gDNA using the respective primers listed in subsection 4.1.5. Digested backbone and amplified candidate gene sequences (inserts) were ligated using Gibson assembly (Gibson et al., 2009). Verification of the constructs was performed by analytical restriction digests followed by Sanger sequencing.

4.2.4 Generation of transgenic parasites

DNA precipitation

Prior to transfection, 50-100 µg plasmid DNA were precipitated with 1/10 volume 3 M sodium acetate and two volumes of 100% cold ethanol for 1 h or over night at -20 °C. After centrifugation at 16000 g for 30 min at 4 °C, the pellet was washed with 1 ml of ice-cold 70% ethanol and centrifuged again at 16000 g for 15 min at 4 °C. The pellet was air-dried for 30 min in a laminar flow hood and dissolved in 30 µl sterile TE buffer at pH 7.5 (10 mM Tris-HCl pH 7.5, 1 mM EDTA). Plasmids were frozen until transfection of parasites.

Electroporation

Transgenic parasites were generated by electroporation using the Gene Pulser II (Bio-Rad) as described in Simon et al. (2021a). For transfection, parasites were synchronized by sorbitol-treatment and ring-stages with a parasitemia of around 4% or higher were transfected with 50-100 µg of purified DNA in TE buffer. Therefore, parasite culture was centrifuged at 800 g for 5 min. For each transfection, 150 µl of iRBC pellet were mixed carefully with the thawed plasmid solution and 300 µl sterile, prewarmed Cytomix (120 mM KCl, 0.15 mM $CaCl_2$, 2 mM EGTA, 5 mM $MgCl_2$,

10 mM K_2HPO_4/KH_2PO_4 pH 7.6, 25 mM HEPES pH 7.6). The mixture of iRBCs, DNA and Cytomix was transferred to a precooled cuvette (Bio-Rad), without creating air bubbles, and electroporated at "high capacity", 310 V and 950 µF. Electroporated cells were immediately transferred to a falcon containing 5 ml prewarmed complete medium and stored at 37 °C while the other transfections were performed. Afterwards, all transfections were centrifuged at 800 g for 5 min, pellets resuspended in 7 ml prewarmed complete medium supplemented with 120-240 µl uninfected RBCs, and cultured in 6-well culture dishes.

Selection for transgenic parasites

To select for parasites containing the pArl_PfCentrin1-GFP and p3xNLS-mCherry plasmids, from day one after transfection cultures were supplemented with 2.5 nM WR99210 (Jacobus Pharmaceuticals) or 5 µg/ml blasticidin S (InVivoGen), respectively. The first two days after transfection, medium was replaced by fresh medium supplemented with respective drugs, on day three the culture was split 1:5. Until day 10 after transfection, medium was changed every day. From day 10 onwards, medium was changed twice a week and once a week a 2/3 split of the culture was performed. Cultures were regularily checked for growth of transfected parasites. In case of the SLI-system using Nup313-3xHA_glmS and GOI-GFP_glmS constructs, selection for episomal plasmids was performed using 2.5 nM WR99210, while selecting for integration was performed using 800 µg/ml Geneticin-G418 (Thermo Fisher Scientific) as described recently by Birnbaum et al. (2017). Selection for integration was performed in duplicates or triplicates. Briefly, medium was changed daily for the first 10 days or, if needed, cultures were split to prevent overgrowth. Afterwards medium was changed every second day until parasites reappeared. To check for correct integration and potential leftover of unmodified locus, gDNA was extracted and PCRs performed across the integration sites. Limiting dilution was performed to exclude cells with wild type locus and obtain a clonal Nup313-3xHA_glmS parasite line.

4.2.5 Seeding of infected red blood cells on imaging dishes

Seeding of red blood cells for immunofluorescence assays or live-cell imaging was performed as described previously (Grüring et al., 2011; Mehnert et al., 2019; Simon et al., 2021a). For immunofluorescence stainings, 8-well chambered glass slides (µ-Slide 8 Well, ibidi, or Lab-Tek II 8 well chambered slides, Thermo Fisher) were used; seeding of cultures for live-cell imaging was performed on round dishes (µ-Dish 35 mm, ibidi). All dishes had glass bottoms for better optical properties during imaging. Briefly, glass bottoms were coated with Concanavalin A (Sigma-Aldrich, 5 mg/ml in water), 90 µl for each well of 8-well glass slides and 300 µl for round dishes, for 20-30 min in an incubator at 37°C. Concanavalin A was removed and surfaces washed twice with prewarmed PBS or incomplete RPMI 1640 (iRPMI) supplemented only

with 25 mM HEPES and 12.5 µg/ml gentamicin (lacking hypoxanthine and Albumax). The desired volume of parasite culture (150 µl/well, 500 µl per round dish) was washed two times with prewarmed PBS or iRPMI by centrifugation (1000 g, 30 sec). PBS/iRPMI on the coated glass surfaces was replaced by cell suspension and erythrocytes were allowed to settle for 10 min at 37 °C. Unbound cells were removed by gently shaking the dishes and washing several times with prewarmed PBS or iRPMI until a monolayer of red blood cells remained on the glass surface. PBS/iRPMI was exchanged for complete culture medium (200 µl/well, 4 ml per round dish). When seeding was performed with washing steps in PBS, cells were allowed to recover for several hours or over night before fixation or live-cell imaging, unless specified otherwise. As analyzed in this study, PBS incubation induces reversible hemispindle microtubule destruction (Mehnert et al., 2019) (subsection 2.2.3). However, cells washed exclusively with iRMPI could immediately be fixed or used for live-cell imaging of microtubules.

4.2.6 Immunofluorescence assay (IFA)

Immunofluorescence stainings were performed as described previously by Mehnert et al. (2019) and Simon et al. (2021a). Briefly, cells seeded in 8-well dishes were quickly washed with PBS and immediately fixed with 200 µl prewarmed 4% PFA/PBS per well for 20 min at 37 °C, unless specified otherwise. After rinsing twice with PBS, cells were either stored in PBS at 4 °C for later immunofluorescence staining, or stained immediately. All following steps were performed at room temperature. Cells were permeabilized with 0.1% Triton X-100/PBS for 15 min, followed by three washing steps with PBS. To quench free aldehyde groups, cells were incubated with minor amounts of freshly prepared $NaBH_4$ (circa 0.1 mg/ml) in PBS for 10 min and washed thrice with PBS. Blocking of unspecific binding sites was performed by incubating cells with 3% BSA/PBS for 30 min to 1 h. While blocking, primary antibodies were diluted in 3% BSA/PBS and centrifuged at 21'100 g for 10 min at 4 °C to remove potential aggregates. After incubation with primary antibodies (subsection 4.1.8) for 1-2 h, cells were washed thrice with 0.5% Tween-20/PBS. Incubation with secondary antibodies (subsection 4.1.8) and Hoechst in 3% BSA/PBS was performed for 30-60 min preceding removal of aggregates as described for primary antibodies. Cells were washed two times with 0.5% Tween-20/PBS and once with PBS only. Imaging was either performed directly, or cells were stored in PBS at 4 °C in the dark until imaging. Occasionally, cells were additionally fixed with 4% PFA/PBS for 10-15 min at room temperature (RT), to retain antibodies at their positions. After washing thrice with PBS, cells were likewise stored in PBS at 4°C in the dark. This second fixation increased storage time from roughly two weeks to several weeks or even months.

4.2.7 Preparation of infected red blood cells for live-cell imaging

For time-lapse microscopy, NF54_PfCentrin1-GFP cells were prepared as described previously (Simon et al., 2021a). After seeding of parasites on a 35 mm round glass-bottom dish (ibidi) as described in subsection 4.2.5, cells were allowed to recover in 4 ml complete medium under standard culture conditions for several hours. For time-lapse microscopy, phenol-red free RPMI 1640 imaging medium with stable glutamine and 2 g/l $NaHCO_3$ (PAN Biotech) containing all supplements used for complete culture medium (subsection 4.2.1) was prepared freshly and equilibrated to the gas conditions of the incubator for several hours. Before imaging, 9 ml of equilibrated imaging medium were supplemented with 4.5 µl (1:2000 dilution) of the live dye SPY555-Tubulin (Spirochrome) to visualize microtubules. Culture medium was removed from the seeded parasites and the dish completely filled with 8 ml of prepared imaging medium. The dish was closed with a lid preventing any air bubbles, tightly sealed with parafilm, and immediately taken to the incubation chamber of the microscope, prewarmed to 37 °C.

4.2.8 Ultrastructure expansion microscopy (U-ExM)

Ultrastructure expansion microscopy (U-ExM) was performed as described previously by Gambarotto et al. (2019, 2021) with minor modifications (Simon et al., 2021a). Coated coverslips used for expansion microscopy were prepared by incubation with poly-D-Lysine (gibco) for 1 h at 37 °C, followed by three washing steps with ddH_20. Coated coverslips were dried completely and stored at 4 °C before usage.

Crosslinking, gelation, denaturation and first expansion of cells

For U-ExM, hemozoin-containing late-stage parasites were magnetically enriched from a culture with a parasitemia of 2-5% using QuadroMACS™ Separator (Miltenyi Biotec) as described in subsection 4.2.2. Eluted parasites were centrifuged at 800 g for 2 min and the pellet was resuspended in 300 µl prewarmed iRPMI. 80 µl suspension were added on a 12 mm poly-D-Lysine-coated coverslip and cells were allowed to settle for 10 min at 37 °C. Excess suspension was removed and parasites fixed with prewarmed 4% PFA/PBS for 20 min at 37 °C. Coverslips were washed thrice with prewarmed PBS and placed in a 12-well plate. To prevent further protein crosslinking, cells were incubated with freshly prepared 1.4% formaldehyde (Sigma)/2% acrylamide (Sigma) in PBS (1 ml/well) for 5 h at 37 °C.

For gelation, 10% TEMED (Thermo Fisher Scientific) and 10% APS (Thermo Fisher Scientific) solution were thawed on ice 30 min before usage and a humid chamber was precooled for 10-15 min at -20 °C. Before gelation, the humid chamber was placed on ice. Coverslips with parasites were taken out of the 12-well plate (maximum two at once), shortly dipped in PBS and excess PBS removed by leaning the coverslips to the well plate. 5 µl 10% TEMED and 5 µl 10% APS solution thawed on ice were added to 90 µl ice-cold monomer solution, mixed, and two 35 µl drops were placed on parafilm in the humid chamber on 4 °C. The drops were rapidly covered with

coverslips, cells facing the solution, to allow for incorporation of cells into the gel. For better gel penetration, cells were incubated for 5 min on ice before incubation for 1 h at 37 °C.

Next, coverslips with gels were transferred to a 6-well plate and incubated with 1-2 ml denaturation buffer (200 mM SDS, 200 mM NaCl, 50 mM Tris in ddH_20, pH 9.0) for 15 min at RT with 120 rpm agitation to allow the gel to detach from the coverslip while already slightly expanding. For denaturation, the wavy gel was transferred carefully to an 1.5 ml reaction tube filled with denaturation buffer and incubated for 1.5 h at 95 °C. For a first expansion, denaturation buffer was removed and the gel transferred to a petri dish with Milli-Q water. After incubation for 30 min at RT, water was replaced by fresh Milli-Q water and incubated over night at RT.

Immunofluorescence staining

The next day, an immunofluorescence staining was performed as described in subsection 4.2.6 with slight adaptations for expansion microscopy. First, gels were shrunken for antibody incubation by replacing water with PBS and incubation of gels for 2x 15 min at RT. Gels were transferred to a 6-well plate, followed by blocking of cells with 3% BSA/PBS for 30 min at RT with agitation. During that time primary antibodies were diluted in 3% BSA/PBS and centrifuged at 21'100 g for 10 min at 4 °C to remove potential aggregates. Antibodies used for expansion microscopy were usually used two times more concentrated in comparison to regular IFAs (subsection 4.1.8). Primary antibodies used for U-ExM are the mouse anti-α-tubulin B-5-1-2 (Sigma, T5168), mouse anti-α-tubulin TAT-1 (Sigma, 00020911), mouse anti-β-tubulin KMX-1 (Sigma, MAB3408), rabbit anti-PfCentrin3 and rat anti-HA 3F10 (Sigma) (subsection 4.1.8), all used at a dilution of 1:250. Gels were incubated in 1 ml primary antibody solution for 2.5-3 h at 37 °C with agitation. Afterwards, cells were washed 5x 10 min with 2 ml 0.5% Tween-20/PBS at RT with agitation.

Parasites were incubated with secondary antibodies and Hoechst33342 (Thermo Fisher Scientific; 1:100) in 3% BSA/PBS for 2.5 h at 37 °C with agitation, after removal of potential aggregates as described for primary antibodies. Secondary antibodies used for U-ExM are the anti-mouse-STAR580 (Abberior) and anti-rabbit-Atto647 (Sigma) at a dilution of 1:100, and anti-rat-Alexa488 (Thermo Fisher Scientific) (subsection 4.1.8) at 1:500. Gels were washed 5x 10 min with 0.5% Tween-20/PBS with agitation, before gels were transferred again to petri dishes for a second expansion. Cells were expanded in Milli-Q water for 2x 30 min at RT, followed by another exchange for fresh Milli-Q water and expansion over night at RT. Stained gels were stored for several days in petri dishes filled with Milli-Q water and sealed with parafilm until imaging.

Imaging of expanded cells

To image expanded cells on a Leica TCS SP8 scanning confocal microscope (subsection 4.2.9), a piece of the gel was cut, carefully put on a tissue to remove excess water, and placed on an uncoated 24 mm coverslip in a metal holder. By microscopy, the side of the gel which contains the cells was determined and the gel with cells facing

the bottom was placed on a 24 mm poly-D-Lysine-coated coverslip, and placed into the metal holder. The holder was closed and an uncoated coverslip loosely placed on top to reduce evaporation during microscopy (subsection 4.2.9). To calculate the expansion factor, the gel diameter was measured and compared with the size of the initial gel (12 mm, as restricted to the size of the cover slip used for seeding of cells). The expansion factor usually measured around 4.5.

4.2.9 Confocal microscopy

Live-cell imaging and imaging of fixed and immunofluorescently labeled parasites were routinely performed on a Leica TCS SP8 point laser scanning confocal microscope (Leica Microsystems) equipped with a lightning (LNG) module for automated adaptive deconvolution after image acquisition. LNG enables super-resolution microscopy down to 120 nm. Parasites were imaged using an HC PL APO CS2 63x oil immersion objective with a numerical aperture (NA) of 1.4. Laser powers (405, 488, 561, 633 nm) were individually adjusted to the respective combinations of fluorescent tags, dyes and antibodies used. Channels were acquired sequentially using GaAsP hybrid detectors (HyD) and spectral emission filters. Brightfield images were taken with a transmitted light PMT detector.

Live-cell imaging
Live-cell imaging of PfCentrin1-GFP expressing parasites was performed using an automated stage for acquisition of cells at multiple positions and the adaptive focus control (AFC) to stabilize the focal plane. For live-cell imaging, the LNG module was used in the adaptive acquisition mode and the pinhole opened to 1.2 airy units. This resulted in a pixel size of 53.8 nm and, using 344 x 344 pixels, in a total image size of 18.45 x 18.45 µm. The pixel dwell time was 488 ns. Z-stacks with a total size of 6 µm and z-intervals of 0.5 µm were acquired every 5 min for up to 13 h (over night imaging). Centrin1-GFP was excited with a 488 nm laser at a laser power of 0.5%, SPY555-Tubulin was excited with a 561 nm laser at a laser power of 2%.

Immunofluorescently labeled parasites
Fixed, immunostained parasites were either imaged with or without LNG. For acquisition without LNG, the pinhole was set to 1 airy unit, resulting in a pixel size of 72.6 nm and a total image size of 9.3 x 9.3 µm (128 x 128 pixels). The pixel dwell time was 488 ns. Z-stacks were acquired with a total size of up to 6.27 µm and z-intervals of 0.3 µm. For overview images, a pixel size of 92 nm with a total image size of 188 x 188 µm (2048 x 2048 pixels) and a z-stack size of 8-10 µm was used. For cells expanded with U-ExM (subsection 4.2.8), the total image size was increased to 46.13 x 46.13 µm (512 x 512 pixels) and z-stacks increased up to 24 µm with a z-interval of 0.3 µm. The pixel size was 72.6 nm.
Non-expanded immunostained cells were often imaged with LNG. Therefore, adaptive acquisition was used. Images were acquired in full resolution mode, resulting in a pinhole of 0.5 airy units and a pixel size of 28.92 nm in an image with a total size

of 9.3 x 9.3 µm (320 x 320 pixels). Z-stacks of 6.23 µm were taken with z-intervals of 0.13 µm.

4.2.10 RescueSTED microscopy

RescueSTED images were acquired on a single-point scanning STED/RESOLFT super resolution microscope (Abberior Instruments GmbH) equipped with a pulsed 775 nm STED depletion laser. For signal detection, three avalanche photodiodes were used. Parasites were imaged with a 100x oil immersion objective (Olympus), 1.4 NA, a pixel size of 20 nm and a pixel dwell time of 10 µs. The STED laser power was ranging between 10-40%, all other lasers (488, 594 and 640 nm) were adjusted to the respective antibody combinations of the immunofluorescence staining. To prevent destruction of hemozoin-containing late-stage parasites by the high-intensity STED laser, we applied RescueSTED adaptive illumination based on CONF levels. The CONF level defines the threshold of the minimum fluorescent signal which needed to be reached in the respective confocal image before automatic activation of the STED laser at this pixel. The CONF levels were adjusted for the staining and on the level of each individual cell, ranging from 10-110. To acquire z-stacks, a total size of 3.9 µm was acquired using z-intervals of 300 nm.

4.2.11 Image analysis and quantifications

Images were analyzed and quantified using Fiji software (Schindelin et al., 2012).

Deconvolution
Adaptive deconvolution of time-lapse microscopy images acquired on the Leica TCS SP8 point laser scanning confocal microscope (subsection 4.2.9) was done automatically by the LNG software, before tubulin structures and centrin signals were analyzed. All deconvolved images shown in this study were either deconvolved using Imspector (Abberior instruments GmbH) or Huygens professional (Scientific Volume Imaging B.V.). Deconvolution with Imspector was based on the Richardson-Lucy algorithm using default settings (regularization parameter of $1x10^5$). Deconvolution with Huygens professional (Scientific Volume Imaging B.V.) was performed after incorporation of all microscopic parameters using deconvolution express with the standard settings.

Quantifications
To quantify durations of individual tubulin stages in the first three divisions during schizogony, I manually assessed maximum intensity projections of live-cell images after LNG adaptive deconvolution (Figure 2.2, Figure 2.3). I determined the first and last time point (frame) of the respective tubulin stages (hemispindle, mitotic spindle, anaphase spindle) and calculated their durations. In addition, 5 min time were added to each duration as images were acquired in 5 min intervals and the time between the last frame of a tubulin stage and the first frame of the subsequent stage was split

between the two stages. In addition, times of a first, stable PfCentrin1-GFP signal and duplicated centrin foci were determined (Figure 2.2, Figure 2.4). I considered a first centrin signal as stable when the signal was associated with tubulin and stayed for more than one time point.
Quantification of the number of microtubule branches per hemispindle (Figure 2.10C) as well as measurement of microtubule length in hemispindles and mitotic spindles (Figure 2.10B) was performed by Johanna Bauer. Therefore, parasites were imaged with U-ExM and the required parameters measured in 3D using Imaris (Oxford Instruments). Microtubule length was corrected by the expansion factor of 4.5-fold.
Percentages of PCNA1-GFP positive and negative schizont nuclei in hemispindle and mitotic spindle stages were determined manually by Julien Guizetti (Figure 2.13).
Width and depth of DNA-free regions in hemispindle and mitotic spindle-stage schizont nuclei were measured in a single focal plane of confocal images after LNG adaptive deconvolution. Only DNA-free regions in lateral view were analyzed. Width of the DNA-free region was measured at the widest diameter where the nuclear envelope was expected to be. Depth of the DNA-free region was determined at a 90° angle to the width and measured from underneath the centrin signal (in direction of the nucleus) to the deepest point of the DNA-free region. A schematic of the measurement is depicted in Figure 2.15.
Dimensions of the NHS-ester-stained intranuclear regions of the centriolar plaque detected in cells imaged by U-ExM were analyzed by Johanna Bauer using Fiji. Width and depth of the full NHS-ester stained region and a smaller, more protein-dense region were measured in single slices after deconvolution of confocal images, as depicted in Figure 2.17C. Measurements were corrected by the expansion factor of 4.5.
Quantification of the shortest distance of microtubule minus-ends to the nuclear membrane in annotated, segmented tomograms of schizont nuclei in hemispindle and mitotic spindle stage, were performed by Charlotta Funaya using the mtk program in the IMOD software package (Figure 2.23).

Data analyses and visualization of plots and figures were performed using Excel, R and the vector-based software Inkscape. Analysis and visualization of flow cytometry data is described in subsection 4.2.18.

4.2.12 Transmission electron microscopy of Spurr-embedded infected red blood cells (iRBCs)

Transmission electron microscopy (TEM) of Spurr-embedded NF54 wt parasites was performed as described previously (Simon et al., 2021a). Briefly, NF54 wt cells were synchronized and grown to a parasitemia of 6% schizonts with a total volume of 500 µl packed red blood cells (in 18 ml culture medium). Infected red blood cells were magnetically separated from non-infected cells and early parasite stages using the QuadroMACS™ Separator system as described in subsection 4.2.2. The eluate

was supplemented with 30 µl uninfected red blood cells and parasites were cultured for 4 h to let them recover from magnetic purification. In later TEM experiments (subsection 4.2.14, subsection 4.2.13), addition of uninfected RBCs and recovery were omitted as they had proven not to be relevant for structural preservation of the parasites. However, importantly, in all TEM experiments parasites were not in contact with PBS before high-pressure freezing, as it was shown in this study that PBS incubation disrupts hemispindle microtubules in *P. falciparum* blood stages (subsection 2.2.3) (Mehnert et al., 2019).

High-pressure freezing (HPF)

For high-pressure freezing (HPF) of parasites, gold or aluminium carriers (3 mm diameter, 100 µm or 200 µm depth; Leica Microsystems) with respective lids were placed on hexadecene-soaked filter paper to exclude air during the freezing process. Parasite culture was centrifuged and the pellet(s) temporarily stored at 37 °C until HPF. For each sample, supernatant was removed. 1-2 µl of concentrated schizont pellet were transferred to the carrier which was carefully closed with the flat side of the lid while preventing inclusion of air. Parasites were high-pressure frozen for 400 ms at 2200 bar in liquid nitrogen using Leica EM ICE (Leica Microsystems). Vitrified samples were stored in a liquid nitrogen tank until freeze-substitution was performed.

Freeze-substitution (FS) and resin-embedding

Freeze-substitution was performed in an automatic freeze substitution system (Leica EM AFS2, Leica Microsystems) for temperature control, while pipetting steps were performed manually. Carriers with high-pressure frozen pellets were transferred to the AFS machine in liquid nitrogen and lids were removed carefully. Red blood cell pellets were transferred into freeze-substitution solution (0.2% Osmium tetroxide (in H_2O), 0.1% uranyl acetate (UA, in methanol), 5% H_2O, in dry acetone) precooled to -90 °C. Samples were freeze-substituted for 1 h at -90 °C, before increasing the temperature from -90 °C to +20 °C in 22 h (slope of 5 °C/h). Samples stayed at 20 °C for circa 1 h until further processing. Next, freeze-substitution solution was removed and samples washed thrice with dry acetone. While inverting the tubes during washing steps, the pellets detached from the carriers and were combined in a 1.5 ml reaction tube for the next steps (carriers were removed). Cells were pelleted for 2 min at 325 g, acetone was removed and the pellet incubated with a 1:1 mixture of Spurr's resin (Serva) and dry acetone for 1-2 h at RT. The mixture was removed and parasites were incubated in 100% Spurr's resin over night at RT. The next day, Spurr's resin was removed, replaced by fresh 100% Spurr's resin and samples embedded by resin polymerization for 1-2 days at 60 °C.

Sample trimming, sectioning and imaging

Embedded samples were trimmed and sectioned on a Leica EM UC7 ultramicrotome (Leica Microsystems). 70 nm ultrathin sections were collected on formvar-coated mesh or slot grids and sections were dried completely. Imaging was performed on a

Jeol JEM-1400 80 kV transmission electron microscope (Jeol) equipped with a 4k by 4k pixel TemCam F416 digital camera (TVIPS). The EM-Menu (TVIPS) software was used for image acquisition.

4.2.13 Preparation of infected RBCs for electron tomography

Electron tomography of infected red blood cells was performed as described by Simon et al. (2021a). Briefly, NF54 schizonts expressing PfCentrin1-GFP were synchronized and grown to a parasitemia of 3-5% with a total volume of 2-4 ml packed red blood cells (cultured in 70-140 ml cRPMI). Red blood cells infected with schizont-stage parasites were purified via magnetic-activated cell sorting using the VarioMACS™ Separator (Miltenyi Biotec, subsection 4.2.2). Purified cells were high-pressure frozen using a Leica EM ICE (Leica Microsystems) as described in subsection 4.2.12.

Freeze-substitution (FS) and resin-embedding

Freeze-substitution and resin-embedding of high-pressure frozen infected red blood cell pellets were performed in an automated Leica EM AFS2 (Leica Microsystems) using a pipetting robot. The indvidual steps are listed in detail in Table 4.1. Before usage, solutions were precooled in the AFS2 machine. Briefly, carriers with high-pressure frozen samples were transferred to the AFS2 in liquid nitrogen, lids were removed carefully and the samples placed into respective plastic holders for FS. Freeze-substitution was performed in 0.3% uranyl acetate (UA) in anhydrous acetone while increasing the temperature from -90 to -45 °C. Cells were resin-embedded in increasing concentrations of the Lowicryl HM20, which was polymerized with UV light. Therefore, HM20 solution was prepared freshly by mixing of monomer E, crosslinker D and initiator C according to the manufacturer's instructions (Polysciences). Embedding of schizonts in HM20 via UV polymerization led to insufficient polymerization of the resin and therefore embedding of the cells, probably due to the hemozoin crystals (pigmentation) of schizonts. Hemozoin absorbs light of 400 nm wavelength (Brémard et al., 1993) (close to the wavelength of UV ligth used for polymerization), which might prevent penetration of UV light deeper into the sample pellet. Indeed, only a thin layer of cells on one side of the pellet in the carrier was adequately infiltrated for further processing.

TABLE 4.1

Temperature (°C)	Time	Solution	UV
-90	24 h	0.3% UA/anhydrous acetone	-
-90 to -45	9 h (5°C/h)	0.3% UA/anhydrous acetone	-
-45	5 h	0.3% UA/anhydrous acetone	-
-45	3x 10 min	anhydrous acetone rinses	-
-45	2 h	25% HM20/anhydrous acetone	-
-45	2 h	50% HM20/anhydrous acetone	-
-45	2 h	75% HM20/anhydrous acetone	-

-45	12 h	100% HM20	-
-45	2 h	100% HM20	-
-45	48 h	100% HM20	+
-45 to +20	13 h (5°C/h)	100% HM20	+
+20	48 h	100% HM20	+

Sample trimming, sectioning, postcontrasting and electron tomography
Areas with properly embedded schizonts were selected, trimmed and sectioned using a Leica EM UC7 ultramicrotome (Leica Microsystems). Thick sections of 200 nm were collected on formvar-coated copper slot grids and and post-contrasted. Therefore, grids were incubated with 3% UA in H_2O for 5 min at RT in the dark and washed 3x 1 min with filtered H_2O. After incubation with Reynold's lead citrate (which is a mixture of tri-Sodium citrate dihydrate and Lead(II) nitrate) for 2 min at RT, 3x 1 min washing steps with filtered H_2O were performed and the sections were dried completely.

Electron tomography
Preservation of ultrastructures was checked on a Jeol JEM-1400 80 kV transmission electron microscope (Jeol) (subsection 4.2.12), before tilt series were acquired. For tomography, grids were placed in a high-tilt holder (Model 2040; Fischione Instruments; Corporate Circle, PA) and schizonts were imaged on a Tecnai F20 EM (FEI, Eindhoven, The Netherlands) operating at 200 kV. Images were acquired every degree over a ±60° range with a magnification of 19'000x and a binning of 2x (1.13 nm pixel size) using an FEI Eagle 4K x 4K CCD camera and the SerialEM software package (Mastronarde, 2005). To reconstruct tomograms, tilt series were aligned via patch tracking in the eTomo graphical user interphase of the IMOD software package (Kremer et al., 1996) and tomograms were generated using R-weighted back-projection algorithm (eTomo). For reconstruction of the complete hemispindle, tilt series of three adjacent sections were collected, aligned and joined with eTomo (Höög et al., 2007). Tomograms were displayed as one voxel-thick slices, modeled, and analyzed using IMOD (Kremer et al., 1996). Capped-ends of hemispindle and mitotic spindle microtubules were classified as minus-ends, as done in previous microtubule studies using similar preservation methods (Gibeaux et al., 2012; Höög et al., 2007; O'Toole et al., 2003).

4.2.14 On-section correlative light and electron microscopy (CLEM) combined with tomography

Correlative light and electron microscopy which was combined with electron tomography was performed as described recently (Simon et al., 2021a). Briefly, schizonts of the NF54 PfCentrin1-GFP strain were magnetically purified using the VarioMACS™ Separator (Miltenyi Biotec) as described in subsection 4.2.2 and subsection 4.2.13.

Purified cells were incubated with 1 µM of the live dye 5-SiR-Hoechst for circa 1 h at 37 °C. After DNA labeling, schizonts were high-pressure frozen using Leica EM ICE (Leica Microsystems) as described in subsection 4.2.12.

Freeze-substitution (FS) and resin-embedding

Freeze-substitution of high-pressure frozen concentrated schizont pellets was performed in an automatic freeze substitution system (AFS2, Leica Microsystems), while all pipetting steps were performed manually. Table 4.2 gives a detailed list of the individual steps of the freeze-substitution and resin-embedding. Freeze-substitution was performed in 0.3% uranyl acetate (UA) in anhydrous acetone while increasing the temperature from -90 to -45 °C. Due to difficulties to UV-polymerize the Lowicryl HM20 in hemozoin-rich schizont pellets (subsection 4.2.13), schizonts were embedded in the resin LRGold (London Resin Company), which can be polymerized by addition of a chemical initiator. The sample was incubated with increasing concentrations of LRGold until 100% were reached. To initiate polymerization, LRGold was freshly supplemented with 1.5% benzoyl peroxide on ice. The solution was carefully mixed by inverting the tube, while oxygen incorporation was avoided. Immediately after, the solution was placed at -20 °C to prevent polymerization of the resin at RT.

TABLE 4.2

Temperature (°C)	Time	Solution
-90	29 h	0.3% UA/anhydrous acetone
-90 to -45	9 h (5°C/h)	0.3% UA/anhydrous acetone
-45	5 h	0.3% UA/anhydrous acetone
-45 to -25	1 h (20°C/h)	anhydrous ethanol
-25	2 h	25% LRGold/anhydrous ethanol
-25	2 h	50% LRGold/anhydrous ethanol
-25	2 h	75% LRGold/anhydrous ethanol
-25	1 min	100% LRGold (washing step)
-25	over night	100% LRGold
-25	26 h	1.5% benzoyl peroxide/LRGold
-25 to +20	9 h (5°C/h)	1.5% benzoyl peroxide/LRGold
+20	24 h	1.5% benzoyl peroxide/LRGold

On-section widefield fluorescence microscopy

After trimming and sectioning of the embedded samples on a Leica EM UC7 ultramicrotome (Leica Microsystems), 300 nm-thick sections were collected on formvar-coated finder grids to enable identification of the same cell for fluorescence and electron microscopy. Immediately after sectioning, the grid was slightly dried with a paper to hinder sections from moving and directly placed in a drop of PBS, pH 8.4 (Ader and Kukulski, 2017) on a 24 mm glass coverslip with the sections facing the bottom. To cover the grid, a second 24 mm glass coverslip was placed on top and the

sandwich was mounted in a metal ring holder (Kukulski et al., 2012). Immediately after mounting, fluorescent signals of the sample were imaged using a widefield Zeiss Axio Observer.Z1 microscope equipped with an AxioCam MR R3 camera. Cells were imaged with a 63x oil objective, 1.4 NA. To visualize PfCentrin1-GFP localization, cells were excited with a 488 nm laser (95% laser power, 900 ms exposure time); 5-SiR-Hoechst signals were excited with a 587 nm laser (same laser power and exposure time than with 488 nm laser). Images were acquired with a pixel size of 102 nm and a total image size of 1388 x 1040 pixels. Immediately after imaging, samples were washed 3x 1 min with filtered H_2O and post-contrasted with 3% UA in H_2O and Reynold's lead citrate as described in subsection 4.2.13.

Electron tomography

Air-dried sections were imaged on a Jeol JEM-1400 80 kV transmission electron microscope (Jeol) to monitor good ultrastructural preservation of the imaged fluorescent cells, before tomography was performed. Tilt-series were acquired on a FEI TECNAI F30 300kV (EMBL Heidelberg) transmission electron microscope at a range of ±60° with 2° intervals using a 4x4k CCD camera (OneView Camera, Gatan). For image acquisition, the Serial-EM software package was used. Reconstruction of tomograms from tilt-series was conducted using the eTomo Image Processing Package (Boulders, Colorado).

Correlation of fluorescence and electron tomography images was performed manually using Fiji, GIMP 2.10.20. and Inkscape.

4.2.15 SDS-PAGE and western blot

Cell harvesting and lysis

NF54 parasites expressing PfCentrin1-, 2-, 3- or 4-GFP were washed once with prewarmed PBS by centrifugation (800 g, 5 min) and were subsequently lysed with 0.15% Saponin/PBS for a few minutes at RT. Isolated parasites were centrifuged (3000 g, 6 min) and the pellet washed once in 1 ml PBS. Next, parasites were dissolved in 1 µl RIPA buffer (50 mM Tris-HCl, pH 8, 150 mM NaCl, 1% NP-40, 0.5% sodium deoxycholate, 0.1% SDS) supplemented with 1x protease inhibitor (Halt™ Protease Inhibitor Cocktail, 78430, Thermo Fisher Scientific) per 2x10^6 parasites and incubated for 30 min on ice, with vortexing from time to time. The sample was pelleted at full speed for 15 min at 4 °C in a table-top centrifuge. Meanwhile, 2-fold concentrated Laemmli buffer (0.1 M Tris-HCl, pH 7.2, 4% SDS, 20% glycerol, 0.8 M β-mercaptoethanol, a pipette tip of bromophenol blue) was preheated to 95 °C. Sample supernatant was incubated with boiling Laemmli buffer (1:2 dilution) for 5 min at 95 °C, vortexed at maximum speed for 1 min and loaded onto an SDS gel. To load the sample pellet, it was first sonicated using the Bioruptor® Pico sonication system (B01060003, diagenode) with 30 sec sonication, 30 sec break, (10 cycles) followed by 5 min incubation in boiling Laemmli buffer, as done for the supernatant, and a short

centrifugation step (1 min, maximum speed). Residual volumes not loaded onto the SDS gel were frozen at -20 °C or -80 °C until usage.

SDS-PAGE

For SDS-PAGE, a 4-12% tris-glycine Gel (Novex™ WedgeWell™, XP04122BOX, Thermo Fisher Scientific) was rinsed with deionized water, put into the respective holder and the holder filled with freshly prepared 1x tris-glycine running buffer (25 mM Tris, 250 mM glycine, 0.1% SDS in deionized water). Samples, usually 1-2x10^7 cells per lane, were loaded onto the gel. As a marker, 4 µl of PageRuler™ Plus Prestained Protein Ladder, 10 to 250 kDa (26619, Thermo Fisher Scientific) were used. Gels were run at 120 V for the first 10 min until switching to 160-200 V.

Wet transfer of proteins

Transfer of proteins from the SDS-Gel to a nitrocellulose membrane was performed using the wet transfer system Mini Trans-Blot® Cell (1703930, Bio-Rad). Therefore, a stack was assembled in freshly prepared tris-glycine-based transfer buffer (25 mM Tris, 192 mM glycine, 0.02% SDS, 0-25% methanol in deionized water) and put into the gel holder cassette. The individual layers of the stack from bottom (cathode) to top (anode) included: sponge, whatman filter paper, the SDS-gel (in mirror image orientation), nitrocellulose membrane (Amersham Protran Premium 0.45 NC nitrocellulose Western blotting membranes, 10600003, Cytiva), whatman filter paper, sponge. The wet transfer was performed in transfer buffer for 14 h at 40 mA on ice.

Ponceau staining and western blotting

To confirm the transfer of proteins, the nitrocellulose membrane was briefly washed with deionized water before incubation with Ponceau solution (0.1% (w/v) in 5% acetic acid, Ponceau S solution, P7170, Sigma-Aldrich) for 3-5 min at RT with agitation. The membrane was very briefly destained with deionized water and immediately imaged using ChemiDoc XRS+ Gel Imaging System (Bio-Rad) equipped with the Image Lab 4.1 software. After imaging, the membrane was completely destained in deionized water, followed by a short rinse in 0.05% Tween-20/PBS.

For western blotting, the membrane was blocked with 5% milk powder in 0.05% Tween-20/PBS for 30 min at RT with slight agitation. The blocking solution was removed and fresh blocking solution added for another 15 min (agitating). Next, the membrane was stained with a 1:2000 dilution of primary antibody mouse anti-GFP (11814460001, Roche) in 5% milk powder/0.05% Tween-20/PBS for 1 h at RT, slightly shaking. The membrane was once rinsed in 0.05% Tween-20/PBS and washed 3x 10 min at RT, slightly shaking. The secondary antibody goat anti-Mouse IgG-HRP (A5278, Sigma-Aldrich) was diluted 1:3000 in 5% milk powder/0.05% Tween-20/PBS and the membrane was incubated for 1 h at RT with slight agitation. The membrane was rinsed in 0.05% Tween-20/PBS and washed 3x 10 min at RT, followed by incubation with 1:1 Amersham ECL Prime Western Blotting Detection Reagent (RPN2232, Amersham) for 5 min at RT. The antibody signals were detected using

the ChemiDoc XRS+ Gel Imaging System and corresponding Image Lab 4.1 software (both Bio-Rad).

4.2.16 Co-immunoprecipitations (IPs)

Co-immunoprecipitations, preceded by harvesting of parasites with or without crosslinking of proteins, was done based on the protocol described by Balestra et al. (2020) and Fang et al. (2017).

Harvesting and crosslinking of proteins
NF54 schizont cultures (total of 4-6 ml packed blood cell pellet) expressing PfCentrin1- and PfCentrin2-GFP were harvested at a parasitemia of 4-8%. Therefore, parasites were pelleted (340 g, 5 min) and red blood cells lysed in 0.1% saponin in cRPMI for 1 min at RT. After centrifugation (3000 g, 6 min), cells were washed again with 0.1% Saponin in iRPMI by centrifugation (3000 g, 6 min). For crosslinking of proteins, the pellet was dissolved in 1% formaldehyde (Pierce™ 16% Formaldehyde (w/v), methanol-free, 28906, Thermo Fisher Scientific) in 500 µl iRPMI and incubated for 10 min at RT with gentle agitation. Next, cells were centrifuged (1000 g, 3 min) at RT and formaldehyde solution removed carefully. The crosslinking reaction was quenched by incubation of the sample with 10 ml 0.125 M glycine solution in PBS for 5 min at RT with gentle agitation. After centrifugation of the cells at 1000 g for 10 min at RT and removal of the supernatant, the pellet was frozen at -80 °C until usage.

Co-immunoprecipitation
Crosslinked or non-crosslinked sample pellets were thawed on ice. Parasites were lysed in 1-4 ml RIPA buffer (50 mM Tris-HCl, pH 8, 150 mM NaCl, 1% NP-40, 0.5% sodium deoxycholate, 0.1% SDS) freshly supplemented with 1 mM DTT (Dithiothreitol) and 1x protease inhibitor (Halt™ Protease Inhibitor Cocktail, 78430, Thermo Fisher Scientific) for a minimum of 30 min on ice. Parasites were mechanically homogenized on ice by passing the lysate 10 times through a needle (0.3 mm diameter) attached to a syringe. 60 µl of the lysed sample ("whole-cell lysate") were saved for Western blot analysis. Therefore, 20 µl NuPAGE™ LDS Sample Buffer (4X) (NP0007, invitrogen) supplemented with 200 mM DTT and 20% β-mercaptoethanol were added (final concentrations are 50 mM and 5%, respectively) and the sample stored at -20 °C. Afterwards, crosslinked samples were sonicated using the Bioruptor® Pico sonication system (B01060003, diagenode) with 30 sec sonication, 30 sec break, 20 cycles in total. The samples were centrifuged at maximum speed (21130 rcf) for 15-30 min at 4 °C. After centrifugation, 60 µl of the supernatant ("input") were supplemented with NuPAGE™ LDS Sample Buffer and frozen for later Western blot analysis as described before.
Per sample, 100 µl Dynabeads™ Protein G for Immunoprecipitation (magnetic, 10003D, invitrogen) were washed twice in 1 ml 0.01% Tween-20/PBS in a magnetic rack and resuspended in 500 µl 0.01% Tween-20/PBS. Beads were incubated with 7 µg mouse anti-GFP antibody (11814460001, Roche) (per 100 µl beads) for at least 10 min

on RT, rotating, to allow binding of antibodies to protein G on the Dynabead surface. Afterwards, beads were washed twice with 1 ml 0.1% Tween-20/PBS, followed by washing the beads once in 1 ml RIPA buffer and resuspending in 100 µl RIPA buffer per 100 µl beads. Dynabeads were transferred into sample supernatants. PfCentrin1- and PfCentrin2-GFP were allowed to bind to GFP-antibody-coupled Dynabeads over night at 4 °C, rotating.

On the next day, 60 µl of the supernatant ("flow-through") were saved for Western blot analysis, as described before. Afterwards, the bead pellets were washed 3-5 times on ice with 1 ml RIPA buffer freshly supplemented with protease inhibitors, but without addition of DTT, followed by another two washes on ice in 1 ml PBS supplemented with protease inhibitors. Again, 60 µl of the sample with beads ("eluate") were saved, prepared for Western blot analysis as described above, followed by removal of the beads. SDS-PAGE and Western blot analysis were performed as described in subsection 4.2.15. Samples on magnetic beads were stored at 4 °C and were soon passed to the proteomics facility for mass spectrometry analysis (subsection 4.2.17).

4.2.17 Mass spectrometry analysis

After immunoprecipitation (subsection 4.2.16), all following steps for protein identification via mass spectrometry analysis were performed by the Proteomics Core Facility, Faculty of Medicine, University of Geneva, Switzerland.

Sample preparation
Samples with beads were resuspended in 100 µl 6 M Urea in 50 mM ammonium bicarbonate (AB) and incubated with 2 µl of 50 mM reducing agent dithioerythritol (DTE) in destilled water for 1 h at 37 °C. Next, the sample was incubated with 2 µl of 400 mM alkylating agent iodoacetamide (in destilled water) for 1 h at RT in the dark. To reduce the urea concentration to 1 M, 500 µl of 50 mM AB were added and protein digestion was performed with 7 µl of freshly prepared 0.1 µg/µl trypsin (Promega) in 50 mM AB over night at 37 °C. Supernatants were collected, dried completely under speed-vacuum and desalted using a C18 microspin column (Harvard Apparatus, Holliston, MA, USA) according to manufacturer's instructions. The samples were dried completely using speed-vacuum and stored at -20 °C until mass spectrometry.

Liquid chromatography-electrospray ionization-tandem mass spectrometry (LC-ESI-MS/MS)
Samples were redissolved in 20 µl loading buffer (5% acetonitrile, 0.1% formic acid) and 2 µl were injected on column. LC-ESI-MS/MS was performed on a Q-Exactive HF Hybrid Quadrupole-Orbitrap Mass Spectrometer (Thermo Scientific) equipped with an Easy nLC 1000 liquid chromatography system (Thermo Scientific). Peptides were trapped on a Acclaim pepmap100, C18, 3 µm, 75 µm x 20 mm nano trap-column (Thermo Scientific) and subsequently separated on a 75 µm x 250 mm, C18, 2 µm, 100 Å Easy-Spray column (Thermo Scientific). The analytical separation was run at a constant flow rate of 250 nl/min for a total time of 90 min. Therefore, a gradient of

99.9% H_2O/ 0.1% formic acid (solvent A) and 99.9% acetonitrile/0.1% formic acid (solvent B) was used, with 0-5 min 95% solvent A and 5% solvent B; 65% solvent A and 35% solvent B for 60 min; 10% solvent A and 90% solvent B for 10 min. The separation finished with a 15 min stay in 10% solvent A and 90% solvent B. The full scan resolution was set to 60'000 full width at half maximum (FWHM) at a mass/charge (m/z) ratio of 200 with an automatic gain control (AGC) target of $3x10^6$ (number of ions) and a maximum injection time of 60 ms. Mass range window was set to 400-2000 m/z. For MS2 data-dependent acquisition, up to twenty precursor ions were isolated and fragmented by higher-energy collisional dissociation (HCD) at 27% Normalized Collision Energy (NCE). Resolution for MS2 scans was set to a FWHM of 15'000 at 200 m/z and an AGC target of $1x10^5$ with a maximum injection time of 60 ms and an isolation window set to 1.6 m/z. Full MS scans were acquired in profile mode, MS2 scans in centroid mode. Dynamic exclusion was set to 20 sec.

Database search

Using the MS Convert conversion tool (ProteoWizard), peak lists were generated from the raw data. Subsequently, the peak lists were searched against the *Plasmodium falciparum* 3D7 database (PlasmoDB.org, release 46, 5548 entries) as well as an in-house database with common contaminants using Mascot (Matrix Science, London, UK; version 2.5.1). For the database search, one potential missed cleavage of the trypsin enzyme was allowed. The precursor ion tolerance was set to 10 ppm and fragment ion tolerance to 0.02 Da. Carbamidomethyl cysteine was set as fixed amino acid modification. Variable amino acid modifications included oxidized methionine and deamination as well as phosphorylated serine, threonine and tyrosine. To validate the Mascot search, Scaffold 4.10.0 (Proteome Software) was used. Peptide identifications were accepted if they could be established at greater than 13.0% (44.0% for replicate) probability to achieve an FDR less than 0.1% using the Peptide Prophet algorithm (Keller et al., 2002) with Scaffold delta-mass correction. To accept protein identifications, they had to be established at greater than 87.0% (99.0% for replicate) probability to achieve an FDR less than 1.0% and they had to contain at least two identified peptides. Protein probabilities were assigned by the Protein Prophet algorithm (Nesvizhskii et al., 2003). Proteins that contained similar peptides and could not be differentiated based on MS/MS analysis alone were grouped to satisfy the principles of parsimony.

4.2.18 Growth assays

To test whether there is a growth defect in asexual blood stages in the cell lines 3D7 Slp-GFP_glmS (GOI 08) and 3D7 PF3D7_1427900-GFP_glmS (GOI 06) upon induced knockdown of the glmS-tagged centrosomal candidate genes via addition of 3.5 mM GlcN, parasitemia was assessed over six days (3 cycles) using flow cytometry. Growth assays were performed by Marta Machado and Tatiany Romão. Therefore, 3D7 Slp-GFP_glmS and 3D7 PF3D7_1427900-GFP_glmS parasite cultures as well

as a 3D7 wt control line were synchronized using sorbitol treatment. The growth assay was started with a parasitemia of 0.025% early ring stages. Each cell line was cultured at a hematocrit of 4.2% in two wells of a 6-well plate without (control) and with addition of 3.5 mM GlcN, respectively. For optimal growth conditions, culture medium was changed in the cultures after 48 h, 96 h and 120 h. To determine the parasitemia via flow cytometry, 100 µl samples were taken in triplicates every 24 h after start of drug treatment for three asexual blood-stage cycles (0 h, 24 h, 48 h, 72 h, 96 h, 120 h and 144 h). Samples were collected and centrifuged in a 96-well U-bottom plate (1500 g, 2 min), the pellets washed once with 200 µl PBS each, and the cells were fixed with 100 µl 0.0075% glutaraldehyde (GA) in 4% PFA/PBS either 45 min at room temperature or over night at 4 °C. Next, cells were washed twice with 200 µl PBS (per well) and stored at 4 °C until all samples at the different time points were collected. 100 µl of each well were transferred into a new 96-well plate, and centrifuged at 1500 g for 2 min. Cells were permeabilized with 0.1% Triton-X-100/PBS for 8 min at room temperature, followed by centrifugation at 1500 g for 2 min. Pellets were washed once with 200 µl PBS, pelleted again by centrifugation (1500 g, 2 min) and DNA was stained with 100 µl of a 1:2000 dilution of SYBR™ Green I Nucleic Acid Gel Stain (S7567, Invitrogen) in PBS for 20 min at room temperature, in the dark. Samples were again pelleted (1500 g, 2 min), washed once with 200 µl PBS/well and resuspended in 200 µl PBS.
Flow cytometry analysis was performed on a BD FACSCelesta™ Cell Analyzer (BD Biosciences). Gating of the acquired cells was performed using FlowJo (Tree Star). Therefore, all RBCs were selected, all doublets excluded, and finally infected RBCs were selected by green fluorescence of the nucleic acid staining using a 525 nm laser. In total, 500-1000 events (infected RBCs) were acquired per sample. Visualization and statistical analyses were performed using GraphPad PRISM (GraphPad).

References

S. Absalon, J. A. Robbins, and J. D. Dvorin. An essential malaria protein defines the architecture of blood-stage and transmission-stage parasites. *Nature communications*, 7(1):1–11, 2016.

N. R. Ader and W. Kukulski. triCLEM: Combining high-precision, room temperature CLEM with cryo-fluorescence microscopy to identify very rare events. *Methods in cell biology*, 140:303–320, 2017.

R. Aguilar, A. Magallon-Tejada, A. H. Achtman, C. Moraleda, R. Joice, P. Cisteró, C. S. Li Wai Suen, A. Nhabomba, E. Macete, I. Mueller, M. Marti, P. L. Alonso, C. Menéndez, L. Schofield, and A. Mayor. Molecular evidence for the localization of Plasmodium falciparum immature gametocytes in bone marrow. *Blood, the journal of the american society of hematology*, 123(7):959–966, 2014.

M. Ahmed and J. Cox-Singh. Plasmodium knowlesi – an emerging pathogen. *ISBT science series*, 10(S1):134–140, 2015.

M. Aikawa and R. L. Beaudoin. Studies on nuclear division of a malarial parasite under pyrimethamine treatment. *The journal of cell biology*, 39(3):749, 1968.

M. Aikawa, C. G. Huff, and H. Sprinz. Fine structure of the asexual stages of Plasmodium elongatum. *The journal of cell biology*, 34(1):229–249, 1967.

A. Akhmanova and M. O. Steinmetz. Microtubule minus-end regulation at a glance. *Journal of cell science*, 132(11): jcs227850, 2019.

R. Amino, S. Thiberge, B. Martin, S. Celli, S. Shorte, F. Frischknecht, and R. Ménard. Quantitative imaging of Plasmodium transmission from mosquito to mammal. *Nature medicine*, 12(2):220–224, 2006.

J. S. Andersen, C. J. Wilkinson, T. Mayor, P. Mortensen, E. A. Nigg, and M. Mann. Proteomic characterization of the human centrosome by protein correlation profiling. *Nature*, 426(6966):570–574, 2003.

D. Arnot and K. Gull. The Plasmodium cell-cycle: facts and questions. *Annals of tropical medicine and parasitology*, 92 (4):361–365, 1998.

D. E. Arnot, E. Ronander, and D. C. Bengtsson. The progression of the intra-erythrocytic cell cycle of Plasmodium falciparum and the role of the centriolar plaques in asynchronous mitotic division during schizogony. *International journal for parasitology*, 41(1):71–80, 2011.

N. Arora, L. C. Anbalagan, and A. K. Pannu. Towards eradication of malaria: Is the WHO's RTS, S/AS01 vaccination effective enough? *Risk management and healthcare policy*, 14:1033, 2021.

D. Balasubramanian, C. M. Rao, and B. Panijpan. The malaria parasite monitored by photoacoustic spectroscopy. *Science*, 223(4638):828–830, 1984.

A. C. Balestra, M. Zeeshan, E. Rea, C. Pasquarello, L. Brusini, T. Mourier, A. K. Subudhi, N. Klages, P. Arboit, R. Pandey, D. Brady, S. Vaughan, A. A. Holder, A. Pain, D. J. Ferguson, A. Hainard, R. Tewari, and M. Brochet. A divergent cyclin/cyclin-dependent kinase complex controls the atypical replication of a malaria parasite during gametogony and transmission. *Elife*, 9:e56474, 2020.

L. H. Bannister, J. M. Hopkins, R. E. Fowler, S. Krishna, and G. H. Mitchell. A brief illustrated guide to the ultrastructure of Plasmodium falciparum asexual blood stages. *Parasitology today*, 16(10):427–433, 2000a.

L. H. Bannister, J. M. Hopkins, R. E. Fowler, S. Krishna, and G. H. Mitchell. Ultrastructure of rhoptry development in Plasmodium falciparum erythrocytic schizonts. *Parasitology*, 121(3):273–287, 2000b.

K. J. Barnum and M. J. O'Connell. Cell cycle regulation by checkpoints. In *Cell cycle control*, pages 29–40. Springer, 2014.

P. Baum, C. Furlong, and B. Byers. Yeast gene required for spindle pole body duplication: homology of its product with Ca2+-binding proteins. *Proceedings of the national academy of sciences*, 83(15):5512–5516, 1986.

J. C. Beier. Malaria parasite development in mosquitoes. *Annual review of entomology*, 43(1):519–543, 1998.

E. Bertiaux, A. C. Balestra, L. Bournonville, V. Louvel, B. Maco, D. Soldati-Favre, M. Brochet, P. Guichard, and V. Hamel. Expansion microscopy provides new insights into the cytoskeleton of malaria parasites including the conservation of a conoid. *PLoS biology*, 19(3):e3001020, 2021.

O. Billker, M. K. Shaw, G. Margos, and R. E. Sinden. The roles of temperature, pH and mosquito factors as triggers of male and female gametogenesis of Plasmodium berghei in vitro. *Parasitology*, 115(1):1–7, 1997.

Biomedical Electron Microscopy Unit, University of Liverpool. Liverpool, United Kingdom. URL `https://www.liverpool.ac.uk/media/livacuk/emunit/centrosome,cell.jpg`.

J. Birnbaum, S. Flemming, N. Reichard, A. B. Soares, P. Mesén-Ramírez, E. Jonscher, B. Bergmann, and T. Spielmann. A genetic system to study Plasmodium falciparum protein function. *Nature methods*, 14(4):450–456, 2017.

J. Birnbaum, S. Scharf, S. Schmidt, E. Jonscher, W. A. M. Hoeijmakers, S. Flemming, C. G. Toenhake, M. Schmitt, R. Sabitzki, B. Bergmann, U. Fröhlke, P. Mesén-Ramírez, A. Blancke Soares, H. Herrmann, R. Bártfai, and T. Spielmann. A Kelch13-defined endocytosis pathway mediates artemisinin resistance in malaria parasites. *Science*, 367 (6473):51–59, 2020.

T. Blisnick, M. E. M. Betoulle, J.-C. Barale, P. Uzureau, L. Berry, S. Desroses, H. Fujioka, D. Mattei, and C. B. Breton. Pfsbp1, a Maurer's cleft Plasmodium falciparum protein, is associated with the erythrocyte skeleton. *Molecular and biochemical parasitology*, 111(1):107–121, 2000.

B. Boettcher and Y. Barral. The cell biology of open and closed mitosis. *Nucleus*, 4(3):160–165, 2013.

I. Bouhlel, M. Laporte, E. Bertiaux, A. Giroud, S. Borgers, J. Azimzadeh, M. Borneans, P. Guichard, A. Paoletti, and V. Hamel. Sfi1 and centrin form a distal end complex critical for proper centriole architecture and ciliogenesis. *bioRxiv*, 2021.

C. Brémard, J. Girerd, P. Kowalewski, J. Merlin, and S. Moreau. Spectroscopic investigations of malaria pigment. *Applied spectroscopy*, 47(11):1837–1842, 1993.

J. Broichhagen and N. Kilian. Chemical biology tools to investigate malaria parasites. *ChemBioChem*, 2021.

G. J. Brouhard. Dynamic instability 30 years later: complexities in microtubule growth and catastrophe. *Molecular biology of the cell*, 26(7):1207–1210, 2015.

J. Bucevičius, J. Keller-Findeisen, T. Gilat, S. W. Hell, and G. Lukinavičius. Rhodamine–Hoechst positional isomers for highly efficient staining of heterochromatin. *Chemical science*, 10(7):1962–1970, 2019.

E. Bullitt, M. P. Rout, J. V. Kilmartin, and C. W. Akey. The yeast spindle pole body is assembled around a central crystal of Spc42p. *Cell*, 89(7):1077–1086, 1997.

P.-C. Burda, M. Schaffner, G. Kaiser, M. Roques, B. Zuber, and V. T. Heussler. A Plasmodium plasma membrane reporter reveals membrane dynamics by live-cell microscopy. *Scientific reports*, 7(1):1–14, 2017.

S. Burns, J. S. Avena, J. R. Unruh, Z. Yu, S. E. Smith, B. D. Slaughter, M. Winey, and S. L. Jaspersen. Structured illumination with particle averaging reveals novel roles for yeast centrosome components during duplication. *Elife*, 4:e08586, 2015.

B. Byers and L. Goetsch. Behavior of spindles and spindle plaques in the cell cycle and conjugation of Saccharomyces cerevisiae. *Journal of bacteriology*, 124(1):511–523, 1975.

C. Cai, K. A. Carey, D. A. Nedosekin, Y. A. Menyaev, M. Sarimollaoglu, E. I. Galanzha, J. S. Stumhofer, and V. P. Zharov. In vivo photoacoustic flow cytometry for early malaria diagnosis. *Cytometry part a*, 89(6):531–542, 2016.

A. Campbell. Synchronization of cell division. *Bacteriological reviews*, 21(4):263–272, 1957.

E. U. Canning and R. E. Sinden. The organization of the ookinete and observations on nuclear division in oocysts of Plasmodium berghei. *Parasitology*, 67(1):29–40, 1973.

J. G. Carlton, H. Jones, and U. S. Eggert. Membrane and organelle dynamics during cell division. *Nature reviews molecular cell biology*, 21(3):151–166, 2020.

V. Carter, A. M. Nacer, A. Underhill, R. E. Sinden, and H. Hurd. Minimum requirements for ookinete to oocyst transformation in Plasmodium. *International journal for parasitology*, 37(11):1221–1232, 2007.

T. G. Carvalho, C. Doerig, and L. Reininger. Nima-and Aurora-related kinases of malaria parasites. *Biochimica et biophysica acta (BBA)-proteins and proteomics*, 1834(7):1336–1345, 2013.

S. Castagnetti, S. Oliferenko, and P. Nurse. Fission yeast cells undergo nuclear division in the absence of spindle microtubules. *PLoS biology*, 8(10):e1000512, 2010.

A. M. Cavanaugh and S. L. Jaspersen. Big lessons from little yeast: budding and fission yeast centrosome structure, duplication, and function. *Annual review of genetics*, 51:361–383, 2017.

B.-C. Chen, W. R. Legant, K. Wang, L. Shao, D. E. Milkie, M. W. Davidson, C. Janetopoulos, X. S. Wu, J. A. Hammer, Z. Liu, B. P. English, Y. Mimori-Kiyosue, D. P. Romero, A. T. Ritter, J. Lippincott-Schwartz, L. Fritz-Laylin, R. D. Mullins, D. M. Mitchell, J. N. Bembenek, A.-C. Reymann, R. Böhme, S. W. Grill, J. T. Wang, G. Seydoux, U. S. Tulu, D. P. Kiehart, and E. Betzig. Lattice light-sheet microscopy: imaging molecules to embryos at high spatiotemporal resolution. *Science*, 346(6208), 2014.

F. Chen, P. W. Tillberg, and E. S. Boyden. Expansion microscopy. *Science*, 347(6221):543–548, 2015.

K. N. Choe and G.-L. Moldovan. Forging ahead through darkness: PCNA, still the principal conductor at the replication fork. *Molecular cell*, 65(3):380–392, 2017.

P. T. Conduit, A. Wainman, and J. W. Raff. Centrosome function and assembly in animal cells. *Nature reviews molecular cell biology*, 16(10):611–624, 2015.

S. V. Connelly, J. Manzella-Lapeira, Z. C. Levine, J. Brzostowski, L. Krymskaya, R. S. Rahman, A. C. Ellis, S. N. Amin, J. M. Sá, and T. E. Wellems. Restructured mitochondrial-nuclear interaction in Plasmodium falciparum dormancy and persister survival after artemisinin exposure. *Mbio*, 12(3):e00753–21, 2021.

L. M. Coronado, C. T. Nadovich, and C. Spadafora. Malarial hemozoin: from target to tool. *Biochimica et biophysica acta (BBA)-general subjects*, 1840(6):2032–2041, 2014.

A. F. Cowman, C. J. Tonkin, W.-H. Tham, and M. T. Duraisingh. The molecular basis of erythrocyte invasion by malaria parasites. *Cell host & microbe*, 22(2):232–245, 2017.

F. E. Cox. History of the discovery of the malaria parasites and their vectors. *Parasites & vectors*, 3(1):1–9, 2010.

M. Cyrklaff, C. P. Sanchez, N. Kilian, C. Bisseye, J. Simpore, F. Frischknecht, and M. Lanzer. Hemoglobins S and C interfere with actin remodeling in Plasmodium falciparum–infected erythrocytes. *Science*, 334(6060):1283–1286, 2011.

N. Dahan-Pasternak, A. Nasereddin, N. Kolevzon, M. Pe'er, W. Wong, V. Shinder, L. Turnbull, C. B. Whitchurch, M. Elbaum, T. W. Gilberger, E. Yavin, J. Baum, and R. Dzikowski. Pfsec13 is an unusual chromatin-associated nucleoporin of Plasmodium falciparum that is essential for parasite proliferation in human erythrocytes. *Journal of cell science*, 126(14):3055–3069, 2013.

T. J. Dantas, Y. Wang, P. Lalor, P. Dockery, and C. G. Morrison. Defective nucleotide excision repair with normal centrosome structures and functions in the absence of all vertebrate centrins. *Journal of cell biology*, 193(2):307–318, 2011.

T. J. Dantas, O. M. Daly, and C. G. Morrison. Such small hands: the roles of centrins/caltractins in the centriole and in genome maintenance. *Cellular and molecular life sciences*, 69(18):2979–2997, 2012.

P. K. Davis, A. Ho, and S. F. Dowdy. Biological methods for cell-cycle synchronization of mammalian cells. *Biotechniques*, 30(6):1322–1331, 2001.

P. De Boer, J. P. Hoogenboom, and B. N. Giepmans. Correlated light and electron microscopy: ultrastructure lights up! *Nature methods*, 12(6):503–513, 2015.

E. De Harven. Early observations of centrioles and mitotic spindle fibers by transmission electron microscopy. *Biology of the cell*, 80(2-3):107–109, 1994.

M. De Niz, P.-C. Burda, G. Kaiser, H. A. Del Portillo, T. Spielmann, F. Frischknecht, and V. T. Heussler. Progress in imaging methods: insights gained into Plasmodium biology. *Nature reviews microbiology*, 15(1):37–54, 2017.

C. Delves, R. Ridley, M. Goman, S. Holloway, J. Hyde, and J. Scaife. Cloning of a β-tubulin gene from Plasmodium falciparum. *Molecular microbiology*, 3(11):1511–1519, 1989.

C. J. Delves, P. Alano, R. G. Ridley, M. Goman, S. P. Holloway, J. E. Hyde, and J. G. Scaife. Expression of α and β tubulin genes during the asexual and sexual blood stages of Plasmodium falciparum. *Molecular and biochemical parasitology*, 43(2):271–278, 1990.

A. Desai and T. J. Mitchison. Microtubule polymerization dynamics. *Annual review of cell and developmental biology*, 13(1):83–117, 1997.

G. Dey, S. Culley, S. Curran, U. Schmidt, R. Henriques, W. Kukulski, and B. Baum. Closed mitosis requires local disassembly of the nuclear envelope. *Nature*, 585(7823):119–123, 2020.

M. Diehl, S. Weber, M. Cyrklaff, C. P. Sanchez, C. A. Beretta, L. Roling, C. S. Simon, J. Guizetti, M. P. Mayer, and J. M. Przyborski. Co-chaperone involvement in knob biogenesis implicates host-derived chaperones in malaria virulence. *bioRxiv*, 2021.

R. Ding, R. R. West, D. Morphew, B. R. Oakley, and J. R. McIntosh. The spindle pole body of Schizosaccharomyces pombe enters and leaves the nuclear envelope as the cell cycle proceeds. *Molecular biology of the cell*, 8(8):1461–1479, 1997.

C. Doerig, J. Endicott, and D. Chakrabarti. Cyclin-dependent kinase homologues of Plasmodium falciparum. *International journal for parasitology*, 32(13):1575–1585, 2002.

D. Dorin-Semblat, A. Sicard, C. Doerig, L. Ranford-Cartwright, and C. Doerig. Disruption of the Pf PK7 gene impairs schizogony and sporogony in the human malaria parasite Plasmodium falciparum. *Eukaryotic cell*, 7(2): 279–285, 2008.

H. G. Elmendorf and K. Haldar. Plasmodium falciparum exports the Golgi marker sphingomyelin synthase into a tubovesicular network in the cytoplasm of mature erythrocytes. *The journal of cell biology*, 124(4):449–462, 1994.

R. S. Erdmann, S. W. Baguley, J. H. Richens, R. F. Wissner, Z. Xi, E. S. Allgeyer, S. Zhong, A. D. Thompson, N. Lowe, R. Butler, J. Bewersdorf, J. E. Rothman, D. St Johnston, A. Schepartz, and D. Toomre. Labeling strategies matter for super-resolution microscopy: a comparison between HaloTags and SNAP-tags. *Cell chemical biology*, 26(4): 584–592, 2019.

S. Eshar, N. Dahan-Pasternak, A. Weiner, and R. Dzikowski. High resolution 3D perspective of Plasmodium biology: advancing into a new era. *Trends in parasitology*, 27(12):548–554, 2011.

H. Fang, N. Klages, B. Baechler, E. Hillner, L. Yu, M. Pardo, J. Choudhary, and M. Brochet. Multiple short windows of calcium-dependent protein kinase 4 activity coordinate distinct cell cycle events during Plasmodium gametogenesis. *Elife*, 6:e26524, 2017.

E. L. Faulkner, S. G. Thomas, and R. K. Neely. An introduction to the methodology of expansion microscopy. *The international journal of biochemistry & cell biology*, 124:105764, 2020.

B. Fennell, Z. Al-Shatr, and A. Bell. Isotype expression, post-translational modification and stage-dependent production of tubulins in erythrocytic Plasmodium falciparum. *International journal for parasitology*, 38(5):527–539, 2008.

B. J. Fennell, J. A. Naughton, E. Dempsey, and A. Bell. Cellular and molecular actions of dinitroaniline and phosphorothioamidate herbicides on Plasmodium falciparum: tubulin as a specific antimalarial target. *Molecular and biochemical parasitology*, 145(2):226–238, 2006.

D. J. Ferguson, N. Sahoo, R. A. Pinches, J. M. Bumstead, F. M. Tomley, and M.-J. Gubbels. Morn1 has a conserved role in asexual and sexual development across the apicomplexa. *Eukaryotic cell*, 7(4):698–711, 2008.

H. A. Fisk, C. P. Mattison, and M. Winey. Centrosomes and tumour suppressors. *Current opinion in cell biology*, 14 (6):700–705, 2002.

R. Fowler, R. Fookes, F. Lavin, L. Bannister, and G. Mitchell. Microtubules in Plasmodium falciparum merozoites and their importance for invasion of erythrocytes. *Parasitology*, 117(5):425–433, 1998.

R. E. Fowler, A. M. Smith, J. Whitehorn, I. T. Williams, L. H. Bannister, and G. H. Mitchell. Microtubule associated motor proteins of Plasmodium falciparum merozoites. *Molecular and biochemical parasitology*, 117(2):187–200, 2001.

M. E. Francia and B. Striepen. Cell division in apicomplexan parasites. *Nature reviews microbiology*, 12(2):125–136, 2014.

M. E. Francia, J.-F. Dubremetz, and N. S. Morrissette. Basal body structure and composition in the apicomplexans Toxoplasma and Plasmodium. *Cilia*, 5(1):1–7, 2015.

U. Frevert, S. Engelmann, S. Zougbédé, J. Stange, B. Ng, K. Matuschewski, L. Liebes, and H. Yee. Intravital observation of Plasmodium berghei sporozoite infection of the liver. *PLoS biology*, 3(6):e192, 2005.

F. Frischknecht, P. Baldacci, B. Martin, C. Zimmer, S. Thiberge, J.-C. Olivo-Marin, S. L. Shorte, and R. Ménard. Imaging movement of malaria parasites during transmission by Anopheles mosquitoes. *Cellular microbiology*, 6 (7):687–694, 2004.

J. Fu, I. M. Hagan, and D. M. Glover. The centrosome and its duplication cycle. *Cold Spring Harbor perspectives in biology*, 7(2):a015800, 2015.

Z. Fu, D. Peng, M. Zhang, F. Xue, R. Zhang, W. He, T. Xu, and P. Xu. mEosEM withstands osmium staining and Epon embedding for super-resolution CLEM. *Nature methods*, 17(1):55–58, 2020.

C. Funaya, S. Samarasinghe, S. Pruggnaller, M. Ohta, Y. Connolly, J. Müller, H. Murakami, A. Grallert, M. Yamamoto, D. Smith, C. Antony, and K. Tanaka. Transient structure associated with the spindle pole body directs meiotic microtubule reorganization in S. pombe. *Current biology*, 22(7):562–574, 2012.

S. Gadde and R. Heald. Mechanisms and molecules of the mitotic spindle. *Current biology*, 14(18):R797–R805, 2004.

D. Gambarotto, F. U. Zwettler, M. Le Guennec, M. Schmidt-Cernohorska, D. Fortun, S. Borgers, J. Heine, J.-G. Schloetel, M. Reuss, M. Unser, E. S. Boyden, M. Sauer, V. Hamel, and P. Guichard. Imaging cellular ultrastructures using expansion microscopy (U-ExM). *Nature methods*, 16(1):71–74, 2019.

D. Gambarotto, V. Hamel, and P. Guichard. Ultrastructure expansion microscopy (U-ExM). In *Methods in cell biology*, volume 161, pages 57–81. Elsevier, 2021.

M. Ganter and F. Frischknecht. Illuminating Plasmodium invasion by lattice-light-sheet microscopy. *Trends in parasitology*, 37(9):777–779, 2021.

M. Ganter, J. M. Goldberg, J. D. Dvorin, J. A. Paulo, J. G. King, A. K. Tripathi, A. S. Paul, J. Yang, I. Coppens, R. H. Jiang, B. Elsworth, D. A. Baker, R. R. Dinglasan, S. P. Gygi, and M. T. Duraisingh. Plasmodium falciparum CRK4 directs continuous rounds of DNA replication during schizogony. *Nature microbiology*, 2(5):1–9, 2017.

C. R. Garcia, R. P. Markus, and L. Madeira. Tertian and quartan fevers: temporal regulation in malarial infection. *Journal of biological rhythms*, 16(5):436–443, 2001.

G. E. Garcia, R. A. Wirtz, J. R. Barr, A. Woolfitt, and R. Rosenberg. Xanthurenic acid induces gametogenesis in Plasmodium, the malaria parasite. *Journal of biological chemistry*, 273(20):12003–12005, 1998.

S. Garg, S. Agarwal, S. Dabral, N. Kumar, S. Sehrawat, and S. Singh. Visualization and quantification of Plasmodium falciparum intraerythrocytic merozoites. *Systems and synthetic biology*, 9(1):23–26, 2015.

P. C. C. Garnham, R. G. Bird, and J. R. Baker. Electron microscope studies of motile stages of malaria parasites. V. Exflagellation in Plasmodium, Hepatocystis and Leucocytozoon. *Transactions of the royal society of tropical medicine and hygiene*, 61(1):58–68, 1967.

P. C. C. Garnham, R. G. Bird, J. R. Baker, S. S. Desser, and H. M. S. El-Nahal. Electron microscope studies on motile stages of malaria parasites VI. The oökinete of Plasmodium berghei yoelii and its transformation into the early oocyst. *Transactions of the royal society of tropical medicine and hygiene*, 63(2):187–194, 1969.

O. Gavet, C. Alvarez, P. Gaspar, and M. Bornens. Centrin4p, a novel mammalian centrin specifically expressed in ciliated cells. *Molecular biology of the cell*, 14(5):1818–1834, 2003.

N. D. Geoghegan, C. Evelyn, L. W. Whitehead, M. Pasternak, P. McDonald, T. Triglia, D. S. Marapana, D. Kempe, J. K. Thompson, M. J. Mlodzianoski, J. Healer, M. Biro, A. F. Cowman, and K. L. Rogers. 4D analysis of malaria parasite invasion offers insights into erythrocyte membrane remodeling and parasitophorous vacuole formation. *Nature communications*, 12(1):1–16, 2021.

N. Gerald, B. Mahajan, and S. Kumar. Mitosis in the human malaria parasite Plasmodium falciparum. *Eukaryotic cell*, 10(4):474–482, 2011.

R. Gibeaux, C. Lang, A. Z. Politi, S. L. Jaspersen, P. Philippsen, and C. Antony. Electron tomography of the microtubule cytoskeleton in multinucleated hyphae of Ashbya gossypii. *Journal of cell science*, 125(23):5830–5839, 2012.

D. G. Gibson, L. Young, R.-Y. Chuang, J. C. Venter, C. A. Hutchison, and H. O. Smith. Enzymatic assembly of DNA molecules up to several hundred kilobases. *Nature methods*, 6(5):343–345, 2009.

P. R. Gilson and B. S. Crabb. Morphology and kinetics of the three distinct phases of red blood cell invasion by Plasmodium falciparum merozoites. *International journal for parasitology*, 39(1):91–96, 2009.

B. Goldenson and J. D. Crispino. The aurora kinases in cell cycle and leukemia. *Oncogene*, 34(5):537–545, 2015.

G. Goshima and J. M. Scholey. Control of mitotic spindle length. *Annual review of cell and developmental biology*, 26: 21–57, 2010.

R. Gräf, M. Grafe, I. Meyer, K. Mitic, and V. Pitzen. The Dictyostelium centrosome. *Cells*, 10(10):2657, 2021.

C. Grüring and T. Spielmann. Imaging of live malaria blood stage parasites. *Methods in enzymology*, 506:81–92, 2012.

C. Grüring, A. Heiber, F. Kruse, J. Ungefehr, T.-W. Gilberger, and T. Spielmann. Development and host cell modifications of Plasmodium falciparum blood stages in four dimensions. *Nature communications*, 2(1):1–11, 2011.

M.-J. Gubbels, S. Vaishnava, N. Boot, J.-F. Dubremetz, and B. Striepen. A MORN-repeat protein is a dynamic component of the Toxoplasma gondii cell division apparatus. *Journal of cell science*, 119(11):2236–2245, 2006.

J. Guizetti, R. M. Martins, S. Guadagnini, A. Claes, and A. Scherf. Nuclear pores and perinuclear expression sites of var and ribosomal DNA genes correspond to physically distinct regions in Plasmodium falciparum. *Eukaryotic cell*, 12(5):697–702, 2013.

K. Günther, M. Tümmler, H.-H. Arnold, R. Ridley, M. Goman, J. G. Scaife, and K. Lingelbach. An exported protein of Plasmodium falciparum is synthesized as an integral membrane protein. *Molecular and biochemical parasitology*, 46(1):149–157, 1991.

M. K. Gupta, M. Agarawal, K. Banu, K. S. Reddy, D. Gaur, and S. K. Dhar. Role of chromatin assembly factor 1 in DNA replication of Plasmodium falciparum. *Biochemical and biophysical research communications*, 495(1):1285–1291, 2018.

V. L. Hale, J. M. Watermeyer, F. Hackett, G. Vizcay-Barrena, C. Van Ooij, J. A. Thomas, M. C. Spink, M. Harkiolaki, E. Duke, R. A. Fleck, M. J. Blackman, and H. R. Saibil. Parasitophorous vacuole poration precedes its rupture and rapid host erythrocyte cytoskeleton collapse in Plasmodium falciparum egress. *Proceedings of the national academy of sciences*, 114(13):3439–3444, 2017.

E. Hanssen, R. Sougrat, S. Frankland, S. Deed, N. Klonis, J. Lippincott-Schwartz, and L. Tilley. Electron tomography of the Maurer's cleft organelles of Plasmodium falciparum-infected erythrocytes reveals novel structural features. *Molecular microbiology*, 67(4):703–718, 2008.

C. R. Harding and M. Meissner. The inner membrane complex through development of Toxoplasma gondii and Plasmodium. *Cellular microbiology*, 16(5):632–641, 2014.

B. Harke, C. K. Ullal, J. Keller, and S. W. Hell. Three-dimensional nanoscopy of colloidal crystals. *Nano letters*, 8(5): 1309–1313, 2008.

P. E. Hart, J. N. Glantz, J. D. Orth, G. M. Poynter, and J. L. Salisbury. Testis-specific murine centrin, Cetn1: genomic characterization and evidence for retroposition of a gene encoding a centrosome protein. *Genomics*, 60(2):111–120, 1999.

F. Hawking. The clock of the malaria parasite. *Scientific American*, 222(6):123–131, 1970.

J. H. Hayden, S. S. Bowser, and C. L. Rieder. Kinetochores capture astral microtubules during chromosome attachment to the mitotic spindle: direct visualization in live newt lung cells. *The journal of cell biology*, 111(3):1039–1045, 1990.

R. Heald and A. Khodjakov. Thirty years of search and capture: The complex simplicity of mitotic spindle assembly. *Journal of cell biology*, 211(6):1103–1111, 2015.

J. Heine, M. Reuss, B. Harke, E. D'Este, S. J. Sahl, and S. W. Hell. Adaptive-illumination STED nanoscopy. *Proceedings of the national academy of sciences*, 114(37):9797–9802, 2017.

R. Heintzmann and T. Huser. Super-resolution structured illumination microscopy. *Chemical reviews*, 117(23):13890–13908, 2017.

S. W. Hell. Toward fluorescence nanoscopy. *Nature biotechnology*, 21(11):1347–1355, 2003.

E. H. Hinchcliffe, F. J. Miller, M. Cham, A. Khodjakov, and G. Sluder. Requirement of a centrosomal activity for cell cycle progression through G1 into S phase. *Science*, 291(5508):1547–1550, 2001.

W. G. Hirst, D. Fachet, B. Kuropka, C. Weise, K. J. Saliba, and S. Reber. Purification of functional Plasmodium falciparum tubulin allows for the identification of parasite-specific microtubule inhibitors. *Current biology*, 2022.

W. A. Hoeijmakers, C. Flueck, K.-J. Françoijs, A. H. Smits, J. Wetzel, J. C. Volz, A. F. Cowman, T. Voss, H. G. Stunnenberg, and R. Bártfai. Plasmodium falciparum centromeres display a unique epigenetic makeup and cluster prior to and during schizogony. *Cellular microbiology*, 14(9):1391–1401, 2012.

S. Holloway, P. Sims, C. Delves, J. Scaife, and J. Hyde. Isolation of α-tubulin genes from the human malaria parasite, Plasmodium falciparum: sequence analysis of α-tubulin. *Molecular microbiology*, 3(11):1501–1510, 1989.

S. P. Holloway, M. Gerousis, C. J. Delves, P. F. Sims, J. G. Scaife, and J. E. Hyde. The tubulin genes of the human malaria parasite Plasmodium falciparum, their chromosomal location and sequence analysis of the α-tubulin II gene. *Molecular and biochemical parasitology*, 43(2):257–270, 1990.

J. L. Höög, C. Schwartz, A. T. Noon, E. T. O'Toole, D. N. Mastronarde, J. R. McIntosh, and C. Antony. Organization of interphase microtubules in fission yeast analyzed by electron tomography. *Developmental cell*, 12(3):349–361, 2007.

R. E. Howells and E. E. Davies. Nuclear division in the oocyst of Plasmodium berghei. *Annals of tropical medicine & parasitology*, 65(4):451–459, 1971.

J. Huff. The Airyscan detector from ZEISS: confocal imaging with improved signal-to-noise ratio and super-resolution. *Nature methods*, 12(12):i–ii, 2015.

J. Huff, A. Bergter, J. Birkenbeil, I. Kleppe, R. Engelmann, and U. Krzic. The new 2D superresolution mode for ZEISS Airyscan. *Nature methods*, 14(12):1223–1223, 2017.

J. Icha, M. Weber, J. C. Waters, and C. Norden. Phototoxicity in live fluorescence microscopy, and how to avoid it. *BioEssays*, 39(8):1700003, 2017.

R. Idro, K. Marsh, C. C. John, and C. R. Newton. Cerebral malaria: mechanisms of brain injury and strategies for improved neurocognitive outcome. *Pediatric research*, 68(4):267–274, 2010.

M. Imwong, W. Madmanee, K. Suwannasin, C. Kunasol, T. J. Peto, R. Tripura, L. von Seidlein, C. Nguon, C. Davoeung, N. P. Day, A. M. Dondorp, and N. J. White. Asymptomatic natural human infections with the simian malaria parasites Plasmodium cynomolgi and Plasmodium knowlesi. *The journal of infectious diseases*, 219(5): 695–702, 2019.

Inkscape Project. Inkscape. URL `https://inkscape.org`.

J. Inselburg and H. S. Banyal. Synthesis of DNA during the asexual cycle of Plasmodium falciparum in culture. *Molecular and biochemical parasitology*, 10(1):79–87, 1984.

C. Janke and M. M. Magiera. The tubulin code and its role in controlling microtubule properties and functions. *Nature reviews molecular cell biology*, 21(6):307–326, 2020.

R. Joice, S. K. Nilsson, J. Montgomery, S. Dankwa, E. Egan, B. Morahan, K. B. Seydel, L. Bertuccini, P. Alano, K. C. Williamson, M. T. Duraisingh, T. E. Taylor, D. A. Milner, and M. Marti. Plasmodium falciparum transmission stages accumulate in the human bone marrow. *Science translational medicine*, 6(244):244re5–244re5, 2014.

B. Kappes and P. Rohrbach. Microtubule inhibitors as a potential treatment for malaria. 2007.

J. Kehrer, C. Kuss, A. Andres-Pons, A. Reustle, N. Dahan, D. Devos, M. Kudryashev, M. Beck, G. R. Mair, and F. Frischknecht. Nuclear pore complex components in the malaria parasite Plasmodium berghei. *Scientific reports*, 8(1):1–10, 2018.

A. Keller, A. I. Nesvizhskii, E. Kolker, and R. Aebersold. Empirical statistical model to estimate the accuracy of peptide identifications made by MS/MS and database search. *Analytical chemistry*, 74(20):5383–5392, 2002.

J. V. Kilmartin. Sfi1p has conserved centrin-binding sites and an essential function in budding yeast spindle pole body duplication. *The journal of cell biology*, 162(7):1211–1221, 2003.

S. M. King and J. S. Hyams. The mitotic spindle of Saccharomyces cerevisiae: assembly, structure and function. *Micron (1969)*, 13(2):93–117, 1982.

M. Kirschner and T. Mitchison. Beyond self-assembly: from microtubules to morphogenesis. *Cell*, 45(3):329–342, 1986.

T. A. Klar, S. Jakobs, M. Dyba, A. Egner, and S. W. Hell. Fluorescence microscopy with diffraction resolution barrier broken by stimulated emission. *Proceedings of the national academy of sciences*, 97(15):8206–8210, 2000.

S. Klaus, P. Binder, J. Kim, M. Machado, C. Funaya, V. Schaaf, D. Klaschka, A. Kudulyte, M. Cyrklaff, V. Laketa, T. Höfer, J. Guizetti, N. B. Becker, F. Frischknecht, U. S. Schwarz, and M. Ganter. Asynchronous nuclear cycles in multinucleated Plasmodium falciparum enable rapid proliferation. *bioRxiv*, 2021.

D. Klug and F. Frischknecht. Motility precedes egress of malaria parasites from oocysts. *Elife*, 6:e19157, 2017.

M. Knop, G. Pereira, and E. Schiebel. Microtubule organization by the budding yeast spindle pole body. *Biology of the cell*, 91(4-5):291–304, 1999.

A. Kodani, T. Moyer, A. Chen, A. Holland, C. A. Walsh, and J. F. Reiter. Sfi1 promotes centriole duplication by recruiting USP9X to stabilize the microcephaly protein STIL. *Journal of cell biology*, 218(7):2185–2197, 2019.

J. M. Kollman, A. Merdes, L. Mourey, and D. A. Agard. Microtubule nucleation by γ-tubulin complexes. *Nature reviews molecular cell biology*, 12(11):709–721, 2011.

M. Kono, D. Heincke, L. Wilcke, T. W. Y. Wong, C. Bruns, S. Herrmann, T. Spielmann, and T. W. Gilberger. Pellicle formation in the malaria parasite. *Journal of cell science*, 129(4):673–680, 2016.

T. W. Kooij, B. Franke-Fayard, J. Renz, H. Kroeze, M. W. van Dooren, J. Ramesar, K. D. Augustijn, C. J. Janse, and A. P. Waters. Plasmodium berghei α-tubulin II: a role in both male gamete formation and asexual blood stages. *Molecular and biochemical parasitology*, 144(1):16–26, 2005.

G. J. Kops, B. Snel, and E. C. Tromer. Evolutionary dynamics of the spindle assembly checkpoint in eukaryotes. *Current biology*, 30(10):R589–R602, 2020.

J. R. Kremer, D. N. Mastronarde, and J. R. McIntosh. Computer visualization of three-dimensional image data using IMOD. *Journal of structural biology*, 116(1):71–76, 1996.

L. K. Krüger and P. T. Tran. Spindle scaling mechanisms. *Essays in biochemistry*, 64(2):383–396, 2020.

W. Kukulski, M. Schorb, S. Welsch, A. Picco, M. Kaksonen, and J. A. Briggs. Correlated fluorescence and 3D electron microscopy with high sensitivity and spatial precision. *Journal of cell biology*, 192(1):111–119, 2011.

W. Kukulski, M. Schorb, S. Welsch, A. Picco, M. Kaksonen, and J. A. Briggs. Precise, correlated fluorescence microscopy and electron tomography of lowicryl sections using fluorescent fiducial markers. *Methods in cell biology*, 111:235–257, 2012.

B. Lacroix, G. Letort, L. Pitayu, J. Sallé, M. Stefanutti, G. Maton, A.-M. Ladouceur, J. C. Canman, P. S. Maddox, A. S. Maddox, N. Minc, F. Nédélec, and J. Dumont. Microtubule dynamics scale with cell size to set spindle length and assembly timing. *Developmental cell*, 45(4):496–511, 2018.

R. Ladda. New insights into the fine structure of rodent malarial parasites. *Military medicine*, 134(9):825–865, 1969.

S. S. Lam, J. D. Martell, K. J. Kamer, T. J. Deerinck, M. H. Ellisman, V. K. Mootha, and A. Y. Ting. Directed evolution of APEX2 for electron microscopy and proximity labeling. *Nature methods*, 12(1):51–54, 2015.

M. H. Laporte, N. Klena, V. Hamel, and P. Guichard. Visualizing the native cellular organization by coupling cryofixation with expansion microscopy (Cryo-ExM). *Nature methods*, pages 1–7, 2022.

E. Lasonder, S. R. Rijpma, B. C. van Schaijk, W. A. Hoeijmakers, P. R. Kensche, M. S. Gresnigt, A. Italiaander, M. W. Vos, R. Woestenenk, T. Bousema, G. R. Mair, S. M. Khan, C. J. Janse, R. Bártfai, and R. W. Sauerwein. Integrated transcriptomic and proteomic analyses of P. falciparum gametocytes: molecular insight into sex-specific processes and translational repression. *Nucleic acids research*, 44(13):6087–6101, 2016.

S. Lawo, M. Hasegan, G. D. Gupta, and L. Pelletier. Subdiffraction imaging of centrosomes reveals higher-order organizational features of pericentriolar material. *Nature cell biology*, 14(11):1148–1158, 2012.

K. Lee, S. Choi, C. Yang, H.-C. Wu, and J. Yu. Autofluorescence generation and elimination: a lesson from glutaraldehyde. *Chemical communications*, 49(29):3028–3030, 2013.

T. Leete and H. Rubin. Malaria and the cell cycle. *Parasitology today*, 12(11):442–444, 1996.

M. Lelek, M. T. Gyparaki, G. Beliu, F. Schueder, J. Griffié, S. Manley, R. Jungmann, M. Sauer, M. Lakadamyali, and C. Zimmer. Single-molecule localization microscopy. *Nature reviews methods primers*, 1(1):1–27, 2021.

S. Li, A. M. Sandercock, P. Conduit, C. V. Robinson, R. L. Williams, and J. V. Kilmartin. Structural role of Sfi1p–centrin filaments in budding yeast spindle pole body duplication. *The journal of cell biology*, 173(6):867–877, 2006.

B. Liffner and S. Absalon. Expansion microscopy reveals Plasmodium falciparum blood-stage parasites undergo anaphase with a chromatin bridge in the absence of mini-chromosome maintenance complex binding protein. *Microorganisms*, 9(11):2306, 2021.

M. Y.-X. Lim, G. LaMonte, M. C. Lee, C. Reimer, B. H. Tan, V. Corey, B. F. Tjahjadi, A. Chua, M. Nachon, R. Wintjens, P. Gedeck, B. Malleret, L. Renia, G. M. Bonamy, P. C.-L. Ho, B. K. Yeung, E. D. Chow, L. Lim, D. A. Fidock, T. T. Diagana, E. A. Winzeler, and P. Bifani. UDP-galactose and acetyl-CoA transporters as Plasmodium multidrug resistance genes. *Nature microbiology*, 1(12):1–12, 2016.

O. Looker, A. J. Blanch, B. Liu, J. Nunez-Iglesias, P. J. McMillan, L. Tilley, and M. W. Dixon. The knob protein KAHRP assembles into a ring-shaped structure that underpins virulence complex assembly. *PLoS pathogens*, 15 (5):e1007761, 2019.

G. V. Los, L. P. Encell, M. G. McDougall, D. D. Hartzell, N. Karassina, C. Zimprich, M. G. Wood, R. Learish, R. F. Ohana, M. Urh, D. Simpson, J. Mendez, K. Zimmerman, P. Otto, G. Vidugiris, J. Zhu, A. Darzins, D. H. Klaubert, R. F. Bulleit, and K. V. Wood. Halotag: a novel protein labeling technology for cell imaging and protein analysis. *ACS chemical biology*, 3(6):373–382, 2008.

G. Lukinavičius, K. Umezawa, N. Olivier, A. Honigmann, G. Yang, T. Plass, V. Mueller, L. Reymond, I. R. Corrêa Jr, Z.-G. Luo, C. Schultz, E. A. Lemke, P. Heppenstall, C. Eggeling, S. Manley, and K. Johnsson. A near-infrared fluorophore for live-cell super-resolution microscopy of cellular proteins. *Nature chemistry*, 5(2):132–139, 2013.

G. Lukinavičius, L. Reymond, E. D'este, A. Masharina, F. Göttfert, H. Ta, A. Güther, M. Fournier, S. Rizzo, H. Waldmann, C. Blaukopf, C. Sommer, D. W. Gerlich, H.-D. Arndt, S. W. Hell, and K. Johnsson. Fluorogenic probes for live-cell imaging of the cytoskeleton. *Nature methods*, 11(7):731–733, 2014.

G. Lukinavičius, C. Blaukopf, E. Pershagen, A. Schena, L. Reymond, E. Derivery, M. Gonzalez-Gaitan, E. D'Este, S. W. Hell, D. W. Gerlich, and K. Johnsson. SiR–Hoechst is a far-red DNA stain for live-cell nanoscopy. *Nature communications*, 6(1):1–7, 2015.

G. MacPherson, M. Warrell, N. White, S. Looareesuwan, and D. Warrell. Human cerebral malaria. A quantitative ultrastructural analysis of parasitized erythrocyte sequestration. *The american journal of pathology*, 119(3):385, 1985.

S. Maessen, J. G. Wesseling, M. A. Smits, R. N. Konings, and J. G. Schoenmakers. The γ-tubulin gene of the malaria parasite Plasmodium falciparum. *Molecular and biochemical parasitology*, 60(1):27–35, 1993.

B. Mahajan, A. Selvapandiyan, N. J. Gerald, V. Majam, H. Zheng, T. Wickramarachchi, J. Tiwari, H. Fujioka, J. K. Moch, N. Kumar, L. Aravind, H. L. Nakhasi, and S. Kumar. Centrins, cell cycle regulation proteins in human malaria parasite Plasmodium falciparum. *Journal of biological chemistry*, 283(46):31871–31883, 2008.

A. G. Maier, B. M. Cooke, A. F. Cowman, and L. Tilley. Malaria parasite proteins that remodel the host erythrocyte. *Nature reviews microbiology*, 7(5):341–354, 2009.

L. Mancio-Silva, J. J. Lopez-Rubio, A. Claes, and A. Scherf. Sir2a regulates rDNA transcription and multiplication rate in the human malaria parasite Plasmodium falciparum. *Nature communications*, 4(1):1–6, 2013.

B. J. Mann and P. Wadsworth. Kinesin-5 regulation and function in mitosis. *Trends in cell biology*, 29(1):66–79, 2019.

S. R. Marques, C. Ramakrishnan, R. Carzaniga, A. M. Blagborough, M. J. Delves, A. M. Talman, and R. E. Sinden. An essential role of the basal body protein SAS-6 in Plasmodium male gamete development and malaria transmission. *Cellular microbiology*, 17(2):191–206, 2015.

G. Marteil, M. A. D. Louro, and M. Bettencourt-Dias. Centrosome assembly: Reconstructing the core cartwheel structure in vitro. *Current biology*, 27(12):R606–R609, 2017.

D. N. Mastronarde. Automated electron microscope tomography using robust prediction of specimen movements. *Journal of structural biology*, 152(1):36–51, 2005.

J. M. Matz, C. Goosmann, V. Brinkmann, J. Grützke, A. Ingmundson, K. Matuschewski, and T. W. Kooij. The Plasmodium berghei translocon of exported proteins reveals spatiotemporal dynamics of tubular extensions. *Scientific reports*, 5(1):1–14, 2015.

D. L. Medica and P. Sinnis. Quantitative dynamics of Plasmodium yoelii sporozoite transmission by infected anopheline mosquitoes. *Infection and immunity*, 73(7):4363–4369, 2005.

A.-K. Mehnert, C. S. Simon, and J. Guizetti. Immunofluorescence staining protocol for STED nanoscopy of Plasmodium-infected red blood cells. *Molecular and biochemical parasitology*, 229:47–52, 2019.

V. Mennella, B. Keszthelyi, K. McDonald, B. Chhun, F. Kan, G. C. Rogers, B. Huang, and D. Agard. Subdiffraction-resolution fluorescence microscopy reveals a domain of the centrosome critical for pericentriolar material organization. *Nature cell biology*, 14(11):1159–1168, 2012.

Y. A. Menyaev, K. A. Carey, D. A. Nedosekin, M. Sarimollaoglu, E. I. Galanzha, J. S. Stumhofer, and V. P. Zharov. Preclinical photoacoustic models: application for ultrasensitive single cell malaria diagnosis in large vein and artery. *Biomedical optics express*, 7(9):3643–3658, 2016.

T. Mitchison. Cell biology: Size scaling of mitotic spindles. *Current biology*, 30(24):R1476–R1478, 2020.

T. Mitchison and M. Kirschner. Dynamic instability of microtubule growth. *Nature*, 312(5991):237–242, 1984.

B. J. Morahan, C. Abrie, K. Al-Hasani, M. B. Batty, V. Corey, A. N. Cowell, J. Niemand, E. A. Winzeler, L.-M. Birkholtz, C. Doerig, and J. F. Garcia-Bustos. Human Aurora kinase inhibitor Hesperadin reveals epistatic interaction between Plasmodium falciparum PfArk1 and PfNek1 kinases. *Communications biology*, 3(1):1–10, 2020.

E. Morrison, B. Wardleworth, J. Askham, A. Markham, and D. Meredith. Eb1, a protein which interacts with the APC tumour suppressor, is associated with the microtubule cytoskeleton throughout the cell cycle. *Oncogene*, 17 (26):3471–3477, 1998.

M. M. Mota, G. Pradel, J. P. Vanderberg, J. C. Hafalla, U. Frevert, R. S. Nussenzweig, V. Nussenzweig, and A. Rodrıguez. Migration of Plasmodium sporozoites through cells before infection. *Science*, 291(5501):141–144, 2001.

O. M'Saad and J. Bewersdorf. Light microscopy of proteins in their ultrastructural context. *Nature communications*, 11(1):1–15, 2020.

J. Naughton and A. Bell. Studies on cell-cycle synchronization in the asexual erythrocytic stages of Plasmodium falciparum. *Parasitology*, 134(3):331–337, 2007.

A. I. Nesvizhskii, A. Keller, E. Kolker, and R. Aebersold. A statistical model for identifying proteins by tandem mass spectrometry. *Analytical chemistry*, 75(17):4646–4658, 2003.

E. A. Nigg and A. J. Holland. Once and only once: mechanisms of centriole duplication and their deregulation in disease. *Nature reviews molecular cell biology*, 19(5):297–312, 2018.

E. T. O'Toole, K. L. McDonald, J. Mantler, J. R. McIntosh, A. A. Hyman, and T. Muller-Reichert. Morphologically distinct microtubule ends in the mitotic centrosome of Caenorhabditis elegans. *The journal of cell biology*, 163(3): 451–456, 2003.

T. D. Otto, D. Wilinski, S. Assefa, T. M. Keane, L. R. Sarry, U. Böhme, J. Lemieux, B. Barrell, A. Pain, M. Berriman, C. Newbold, and M. Llinás. New insights into the blood-stage transcriptome of Plasmodium falciparum using RNA-Seq. *Molecular microbiology*, 76(1):12–24, 2010.

E. T. O'Toole, M. Winey, and J. R. McIntosh. High-voltage electron tomography of spindle pole bodies and early mitotic spindles in the yeast Saccharomyces cerevisiae. *Molecular biology of the cell*, 10(6):2017–2031, 1999.

L. Pan, R. Yan, W. Li, and K. Xu. Super-resolution microscopy reveals the native ultrastructure of the erythrocyte cytoskeleton. *Cell reports*, 22(5):1151–1158, 2018.

A. Paoletti, N. Bordes, R. Haddad, C. L. Schwartz, F. Chang, and M. Bornens. Fission yeast cdc31p is a component of the half-bridge and controls SPB duplication. *Molecular biology of the cell*, 14(7):2793–2808, 2003.

G. Pishchany and E. P. Skaar. Taste for blood: hemoglobin as a nutrient source for pathogens. *PLoS pathogens*, 8(3): e1002535, 2012.

T. Ponnudurai, A. Leeuwenberg, and J. Meuwissen. Chloroquine sensitivity of isolates of Plasmodium falciparum adapted to in vitro culture. *Tropical and geographical medicine*, 33(1):50–54, 1981.

B. Pouvelle, P. J. Farley, C. A. Long, and T. F. Taraschi. Taxol arrests the development of blood-stage Plasmodium falciparum in vitro and Plasmodium chabaudi adami in malaria-infected mice. *The journal of clinical investigation*, 94(1):413–417, 1994.

M. Prado, N. Eickel, M. De Niz, A. Heitmann, C. Agop-Nersesian, R. Wacker, J. Schmuckli-Maurer, R. Caldelari, C. J. Janse, S. M. Khan, J. May, C. G. Meyer, and V. T. Heussler. Long-term live imaging reveals cytosolic immune responses of host hepatocytes against Plasmodium infection and parasite escape mechanisms. *Autophagy*, 11(9): 1561–1579, 2015.

G. Prensier and C. Slomianny. The karyotype of Plasmodium falciparum determined by ultrastructural serial sectioning and 3D reconstruction. *The journal of parasitology*, pages 731–736, 1986.

P. Prommana, C. Uthaipibull, C. Wongsombat, S. Kamchonwongpaisan, Y. Yuthavong, E. Knuepfer, A. A. Holder, and P. J. Shaw. Inducible knockdown of Plasmodium gene expression using the glmS ribozyme. *PloS one*, 8(8): e73783, 2013.

S. L. Prosser and C. G. Morrison. Centrin2 regulates CP110 removal in primary cilium formation. *Journal of cell biology*, 208(6):693–701, 2015.

M. Prudêncio, A. Rodriguez, and M. M. Mota. The silent path to thousands of merozoites: the Plasmodium liver stage. *Nature reviews microbiology*, 4(11):849–856, 2006.

V. Quarantotti, J.-X. Chen, J. Tischer, C. Gonzalez Tejedo, E. K. Papachristou, C. S. D'Santos, J. V. Kilmartin, M. L. Miller, and F. Gergely. Centriolar satellites are acentriolar assemblies of centrosomal proteins. *The EMBO journal*, 38(14):e101082, 2019.

R Core Team. *R: A Language and Environment for Statistical Computing*. R Foundation for Statistical Computing, Vienna, Austria, 2021. URL `https://www.R-project.org/`.

R. Rashpa and M. Brochet. Expansion microscopy of Plasmodium gametocytes reveals the molecular architecture of a bipartite microtubule organisation centre coordinating mitosis with axoneme assembly. *PLoS pathogens*, 18 (1):e1010223, 2022.

M. Read, T. Sherwin, S. Holloway, K. Gull, and J. Hyde. Microtubular organization visualized by immunofluorescence microscopy during erythrocytic schizogony in Plasmodium falciparum and investigation of post-translational modifications of parasite tubulin. *Parasitology*, 106(3):223–232, 1993.

H. B. Reilly, H. Wang, J. A. Steuter, A. M. Marx, and M. T. Ferdig. Quantitative dissection of clone-specific growth rates in cultured malaria parasites. *International journal for parasitology*, 37(14):1599–1607, 2007.

L. Reininger, J. M. Wilkes, H. Bourgade, D. Miranda-Saavedra, and C. Doerig. An essential Aurora-related kinase transiently associates with spindle pole bodies during Plasmodium falciparum erythrocytic schizogony. *Molecular microbiology*, 79(1):205–221, 2011.

D. Richmond, R. Rizkallah, F. Liang, M. M. Hurt, and Y. Wang. Slk19 clusters kinetochores and facilitates chromosome bipolar attachment. *Molecular biology of the cell*, 24(5):566–577, 2013.

E. M. Rieckhoff, F. Berndt, M. Elsner, S. Golfier, F. Decker, K. Ishihara, and J. Brugués. Spindle scaling is governed by cell boundary regulation of microtubule nucleation. *Current biology*, 30(24):4973–4983, 2020.

C. L. Rieder and S. P. Alexander. Kinetochores are transported poleward along a single astral microtubule during chromosome attachment to the spindle in newt lung cells. *Journal of cell biology*, 110(1):81–95, 1990.

D. T. Riglar, D. Richard, D. W. Wilson, M. J. Boyle, C. Dekiwadia, L. Turnbull, F. Angrisano, D. S. Marapana, K. L. Rogers, C. B. Whitchurch, J. G. Beeson, A. F. Cowman, S. A. Ralph, and J. Baum. Super-resolution dissection of coordinated events during malaria parasite invasion of the human erythrocyte. *Cell host & microbe*, 9(1):9–20, 2011.

D. Ronnlund, L. Xu, A. Perols, A. K. Gad, A. Eriksson Karlstrom, G. Auer, and J. Widengren. Multicolor fluorescence nanoscopy by photobleaching: concept, verification, and its application to resolve selective storage of proteins in platelets. *ACS nano*, 8(5):4358–4365, 2014.

J. Roostalu and T. Surrey. Microtubule nucleation: beyond the template. *Nature reviews molecular cell biology*, 18(11): 702–710, 2017.

M. Roques, R. R. Stanway, E. I. Rea, R. Markus, D. Brady, A. A. Holder, D. S. Guttery, and R. Tewari. Plasmodium centrin PbCEN-4 localizes to the putative MTOC and is dispensable for malaria parasite proliferation. *Biology open*, 8(1), 2019.

R. Rosenberg and J. Rungsiwongse. The number of sporozoites produced by individual malaria oocysts. *The american journal of tropical medicine and hygiene*, 45(5):574–577, 1991.

R. M. Rudlaff, S. Kraemer, V. A. Streva, and J. D. Dvorin. An essential contractile ring protein controls cell division in Plasmodium falciparum. *Nature communications*, 10(1):1–13, 2019.

R. M. Rudlaff, S. Kraemer, J. Marshman, and J. D. Dvorin. Three-dimensional ultrastructure of Plasmodium falciparum throughout cytokinesis. *PLoS pathogens*, 16(6):e1008587, 2020.

D. Rüthnick, J. Vitale, A. Neuner, and E. Schiebel. The N-terminus of Sfi1 and yeast centrin Cdc31 provide the assembly site for a new spindle pole body. *Journal of cell biology*, 220(3), 2021.

S. J. Sahl, S. W. Hell, and S. Jakobs. Fluorescence nanoscopy in cell biology. *Nature reviews molecular cell biology*, 18 (11):685–701, 2017.

S. Salas-Pino and R. R. Daga. Spatiotemporal control of spindle disassembly in fission yeast. *Cellular and molecular life sciences*, 76(18):3543–3551, 2019.

J. L. Salisbury, K. M. Suino, R. Busby, and M. Springett. Centrin-2 is required for centriole duplication in mammalian cells. *Current biology*, 12(15):1287–1292, 2002.

C. P. Sanchez, C. Karathanasis, R. Sanchez, M. Cyrklaff, J. Jäger, B. Buchholz, U. S. Schwarz, M. Heilemann, and M. Lanzer. Single-molecule imaging and quantification of the immune-variant adhesin VAR2CSA on knobs of Plasmodium falciparum-infected erythrocytes. *Communications biology*, 2(1):1–9, 2019.

S. Sato. Plasmodium – a brief introduction to the parasites causing human malaria and their basic biology. *Journal of physiological anthropology*, 40(1):1–13, 2021.

J. Schindelin, I. Arganda-Carreras, E. Frise, V. Kaynig, M. Longair, T. Pietzsch, S. Preibisch, C. Rueden, S. Saalfeld, B. Schmid, J.-Y. Tinevez, D. J. White, V. Hartenstein, K. Eliceiri, P. Tomancak, and A. Cardona. Fiji: an open-source platform for biological-image analysis. *Nature methods*, 9(7):676–682, 2012.

J.-G. Schloetel, J. Heine, A. F. Cowman, and M. Pasternak. Guided STED nanoscopy enables super-resolution imaging of blood stage malaria parasites. *Scientific reports*, 9(1):1–10, 2019.

J. Schrével, G. Asfaux-Foucher, and J. M. Bafort. Etude ultrastructurale des mitoses multiples au cours de la sporogonie du Plasmodium b. berghei. *Journal of ultrastructure research*, 59(3):332–350, 1977.

J. Schrével, V. Sinou, P. Grellier, F. Frappier, D. Guénard, and P. Potier. Interactions between docetaxel (Taxotere) and Plasmodium falciparum-infected erythrocytes. *Proceedings of the national academy of sciences*, 91(18):8472–8476, 1994.

O. Sen, A. T. Saurin, and J. M. Higgins. The live cell DNA stain SiR-Hoechst induces DNA damage responses and impairs cell cycle progression. *Scientific reports*, 8(1):1–8, 2018.

H. E. Shortt, N. H. Fairley, G. Covell, P. G. Shute, and P. C. C. Garnham. The pre-erythrocytic stage of Plasmodium falciparum. *Transactions of the royal society of tropical medicine and hygiene*, 44(4):405–419, 1951.

S. Sidjanski and J. P. Vanderberg. Delayed migration of Plasmodium sporozoites from the mosquito bite site to the blood. *The american journal of tropical medicine and hygiene*, 57(4):426–429, 1997.

D. Simmons, G. Woollett, M. Bergin-Cartwright, D. Kay, and J. Scaife. A malaria protein exported into a new compartment within the host erythrocyte. *The EMBO journal*, 6(2):485–491, 1987.

C. S. Simon, C. Funaya, J. Bauer, Y. Voβ, M. Machado, A. Penning, D. Klaschka, M. Cyrklaff, J. Kim, M. Ganter, and J. Guizetti. An extended DNA-free intranuclear compartment organizes centrosome microtubules in malaria parasites. *Life science alliance*, 4(11), 2021a.

C. S. Simon, V. S. Stürmer, and J. Guizetti. How many is enough?-Challenges of multinucleated cell division in malaria parasites. *Frontiers in cellular and infection microbiology*, 11, 2021b.

R. E. Sinden and M. E. Smalley. Gametocytogenesis of Plasmodium falciparum in vitro: the cell-cycle. *Parasitology*, 79(2):277–296, 1979.

R. E. Sinden and K. Strong. An ultrastructural study of the sporogonic development of Plasmodium falciparum in Anopheles gambiae. *Transactions of the royal society of tropical medicine and hygiene*, 72(5):477–491, 1978.

R. E. Sinden, E. U. Canning, and B. Spain. Gametogenesis and fertilization in Plasmodium yoelii nigeriensis: a transmission electron microscope study. *Proceedings of the royal society of London. Series B. Biological sciences*, 193 (1110):55–76, 1976.

R. E. Sinden, E. U. Canning, R. S. Bray, and M. E. Smalley. Gametocyte and gamete development in Plasmodium falciparum. *Proceedings of the royal society of London. Series B. Biological sciences*, 201(1145):375–399, 1978.

R. E. Sinden, G. A. Butcher, O. Billker, and S. L. Fleck. Regulation of infectivity of Plasmodium to the mosquito vector. *Advances in parasitology*, 38:53–117, 1996.

R. E. Sinden, A. Talman, S. R. Marques, M. N. Wass, and M. J. E. Sternberg. The flagellum in malarial parasites. *Current opinion in microbiology*, 13(4):491–500, 2010.

B. Singh and C. Daneshvar. Human infections and detection of Plasmodium knowlesi. *Clinical microbiology reviews*, 26(2):165–184, 2013.

B. Singh, L. K. Sung, A. Matusop, A. Radhakrishnan, S. S. Shamsul, J. Cox-Singh, A. Thomas, and D. J. Conway. A large focus of naturally acquired Plasmodium knowlesi infections in human beings. *The lancet*, 363(9414): 1017–1024, 2004.

V. Sinou, Y. Boulard, P. Grellier, and J. Schrevel. Host cell and malarial targets for docetaxel (Taxotere™) during the erythrocytic development of Plasmodium falciparum. *Journal of eukaryotic microbiology*, 45(2):171–183, 1998.

R. W. Snow. Global malaria eradication and the importance of Plasmodium falciparum epidemiology in Africa. *BMC medicine*, 13(1):1–3, 2015.

A. Spang, I. Courtney, U. Fackler, M. Matzner, and E. Schiebel. The calcium-binding protein cell division cycle 31 of Saccharomyces cerevisiae is a component of the half bridge of the spindle pole body. *The journal of cell biology*, 123(2):405–416, 1993.

T. Spielmann, D. J. Fergusen, and H.-P. Beck. etramps, a new Plasmodium falciparum gene family coding for developmentally regulated and highly charged membrane proteins located at the parasite–host cell interface. *Molecular biology of the cell*, 14(4):1529–1544, 2003.

T. Spielmann, P. L. Hawthorne, M. W. Dixon, M. Hannemann, K. Klotz, D. J. Kemp, N. Klonis, L. Tilley, K. R. Trenholme, and D. L. Gardiner. A cluster of ring stage–specific genes linked to a locus implicated in cytoadherence in Plasmodium falciparum codes for PEXEL-negative and PEXEL-positive proteins exported into the host cell. *Molecular biology of the cell*, 17(8):3613–3624, 2006.

B. Spreng, H. Fleckenstein, P. Kübler, C. Di Biagio, M. Benz, P. Patra, U. S. Schwarz, M. Cyrklaff, and F. Frischknecht. Microtubule number and length determine cellular shape and function in Plasmodium. *The EMBO journal*, 38 (15):e100984, 2019.

S. Stanojcic, N. Kuk, I. Ullah, Y. Sterkers, and C. J. Merrick. Single-molecule analysis reveals that DNA replication dynamics vary across the course of schizogony in the malaria parasite Plasmodium falciparum. *Scientific reports*, 7(1):1–12, 2017.

T. Staudt, A. Engler, E. Rittweger, B. Harke, J. Engelhardt, and S. W. Hell. Far-field optical nanoscopy with reduced number of state transition cycles. *Optics express*, 19(6):5644–5657, 2011.

L. B. Stewart, O. Diaz-Ingelmo, A. Claessens, J. Abugri, R. D. Pearson, S. Goncalves, E. Drury, D. P. Kwiatkowski, G. A. Awandare, and D. J. Conway. Intrinsic multiplication rate variation and plasticity of human blood stage malaria parasites. *Communications biology*, 3(1):1–9, 2020.

B. Striepen, C. N. Jordan, S. Reiff, and G. G. Van Dooren. Building the perfect parasite: cell division in Apicomplexa. *PLoS pathogens*, 3(6):e78, 2007.

A. Sturm, R. Amino, C. Van de Sand, T. Regen, S. Retzlaff, A. Rennenberg, A. Krueger, J.-M. Pollok, R. Menard, and V. T. Heussler. Manipulation of host hepatocytes by the malaria parasite for delivery into liver sinusoids. *Science*, 313(5791):1287–1290, 2006.

X. Sun, A. Zhang, B. Baker, L. Sun, A. Howard, J. Buswell, D. Maurel, A. Masharina, K. Johnsson, C. J. Noren, M.-Q. Xu, and I. R. Corrêa Jr. Development of SNAP-tag fluorogenic probes for wash-free fluorescence imaging. *ChemBioChem*, 12(14):2217, 2011.

E. S. Suvorova, M. Francia, B. Striepen, and M. W. White. A novel bipartite centrosome coordinates the apicomplexan cell cycle. *PLoS biology*, 13(3):e1002093, 2015.

A. L. Szymczak, C. J. Workman, Y. Wang, K. M. Vignali, S. Dilioglou, E. F. Vanin, and D. A. Vignali. Correction of multi-gene deficiency in vivo using a single'self-cleaving'2A peptide–based retroviral vector. *Nature biotechnology*, 22(5):589–594, 2004.

J. Tavares, P. Formaglio, S. Thiberge, E. Mordelet, N. Van Rooijen, A. Medvinsky, R. Ménard, and R. Amino. Role of host cell traversal by the malaria sporozoite during liver infection. *Journal of experimental medicine*, 210(5): 905–915, 2013.

J. A. Terzakis, H. Sprinz, and R. A. Ward. The transformation of the Plasmodium gallinaceum oocyst in Aedes aegypti mosquitoes. *The journal of cell biology*, 34(1):311–326, 1967.

The GIMP Development Team. Gimp. URL `https://www.gimp.org`.

I. M. Tolić-Nørrelykke. Push-me-pull-you: how microtubules organize the cell interior. *European biophysics journal*, 37(7):1271–1278, 2008.

R. Tomasina, F. C. González, and M. E. Francia. Structural and functional insights into the microtubule organizing centers of Toxoplasma gondii and Plasmodium spp. *Microorganisms*, 9(12):2503, 2021.

R. Tomasina, É. S. Martins-Duarte, P. Bastin, M. Gissot, and M. E. Francia. Separate to operate: the centriole-free inner core of the centrosome regulates the assembly of the intranuclear spindle in Toxoplasma gondii. *bioRxiv*, 2022.

C. J. Tonkin, G. G. van Dooren, T. P. Spurck, N. S. Struck, R. T. Good, E. Handman, A. F. Cowman, and G. I. McFadden. Localization of organellar proteins in Plasmodium falciparum using a novel set of transfection vectors and a new immunofluorescence fixation method. *Molecular and biochemical parasitology*, 137(1):13–21, 2004.

K. L. Tosheva, Y. Yuan, P. M. Pereira, S. Culley, and R. Henriques. Between life and death: strategies to reduce phototoxicity in super-resolution microscopy. *Journal of physics D: Applied physics*, 53(16):163001, 2020.

M. Tsuji, D. Mattei, R. S. Nussenzweig, D. Eichinger, and F. Zavala. Demonstration of heat-shock protein 70 in the sporozoite stage of malaria parasites. *Parasitology research*, 80(1):16–21, 1994.

M. Ueda, M. Schliwa, and U. Euteneuer. Unusual centrosome cycle in Dictyostelium: correlation of dynamic behavior and structural changes. *Molecular biology of the cell*, 10(1):151–160, 1999.

M. Urh and M. Rosenberg. Halotag, a platform technology for protein analysis. *Current chemical genomics*, 6:72, 2012.

R. Van Biljon, J. Niemand, R. van Wyk, K. Clark, B. Verlinden, C. Abrie, H. von Grüning, W. Smidt, A. Smit, J. Reader, H. Painter, M. Llinás, C. Doerig, and L.-M. Birkholtz. Inducing controlled cell cycle arrest and re-entry during asexual proliferation of Plasmodium falciparum malaria parasites. *Scientific reports*, 8(1):1–14, 2018.

J. P. Vanderberg and U. Frevert. Intravital microscopy demonstrating antibody-mediated immobilisation of Plasmodium berghei sporozoites injected into skin by mosquitoes. *International journal for parasitology*, 34(9):991–996, 2004.

R. Varadarajan and N. M. Rusan. Bridging centrioles and PCM in proper space and time. *Essays in biochemistry*, 62 (6):793–801, 2018.

A. M. Vaughan and S. H. Kappe. Malaria parasite liver infection and exoerythrocytic biology. *Cold Spring Harbor perspectives in medicine*, 7(6):a025486, 2017.

K. Venugopal, F. Hentzschel, G. Valkiūnas, and M. Marti. Plasmodium asexual growth and sexual development in the haematopoietic niche of the host. *Nature reviews microbiology*, 18(3):177–189, 2020.

G. Verma and N. Surolia. Plasmodium falciparum CENH3 is able to functionally complement Cse4p and its, C-terminus is essential for centromere function. *Molecular and biochemical parasitology*, 192(1-2):21–29, 2013.

K. Vickerman and F. Cox. Merozoite formation in the erythrocytic stages of the malaria parasite Plasmodium vinckei. *Transactions of the royal society of tropical medicine and hygiene*, 61(3):303–312, 1967.

D. Vlachou, T. Schlegelmilch, E. Runn, A. Mendes, and F. C. Kafatos. The developmental migration of Plasmodium in mosquitoes. *Current opinion in genetics & development*, 16(4):384–391, 2006.

J. Volz, T. G. Carvalho, S. A. Ralph, P. Gilson, J. Thompson, C. J. Tonkin, C. Langer, B. S. Crabb, and A. F. Cowman. Potential epigenetic regulatory proteins localise to distinct nuclear sub-compartments in Plasmodium falciparum. *International journal for parasitology*, 40(1):109–121, 2010.

J. C. Volz, A. Yap, X. Sisquella, J. K. Thompson, N. T. Lim, L. W. Whitehead, L. Chen, M. Lampe, W.-H. Tham, D. Wilson, T. Nebl, D. Marapana, T. Triglia, W. Wong, K. L. Rogers, and A. F. Cowman. Essential role of the PfRh5/PfRipr/CyRPA complex during Plasmodium falciparum invasion of erythrocytes. *Cell host & microbe*, 20 (1):60–71, 2016.

R. Walker, E. O'brien, N. Pryer, M. Soboeiro, W. Voter, H. Erickson, and E. D. Salmon. Dynamic instability of individual microtubules analyzed by video light microscopy: rate constants and transition frequencies. *The journal of cell biology*, 107(4):1437–1448, 1988.

R. J. Wall, M. Roques, N. J. Katris, L. Koreny, R. R. Stanway, D. Brady, R. F. Waller, and R. Tewari. Sas6-like protein in Plasmodium indicates that conoid-associated apical complex proteins persist in invasive stages within the mosquito vector. *Scientific reports*, 6(1):1–12, 2016.

R. J. Wall, D. J. Ferguson, A. Freville, B. Franke-Fayard, D. Brady, M. Zeeshan, A. R. Bottrill, S. Wheatley, A. M. Fry, C. J. Janse, H. Yamano, A. A. Holder, D. S. Guttery, and R. Tewari. Plasmodium APC3 mediates chromosome condensation and cytokinesis during atypical mitosis in male gametogenesis. *Scientific reports*, 8(1):1–10, 2018.

D. Walliker, I. A. Quakyi, T. E. Wellems, T. F. McCutchan, A. Szarfman, W. T. London, L. M. Corcoran, T. R. Burkot, and R. Carter. Genetic analysis of the human malaria parasite Plasmodium falciparum. *Science*, 236(4809):1661–1666, 1987.

G. Wang, Q. Jiang, and C. Zhang. The role of mitotic kinases in coupling the centrosome cycle with the assembly of the mitotic spindle. *Journal of cell science*, 127(19):4111–4122, 2014.

L. Wang, M. Tran, E. D'Este, J. Roberti, B. Koch, L. Xue, and K. Johnsson. A general strategy to develop cell permeable and fluorogenic probes for multicolour nanoscopy. *Nature chemistry*, 12(2):165–172, 2020.

Y. Wang, H. Schellenberg, V. Walhorn, K. Toensing, and D. Anselmetti. Binding mechanism of fluorescent dyes to DNA characterized by magnetic tweezers. *Materials today: proceedings*, 4:S218–S225, 2017.

A. Weiner, N. Dahan-Pasternak, E. Shimoni, V. Shinder, P. von Huth, M. Elbaum, and R. Dzikowski. 3D nuclear architecture reveals coupled cell cycle dynamics of chromatin and nuclear pores in the malaria parasite Plasmodium falciparum. *Cellular microbiology*, 13(7):967–977, 2011.

M. E. Wickham, J. G. Culvenor, and A. F. Cowman. Selective inhibition of a two-step egress of malaria parasites from the host erythrocyte. *Journal of biological chemistry*, 278(39):37658–37663, 2003.

M. Winey, C. L. Mamay, E. T. O'toole, D. N. Mastronarde, T. H. Giddings Jr, K. L. McDonald, and J. R. McIntosh. Three-dimensional ultrastructural analysis of the Saccharomyces cerevisiae mitotic spindle. *The journal of cell biology*, 129(6):1601–1615, 1995.

F. Wissing, C. P. Sanchez, P. Rohrbach, S. Ricken, and M. Lanzer. Illumination of the malaria parasite Plasmodium falciparum alters intracellular pH: implications for live cell imaging. *Journal of biological chemistry*, 277(40):37747–37755, 2002.

U. Wolfrum and J. L. Salisbury. Expression of centrin isoforms in the mammalian retina. *Experimental cell research*, 242(1):10–17, 1998.

J. B. Woodruff, O. Wueseke, and A. A. Hyman. Pericentriolar material structure and dynamics. *Philosophical transactions of the royal society B: Biological sciences*, 369(1650):20130459, 2014.

L. Wordeman. How kinesin motor proteins drive mitotic spindle function: Lessons from molecular assays. In *Seminars in cell & developmental biology*, volume 21, pages 260–268. Elsevier, 2010.

World Health Organization. World malaria report 2021. 2021.

M. Wühr, Y. Chen, S. Dumont, A. C. Groen, D. J. Needleman, A. Salic, and T. J. Mitchison. Evidence for an upper limit to mitotic spindle length. *Current biology*, 18(16):1256–1261, 2008.

L. Xue, I. A. Karpenko, J. Hiblot, and K. Johnsson. Imaging and manipulating proteins in live cells through covalent labeling. *Nature chemical biology*, 11(12):917–923, 2015.

K. Yahata, M. N. Hart, H. Davies, M. Asada, S. C. Wassmer, T. J. Templeton, M. Treeck, R. W. Moon, and O. Kaneko. Gliding motility of Plasmodium merozoites. *Proceedings of the national academy of sciences*, 118(48), 2021.

C.-H. Yang, C. Kasbek, S. Majumder, A. M. Yusof, and H. A. Fisk. Mps1 phosphorylation sites regulate the function of centrin 2 in centriole assembly. *Molecular biology of the cell*, 21(24):4361–4372, 2010.

J. A. Yeoman, E. Hanssen, A. G. Maier, N. Klonis, B. Maco, J. Baum, L. Turnbull, C. B. Whitchurch, M. W. Dixon, and L. Tilley. Tracking glideosome-associated protein 50 reveals the development and organization of the inner membrane complex of Plasmodium falciparum. *Eukaryotic cell*, 10(4):556–564, 2011.

M. Zeeshan, D. J. Ferguson, S. Abel, A. Burrrell, E. Rea, D. Brady, E. Daniel, M. Delves, S. Vaughan, A. A. Holder, K. G. Le Roch, C. A. Moores, and R. Tewari. Kinesin-8b controls basal body function and flagellum formation and is key to malaria transmission. *Life science alliance*, 2(4), 2019a.

M. Zeeshan, F. Shilliday, T. Liu, S. Abel, T. Mourier, D. J. Ferguson, E. Rea, R. R. Stanway, M. Roques, D. Williams, E. Daniel, D. Brady, A. J. Roberts, A. A. Holder, A. Pain, K. G. Le Roch, C. A. Moores, and R. Tewari. Plasmodium kinesin-8X associates with mitotic spindles and is essential for oocyst development during parasite proliferation and transmission. *PLoS pathogens*, 15(10):e1008048, 2019b.

M. Zeeshan, D. Brady, R. R. Stanway, C. A. Moores, A. A. Holder, and R. Tewari. Plasmodium berghei kinesin-5 associates with the spindle apparatus during cell division and is important for efficient production of infectious sporozoites. *Frontiers in cellular and infection microbiology*, 10:638, 2020.

M. Zeeshan, R. Pandey, D. J. Ferguson, E. C. Tromer, R. Markus, S. Abel, D. Brady, E. Daniel, R. Limenitakis, A. R. Bottrill, K. G. Le Roch, A. A. Holder, R. F. Waller, D. S. Guttery, and R. Tewari. Real-time dynamics of Plasmodium NDC80 reveals unusual modes of chromosome segregation during parasite proliferation. *Journal of cell science*, 134(5):jcs245753, 2021a.

M. Zeeshan, R. Rashpa, D. J. Ferguson, S. Abel, Z. Chahine, D. Brady, C. A. Moores, K. G. Le Roch, M. Brochet, A. A. Holder, and R. Tewari. Location and function of all Plasmodium kinesins: key roles in parasite proliferation, polarity, and transmission. *bioRxiv*, 2021b.

M. Zhang, C. Wang, T. D. Otto, J. Oberstaller, X. Liao, S. R. Adapa, K. Udenze, I. F. Bronner, D. Casandra, M. Mayho, J. Brown, S. Li, J. Swanson, J. C. Rayner, R. H. Jiang, and J. H. Adams. Uncovering the essential genes of the human malaria parasite Plasmodium falciparum by saturation mutagenesis. *Science*, 360(6388), 2018.

C. E. Zimmerli, M. Allegretti, V. Rantos, S. K. Goetz, A. Obarska-Kosinska, I. Zagoriy, A. Halavatyi, G. Hummer, J. Mahamid, J. Kosinski, and M. Beck. Nuclear pores dilate and constrict in cellulo. *Science*, 374(6573):eabd9776, 2021.

Acknowledgements

First of all, I would like to thank Julien for his constant support during my PhD starting from the very first *Plasmodium* cell culture basics over plenty of scientific discussions and finally publications and suggestions on my thesis. I am deeply grateful for everything I learned from you during the last four years, for your trust in my work, your encouragement and giving me the opportunity to present my work at various conferences, do the CLEM course in Portugal and spend two months in the lab of Prof. Mathieu Brochet in Geneva.

Second, I would like to thank Prof. Michael Lanzer for this great opportunity to do my doctoral studies in his department, for his suggestions during seminars and TAC meetings and his support when my funding was very uncertain.

I am grateful to Prof. Michael Lanzer, Dr. Sergio Acebrón, Prof. Gislene Pereira, Markus and Julien for fruitful scientific discussions and input in a very supportive and encouraging environment during my TAC meetings. Further, I would like to thank Prof. Michael Lanzer, Dr. Sergio Acebrón, Prof. Gislene Pereira and Dr. Gautam Dey for being part of my examination committee.

Many thanks to Markus for his countless ideas and suggestions during the lab and departmental meetings, his enthusiasm for the special biology of the parasite and many funny moments. Thanks also to Freddy for being "next door" and always open for scientific input and sharing his experiences.

My heartfelt thanks to our collaborator Prof. Mathieu Brochet and his group for the great time in Geneva. Many thanks to Natacha and Lorenzo for helping me with IPs and thanks to Aurélia and Ravish for their help in the lab. Thanks also to the mass spec core facility in Geneva. Furthermore, I would like to thank Aarti, Caty, David and Mary from the lab of Prof. Dominique Soldati-Favre for their support. I am thankful for Prof. Paul Guichard/Dr. Virginie Hamel for providing their U-ExM protocol and especially for Dr. Eloïse Bertiaux for showing me the entire hands-on work of the protocol and answering my questions.

I am very grateful for all the help and support I got from the microscopy core facilities. Many thanks to Vibor and Silvia from the IDIP for their constant support concerning various imaging techniques and instruments. I am deeply grateful for the huge support from the EMCF core facility, most of all to Charlotta for showing me the individual steps of TEM sample preparation, her enthusiasm for *Plasmodium* and my project and her endless help with trouble shooting, tomography and data analysis. Thanks also to Stefan and Sebastian from the facility for their support concerning electron microscopy and sample preparation.

I am very grateful to the entire "Ganzetti" lab. All of you made this lab the best place I can imagine for doing my PhD! Many thanks to Marta, Yannik, Severina and Anja and

all the current and former students in our lab including Ann-Kathrin, Vanessa, Alex, Wendy, Aiste, Marius, Nic, Annika (from Freddy's lab) and all the ones that I might have forgotten here. I am happy for all the scientific and non-scientific discussions, barbecues, board games nights, beer hours, walks and hikes, swimming and boat tours and for all the little funny moments in the lab. Thanks also to Taty and Chris for their great work and support of my project by validating centriolar plaque candidates and characterizing Slp, respectively. I am very grateful to Johanna for establishing the expansion microscopy protocol in our lab and for providing important last minute data for my paper.

Furthermore, I would like to thank Ann-Kathrin for her work on improving our imaging protocol and taking first RescueSTED images, Ju and Marek for acquiring tilted TEM series at the EMBL and for tomogram reconstructions, Nic for generating Centrin-GFP expressing cell lines and Marta for providing the Nup313-HA strain and helping Taty with growth assays. I would like to thank Yannik for the amazing PfCentrin3 antibody and Nicole for help with magnetic purification of schizonts for high pressure freezing.

Last but not least I would like to thank my family.
Vielen Herzlichen Dank an meine Eltern für eure Unterstützung während meines gesamten Studiums und meines PhDs. Ich danke dir, Mama, für die vielen Telefonate, herzlichen Worte und Aufmunterungen und dir, Papa, für die Hilfe bei vielen kleinen und großen Fragen des Lebens und der Technik. Ich bin immer froh aus dem verregneten Heidelberg zu euch ins sonnige Wuppertal zu kommen. Außerdem danke ich Diana, da du es immer schaffst mich mit deiner Lebensfreude und deinem Tatendrang aus dem Alltagstrott zu reißen und Fredi für die Erinnerung was wirklich wichtig ist im Leben.

Vielen Dank an dich, Lukas, für deine Liebe, dass du mir immer zuhörst wenn ich alle alltäglichen Kleinigkeiten berichte, dass du mich mit leckerem Essen verwöhnst und seit fast 6 Jahren dein Leben mit mir teilst.

Appendix A

Supplementary Figures

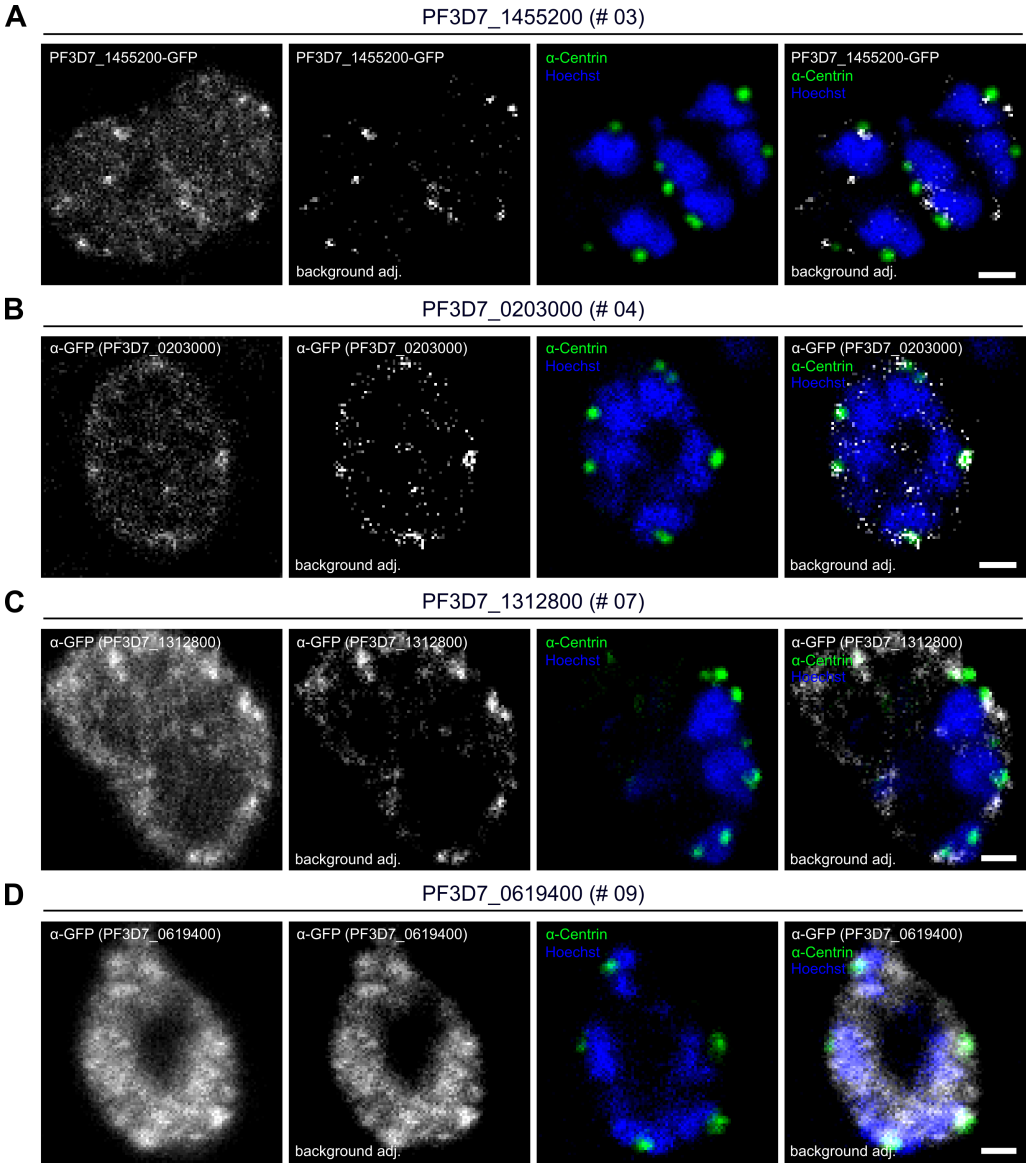

FIGURE A.1: Preliminary localization data of four centriolar plaque candidates during *P. falciparum* blood-stage schizogony. Confocal images show the localization of four centriolar plaque candidates identified by co-immunoprecipitations using PfCentrin1- and 2-GFP expressing NF54 cells and subsequent mass spectrometry analysis. All four candidates were endogenously tagged with GFP and a glmS ribozyme sequence (3D7 GOI-GFP_glmS) and integration confirmed by PCRs. Confocal images show endogenous GFP signal (A) or GFP signal enhanced via an anti-GFP antibody (B, C, D) (grey). Cells were immunolabeled with anti-centrin antibody (green) and DNA stained with Hoechst (blue). Contrast settings were set individually for each cell and stained structure. For each candidate, GFP signals are shown with two different contrast settings; first image with background, second image with adjusted background. Centriolar plaque candidates include the putative methyltransferase PF3D7_1455200 (A), the putative repetitive organellar protein PF3D7_0203000 (B), the uncharacterized protein PF3D7_1312800 (C) and the putative cell division cycle protein 48 homologue PF3D7_061940 (D). Please note that images in (A, B) were acquired on a STED/Resolft microscope (Abberior) in confocal mode, while (C, D) were acquired on an Sp8 (Leica). Images in (A) and (C) show double-infected erythrocytes. All images are single slices; scale bars, 1 µm.

Sfi1-like protein (Slp):

centrin-binding motif based on Suvorova et al., 2015: 6xxxxxxxx6xxx6xxWx
6 = hydrophobic amino acid; x = any amino acid; W = trypthophan

MTDINDIIKEIIYRSADECNFNNEELNFTSILKFFYDITNKYNVKKQICDEIFNKLLIICKNIIDDNS
ITDHDNNIINHHHNNIDNNVDKFNFYYNTNDEYMKTNIKHSDKYQIRDIKNCHNNNNNNNNS
SRENNSYYKNSEYVNPLIILKSDEHKNNINNKNNTCSSIVKINPLYNEKPKEEKLDLYYYDINK
DKKLNNLYSSYLYKNHQKEQKGIIYNDNNNNNINNHNNNIIISYNNQNVPIHKEKYSCVYLIED
DNIKNNGNHNNIIHIDEKSFLHKNNRNLLKLFLNGDIIHNVYNKIIKNKHLKKTNKYSLQDKNSK
MKLYNESNIFFTFYILKKYYHTWFQLSYKQKILQKRLEKYNKVIRKKILIKYYDLWFYYNEKKN
YLKSAYDKFVNKKNKNSLKQFFHNFINKYKKRKKKNFIYLVHIFNEWKNYTKKRKTLQYATK
KITQKKKKKFFLLWKNNFFIKKMKKKKKNEIQNIYNKNLVIKCYVHFILFYKKRKKEHMNYSTI
YDNTKYKLSYKYFSLFIQIYRENIFFKQYYTLYLEKVQNIFFKKYFTILKEYVSKRKKLQTLFLNI
NRNKQINFLMLYMRKWIHRYNEKAKFNNILQIYNDKNKLYIFKKYFHIIKKYKEKSFDLKKKFL
FLYEKKNKEQVQHIFTNWKNYYSINSTKYILLYNKYKYKLLINYFHFLYNYKNYRISKKKKTKQ
MDDYSKNKLKRKAYIKWIFYHKNYKINILTFYNFKNDGNFFVYFILKMLWKYQTIDNKTHSKT
FFDLINFSNININTLIYIHKKYFTKKNIQNNVNIFYENVMFVYKTLNIVFSYIPVLFFVNMNKLK
FNLPYISFSIKMALYKRIFDTWLVDCRRIKQFKNLVNNKLLKNYFMRFFSLIQKKKKLNNEFLK
YKHKRKIILKKKLFSTWVFLWNKYINFRTNFEKFDGNNKKKRIKKIWLKWLAITKENKLKKEKI
VEFFKSLLKKKKKKVWDILNEYVSVCRRKKIQNKIAHLYCMKKYKKKAFMSLFMYSKNVMYF
NTLNNIAQSYLKRLCIIKWRNITREFFKRKKELQNRQYHFDLNIQRKYFRILLLFVHFRAIKKKK
FLHFKEIQYKIWIYQYFNEWKNYIKIKQNKKEFLENMKNLFNRKKKLHFLSKWYTSFIINVKFK
EVEKIIAFKISILTFEKLILYNQKMKRIELFLRNRSKVFICQNIIKRWKHYIKIKRLKKHIRLKNFHL
IKDKYFSTWKKTFEKVRKRKIRESKIYKYRQTKDKNIVHLFYNEWKSVFLQNKNIKHFVYVIN
NHLLYKLKYRSFVVIYKNCEYYSTLQFLFNNFLIDKRSKIKRNVFSILKCNTKNRRTYKKAIRF
FYNNIMSKYFNVIKIYRQRRVTYRKNEQTLINKRKATYFYTIMNFYNFLNKVKYNFFQIRMRV
DNKIKKEFFNIWFLFVMKRKKERNTFLSVLRKRVNKVKSEIFFNMKRRVNKKKYVLLLLNRM
EELIKSKIYRYGINQLKINRKCSKIHEKLYLKMQKKMNQKILEKCLKTLKNRISKKRKRELEKQ
MVSFFCEQLFKKKYFNIICHVSKIKMMERNMIIFKIVNNHLIYLLRRHFHIWKYYIDKKKEYKKK
IELININKKAKIFYFMLYLKIKSNYDNICVLYKIYNLFHSSSCKMINLDEALTYRNKSKCCNIYED
GNYILGYYESQNKDLKDRVYEYMDFALYNKKNILQKYVHLKKKVVMLSKIYNEIKFKDDDLLY
LNKIKNKGKKKQQGIQNHIHICYMLRNSNMSSLLLNYLLMYDYYDMYYFCLHIKKHFNVLYN
YFFNFLSVKMKKLLFKFFKKSVSLSNFIKMVSVTDKDIHQHFKILIFIYYLFNGFIGYYHRNDQ
GGNTMDGNNEMMSDINKIGDDNNNNNIYIIITKVINNFLCIKESYVDEQESVYDMPKNNLKIN
KINLKGSNKLNKKYISKREKKKKCIYVDKKIKRENKNMIIKSCNNKYTVYFNTDQKNKYEKKK
KNVDEYMNSKLNKMSNLNLFMSHVSYISSVGSSNNSREYIISRKEEINEKEKNIRNIHINNIYN
NKNYYHYFYSDKCRSINKMSILKDYKNIQDDLLKKRIEEDMKEYIRQFYEHLKIYILSNFRETD
NSTISIKINYSFLLNVEKNKIIEMYIFFKRFKKVVISWKMYCKYKKERREDDINKMNNIQNKIRK
EIVEKYFGIWILIFNEKVKEIKRKRKIFLKKHIHMIFVSWHKLIQVNNYDKEKFKELKQVCFNRM
KKTYFEKLYLYSIKMKNEKRNYVIIKKQCNNKRKQTFFYVWLLLYQYEKKYYY IHKQMNNKK
LQEYFYKWIYIYEKKQIYIHFCNTLNELFLKKNIFVPIIKQFKFYNYIKEKKDNIEKKYFLIYYNIIK
KNNILNKLQLY IYTSIQYKELKYLFNIWNKKYKKRKICRDELHQIIINKKRKYLDHWLATYKQSK
NNVIKKYMHLNNFKTMLYWNKWMSYHRYMKIIKKNNKYLLLKYFSIYKRKYNTNVVIQNFIKK
KNSKIIKDIFTVLKEYKEVKKYHKHIKEYCNTYYKKKTLKILYSSWLYEYYKIKKIKNVLHYMFKI
YDDKMKRVILNEWITYVNKKRFIKNIHNNIVKSKNNIIIKKCFFMWNRLYNFLNKKKRNIMYTYI
HIWNIHYTFVGFIKKINIYLYNIYQNNIFSFYYILKKKNENYYCLQEKGKFVFIQNQICEYLKYKN
DILYDTFRSLYMYKEKNKTLRKYLELYKMRNIQKEKRKIFFILLKYKNIKKKKKFLLSNLYTNIM
NQKKEYLLKKYFIILTNIYFYNYHLNICAKTINDRREKRIINFYLNKWIEYIKECKQLNHLDMLS
QQFLNYRRRSEFIISLKQYYVEHKWKNYCEYNSLIFYKKVQERMLSNFIKFWIIKSKQFEYFQ
QKLDEFQKQYNKNIIKKYFFLLIFSINKIKIEKKNFDIVHLKRIKMIKYKVFYYLYDMSMSSIKKY
EQVMTTLKDQKGNEKYLKRKFYFAFFNYIKYKNRIHHIFITLQEKKNLNLLRKHFYIFIYKYVT
NMNHYKYYYYNKFLSLWKYYIVMRKGYPSSEKTDEGESISGQVEDDEEDDDIDEDDDDIDE
DDDDIDEDDDNVDEDDDNVDEEDDNVDEDDVEEGGIHDEKEDDHDKKEDVHNDENDINKY
NNDDNHNEEENSSYEKFSSENHINNKDHVDFSVDMFDDEINVQKQTKTFDNSSNSNDSLG

Sfi1-like protein (Slp):

centrin-binding motif based on Kilmartin, 2003: F/LxxWK/R
F = Phenylalanine; L = Leucine; x = any amino acid; W = trypthophan;
K = Lysine ; R = Arginine

MTDINDIIKEIIYRSADECNFNNEELNFTSILKFFYDITNKYNVKKQICDEIFNKLLIICKNIIDDNS
ITDHDNNIINHHHNNIDNNVDKFNFYYNTNDEYMKTNIKHSDKYQIRDIKNCHNNNNNNNNS
SRENNSYYKNSEYVNPLIILKSDEHKNNINNKNNTCSSIVKINPLYNEKPKEEKLDLYYYDINK
DKKLNNLYSSYLYKNHQKEQKGIIYNDNNNNNINNHNNNIIISYNNQNVPIHKEKYSCVYLIED
DNIKNNGNHNNIIHIDEKSFLHKNNRNLLKLFLNGDIIHNVYNKIIKNKHLKKTNKYSLQDKNSK
MKLYNESNIFFTFYILKKYYHTWFQLSYKQKILQKRLEKYNKVIRKKILIKYYDLWFYYNEKKN
YLKSAYDKFVNKKNKNSLKQFFHNFINKYKKRKKKNFIYLVHI FNEWKNYTKKRKTLQYATK
KITQKKKKKF FLLWK NNFFIKKMKKKKKNEIQNIYNKNLVIKCYVHFILFYKKRKKEHMNYSTI
YDNTKYKLSYKYFSLFIQIYRENIFFKQYYTLYLEKVQNIFFKKYFTILKEYVSKRKKLQTLFLNI
NRNKQINFLMLYMRKWIHRYNEKAKFNNILQIYNDKNKLYIFKKYFHIIKKYKEKSFDLKKKFL
FLYEKKNKEQVQHI FTNWK NYYSINSTKYILLYNKYKYKLLINYFHFLYNYK NYRISKKKKTKQ
MDDYSKNKLKRKAYIKWIFYHKNYKINILTFYNFKNDGNFFVYFILKMLWKYQTIDNKTHSKT
FFDLINFSNINININTLIYIHKKYFTKKNIQNNVNIFYENVMFVYKTLNIVFSYIPVLFFVNMNKLK
FNLPYISFSIKMALYKRIFDTWLVDCRRIKQFKNLVNNKLLKNYFMRFFSLIQKKKKLNNEFLK
YKHKRKIILKKKLFSTWVFLWNKYINFRTNFEKFDGNNKKKRIKKIWLKWLAITKENKLKKEKI
VEFFKSLLKKKKKKVWDILNEYVSVCRRKKIQNKIAHLYCMKKYKKKAFMSLFMYSKNVMYF
NTLNNIAQSYLKRLCIIKWRNITREFFKRKKELQNRQYHFDLNIQRKYFRILLLFVHFRAIKKKK
FLHFKEIQYKIWIYQY FNEWK NYIKIKQNKKEFLENMKNLFNRKKKLHFLSKWYTSFIINVKFK
EVEKIIAFKISILTFEKLILYNQKMKRIELFLRNRSKVFICQNIIKRWKHY IKIKRLKKHIRLKNFHL
IKDKY FSTWK KTFEKVRKRKIRESKIYKYRQTKDKNIVHLFYNEWKSVFLQNKNIKHFVYVIN
NHLLYKLKYRSFVVIYKNCEYYSTLQFLFNNFLIDKRSKIKRNVFSILKCNTKNRRTYKKAIRF
FYNNIMSKYFNVIKIYRQRRVTYRKNEQTLINKRKATYFYTIMNFYNFLNKVKYNFFQIRMRV
DNKIKKEFFNIWFLFVMKRKKERNTFLSVLRKRVNKVKSEIFFNMKRRVNKKKYVLLLLNRM
EELIKSKIYRYGINQLKINRKCSKIHEKLYLKMQKKMNQKILEKCLKTLKNRISKKRKRELEKQ
MVSFFCEQLFKKKYFNIICHVSKIKMMERNMIIFKIVNNHLIYLLRRH FHIWK YYIDKKKEYKKK
IELININKKAKIFYFMLYLKIKSNYDNICVLYKIYNLFHSSSCKMINLDEALTYRNKSKCCNIYED
GNYILGYYESQNKDLKDRVYEYMDFALYNKKNILQKYVHLKKKVVMLS KIYNEIKFKDDDLLY
LNKIKNKGKKKQQGIQNHIHICYMLRNSNMSSLLLNYLLMYDYYDMYYFCLHIKKHFNVLYN
YFFNFLSVKMKKLLFKFFKKSVSLSNFIKMVSVTDKDIHQHFKILIFIYYLFNGFIGYYHRNDQ
GGNTMDGNNEMMSDINKIGDDNNNNNIYIIITKVINNFLCIKESYVDEQESVYDMPKNNLKIN
KINLKGSNKLNKKYISKREKKKKCIYVDKKIKRENKNMIIKSCNNKYTVYFNTDQKNKYEKKK
KNVDEYMNSKLNKMSNLNLFMSHVSYISSVGSSNNSREYIISRKEEINEKEKNIRNIHINNIYN
NKNYYHYFYSDKCRSINKMSILKDYKNIQDDLLKKRIEEDMKEYIRQFYEHLKIYILSNFRETD
NSTISIKINYSFLLNVEKNKIIEMYIFFKRFKKVVISWKMYCKYKKERREDDINKMNNIQNKIRK
EIVEKYFGIWILIFNEKVKEIKRKRKIFLKKHIHMIFVSWHKLIQVNNYDKEKFKELKQVCFNRM
KKTYFEKLYLYSIKMKNEKRNYVIIKKQCNNKRKQTFFYVWLLLYQYEKKYYYIHKQMNNKK
LQEYFYKWIYIYEKKQIYIHFCNTLNELFLKKNIFVPIIKQFKFYNYIKEKKDNIEKKYFLIYYNIIK
KNNILNKLQLYIYTSIQYKELKYLFNIWNKKYKKRKICRDELHQIIINKKRKYLDHWLATYKQSK
NNVIKKYMHLNNFKTMLYWNKWMSYHRYMKIIKKNNKYLLLKYFSIYKRKYNTNVVIQNFIKK
KNSKIIKDIFTVLKEYKEVKKYHKHIKEYCNTYYKKKTLKILYSSWLYEYYKIKKIKNVLHYMFKI
YDDKMKRVILNEWITYVNKKRFIKNIHNNIVKSKNNIIIKKCFFMWNRLYNFLNKKKRNIMYTYI
HIWNIHYTFVGFIKKINIYLYNIYQNNIFSFYYILKKKNENYYCLQEKGKFVFIQNQICEYLKYKN
DILYDTFRSLYMYKEKNKTLRKYLELYKMRNIQKEKRKIFFILL KYKNIKKKKKFLLSNLYTNIM
NQKKEYLLKKYFIILTNIYFYNYHLNICAKTINDRREKRIINFYLNKWIEYIKECKQLNHLDMLS
QQFLNYRRRSEFIISLKQYYVEHKWKNYCEYNSLIFYKKVQERMLSNFIKFWIIKSKQFEYFQ
QKLDEFQKQYNKNIIKKYFFLLIFSINKIKIEKKNFDIVHLKRIKMIKYKVFYYLYDMSMSSIKKY
EQVMTTLKDQKGNEKYLKRKFYFAFFNYIKYKNRIHHIFITLQEKKNLNLLRKHFYIFIYKYVT
NMNHYKYYYYNKF LSLWK YYIVMRKGYPSSEKTDEGESISGQVEDDEEDDDIDEDDDDIDE
DDDDIDEDDDNVDEDDDNVDEEDDNVDEDDVEEGGIHDEKEDDHDKKEDVHNDENDINKY
NNDDNHNEEENSSYEKFSSENHINNKDHVDFSVDMFDDEINVQKQTKTFDNSSNSNDSLG

FIGURE A.2: Predicted centrin-binding repeat sequences in *P. falciparum* Sfi-like protein (Slp). Centrin-binding sequences were based on previous studies by Suvorova et al. (2015) and Kilmartin (2003), identifying 16 and 7 repeat regions in *Plasmodium* Slp, respectively. Please note that the complete repeat region determined by Kilmartin (2003) does not exist in any *Plasmodium* protein. Therefore, only the part of the sequence which is more conserved was used.